Numerical modelling of the stress regime at subduction zones

G. D. Waghorn

NUMERICAL MODELLING OF THE STRESS REGIME AT SUBDUCTION ZONES

by

G.D. WAGHORN

A thesis submitted to the University of Durham for the Degree of Doctor of Philosophy

Graduate Society November 1984

ABSTRACT

The stress regime at subduction zones has been modelled using a visco-elastic, quadratic isoparametric finite element model. An isoparametric model is used because it performs more accurately than constant strain triangular elements (CST) and also allows curved sided elements to be introduced.

A method for modelling the frictional sliding on isoparametric fault elements has been developed by extending Mithen's (1980) CST model. The resulting method is suitable for modelling the deformation on both plane and listric, normal and thrust faults. Graben widths predicted by normal fault models agree with analytic solutions and this implies that Mithen's CST models failed to do so because they were too stiff.

Application of this model to subduction zones demonstrates that the slab pull force induces tension in the subducting plate and compression in the overlying plate. Part of the lateral variation in stress which is observed at all subduction zones is therefore inferred to arise from the slab pull force. Differences in the magnitude of these stresses at different subduction zones may therefore be accounted for by local variations in the magnitude or dip of the slab pull force, and also by the extent of the coupling across the plate boundary.

Various forces account for the stress regime in back arc regions. Tensional stress is generated by lateral density variations, and the heating and shearing caused by slab induced convection. Compressive stress, arising from the slab pull force, is superimposed upon this. The magnitude of the compression, however, is dependent upon the dip and size of the slab pull force and also the degree of mechanical coupling between the plates at the subduction zone fault. Local variations in the magnitude of the compressive stress may therefore explain why the stress regime is observed to be so variable in back arc regions, and is more commonly tension than compression.

ACKNOWLEDGEMENTS

I would like to express my gratitude to my supervisor, Prof. M.H.P. Bott, for his helpful criticisms during the 3 years of my research, and to Dr. M.D. Linton for many illuminating discussions about finite element techniques. I would also like to thank M.J. Smith for forwarding some final plots to me in London.

This research was done whilst I was in receipt of a studentship from NERC, to whom I am very grateful.

Finally, I would like to express my gratitude to B.P. for providing the support and facilities to complete this thesis.

" On the first day they had gone up to the
mountains and had a picnic in the pine forest.
'We got a course in picnicking at this university,'
said Dr. Bourbon.
'It's called geology, but it's really picnicking' "

M. Bradbury

CONTENTS

CHAPTER 1

AN INTRODUCTION TO SUBDUCTION ZONES

The aim of this thesis is to use the finite element method to model the lateral variation in the stress regime at subduction zones. The finite element methods are developed in chapters 2 to 6, and they are applied to subduction zones in chapter 7. This chapter is therefore an introduction to current ideas on the location, structure, stress regime, sources of stress and the physical processes occuring at subduction zones.

Some of the most active tectonic provinces in the world are located in the vicinity of the deep sea trenches which border the Pacific Ocean, the Scotia Sea, the Antilles, the Aegean and Java-Sumatra. Deep sea trenches are typically V-shaped depressions in the ocean floor which are persistent for thousands of kilometres and are associated with the largest known negative isostatic anomalies in the world. These regions are the most seismically active in the world and release over 90% of the global earthquake strain energy. This earthquake activity, which occurs mainly landwards of deep sea trenches, is characterised by diffuse shallow seismic activity and by deep and intermediate earthquakes concentrated on planes which dip at around 45 degrees away from the oceans. These planes are known as Benioff-Wadati zones. Another characteristic feature of these areas are the active andesitic volcanic chains which occur at around 150 km landwards of the deep sea trenches and above the Benioff-Wadati zone.

During the last twenty years it has been realised that the tectonic activity which occurs at deep sea trenches originates from a common cause, the subduction of oceanic lithosphere. In the subduction hypothesis deep sea trenches are considered to be the sites at which two lithospheric plates are converging with the result that an oceanic plate is thrust beneath the other plate and recycled into the mantle. This concept forms an integral part of the theory of plate tectonics.

The evidence which supports the hypothesis that subduction occurs at deep sea trenches is discussed in the next section.

1.1 Evidence For Subduction

The concept that the oceanic lithosphere is being subducted arises from two important geophysical observations. The first of these is that new rigid plates of oceanic lithosphere are being created at mid ocean ridges by the process of sea floor spreading (Vine and Matthews, 1963). The second piece of evidence, which has recently been reviewed by Bott (1982a), is that the earth is probably not expanding by any significant amount. The logical consequence of these two observations is that oceanic lithosphere must be continuously recycled (i.e. subducted) back into the mantle somewhere.

This process is probably occuring at deep sea trenches. The observations which support this hypothesis are mainly seismological but other geophysical evidence has been important in demonstrating the feasibility of this concept.

1.1.1 Seismological evidence

The most convincing evidence which supports the hypothesis that subduction occurs at deep sea trenches is based on the following seismological observations (Isacks et al, 1968):

1. Almost all deep and intermediate earthquakes are spatially concentrated at deep sea trenches.

2. The hypocentres of these earthquakes fall on a plane which dips at 30-80 degrees away from the trench and towards the volcanic arc (Benioff, 1954; Sykes, 1966; Isacks and Barazangi, 1977). This plane is known as the Benoiff-Wadati zone.

3. The Benioff-Wadati zone intersects the earth's surface close to the axis of deep sea trenches (Sykes, 1966).

4. The Benioff-Wadati zone is located in the upper 30 km of an anomalous region of high Q in an otherwise low Q upper mantle (Oliver and Isacks, 1967). This tongue of high Q is approximately 100 km thick and is continuous with, and has similar properties to, the oceanic lithosphere (Figure 1.1). This feature was initially observed in the the Fiji-Tonga region but it has subsequently been observed at other subduction zones (e.g. Utsu, 1971).

   Recent investigations have demonstrated that a region of extremely low Q occurs immediately above the high Q tongue (Barazangi and Isacks, 1971).

5. Additional evidence, which was reviewed by Isacks et al (1968), comes from the focal mechanism solutions of the earthquakes in

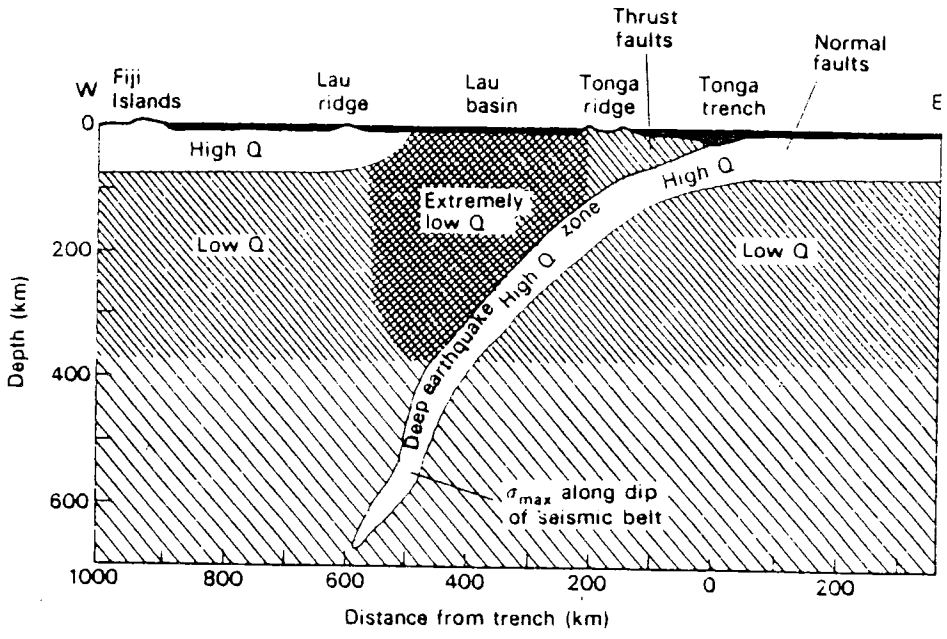

Figure 1.1: Variation of Q in the top 700 km of the earth (Barazangi and Isacks, 1971).

subduction zones. The shallow earthquakes have two types of focal mechanisms. These are tensional in the subducting plate and compressive in the overlying plate. This suggests that underthrusting is occuring in these regions.

Intermediate and deep earthquakes have their axes of maximum and minimum principal stress aligned down the dip of the Benioff-Wadati zone and intermediate principal stress parallel and horizontal to the strike of the Benioff Zone. These observations are consistent with the release of stress which would occur within a sinking plate of oceanic lithosphere (Isacks and Molnar, 1969).

Double planed Benioff-Wadati zones have been observed between 100 and 150 km depth at some, but not all, subduction zones (Fujita and Kanamori, 1981). The earthquakes on the upper plane are located near to the top of the subducting plate and have compressive focal mechanisms. About 30 km beneath this a lower plane of earthquakes with tensional focal mechanisms is observed. This stress regime may be caused either by thermal stress (Woodward, 1975), an unbending (Samowitz and Forsyth, 1981) or a sagging of the subducting plate (Sleep, 1979).

This evidence suggests that at deep sea trenches a plate of rigid oceanic lithosphere is recycled into the weak upper mantle.

1.1.2 Other geophysical evidence

There are four main other geophysical observations which support the subduction hypothesis. These are:

1. In some seismic reflection profiles across the accretionary prism the convex surface of the oceanic basement can be seen dipping at 5 to 10 degrees towards the volcanic arc (e.g. Seely et al, 1974) Some of the most striking examples of this have been obtained in the Lesser Antilles island arc (Westbrook, 1982) where the oceanic basement can be traced for over 50 km from the trench axis.

2. The magnetic lineations in the North-East Pacific are discordant with, and truncated at, the axis of the Aleutian trench (Pitman and Hayes, 1968). This suggests that the oceanic lithosphere of the Pacific plate has been subducted at the Aleutian trench.

3. The positive geoid anomaly which occurs landwards of deep sea trenches is partially explained by the presence of a high density slab of subducting oceanic lithosphere at depth (Davies, 1981; Chapman and Talwani, 1982).

4. The geometry of the present day plate motions can be described as the rotation of a series of rigid plates on a sphere (McKenzie and Parker, 1967; Morgan, 1968). The pole of rotation and the relative angular velocity between each pair of plates can be determined by inverting the observed rate and direction of sea-floor spreading, the orientation of transform faults and the direction of the slip vectors of the thrust earthquakes at subduction zones (Le Pichon, 1968; Minster et al, 1974; Minster and Jordan, 1978). These studies demonstrate that several pairs of plates are converging at deep-sea trenches (e.g. the Pacific and Eurasian plates, and the Nazca and South American plates). This crustal shortening must be mainly accomodated by subduction. It is therefore predicted that the average rate of subduction at

the deep sea trenches which border the Pacific is about 9 cm/yr.

1.2 Morphology And Deep Structure Of Subduction Zones

In this thesis the term subduction zone is used in its broadest sense to describe the wide range of features which are produced by, or associated with, the subduction of oceanic lithosphere. Subduction zones have characteristic morphological features which are continuous for thousands of kilometres along their strike. The major structural units will therefore be defined by describing a cross section through a typical subduction zone.

The evidence discussed in Section 1.1 suggests that a subduction zone is formed where two lithospheric plates, of which at least one is oceanic, are converging. These two plates are referred to as the subducting and overlying plates. The subducting plate is defined as the plate which is bent into the mantle, whilst the overlying plate is the one which overrides the subducting plate and suffers little vertical displacement. The subducting plate is always composed of oceanic lithosphere. This is because continental lithosphere has a thick low density crust which is too buoyant to be subducted (McKenzie, 1969). The overlying plate, however, can be composed of either oceanic or continental lithosphere. Where the overlying plate is oceanic we refer to it as an island arc subduction zone, and where the overlying plate is continental we refer to it as an active continental margin subduction zone. Island arcs are common in the West Pacific whilst active continental margins are common in the East Pacific. The detailed morphology and deep structure of island arcs (figure 1.2) and active continental margins (figure 1.3), however, is similar and therefore the description which is given below is common to both types unless stated otherwise.

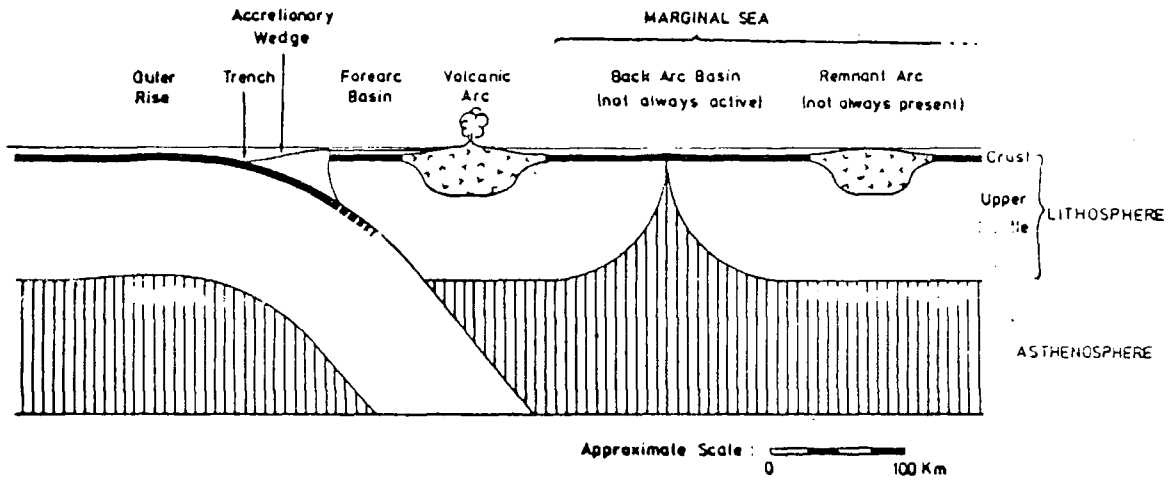

Figure 1.2: Morphologic features of island arc subduction zones.

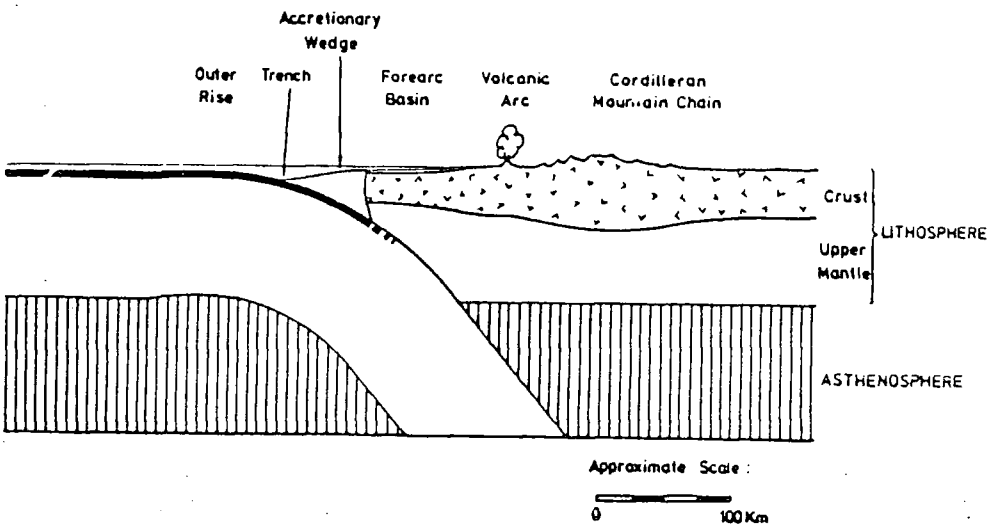

Figure 1.3: Morphologic features of active continental margin subduction zones.

The topography of the subducting plate in the vicinity of the trench exhibits remarkable similarity between different geographic regions (Hayes and Ewing, 1970). The characteristic features are a depression known as the deep sea trench and a positive deflection of the sea floor known as the outer rise. The outer rise has a maximum amplitude of 300-500 metres above undisturbed sea floor at 120-150 km from the trench axis. Between the outer rise and the trench axis the sea floor is convex and dips gently downwards at 2-5 degrees reaching its maximum depth at the trench axis. The bottom of the trench is generally covered by a thin layer of undeformed sediment, although up to 2 km thick accumulations occur in the Chile trench (Kulm et al., 1977) and much thicker deposits occur in the Lesser Antilles arc where the trench is swamped (Westbrook, 1975). Gravity profiles across the trench-outer rise system mirror the topography and typically have a positive amplitude of about 50 mgal over the outer rise and a low of about -200 mgal over the trench (Watts and Talwani, 1974). This correlation between the topography and gravity is generally attributed to the flexure of the subducting oceanic lithosphere as it approaches the trench.

The subsurface geometry of the subducting plate is inferred from earthquake hypocenters. At shallow depths these occur in the interplate shear zone and the wedge of the overlying plate. At intermediate and great depths they occur near the top of the subducted slab. Isacks and Barazangi (1977) reviewed the distribution of hypocenters at major subduction zones and demonstrated that above 150 km they are located on a curve with a radius of 150-300 km, while below this depth they lie on a plane with a constant dip of 30 to 80 degrees. This suggests that the subducting plate is bent in the vicinity of the interplate shear zone but descends into the mantle as a planar body. The deepest earthquakes in the Benioff-Wadati zones varies between 150 and 680 km.

A forearc complex lies landwards of the trench and seawards of the volcanic arc at all subduction zones (Dickinson and Seely, 1979). It is composed of two main units, an accretionary wedge and a forearc basin. The accretionary wedge lies between the overlying plate and the trench. It is bounded at depth by the subducting plate, and is mainly composed of oceanic sediments scraped off the subducting oceanic plate. This unit is characteristically 50-150 km wide and 10-25 km thick at its contact with the overlying plate. The forearc basin lies between the volcanic arc and the accretionary wedge and it is composed of terriginous sediments deposited on the overlying plate.

A volcanic arc lies 150-250 km landwards of the trench axis and 100-150 km above the subducting plate (Isacks and Barazangi, 1977). The volcanic arc is characterised by andesitic volcanism and the emplacement of plutons at depth. This causes the arc to develop into a mountain belt or a chain of mountainous islands. The volcanic arc is absent in Peru and Central Chile, possibly due to the absence of an asthenospheric wedge between the subducting plate and the overlying plate because of the low dip of the Benioff zone in this region (Isacks and Barazangi, 1977).

The morphology of the region behind the arc at active continental margins is generally dominated by cordilleran mountain chains. At island arc subduction zones the back arc area is composed of oceanic lithosphere which forms marginal seas. A back arc basin exists behind the volcanic arc at some subduction zones. Back arc basins are characterised by thin sediment cover, active shallow seismic activity, high heat flow, and magnetic lineations. They often separate the active volcanic arc from an inactive remnant volcanic arc (Karig, 1971). This suggests that back arc basins are usually formed by episodes of sea floor spreading.

1.3 Thermal Structure Of Subduction Zones

The concept that the oceanic lithosphere is subducted into the mantle along deep sea trenches has two important implications for the thermal structure of subduction zones. The first of these relates to the temperature distribution within the subducting oceanic lithosphere and the second relates to the thermal regime in the overlying plate and asthenospheric wedge.

1.3.1 Thermal structure of the subducting plate

McKenzie (1969) demonstrated quantitatively that the subducted oceanic lithosphere must remain significantly cooler than the surrounding hot upper mantle down to considerable depth because of the low thermal conductivity of the lithosphere. Realistic thermal models of the subduction process have subsequently been developed to include the effects of shear heating along the slip zone at the slab-mantle contact and the effect of phase changes in the subducting lithosphere (Minear and Toksoz, 1970 a, b; Hasbe et al, 1971; Toksoz et al, 1971, 1973; Turcotte and Schubert 1971; Griggs, 1972; Schubert et al, 1975; Toksoz and Hsui, 1979). All of these models show the same general pattern of geotherms (figure 1.4) in which the subducting plate retains its relatively low temperature to great depths and the coolest part of the slab lies between its top surface and its centre. These models indictate that the temperature regime in the subducting plate is a function of its thermal conductivity, descent velocity, thickness (i.e. age) and angle of descent.

Part of the success of this model is that it explains some of the seismological observations at deep sea trenches. The first is that the presence of a cool oceanic plate explains the high Q tongue which is observed beneath most subduction zones. The second is that the

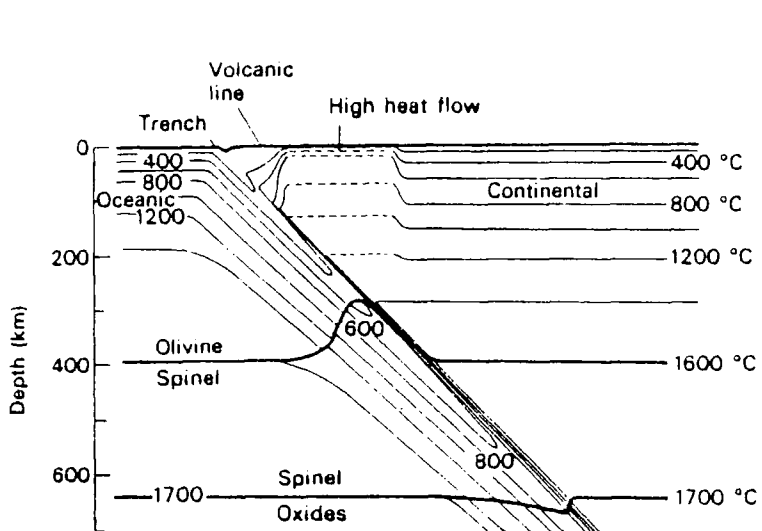

Figure 1.4: Thermal structure of subduction zones (Schubert et al, 1975)

Benioff-Wadati zone of seismicity occurs in the upper section of the subducting plate because temperatures remain low enough to enable brittle fracture to occur. Finally, the variation in the depth of the deepest earthquakes at different subduction zones can be qualitatively explained by the depth at which the subducting plate reaches a critical temperature above which brittle fracture cannot occur (Molnar et al., 1979; Wortel, 1982).

An important implication of these models is that the subducting plate has a large negative buoyancy. This arises because the subducting oceanic plate is cooler, and consequently denser, than the surrounding asthenosphere and also because some phase changes to denser mineralogies occur at shallower depths within the slab than in the adjacent mantle.

1.3.2 The thermal regime of the overlying plate and the asthenospheric wedge

The volcanic arc and back arc region of the overlying plate are sites of active volcanism, high heat flow (Watanbe et al, 1978) and are underlain by a region of very low Q (Barazangi and Isacks, 1971; Barazangi et al, 1975). These observations suggest that the asthensophere is hot in these regions and there is an associated thinning of the overlying lithosphere.

The possibility that this hot region is caused by the subducting plate inducing a viscous drag convective flow in the overlying asthenospheric wedge was initially proposed by McKenzie (1969). He demonstrated that such a flow would cause upwelling of hot material in back arc regions which has the combined effect of shearing and heating of the overlying plate. More sophisticated models of this flow have recently been developed but they mainly confirm the potency of this mechanism in producing the observed heat

flow in back arc regions (e.g. Toksoz and Hsui, 1978). These authors have implied from these models that this flow could also provide the major driving force of back arc spreading.

An additional process which may contribute to the development of the hot, very low Q zone in the asthenospheric wedge and the surface andesitic volcanism is the release of water from the subducted oceanic crust (Ringwood, 1977).

1.4 The Observed State Of Stress At Subduction Zones

The first aim of this section is to review the observed state of stress at subduction zones. These observations will be used to constrain the models which will be developed in chapter 7. The second aim is to review current ideas on the origin of the stress regime at subduction zones.

The present-day state of stress in the the lithosphere can be determined by three main methods. The first is to infer the principal stress orientations from the focal mechanisms of earthquakes. This method can only be used in limited areas, such as new plate boundaries, which are seismically active. The second method is to infer the principal stress orientation from stress sensitive geological structures. This method requires reliable dating of the structures and is restricted to geographically accessible areas, but it is useful in regions where focal mechanism studies are absent. The third method is to evaluate the stress regime using in situ techniques (McGarr and Gay, 1978). These methods are restricted to geographically accessible areas and have not been applied at subduction zones.

The subducting plate and the leading edge of the overlying plate are both seismically active and consequently their stress regime can generally be inferred from seismic focal mechanism solutions. The back arc area, however, is less seismically active and consequently the stress regime is principally inferred from stress sensitive geological features.

The state of stress is observed to be regionally consistent along the strike of subduction zones. The stress regime at subduction zones can therefore be adequately modelled in two dimensions. The observed state of stress is consequently described in this section as a two dimensional cross section through the tectonic provinces of a subduction zone.

1.4.1 Trench-outer rise system

Seismic reflection profiles show that the seismic basement and overlying sediments in the trench-outer rise system are dissected by numerous normal faults (Ludwig et al, 1973). The earthquakes in this area are located at depths of less than 25 km and are inferred from their focal mechanism solutions to be produced by horizontal tensional stresses which are orientated normal to the trench axis (Chapple and Forsyth, 1979). This stress pattern is generally considered to result from the flexure of the oceanic lithosphere as it is bent into the subduction zone (e.g. Watts and Talwani, 1974).

Recently, however, Christensen and Ruff (1983) have presented evidence which suggests that the state of stress in this region may be more complicated. They demonstrated that a small number of compressional earthquakes are observed in the shallow portion of the subducting plate prior to major subduction zone earthquakes. This evidence suggests that horizontal compressive stress may build up in the trench-outer rise

immediately before major underthrusting occurs.

1.4.2 The leading edge of the overlying plate

The leading edge of the overlying plate, which comprises the region between the trench axis and the volcanic arc, is the most seismically active environment in the world. It is characterised by numerous shallow earthquakes. Kanamori (1977) demonstrated that ten great earthquakes (magnitude greater than 7.5) releasing over 90% of the worlds total seismic energy occurred in this region between 1904 and 1976. He also demonstrated that these earthquakes occurred predominantly on low angle thrust faults. The numerous smaller magnitude earthquakes which occur in this region are also considered to be produced by thrust faults (Stauder, 1968; 1975). Seismic reflection profiles across the sedimentary wedge have also shown that the major structural features in this region are landward dipping thrust faults (Dickenson and Seely, 1979).

The observation that the deformation at the leading edge of the overlying plate occurs almost exclusively on low angle thrust faults suggests that the principal stress in this region is predominantly horizontal compression orientated perpendicular to the trench axis. It is generally considered that this stress regime is caused by the relative motion of the two converging plates (e.g. Isacks et al, 1968). This interpretation is supported by the observed surface deformation which follows large thrust earthquakes (e.g. Plafker, 1965).

Kanamori (1977) demonstrated that the magnitude of the compression in this region may vary between subduction zones. He has shown that:

1. Great thrust earthquakes are spatially concentrated at certain subduction zones.

2. At the subduction zones where great thrust earthquakes occur (e.g. Chile, Alaska, the Aleutians and Kuril-Kamchatka) the seismic slip rate (estimated from the displacement on the rupture plane and the recurrence time) is equal to the displacement predicted by the kinematic plate motions. These subduction zones correlate with strong regional compression in the overlying plate.

3. At subduction zones where great earthquakes do not occur (e.g the Marianas, Izu-Bonin, Java-Sumatra and Tonga-Kermadec), the seismic slip rate is less than the displacement predicted by the kinematic models of plate motion. These subduction zones are characterised by tensional stress in the back arc areas.

Kanamori has explained these observations by a model in which the degree of mechanical coupling of the plates varies between subduction zones. He suggested that where the coupling is strong great earthquakes occur and the stress is regional compression, but where the coupling is weak great earthquakes are absent and tensional stresses may occur in the back arc areas. This model suggests that the mechanical coupling between the plates controls the amount of compression which is transmitted into the overlying plate.

Ruff and Kanamori (1983a, 1983b) demonstrated that the thrust earthquakes at coupled subduction zones have relatively larger asperities (regions resisting motion on the fault plane) than those at uncoupled subduction zones. They suggested that the magnitude of the horizontal compressive stress at the leading edge of the overlying plate is

proportional to the ratio of the area of the asperites to the total area of the fault plane.

1.4.3 Subducting plate

Intermediate depth earthquakes occur within the cool, elastic portion of the descending lithospheric plate (Isacks et al, 1968; Stefani et al, 1982). Isacks and Molnar (1969; 1971) demonstrated that the focal mechanisms of these earthquakes indicate that the principal axis of either tension or compression is aligned down the dip of the subducting plate. The dominant downdip stress in the slab is spatially variable (fig 1.5) which Isacks and Molnar explained in terms of the depth to which the subducting plate penetrates (Fig 1.6). In this model tensional stresses dominate short slabs because they sink under their own weight without encountering significant resistance from the surrounding asthenosphere. Slabs which penetrate into and beyond the mantle transition zone, however, encounter progressively more resistant mantle so that compression is transmitted up the subducting plate.

The results of a recent survey of intermediate focal mechanisms by Fujita and Kanamori (1981) are shown in figure 1.7. There are two significant differences between these results and those of Isacks and Molnar. The first is the recognition that double seismic zones occur at intermediate depths in some, but not all, subducting slabs. The second is that recently available focal mechanisms for the 650 km deep subducting plates in the Marianas and and Kermadec areas are predominantly tensional. Fujita and Kanamori pointed out that these results do not agree with the depth of penetration model and proposed that the dominant factors which control the stress regime in the descending plate are the convergence rate and the age of the subducting lithosphere (figure 1.8):

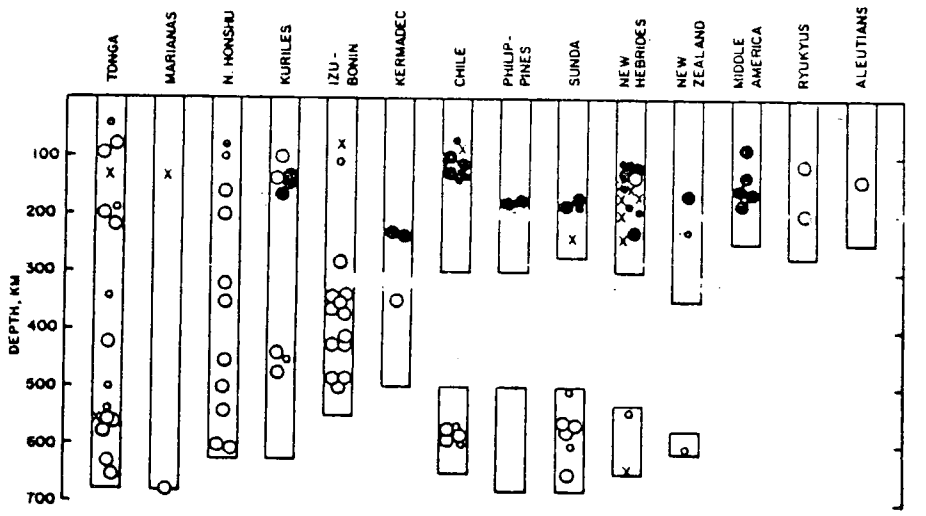

Figure 1.5: Focal mechanisms of deep and intermediate earthquakes (Isacks and Molnar, 1969). Symbol o indicates compression and symbol ● represents tension.

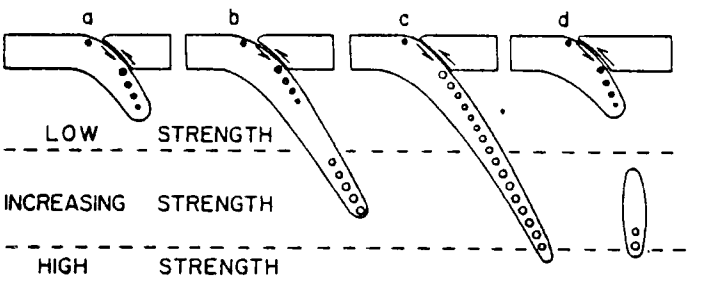

Figure 1.6: Depth of penetration model (Isacks and Molnar, 1969).

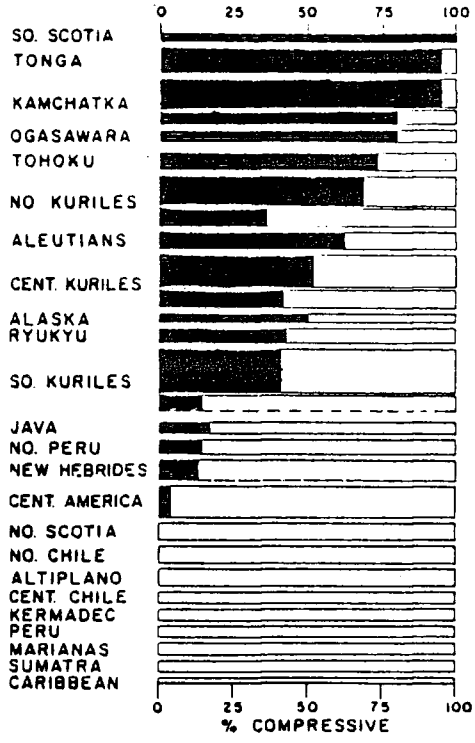

Figure 1.7: Focal mechanisms of intermediate earthquakes (Fujita and Kanamori, 1981).

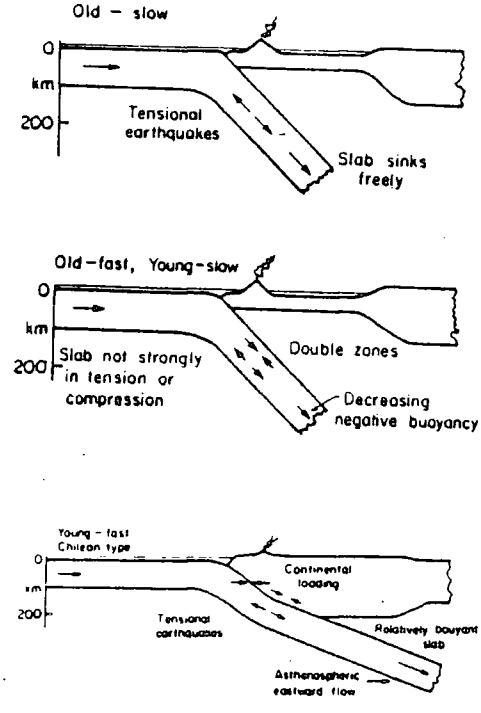

Figure 1.8: Model of intermediate stresses in the subducted plate (Fujita and Kanamori, 1981).

1. Old and slow slabs: The state of stress in old slabs with a low convergence rate is dominantly tensional. This is because the old lithosphere has a large negative buoyancy and therefore tends to sink into the mantle faster than the plates are converging. This causes the subducting plate to 'pull' itself into the mantle and therefore tensional streses dominate it.

2. Old and fast, and young and slow: These conditions favour the development of double seismic zones. This is because the convergence rate is almost equivalent to the age controlled rate at which the slab is sinking into the mantle and therefore local effects such as unbending (Engdahl and Scholz, 1977), sagging (Sleep, 1979), or thermal effects (Veith, 1977) dominate the stress in the slab and produce double seismic zones.

3. Young and fast: Under these conditions compression dominates the sinking plate. This is because the convergence rate is faster than the speed at which the slab is sinking due to its negative buoyancy, and therefore, the subducting plate is pushed into the mantle and is consequently dominated by compressional stresses.

1.4.4 Back arc regions

Because of the limited seismic activity in the back arc areas of subduction zones, the stress regime has to be principally inferred from stress sensitive geological features and marine observations. These observations have shown that, unlike other provinces associated with subduction zones the dominant horizontal principal stress in back arc areas varies from region to region (Table 1.1).

SUBDUCTION ZONE	STATE OF STRESS	REFERENCE
Island arcs		
Tonga-Kermadec	Tensional	Weissel (1981)
New Hebrides	Tensional	Karig & Mammerickx (1972)
Ryukyu	Tensional	Weissel (1981)
Marianas	Tensional	Bibee et al (1980)
Izu-Bonin	Tensional	Karig (1974)
Japan	Tensional	Nakamura & Uyeda (1980)
Kuril-Kamchatka	?	England and Wortel (1980)
Alaska	Compressive	Lathram et al (1974)
Aleutian	Tensional	Nakamura & Uyeda (1980)
S. Sandwich	Tensional	Barker & Hill (1981)
Aegean	Tensional	Le Pichon & Angelier (1980)
Caribbean	?	Molnar and Atwater (1978)
Active continental margins		
Chile	Tensional	Megard & Phillip (1976)
Peru	Compressive	Stauder (1975)
Central America	Tensional	Molnar and Sykes (1969)
Cascades	?	
Java	?	

Table 1.1: Observed state of stress in the back arc region of subduction zones ? signifies subduction zones where neither tensional or compression stresses are dominant.

The stress regime behind some island arc subduction zones is considered to be tensional because marine geological and geophysical observations have demonstrated that active sea floor spreading is currently occuring. This phenomena is known as back-arc spreading. Examples of presently active back arc basins are the Marinas basin (Karig et al, 1978; Bibee et al, 1980), the Scotia sea (Barker and Hill, 1981), the Lau basin (Weissel, 1977) and possibly the Andaman sea (Eguchi et al, 1979) and the Aegean (Le Pichon and Angelier, 1981). Recognisable symmetric magnetic anomalies have also been identified in other marginal seas (Weissel, 1981) which suggests that back arc spreading was common in the past. Figure 1.9 summarises the location of past and present areas of back arc spreading and demonstrates that it is spatially and temporally episodic. Nakamura and Uyeda (1980) have also proposed, on the basis of stress sensitive geological features, that the stress regime in Japan and the Aleutians is presently tensional even though back arc spreading is not currently active in these regions.

Geological observations of faulting in the Cordilleran mountain chains of the Pacific American coast suggest that these regions were formed during the Quaternary by dominantly tensional processes. The focal mechanism solutions for Peru and North Chile (Stauder, 1975) and Alaska, however, suggest that these regions are presently under compression.

In the back arc areas of Java-Sumatra, Kuril-Kamchatka, the Cascades, Central America, and the Caribbean subduction zones the present day stress regime is not observed to be dominated by either tensional or compressive stresses.

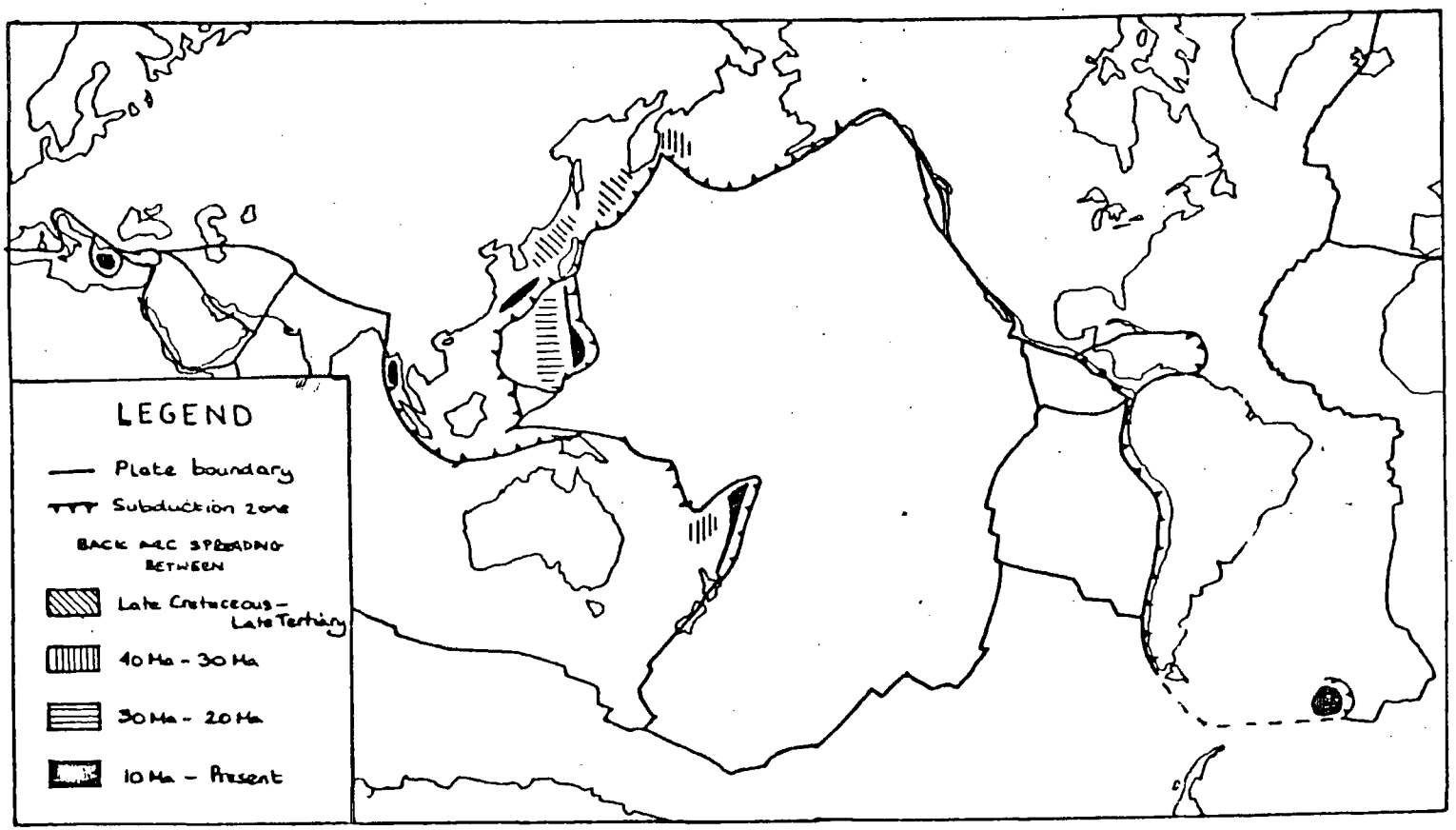

Figure 1.9: Location of present and past areas of back arc spreading (complied from various authors, principally Weissel (1981)).

Because the kinematics of the subduction process predicts that subduction zones are sites of crustal shortening they would be predicted to be sites of regional compression. The observations reviewed in this section, however, demonstrate that tension is more common in back arc regions. Several models have been proposed to explain the origin of this tensional stress:

1. Slab induced convection. Several authors have proposed that the tension in back arc basins, and more specifically the force driving back arc spreading, is produced by the combination of heating and shearing which is associated with slab induced convection (Figure 1.10). This mechanism should produce tensional stresses at those subduction zones where the slab penetrates deeper than several hundred kilometres. Because the Kuril-Kamchatka and Java-Sumatra subduction zones have deep slabs but are not tensional, this prediction is not supported by observations. A further limitation of this model is that it does not provide a satisfactory mechanism to stop back arc spreading other than by cessation of subduction.

2. Negative buoyancy. Observations indicate that compression is dominant in regions where young slabs are being subducted and tension where old slabs are being subducted. This suggests that the stress regime in the overlying plate may be controlled by the age of the subducting plate because of the increasing negative buoyancy of the oceanic lithosphere as it ages (Molnar and Atwater, 1978; England and Wortel, 1980). Because the stresses are tensional at some subduction zones where very young slabs are being subducted (e.g. Chile) and are not tensional where every

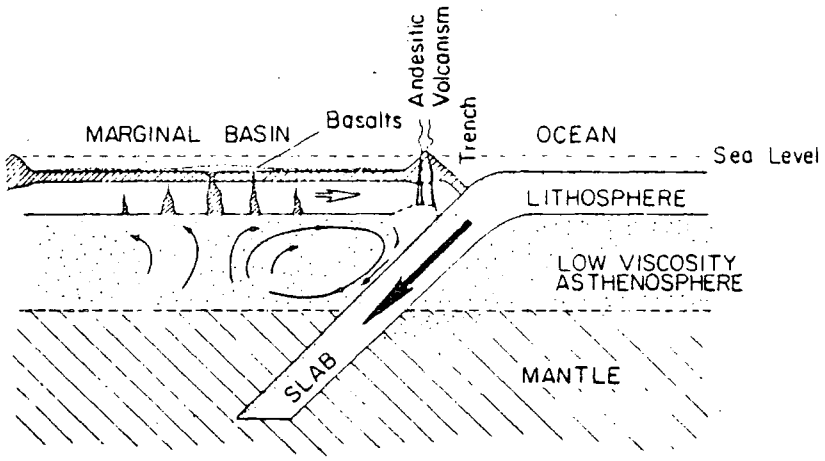

Figure 1.10: Development of tensional feature in back arc regions by heating and shearing produced by the slab induced convection cell (Toksoz and Hsui, 1978).

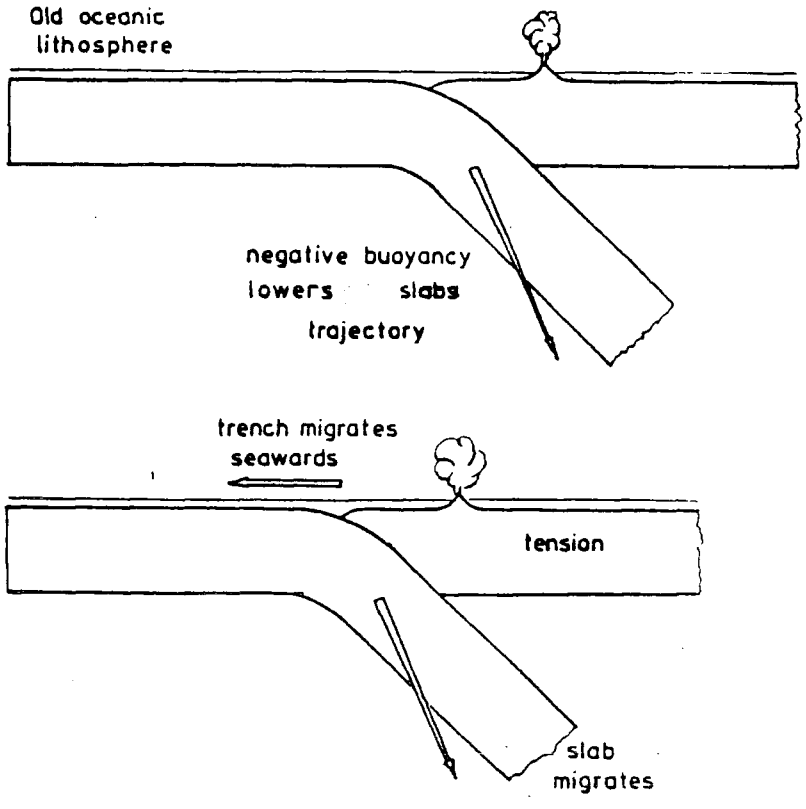

Figure 1.11: Development of tension behind the arc in response to the negative buoyancy of the old subducting lithosphere (after Molnar and Atwater (1978)).

old plate is being subducted, however, this model does not agree completely with observations.

3. Coupling of the plates. It has been proposed that the degree of mechanical coupling of the subducting and overlying plates at the subduction zone fault controls the stress regime in the overlying plate (Kanamori, 1977; Uyeda and Kanamori, 1979). This model suggests that where the plates are highly coupled the overlying plate is characterised by regional compression but where the plates are weakly coupled the overlying plate is characterised by tension. Some subduction zones which are considered to be strongly coupled (e.g. the Aleutian and Tonga-Kermadec), however, are observed to have tensional stresses in the back arc regions. This model therefore does not completely explain observations.

4. Absolute motion of the overlying plate. Several authors have suggested that back arc spreading only occurs where the overlying plate is retreating from the trenchline in an absolute reference frame (Chase, 1978; Uyeda and Kanamori, 1979). This observation, however, only explains why tensional stresses are present in the Marianas and Scotia arcs. It does not explain why the stresses in many other back arc regions are observed to be tensional.

There is consequently no current model which can satisfactorily explain the spatial and temporal episodicity of the tensional stresses in the back arc area of subduction zones.

1.5 Sources Of Stress

Stresses are produced in the lithosphere by the action of boundary and body forces. The stress regime which these forces produce, in particular their response over time, is controlled by the rheology of the lithosphere. The rheology of the lithosphere is reviewed in chapter 2 and it is therefore the aim of this section to review the sources of lithospheric stress.

The sources of stress in an elastic lithsophere were reviewed by Turcotte and Oxburgh (1976). They considered that the lithospheric stress regime is the product of the system of boundary and body forces which presently act upon it and the initial strains which were produced by earlier tectonic events. Since then, however, several advances in our knowledge of the time dependent nature of the rheology of the lithosphere have improved our understanding of the sources of tectonic stress. These advances led Bott (1982a) to reclassify the sources of lithospheric stress into renewable or non-renewable stress systems. Renewable sources of stress are produced by forces which continuously regenerate strain energy (e.g. body forces and plate driving forces). Non-renewable stresses are produced by initial strains which do not continuously generate strain energy (e.g. thermal and bending stresses). Unlike non-renewable stress, renewable stresses are not relieved by transient creep and they are consequently subject to stress amplification in the upper elastic layer of the lithosphere (Kusznir and Bott, 1977; Bott and Kusznir, 1979). The forces which generate renewable stress are therefore the major sources of tectonic stress in the lithosphere.

The main sources of stress in the lithosphere are:

1. Plate driving forces. These forces, which are a renewable source of stress, are of plate tectonic origin (Forsyth and Uyeda, 1975). They include;

    1. Ridge push. Which results from the continuous upwelling of hot, low density material beneath mid ocean ridges.

    2. Slab pull. Which arises from the large negative buoyancy of the cool, and consequently dense, subducting slab.

    3. Trench suction. This is a force which pulls the overlying plate towards the subducting plate (Elsasser, 1971). The origin of trench suction is not well understood. It may possibly result from the roll-back of the subducting plate (Chase, 1978; Molnar and Atwater, 1978) or the shear stress arising from slab induced convection (Richter, 1975).

    These forces, which are probably the largest of plate tectonic origin, are resisted by viscous drag along the interface of the plates with the mantle and by frictional resistance along interplate boundaries.

2. Loading forces. Body forces, resulting from the weight of the lithosphere, produce large stresses in the lithosphere. Important deviatoric stress regimes are produced where there are local changes in the magnitude of loading forces, either resulting from lateral variations in the density of the lithosphere or from changes in the magnitude of topographic loads:

    1. Topographic surface loads with a short wavelength (less than half the thickness of the lithosphere) do not result in

significant bending, and produce local deviatoric tension in the lithosphere beneath the load and compression at its edges (Bott, 1971). Although these stresses are of relatively low magnitude they may be tectonically significant when superimposed upon regional stress regimes.

2. Isostatically compensated loads produce local deviatoric tension in the lithosphere (Bott, 1971; Artyushkov, 1973). This occurs because the downthrust of the topographic load is balanced by an equal upthrust from the compensating region, which may be either a thickened crustal root or a low density region resuting from a thermal anomaly.

Both of these types of stress system produce renewable stress in the lithosphere which is subject to stress amplification.

3. Bending stresses. Long wavelength isostatically uncompensated loads cause flexure of the lithosphere. The bending stresses produced by lithospheric flexure are tensional on the convex side and compressive on the concave side. Although very large bending stresses are produced by lithopheric flexure they do not appear to cause significant tectonic activity. Bending stresses are therefore probably relieved by creep and are therefore non-renewable.

4. Thermal stress. This is caused by the thermal volume changes which result from the heating and cooling of the lithosphere, e.g. due to the cooling of the oceanic lithosphere as it moves away from a mid ocean ridge (Kusznir, 1976). Thermal stresses, however, are probably relieved by transient creep and they are

therefore non-renewable.

5. Membrane stresses. These are caused by the motion of the lithosphere over an ellipsoidal earth (Turcotte, 1974). The stresses produced by this mechanism, however, are non-renewable and are almost certainly relieved by transient creep.

1.6 Aims Of The Thesis

There are two aims of this thesis. The first is to determine the origin of the lateral variation in the stress regime which is observed between the subducting plate and the leading edge of the overlying plate at all subduction zones. The second is to determine the origin of the various stress regimes which are observed in the back arc areas of different subduction zones.

The stress regime at subduction zones is modelled in chapter 7. Before quantitative models of the stress regime can be constructed, however, it is necessary to obtain a predictive rheological model of the lithosphere (Chapter 2) and to develop two modelling techniques. The first of these is a numerical method which is capable of accurately modelling the complex geometry and physical processes occurring at subduction zone (Chapters 3 and 4). The second is a method which can model the deformation associated with the curved sided subduction zone fault (Chapters 5 and 6).

CHAPTER 2

THE RHEOLOGY OF THE LITHOSPHERE

2.1 Introduction

A rheological model describes the deformation which a material undergoes in response to loading. The initial problem in stress analysis is to define this model. It can subsequently be used to predict the stress regime which will be produced by a specified system of boundary conditions and body forces.

The rheology of a material is defined by inverting its observed stress-strain behaviour in response to loading. The stress-strain response at depths greater than several kilometres cannot be sampled in situ in the earth, and consequently, its rheology has to be inferred from seismological observations, rock mechanics and its observed response to persistent geological loads.

A consenus model of the rheology of the near surface layers of the earth is beginning to emerge from such analyses. This model suggests that there is a mobile near surface layer of strength, known as the lithosphere, which overlies a weaker layer, known as the asthenosphere. The observed response of the lithosphere to loads of different durations, however, suggests that this layer can be subdivided into two units. The first is an upper layer which responds in an elastic-brittle fashion to loads of all durations. The second is a lower ductile layer which responds elastically to short term loads but which creeps in response to loads of a longer duration. The thickness of both layers is observed to increase with the

age of the lithosphere. This is because the rheological properties of the lithosphere are dominantly thermally controlled.

There are two aims of this chapter. The first is to review the evidence upon which this rheological model is based. The second is to define its mechanical properties as a function of depth. This rheological model forms the basis for the mathematical models which are developed in subsequent chapters.

2.2 Rheological Response Of The Earth To Persistent Geological Loads

The concept that the outer layers of the earth are divided into a strong elastic lithosphere overlying a weak asthenosphere was initially introduced by Barrell (1914) to explain the observation that persistent short wavelength loads, such as deltas, are isostatically uncompensated whilst persistent long wavelength loads, such as mountain chains, are isostatically compensated. In this rheological model the lithosphere is defined as the strong near surface layer which supports long term short wavelength loads, while the asthenosphere is defined as the weak underlying layer which flows in response to long wavelength loads.

A recent justification of this model has been provided by plate tectonics. This theory postulates that the outer layer of the earth is divided into a number of lithospheric plates which move relative to one another. These plates suffer little internal deformation which suggests that this outer layer behaves as a rigid (i.e. elastic) layer which acts as a stress guide (Elsasser, 1969).

2.3 Seismological Evidence

Seismic sources locally stress the earth and produce elastic waves which propagate through it. The typical time span of seismic disturbances is 1-100 seconds and they consequently provide information on the rheological response of the earth to short term loads.

Seismological observations provide direct evidence for a seismic lithosphere-asthenosphere subdivision. They also provide information on the variation of elastic properties of the lithosphere with depth, and demonstrate that the top of the seismic lithosphere deforms anelastically by brittle fracture.

2.3.1 Seismic evidence for the lithosphere and asthenosphere

A major change in the seismological properties of the upper mantle is observed between 100 and 200 km depth (e.g. Bott, 1982a). The principal seismological characteristics of this zone, which distinguish it from the overlying region, are that it has a low velocity to S waves and a low Q. There have been many attempts to explain this observation, but the most widely accepted view is that it represents the region where the mantle is closest to its melting point.

The low velocity zone is generally considered to provide direct evidence for the existence of an asthenosphere. The seismic definition of the lithosphere is therefore as the region which lies above the low velocity zone (Le Pichon et al, 1973).

Much attention has been directed to establishing the thickness of the seismic lithosphere. Surface wave analyses have demonstrated (Figure 2.1) that the oceanic lithosphere increases in thickness from 25 km at 5 million years to 90 km at 100 million years (Leeds et al, 1974; Forsyth, 1977).

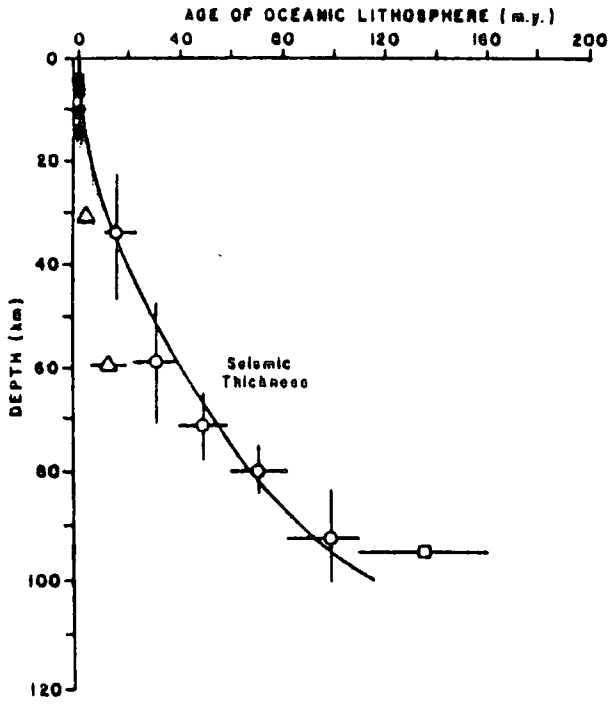

Figure 2.1: Variation in the thickness of the seismic lithosphere with age (Watts et al, 1980).

These observations suggest that the lithosphere increases in thickness as it cools. The continental lithosphere is generally thicker than the oceanic lithosphere.

2.3.2 Variation of elastic parameters with depth

The velocity of seismic waves are dependent upon the elastic properties and density of the medium through which they travel. The well known velocity and density distribution in the seismic lithosphere can consequently be inverted to yield the variation in Young's modulus, E, and Poisson's ratio, ν, with depth (e.g. Mithen, 1980). This procedure yields a different profile of elastic parameters in the continental and oceanic lithospheres because of the differences in their velocity distribution. The variation in the elastic parameters with depth in the oceanic and continental lithosphere which were calculated by Park (1981) from their average velocity and density distribution are shown in figure 2.2. These parameters will be used in subsequent chapters to model the lithospheric stress regime.

2.3.3 Non-elastic deformation

Earthquakes are natural seismic sources which arise from the non-elastic deformation of the earth. The radial distribution of earthquake foci, outside of plate collision zones, is observed to be restricted to the upper 10-30 km of the seismic lithosphere (Vetter and Meissner, 1979). This observation suggests that the lithosphere has a finite strength and deforms as a brittle solid in the near surface when the load exceeds the strength of the rocks.

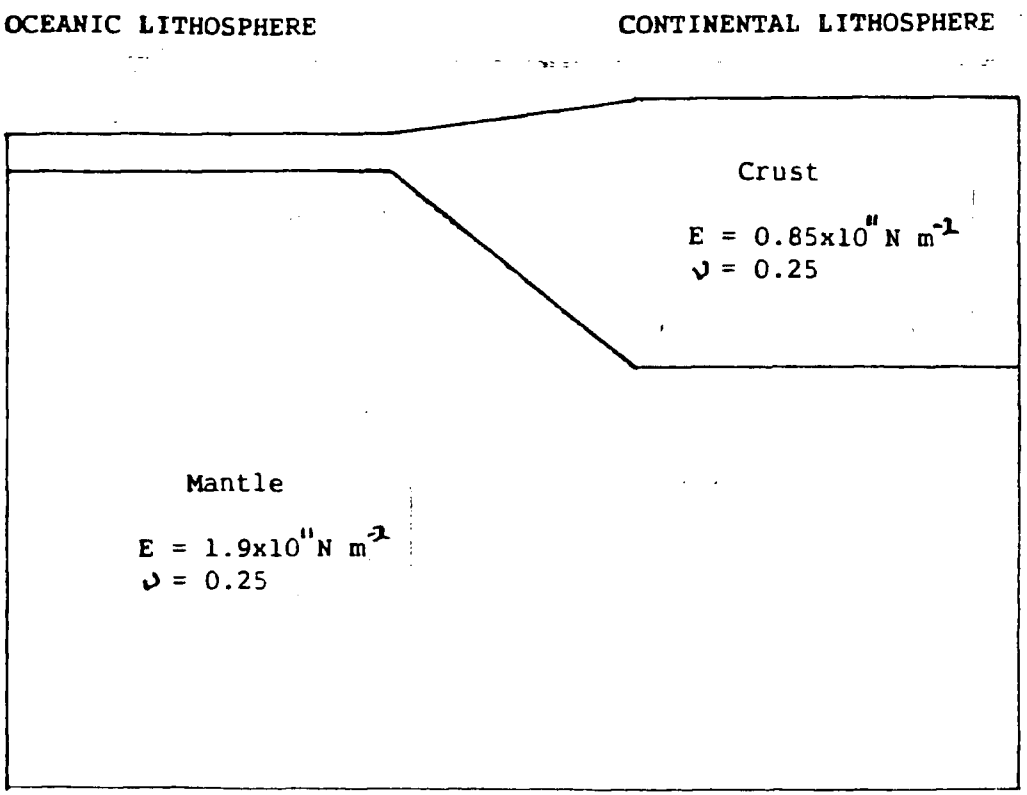

Figure 2.2: Variation of elastic parameters with depth in the oceanic and continental lithosphere.

2.4 Lithospheric Flexure

The lithosphere responds to vertical loads, such as those at seamounts and deep sea trenches, by bending. The characteristic features of this flexure are an uparching of the seafloor (known as the outer rise at trenches and the peripheral bulge at seamounts) some 100-150 km from the load and a downwards displacement towards it. This flexure originates at seamounts from a static volcanic load, while at trenches it results from the dynamic forces associated with plate convergence. Although the forces causing flexure at trenches and seamounts are different the implications for the the mid to long term rheology of the lithosphere are similar. These implications are reviewed in this section.

The lithospheric flexure seawards of trenches and seamounts has been successfully modelled using thin elastic plate theory (Walcott, 1970, 1976; Hanks, 1971; Watts and Talwani, 1974; Watts and Cochran, 1974; Watts et al, 1975; Parsons and Molnar, 1976; Caldwell et al, 1976; Watts, 1978). This model represents the lithosphere as an elastic layer and the asthenosphere as a fluid substratum. The two major results which have been obtained from these models are (figure 2.3):

1. The mechanical thickness of the elastic layer which supports the load is between a half or a third of the seismic thickness of the lithosphere.

2. The thickness of the elastic layer increases with age and follows the 300-700°C isotherm of Parsons and Sclater (1977).

These results have been interpreted as demonstrating that the entire seismic thickness of the lithosphere does not support long term loads and therefore that the seismic lithosphere is divided into an elastic upper

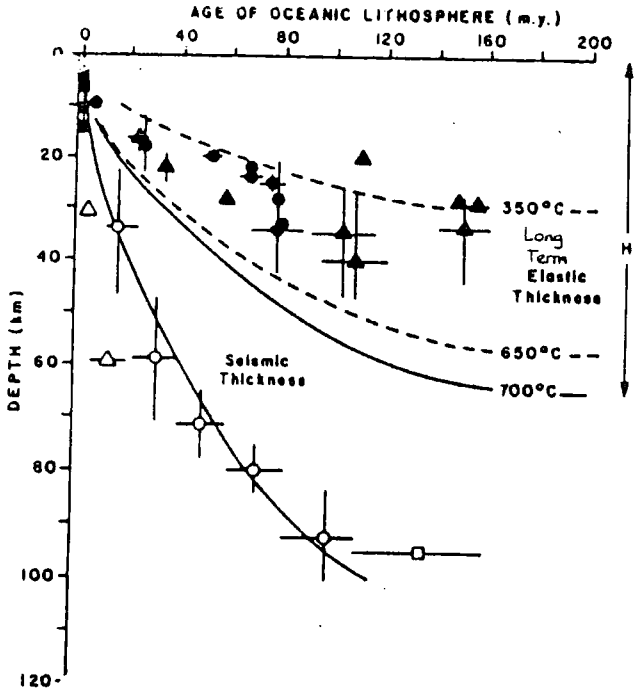

Figure 2.3: Comparison of the seismic and long term elastic thickness of the oceanic lithosphere (Kirby, 1983).

layer and a ductile lower layer whose position is thermally controlled.

Recent models of the topography of these features have shown that better fits to profiles which have a large curvature can be obtained using a rheology which allows some non-elastic deformation to occur in the elastic layer (McAdoo et al, 1978; Turcotte et al, 1978; Bodine and Watts, 1979; Chapple and Forsyth, 1979). These models use an elastic-plastic rheology for the lithosphere which yields plastically when the stress in the elastic layer exceeds the yield strength of the rocks. The advantages of this model are that it produces much more realistic stresses in the elastic layer and is compatible with the observations of rock mechanics.

The continental lithosphere, however, has not been subjected to such exhaustive modelling. This is because it is less homogeneous than the oceanic lithosphere and because suitable loading structures do not readily occur. The available evidence, however, demonstrates that the continental lithosphere behaves like the oceanic lithosphere in that the mechanical thickness of the elastic layer is thermally controlled and substantially thinner than the seismic thickness (Karner et al, 1983).

2.5 Rock Mechanics

Rock mechanics can be used to measure the stress-strain behaviour of various lithospheric constituents at different pressures and temperatures to simulate their physical behaviour at depths within the earth. Such experiments provide information on the physical mechanisms of deformation within the lithosphere and help to explain its observed time dependent response to loading.

2.5.1 Brittle fracture: modified Griffith theory

The great number of micro- and macro-fractures which are observed in crustal rocks demonstrates that non-elastic deformation occurs near to the earths surface. The hypocentres of the earthquakes which occur in the upper elastic lithosphere demonstrates that this brittle fracture extends to depths of 10-30 km.

These observations are in agreement with the known behaviour of lithospheric rocks in laboratory experiments conducted at low temperatures and pressures. These analyses show that rocks have a finite strength and fracture when the magnitude of the load exceeds a critical value.

Mathematical descriptions of the failure of rocks have been proposed by Coulomb, Mohr and Griffiths and are reviewed in Jaeger and Cook (1977). For reasons discussed in Mithen (1980), it is generally accepted that a modified form of the Griffith fracture criterion fits best with laboratory experiments and with the observed failure of lithospheric rocks. This failure criteria has been used in this thesis.

It is convenient to describe the modified Griffith failure criteria in terms of the mean stress, σ_m, and the mean shear stress, τ_m, which are defined

$$\sigma_m = \frac{\sigma_1 + \sigma_2}{2}$$

$$\tau_m = \frac{\sigma_1 - \sigma_2}{2}$$

where σ_1 and σ_2 are the maximum and minimum principal stresses (with the convention that tension is positive). The modified Griffith failure criteria can then be defined in terms of the tensile strength of the rock,

T, the stress required to close the Griffith cracks, σ_c , and the coefficient of internal friction on these cracks, μ_F . It is also convenient to define a dimensionless parameter, C, which assesses the degree by which the rock has failed (Park, 1981), and is defined by

$$C = 1 - \frac{\tau_m}{r}$$

where r is the value of τ_m at which failure occurs. This factor is useful because it give an impression of the degree of failure within the body: if C is positive failure has not occured, but when C is equal to zero failure occurs and increases strongly as C becomes more negative.

Using these parameters it is possible to define the four regimes of the modified Griffith failure criteria as follows:

1. Tensional failure. This occurs in the region

   $$|2\sigma_m| \leqslant |\tau_m|$$

   Failure is predicted when

   $$\tau_m \geqslant T - \sigma_m$$

   where θ, the angle between the fracture plane and the minimum principal stress, is equal to zero.

   The degree of failure is defined by

   $$C = \frac{T - \sigma_1}{T - \sigma_m}$$

2. Open crack shear failure. This occurs in the region

   $$|2\sigma_m| > |\tau_m| \quad \text{where} \quad \sigma_m > \sigma_c - 2T.$$

Failure is predicted when

$$\tau_m^2 \geq -4T\sigma_m$$

with

$$\theta = \frac{1}{2} \arccos\left(-\frac{\tau_m}{2\sigma_m}\right)$$

The degree of failure is

$$C = 1 - \frac{\tau_m}{(-4T\sigma_m)^{1/2}}$$

3. Intermediate failure: This occurs in the region

$$|2\sigma_m| > |\tau_m|$$

where

$$\sigma_m < \sigma_c - 2T \quad \text{and} \quad \sigma_m > \sigma_c - 2\mu_F(T^2 - \sigma_c T)^{1/2}$$

Failure is predicted when

$$\tau_m^2 \geq (\sigma_c - \sigma_m)^2 + 4T(T - \sigma_c)$$

where

$$\theta = \frac{1}{2} \arctan\left(\frac{4T(T-\sigma_c)}{\sigma_c - \sigma_m}\right)$$

The degree of failure is

$$C = 1 - \frac{\tau_m}{((\sigma_c - \sigma_m)^2 + 4T(T - \sigma_c))^{1/2}}$$

4. Closed crack shear failure: This occurs in the region

$$|2\sigma_m| > |\tau_m|$$

where

$$\sigma_m < \sigma_c - 2\mu_F(T^2 - \sigma_c T)^{1/2}$$

Failure is predicted when

$$\tau_m \geq \frac{\mu_F(\sigma_c - \sigma_m) + 2(T^2 - T\sigma_c)^{1/2}}{(\mu_F^2 + 1)^{1/2}}$$

and the degree of failure is

$$C = 1 - \frac{\tau_m(\mu_F^2 + 1)^{1/2}}{\mu_F(\sigma_c - \sigma_m) + 2(T^2 - T\sigma_c)^{1/2}}$$

To use the modified Griffith theory to test for failure in the finite element models it is necessary to assign values to the tensile strength. The average tensile strength of the igneous rocks in the upper crust appears to be 12 MPa (Goldsmith et al, 1975) whilst an average value of 50 MPa appears to be appropriate for the rocks in the lower crust (Service and Douglas, 1973). The value of σ_c, the stress to close the cracks was taken as -10T (Ashby and Verall, 1978) and the value of μ_F, the coefficient of internal friction of the cracks, is taken as 0.1 (Brace, 1964).

2.5.2 Ductile behaviour

Metals deform by creep at stresses above their elastic limit. Kirby (1983) has reviewed recent experimental work on possible upper mantle constituents which suggests that creep is also likely to be the dominant deformation process in the asthenosphere and the lower part of the seismic lithosphere. The results of these experiments are conveniently summarised in the form of a deformation map for olivine (figure 2.4). This figure demonstrates that the rheology of olivine is strongly temperature dependent. Three creep mechanisms are thought to control this observed behaviour:

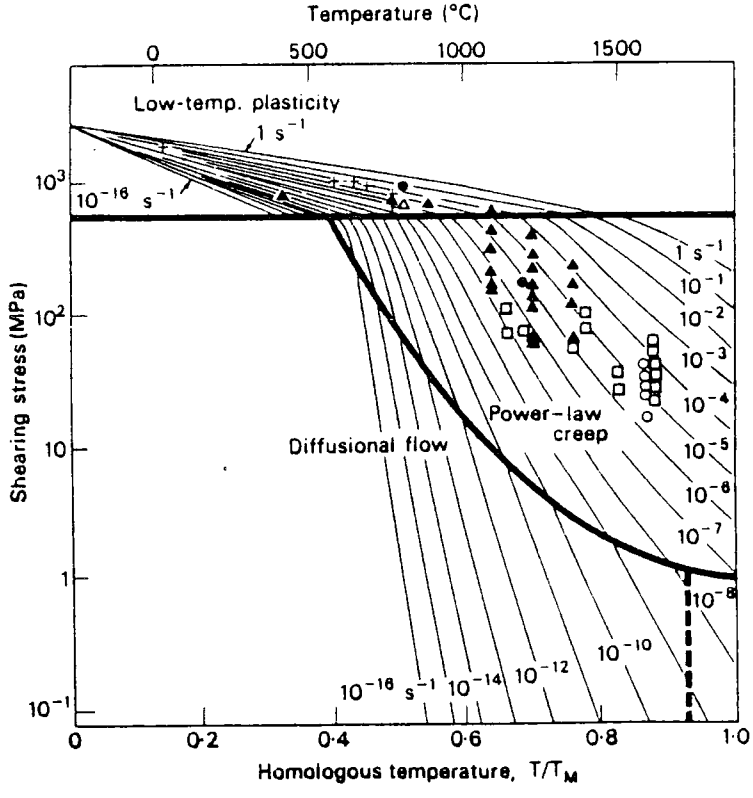

Figure 2.4: Deformation map for olivine

1. Low temperature plastic flow: This style of deformation is controlled by the motion of dislocations on their glide planes and occurs at temperature less than 0.5 Tm, where Tm is the absolute melting temperature. It is thought that this mechanism is the dominant style of deformation below the brittle-ductile transition and occurs where the temperature is too low for power law creep to be the dominant process (Carter, 1976).

2. Power law creep: This is a form of steady state creep and occurs when dislocations are able to move both on and normal to their glide planes. Power law creep is observed in olivine at temperatures between 0.5 Tm and 0.9 Tm and its onset corresponds with a sudden loss of strength. Considerable work, which is reviewed by Kirby (1983), has shown that in this behaviour the strain rate, $\dot{\varepsilon}$, is dependent upon the power law of the differential stress, σ_d, and has the form

$$\dot{\varepsilon} = A \sigma_d^n \exp\left(\frac{-(Q+PV)}{kT}\right)$$

where Q is the activation energy, P is the pressure, V is the activation volume, k is Boltzman's constant, T is the temperature in degrees Kelvin, and A is some constant for the material. The value taken by the power law exponent, n, is considered to be 3 at low stresses and 5 at high stresses.

3. Diffusion creep: This behaviour has not been directly observed in lithospheric materials but it is well established in metals. This style of deformation has not been observed in experiments because it is not possible to recreate the low creep rates and

temperatures under which it would occur. Diffusion creep takes two forms in metals known as cobble creep and Nabarro-Herring creep and it is assumed that similar processes occur in the earth at temperatures around 0.9 Tm.

Because of the high temperature conditions (greater than 0.5 Tm) in the lower seismic lithosphere the ductile flow in this region is probably dominated by power law creep. This is supported by the dislocation structures observed in peridotite nodules originating from the mantle (Nicholas and Poirier, 1976).

There are, however, some uncertanties in the application of power law creep to the earth. These are:

1. All of the experiments which have been performed on likely lithospheric constituents have been conducted at strain rates which are several orders of magnitude higher than actually exist in the earth. The extrapolation of the results of these experiments to the much lower strain rates in the lithosphere consequently depends on the validity of the assumed constitutive equation for power law creep.

2. The chemical environment, particularly the presence or absence of water, has an important influence on the creep rates and therefore on the parameters of the constitutive equation.

3. The effect of pressure on the parameters in the power law creep equations is also poorly understood.

It is therefore clear that although power law creep is considered to be the dominant deformation mechanism in the lower seismic lithosphere there is still considerable uncertainty about the values to assign to the parameters in the constitutive equation.

2.6 Conclusion: A Rheological Model Of The Lithosphere

In this thesis the lithosphere is defined as the relatively strong layer above the low velocity zone. The observations which have been reviewed in this chapter suggest it is subdivided into two layers whose boundary is gradational and thermally controlled (Figure 2.4):

1. The upper elastic-brittle lithosphere. This is the region above the 300-700°C isotherm which responds elastically to long and short term loads. The top 10-30 km of this region, however, deforms non-elastically by brittle fracture when the load exceeds the elastic strength of the rocks. The brittle fracture is described by modified Griffith theory.

2. The lower ductile lithosphere. This layer lies between the upper elastic-brittle lithosphere and the asthensophere. The lower lithosphere responds elastically to short term loads but deforms by ductile creep in response to loads of a longer duration. The dominant deformation mechanism in the lower lithosphere is power law creep. Because of current uncertainties about the extrapolation of experimental strain rates to those in the earth and about the influence of pressure and the chemical environment on the physical parameters in the constitutive equation it is necessary to make many approximations to use a power law creep

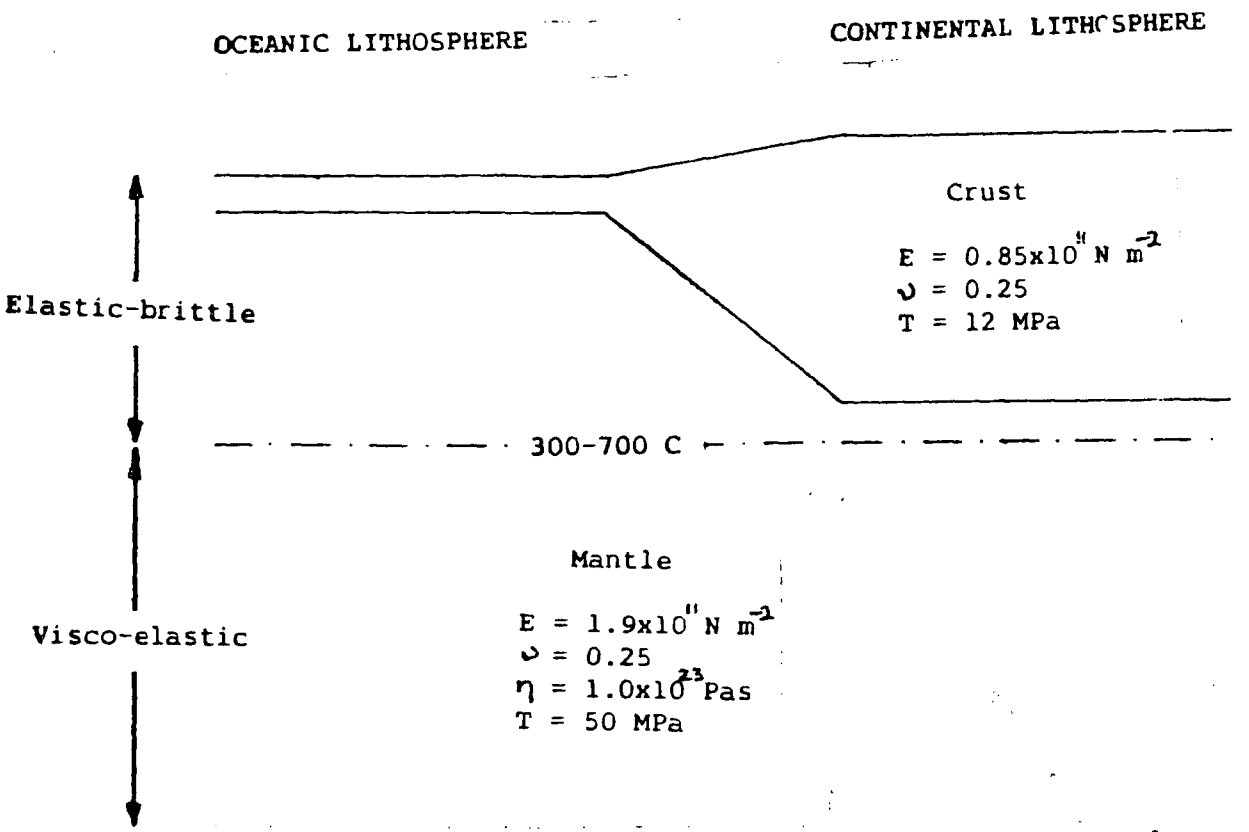

Figure 2.5: The rheological model of the lithosphere.

rheology to model deformation in the lower lithosphere. An alternative and simpler approach is to use a Maxwell visco-elastic rheology to model deformation in this layer. Recent studies (Mithen, 1980; Melosh and Raefsky, 1980) have demonstrated that the final stress regime using either power law creep or a visco-elastic rheology with a viscosity of 1.0×10^{23} Pa s are almost identical. The major difference between these two deformation mechanisms is that higher deviatoric stresses initially relax faster in a power law creep material. The deformation predicted by these two rheological models, however, converges once equilibrium is reached and both mechanisms produce stress concentration in the upper elastic lithosphere (Bott and Kusznir, 1979; Mithen, 1980). In this thesis the deformation of this layer will consequently be modelled by a visco-elastic substance with a viscosity of 1.0×10^{23} Pa s. It is important, however, to appreciate that this is just a convenient simplification to model the stress regime at subduction zones.

This model is summarised in figure 2.5.

CHAPTER 3

THE ISOPARAMETRIC FINITE ELEMENT METHOD

3.1 Introduction

To obtain realistic models of the stress regime at subduction zones it is necessary to use a solution technique which is capable of giving accurate and predictive answers to problems involving:

1. Flexure of the lithosphere.
2. Bodies with various material types.
3. Bodies with complex geometries.
4. Complex boundary conditions.
5. The curved discontinuity of the subduction zone fault.
6. Elastic and time dependent rheologies.

Analytic solutions to problems of this complexity are impracticable. It is therefore desirable to use digital computers to obtain approximate solutions using numerical mathematical techniques. One numerical method which has been extensively and successfully used in stress analysis is the finite element method. This technique will consequently be used in this thesis to model lithospheric stress regimes.

The first step in the finite element method is to divide the body into a number of finite elements which interconnect at a series of nodes. Assumptions are then made about the behaviour of the major variables within each element. The main assumption is the choice of the order of the displacement function, which defines the variation of the displacements within each element. Once this function has been chosen it is possible to

express the displacement of a general point within an element as an interpolation of its known nodal values. Expressions can then be obtained for the stress and strain at a general point within an element so that, by considering the energy of the system, an equilibrium equation can be derived which relates the displacement and the applied forces at the nodes to the stiffness of the body.

The finite elements used by previous researchers at Durham (Dean, 1973; Kusznir, 1976; Woodward, 1976; Mithen, 1980; Park, 1981; Linton, 1982) were based upon a linear displacement function. This results in a constant strain within each element. This is the simplest of the two dimensional finite elements and its major advantage is that it allows an explicit expression to be derived for the stiffness of the body. For reasons discussed in Chapter 4, however, this element does not perform well in many elastic and visco-elastic problems where the strain gradient is high.

Because of these limitations a higher order finite element, which is based upon a quadratic displacement function, is used in this thesis. Since the strain varies linearly within these elements they should perform better in regions with a high strain gradient.

The simplest two dimensional finite element which is based upon a quadratic displacement function is the plane sided triangular element (Felippa, 1966; Desai and Abel, 1972). The advantage of this element is that an explicit expression can be obtained for the stiffness of the body by using a special local co-ordinate system. This approach provides a simple transition between the linear and quadratic displacement function methods but it cannot be used to introduce curved sided elements.

Another technique which is based upon a quadratic displacement function is the isoparametric finite element method (Zienkiewicz, 1977; Cook, 1981). This method allows curved sided finite elements to be introduced, and consequently, it is used in this thesis to model lithospheric stress regimes.

In this chapter the theory of the isoparametric method in elastic and visco-elastic problems is given for both triangular and quadrilateral finite elements. A computer program (ISOFELP) which is based upon this technique is described in the Appendix.

3.2 The Local Co-ordinate System

When curved sided isoparametric finite elements are being used it is convenient to perform the necessary mathematical operations in a simple local co-ordinate system.

3.2.1 Local co-ordinate system for triangular elements

The triangular element which will be used in this thesis has a total of six nodes, three of which lie at the vertices and three at the midpoints of the sides of the triangle. The nodes of the element are numbered clockwise or anticlockwise around the element starting with one of the nodes at an apex. Figure 3.1 illustrates the geometry of this element and figure 3.2 shows how the global element geometry is mapped onto the local (s,t) space. It can be seen that the curved sides of the element in global co-ordinates are transformed to straight sided sections of unit length in the local reference system, which has its origin at node 1.

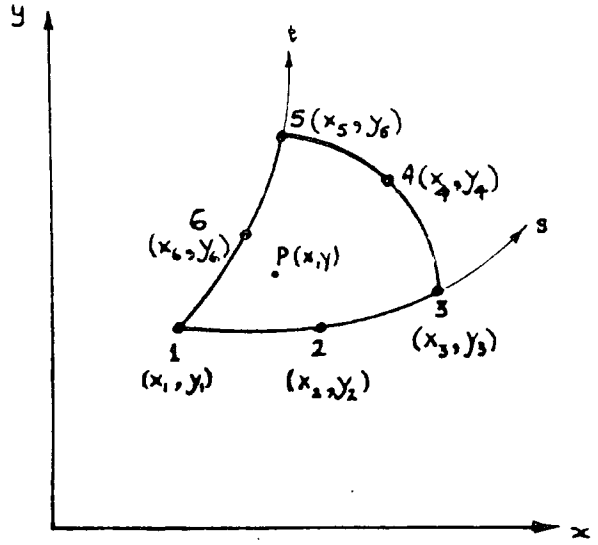

Figure 3.1: The global (x,y) co-ordinate system for the triangular isoparametric element.

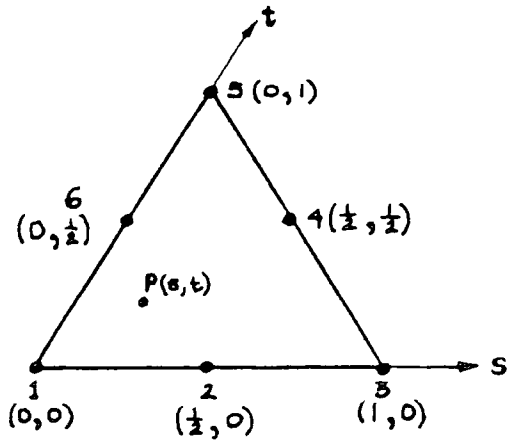

Figure 3.2: The local (s,t) co-ordinate system for the triangular isoparametric element.

3.2.2 Local co-ordinate system for quadrilateral elements

The quadrilateral element has eight nodes in total, four of which lie at its corners and four at the midpoints of the sides of the element. The nodes of the element are numbered clockwise or anticlockwise around the element starting with one of the corner nodes. Figure 3.3 illustrates the geometry of this element and figure 3.4 shows how the global element geometry is mapped onto the local (s,t) co-ordinate system. The curved sides of the element in global co-ordinates are transformed to straight sided sections of 2 units length in the local reference system. The origin of the local co-ordinate system is at the centroid of the element and the axes pass through the midpoint of each side.

3.3 The Isoparametric Concept

The displacements and the co-ordinates (i.e. geometry) of a finite element are defined at its nodes. We may consequently define the co-ordinates and displacements of a general point within a finite element by interpolating from the known nodal values using the element shape functions, [L].

To illustrate these properties we define the displacements of a general point within an element, $\{\delta\}$, as

$$\{\delta\} = \begin{Bmatrix} u \\ v \end{Bmatrix}$$

where u and v are the components of displacement in the x and y directions. The displacements of this point may then be written in terms of the nodal displacements of the element, {d}, using the displacement shape functions, $[L_\delta]$, as

$$\{\delta\} = [L_\delta]\,\{d\} \qquad 3.1$$

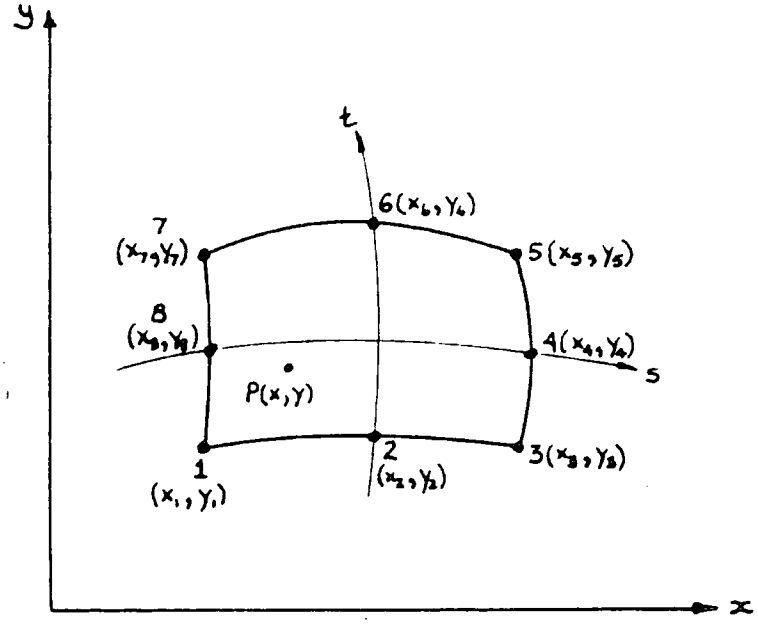

Figure 3.3: The global (x,y) co-ordinate system for the quadrilateral isoparametric finite element.

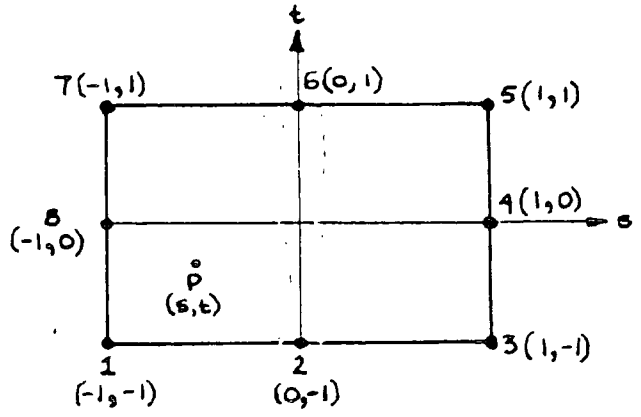

Figure 3.4: The local (s,t) co-ordinate system for the quadrilateral isoparametric finite element.

The variation of displacement within an element is therefore dependent upon the order of the displacement shape functions.

Similarly, we may define the global co-ordinates of a general point within the element, $\{g\}$, in terms of the known nodal co-ordinates, $\{c\}$, through the geometric shape functions, $[L_g]$, as

$$\{g\} = \begin{Bmatrix} x \\ y \end{Bmatrix} = [L_g]\{c\} \qquad 3.2$$

The variation of geometry within an element is therefore dependent upon the order of the geometric shape functions.

A finite element becomes isoparametric in the special case when the displacement shape functions are equal to the geometric shape functions, that is

$$[L_\delta] = [L_g] \qquad 3.3$$

In this thesis the shape functions, which will be derived in the next section, are quadratic and this allows us to introduce curved sided finite elements.

3.4 Shape Functions

In this section a general method for obtaining expressions for the shape functions in terms of the local co-ordinates is presented. This approach is used in subsequent sections to obtain the geometric and displacement shape functions of triangular and quadrilateral elements.

3.4.1 General definition and evaluation of shape functions

Shape functions, N_i, define the value of an arbitrary function, f, at any point within an element through an interpolation of the known nodal values, f_n, of the function.

We may define the shape functions $N_1(s,t)$, $N_2(s,t)$, ..., $N_m(s,t)$, of an m-noded finite element with nodal values f_1, f_2, ..., f_m, of the function f such that its value at a general point, f(s,t), within the element is given by

$$f(s,t) = N_1(s,t)\, f_1 + N_2(s,t)\, f_2 + \ldots\ldots + N_m(s,t)\, f_m \qquad 3.4$$

We must also choose the shape functions for the i-th node such that $f(s_i,t_i) = f_i$, and therefore we define

$$N_i(s_i,t_i) = 1$$

$$N_j(s_i,t_j) = 0 \qquad i \neq j$$

Expressions for the shape functions can be obtained by defining the way in which the function f varies within an element. The most general representation is by a polynomial chosen such that

$$f(s,t) = a_1 + a_2 s + a_3 t + a_4 s^2 + \ldots\ldots + a_m s^q t^q \qquad 3.5$$

where the coefficients of the polynomial, a_i, are constant for any element.

Equation 3.5 can be rewritten in matrix form as

$$f = [Q]\,\{a\} \qquad 3.6$$

where

$$[Q] = [\,1 \quad s \quad t \quad s^2 \ldots\ldots s^q t^q\,]$$

and

$$\{a\}^T = \{\,a_1 \quad a_2 \quad a_3 \ldots\ldots a_m\,\}$$

We now seek to solve equation 3.6 for the unknown constants {a}. Examination of equation 3.6 demonstrates that the value taken by the function f is dependent upon position in the element, and therefore, because the position of the nodes are known it is possible to use this equation to obtain expressions for the nodal values of the function f.

$$f_1(s_1,t_1) = a_1 + a_2 s_1 + a_3 t_1 + \ldots\ldots + a_m t_1^q s_1^q$$
$$f_2(s_2,t_2) = a_1 + a_2 s_2 + a_3 t_2 + \ldots\ldots + a_m t_2^q s_2^q$$
$$\vdots$$
$$f_m(s_m,t_m) = a_1 + a_2 s_m + a_3 t_m + \ldots\ldots + a_m t_m^q s_m^q$$

These nodal values, $\{f_n\}$, of the function f can be written in matrix form as

$$\{f_n\} = [A]\{a\} \qquad 3.7$$

where

$$[A] = \begin{bmatrix} 1 & s_1 & t_1 & \ldots\ldots\ldots & s_1^q t_1^q \\ 1 & s_2 & t_2 & \ldots\ldots\ldots & s_2^q t_2^q \\ & & & \vdots & \\ 1 & s_m & t_m & \ldots\ldots\ldots & s_m^q t_m^q \end{bmatrix}$$

We can therefore obtain expressions for the coefficients, {a}, by inverting equation 3.7. This gives

$$\{a\} = [A]^{-1}\{f_n\} \qquad 3.8$$

An expression for the value of the function f at a general point can now be obtained by substituting the above equation into equation 3.6, giving

$$f = [Q][A]^{-1}\{f_n\} \qquad 3.9$$

Recalling equation 3.4, we are seeking shape functions, N_i, such that

$$f = N_1 f_1 + N_2 f_2 + \ldots\ldots + N_m f_m$$

which may be written in matrix form as

$$f = [N] \{f_n\} \qquad 3.10$$

where

$$[N] = [\, N_1 \quad N_2 \quad N_3 \quad \ldots\ldots \quad N_m \,]$$

Comparing equations 3.9 and 3.10 we may write the shape functions as

$$[N] = [Q] [A]^{-1} \qquad 3.11$$

We can therefore obtain expressions for the shape functions if we can obtain an inverse of the matrix [A].

3.4.2 Shape functions of a triangular element

We now proceed to evaluate the shape functions for a six noded triangular isoparametric finite element.

3.4.3 Displacement shape functions

The displacement shape functions can be evaluated by defining the way in which the displacements vary within the element. In this thesis a quadratic displacement function has been chosen and we may therefore express the components of the displacements of a general point, using the quadratic form of the polynomial (equation 3.5), as

$$\begin{aligned} u(s,t) &= a_1 + a_2 s + a_3 t + a_4 s^2 + a_5 t^2 + a_6 st \\ v(s,t) &= b_1 + b_2 s + b_3 t + b_4 s^2 + b_5 t^2 + b_6 st \end{aligned} \qquad 3.12$$

where the u component of displacement may be written in matrix form as

$$u = [Q] \{a\} \qquad 3.13$$

in which

$$[Q] = [\, 1 \quad s \quad t \quad s^2 \quad t^2 \quad st \,]$$

and

$$\{a\}^T = \{\, a_1 \quad a_2 \quad a_3 \quad a_4 \quad a_5 \quad a_6 \,\}$$

Since the displacement is a function of position within the element and the local co-ordinate of each node is known (figure 3.1) we can evaluate equation 3.12 at each node, giving

$$u_1(0,0) = a_1$$

$$u_2\left(\frac{1}{2},0\right) = \frac{1}{4}(4a_1 + 2a_2 + a_4)$$

$$u_3(1,0) = a_1 + a_2 + a_4$$

$$u_4\left(\frac{1}{2},\frac{1}{2}\right) = \frac{1}{4}(4a_1 + 2a_2 + 2a_3 + a_4 + a_5 + a_6)$$

$$u_5(0,1) = a_1 + a_3 + a_5$$

$$u_6\left(0,\frac{1}{2}\right) = \frac{1}{4}(4a_1 + 2a_3 + a_5)$$

which may be written in matrix form as

$$\{u_n\} = [A]\{a\} \qquad 3.14$$

where

$$[A] = \frac{1}{4}\begin{bmatrix} 4 & 0 & 0 & 0 & 0 & 0 \\ 4 & 2 & 0 & 1 & 0 & 0 \\ 4 & 4 & 0 & 4 & 0 & 0 \\ 4 & 2 & 2 & 1 & 1 & 1 \\ 4 & 0 & 4 & 0 & 4 & 0 \\ 4 & 0 & 2 & 0 & 1 & 0 \end{bmatrix}$$

and

$$\{u_n\}^T = \{u_1 \; u_2 \; u_3 \; u_4 \; u_5 \; u_6\}$$

We can obtain expressions for the coefficients, $\{a\}$, by inverting equation 3.14, which gives

$$\{a\} = [A]^{-1}\{u_n\} \qquad 3.15$$

where it can be verified that

$$[A]^{-1} = \begin{bmatrix} 1 & 0 & 0 & 0 & 0 & 0 \\ -3 & 4 & -1 & 0 & 0 & 0 \\ -3 & 0 & 0 & 0 & -1 & 4 \\ 2 & -4 & 2 & 0 & 0 & 0 \\ 2 & 0 & 0 & 0 & 2 & -4 \\ 4 & -4 & 0 & -4 & 0 & -4 \end{bmatrix}$$

We may now write an expression for the displacement of a general point by substituting equation 3.15 into equation 3.13, which gives

$$u = [Q] [A]^{-1} \{u_n\} \qquad 3.16$$

We now recall that we are seeking shape functions, N , such that

$$u = N_1 u_1 + N_2 u_2 + N_3 u_3 + N_4 u_4 + N_5 u_5 + N_6 u_6$$

which may be written in matrix form as

$$u = [N] \{u_n\} \qquad 3.17$$

where

$$[N] = [\, N_1 \;\; N_2 \;\; N_3 \;\; N_4 \;\; N_5 \;\; N_6 \,]$$

Comparing equations 3.16 and 3.17, and using the fact that they must be valid for any nodal displacements, we may define the desired shape functions as

$$[N] = [Q] [A]^{-1}$$

The desired shape functions for the triangular finite element can therefore be found by evaluating the right hand side of this expression. This gives

$$\begin{aligned} N_1 &= 1 - 3s - 3t + 2s^2 + 2t^2 + 4st \\ N_2 &= 4s - 4s^2 - 4st \\ N_3 &= 2s^2 - s \\ N_4 &= 4st \end{aligned} \qquad 3.18$$

$$N_5 = 2t^2 - t$$

$$N_6 = 4t - 4t^2 - 4st$$

Identical expressions for the shape functions can be found by considering the v component of displacement.

3.4.3.1 Geometric shape functions

In order to obtain an isoparametric representation we must define the geometric polynomial as a quadratic function

$$x(s,t) = a_1 + a_2 s + a_3 t + a_4 s^2 + a_5 t^2 + a_6 st$$

$$y(s,t) = b_1 + b_2 s + b_3 t + b_4 s^2 + b_5 t^2 + b_6 st$$

The procedure to obtain expressions for the geometric shape functions is identical to that of the preceeding section. The resulting geometric shape functions are identical to those which have been found for the displacement function (equations 3.18).

3.4.4 Shape functions for quadrilateral elements

In this section we find expressions for the displacement and geometric shape functions for the eight noded quadrilateral finite element.

3.4.4.1 Displacement shape functions

The quadratic displacement function for a quadrilateral isoparametric finite element may be written

$$u(s,t) = a_1 + a_2 s + a_3 t + a_4 s^2 + a_5 t^2 + a_6 st + a_7 s^2 t + a_8 t^2 s$$

$$v(s,t) = b_1 + b_2 s + b_3 t + b_4 s^2 + b_5 t^2 + b_6 st + b_7 s^2 t + b_8 t^2 s$$

where the u component of displacement may be written in matrix form as

$$u = [Q] \{a\} \qquad 3.19$$

in which

$$[Q] = [\ 1 \quad s \quad t \quad s^2 \quad t^2 \quad st \quad s\,t \quad t\,s\ ]$$

and

$$\{a\}^T = \{\ a_1 \quad a_2 \quad a_3 \quad a_4 \quad a_5 \quad a_6 \quad a_7 \quad a_8\}$$

We can evaluate equation 3.19 at each of the nodes, which gives

$$\{u_n\} = [A]\{a\}$$

where

$$[A] = \begin{bmatrix} 1 & -1 & -1 & 1 & 1 & 1 & -1 & -1 \\ 1 & 0 & -1 & 0 & 1 & 0 & 0 & 0 \\ 1 & 1 & -1 & 1 & 1 & -1 & -1 & 1 \\ 1 & 1 & 0 & 1 & 0 & 0 & 0 & 0 \\ 1 & 1 & 1 & 1 & 1 & 1 & 1 & 1 \\ 1 & 0 & 1 & 0 & 1 & 0 & 0 & 0 \\ 1 & -1 & 1 & 1 & 1 & -1 & 1 & -1 \\ 1 & -1 & 0 & 1 & 0 & 0 & 0 & 0 \end{bmatrix}$$

and

$$\{u_n\}^T = \{\ u_1 \quad u_2 \quad u_3 \quad u_4 \quad u_5 \quad u_6 \quad u_7 \quad u_8\ \}$$

Inverting this equation we obtain

$$\{a\} = [A]^{-1}\{u_n\}$$

where it can be verified that

$$
[A]^{-1} = \frac{1}{4}\begin{bmatrix}
-1 & 2 & -1 & 2 & -1 & 2 & -1 & 2 \\
0 & 0 & 0 & 2 & 0 & 0 & 0 & -2 \\
0 & -2 & 0 & 0 & 0 & 2 & 0 & 0 \\
1 & -2 & 1 & 0 & 1 & -2 & 1 & 0 \\
1 & 0 & 1 & -2 & 1 & 0 & 1 & -2 \\
1 & 0 & -1 & 0 & 1 & 0 & -1 & 0 \\
-1 & 2 & -1 & 0 & 1 & -2 & 1 & 0 \\
-1 & 0 & 1 & -2 & 1 & 0 & -1 & 2
\end{bmatrix}
$$

We may now write an expression for the displacement of a general point by substituting these values of {a} into equation 3.19. This gives

$$u = [Q]\,[A]^{-1}\,\{u_n\}$$

and therefore we may write the shape functions of a quadrilateral element as

$$
\begin{aligned}
N_1 &= \frac{1}{4}\,(-1 + s^2 + t^2 + st - s^2t - t^2s) \\
N_2 &= \frac{1}{2}\,(1 - t - s^2 + s^2t) \\
N_3 &= \frac{1}{4}\,(-1 + s^2 + t^2 - st - s^2t + t^2s) \\
N_4 &= \frac{1}{2}\,(1 + s - t^2 - t^2s) \\
N_5 &= \frac{1}{4}\,(-1 + s^2 + t^2 + st + s^2t + t^2s) \\
N_6 &= \frac{1}{2}\,(1 + t - s^2 - s^2t)
\end{aligned}
\qquad 3.20
$$

$$N_7 = \frac{1}{4} (-1 + s^2 + t^2 - st + s^2t + t^2s)$$

$$N_8 = \frac{1}{2} (1 - s - t^2 + t^2s)$$

It can be verified that the shape functions for the v component of displacement are identical to those given above.

3.4.4.2 Geometric shape functions

As a result of the isoparametric formulation used in this thesis the geometric shape functions for the quadrilateral element are identical to the displacement shape functions (equation 3.20).

3.4.5 Summary

It is useful at this point to generalise the results which have been obtained in the previous section and also to examine the properties of the quadratic shape functions which have been obtained for the triangular and quadrilateral isoparametric finite elements.

The displacement of a general point, $\{\delta\}$, within a finite element may be written

$$\{\delta\} = \begin{Bmatrix} u \\ v \end{Bmatrix} = [L] \{d\} \qquad 3.21$$

where for an m-noded finite element the global displacement vector, $\{d\}$, is defined

$$\{d\}^T = \{ u_1 \quad v_1 \quad u_2 \quad v_2 \quad \ldots\ldots \quad u_m \quad v_m \}$$

and the shape function matrix, [L], is defined

$$[L] = \begin{bmatrix} N_1 & 0 & N_2 & 0 & \cdots\cdots & N_m & 0 \\ 0 & N_1 & 0 & N_2 & \cdots\cdots & 0 & N_m \end{bmatrix} \qquad 3.22$$

in which the nodal shape functions, N_i, are given for triangular and quadrilateral elements by equations 3.18 and 3.20 respectively.

For an isoparametric finite element the global co-ordinates, $\{g\}$, of a general point within the element can be written

$$\{g\} = \begin{Bmatrix} x \\ y \end{Bmatrix} = [L]\{c\} \qquad 3.23$$

where the nodal co-ordinates, $\{c\}$, of an m-noded finite element may be written

$$\{c\}^T = \{ x_1 \;\; y_1 \;\; x_2 \;\; y_2 \;\; \cdots\cdots \;\; x_m \;\; y_m \}$$

and the shape function matrix, $[L]$, is defined by equation 3.22.

We may rewrite equation 3.23 as

$$x = \sum_{i=1}^{m} N_i x_i$$

$$y = \sum_{i=1}^{m} N_i y_i \qquad 3.24$$

Examination of these equations reveals that if the sides of the element are straight the x and y co-ordinates vary linearly over the element. For example, consider a straight sided triangular element, such that the x co-ordinates of the mid-point nodes are

$$x_2 = \frac{x_1 + x_3}{2}, \qquad x_4 = \frac{x_3 + x_5}{2}, \qquad x_6 = \frac{x_1 + x_5}{2}$$

Substitution of these expressions and equations 3.18 into equation 3.24

gives

$$x = x_1(1-s-t) + x_3(s) + x_5(t)$$

which is a linear interpolation of the corner nodal values.

Equations 3.24 also have the property that if the global co-ordinates of the nodes on a side of an element do not fall on a straight line a quadratic function will be fitted through them. This is the property which allows us to introduce curved sided finite elements.

Consequently, the formulation given here is a general purpose one and can be used to model plane or curved sided finite elements.

3.5 Differentiation And Integration Of The Shape Functions

In some calculations in the finite element method we are required to differentiate or integrate the shape functions, which have been defined in terms of the local (s,t) co-ordinate system, with respect to the global (x,y) reference frame. In this section we obtain expressions which allow these calculations to be performed.

3.5.1 Differentiation: The Jacobian matrix

We may write the derivatives with respect to the local reference frame as

$$\frac{\partial}{\partial s} = \frac{\partial x}{\partial s}\cdot\frac{\partial}{\partial x} + \frac{\partial y}{\partial s}\cdot\frac{\partial}{\partial y}$$

$$\frac{\partial}{\partial t} = \frac{\partial x}{\partial t}\cdot\frac{\partial}{\partial x} + \frac{\partial y}{\partial t}\cdot\frac{\partial}{\partial y}$$

which may be expressed in matrix form as

$$\begin{Bmatrix} \frac{\partial}{\partial s} \\ \\ \frac{\partial}{\partial t} \end{Bmatrix} = [J] \begin{Bmatrix} \frac{\partial}{\partial x} \\ \\ \frac{\partial}{\partial y} \end{Bmatrix} \qquad 3.25$$

where [J] is the Jacobian matrix and is defined

$$[J] = \begin{bmatrix} \frac{\partial x}{\partial s} & \frac{\partial y}{\partial s} \\ \\ \frac{\partial x}{\partial t} & \frac{\partial y}{\partial t} \end{bmatrix} \qquad 3.26$$

We may therefore obtain expressions for the global derivatives by inverting equaton 3.25, which gives

$$\begin{Bmatrix} \frac{\partial}{\partial x} \\ \\ \frac{\partial}{\partial y} \end{Bmatrix} = [J]^{-1} \begin{Bmatrix} \frac{\partial}{\partial s} \\ \\ \frac{\partial}{\partial t} \end{Bmatrix} \qquad 3.27$$

where

$$[J]^{-1} = \begin{bmatrix} \Gamma_{11} & \Gamma_{12} \\ \\ \Gamma_{21} & \Gamma_{22} \end{bmatrix} = \frac{1}{\det J} \begin{bmatrix} \frac{\partial y}{\partial t} & -\frac{\partial y}{\partial s} \\ \\ -\frac{\partial x}{\partial t} & \frac{\partial x}{\partial s} \end{bmatrix} \qquad 3.28$$

This expression can be evaluated by substitution of equations 3.24.

3.5.2 Integration: Numerical integration

If the integrand $\phi(s,t)$ is expressed in local co-ordinates but the integration is with respect to the global co-ordinates then we must apply

the following transformation

$$I = \int\int \phi(s,t)\ dx\ dy = \int\int \phi(s,t)\ \det J\ ds\ dt \qquad 3.29$$

where det J is the determinant of the Jacobian matrix.

The integral in equation 3.29 can be evaluated numerically and it is desirable to rewrite it for this purpose as

$$I = \sum_i \sum_j' W_i W_j \phi(s_i, t_j) \qquad 3.30$$

where s_i and t_j are the location of the integration points and W_i and W_j are the weighting functions of these points. The location of the integration points and the values of the weights for triangular and quadrilateral elements are given in tables 3.1 and 3.2 respectively.

A more detailed discussion of numerical integration techniques in finite element applications is given in Cook (1981).

no. of Gauss points	location of Gauss points		weight of Gauss points	
	s_i	t_j	W_i	W_j
4	.577350269	.57735026	1.0	1.0
	-.577350269	.57735026	1.0	1.0
	.577350269	-.57735026	1.0	1.0
	-.577350269	-.57735026	1.0	1.0
9	.774596669	.77459666	.555555555	.55555555
	.774596669	-.77459666	.555555555	.55555555
	-.774596669	-.77459666	.555555555	.55555555
	-.774596669	.77459666	.555555555	.55555555
	0.0	.77459666	.888888888	.88888888
	0.0	-.77459666	.888888888	.88888888
	0.0	0.0	.888888888	.88888888
	.774596669	0.0	.555555555	.88888888
	-.774596669	0.0	.555555555	.88888888

Table 3.1: Numerical integration points for quadrilateral finite elements.

no. of Gauss points	location of Gauss points		weight of Gauss points	
	s_i	t_j	W_i	W_j
4	.3333333333	.333333333	-0.28125	-0.28125
	0.6	0.2	.260416667	.26041667
	0.2	0.6	.260416667	.26041667
	0.2	0.2	.260416667	.26041667
6	.8168472729	.091576313	.05497587	.05497587
	.0915763135	.091576313	.05497587	.05497587
	.0915763135	.816847273	.05497587	.05497587
	.1081030181	.445948490	.1116907	.1116907
	.4459484909	.108103018	.1116907	.1116907
	.4459484909	.445948490	.1116907	.1116907

Table 3.2: Numerical integration points for triangular finite elements.

3.6 Evaluation Of The Stiffness Matrix

We now proceed to evaluate the stiffness matrix for isoparametric finite elements. The method which is given in this section is generalised so that it can be applied to either triangular or quadrilateral elements.

3.6.1 The strain matrix

For two dimensional problems it is convenient to write the strain tensor, ε_{ij}, which is defined in terms of the derivatives of the displacements as

$$\varepsilon_{ij} = \frac{1}{2}\left(\frac{\partial u_i}{\partial x_j} + \frac{\partial u_j}{\partial x_i}\right)$$

as a two component column vector

$$\begin{Bmatrix} \varepsilon_x \\ \varepsilon_y \\ \gamma_{xy} \end{Bmatrix} = \begin{Bmatrix} \dfrac{\partial u}{\partial x} \\ \dfrac{\partial v}{\partial y} \\ \dfrac{\partial u}{\partial y} + \dfrac{\partial v}{\partial x} \end{Bmatrix} \qquad 3.31$$

where

$$\gamma_{xy} = \varepsilon_{xy} + \varepsilon_{yx}$$

For a point within an m-noded element we may write the derivatives of the displacement in the x direction, using equation 3.24, as

$$\frac{\partial u}{\partial x} = \frac{\partial \sum_{i=1}^{m} N_i u_i}{\partial x}$$

$$\frac{\partial v}{\partial x} = \frac{\partial \sum_{i=1}^{m} N_i v_i}{\partial x} \qquad 3.32$$

and we can also write similar expressions for the derivatives in the y direction

$$\frac{\partial u}{\partial y} = \frac{\partial \sum_{i=1}^{m} N_i u_i}{\partial y}$$

$$\frac{\partial v}{\partial y} = \frac{\partial \sum_{i=1}^{m} N_i v_i}{\partial y} \qquad 3.33$$

From these expressions we can write the strain at a general point within the element, $\{\varepsilon\}$, in terms of the nodal displacements, $\{d\}$, by substituting equations 3.32 and 3.33 into equation 3.31, which gives

$$\{\varepsilon\} = [B]\{d\} \qquad 3.34$$

where

$$[B] = \begin{bmatrix} \frac{\partial}{\partial x} & 0 \\ 0 & \frac{\partial}{\partial y} \\ \frac{\partial}{\partial y} & \frac{\partial}{\partial x} \end{bmatrix} [L] \qquad 3.35$$

and [L] is the shape function matrix defined in equation 3.22.

Since the element shape functions have been defined in terms of the local co-ordinate system we must use the Jacobian to evaluate the global derivatives required in equation 3.35. Recalling the Jacobian, equation 3.28, we may write

$$\begin{bmatrix} \frac{\partial}{\partial x} & 0 \\ 0 & \frac{\partial}{\partial y} \\ \frac{\partial}{\partial y} & \frac{\partial}{\partial x} \end{bmatrix} = \begin{bmatrix} \Gamma_{11} & \Gamma_{12} & 0 & 0 \\ 0 & 0 & \Gamma_{21} & \Gamma_{22} \\ \Gamma_{21} & \Gamma_{22} & \Gamma_{11} & \Gamma_{12} \end{bmatrix} \begin{bmatrix} \frac{\partial}{\partial s} & 0 \\ \frac{\partial}{\partial t} & 0 \\ 0 & \frac{\partial}{\partial s} \\ 0 & \frac{\partial}{\partial t} \end{bmatrix}$$

and therefore the strain matrix, equation 3.35, may be written

$$[B] = \begin{bmatrix} \Gamma_{11} & \Gamma_{12} & 0 & 0 \\ 0 & 0 & \Gamma_{21} & \Gamma_{22} \\ \Gamma_{21} & \Gamma_{22} & \Gamma_{11} & \Gamma_{12} \end{bmatrix} \begin{bmatrix} \frac{\partial}{\partial s} & 0 \\ \frac{\partial}{\partial t} & 0 \\ 0 & \frac{\partial}{\partial s} \\ 0 & \frac{\partial}{\partial t} \end{bmatrix} [L] \qquad 3.36$$

This expression can be evaluated if the appropriate shape functions, equation 3.22, are substituted into it.

3.6.2 The elasticity matrix

For two dimensional problems it is convenient to write the stress tensor, which is defined in terms of the strain through Hooke's law as

$$\sigma_{ij} = \lambda \theta \delta_{ij} + 2 \mu \varepsilon_{ij}$$

where λ and μ are Lame's constants and δ_{ij} is the Kroneker delta function, as a two component column vector

$$\{\sigma\} = \begin{Bmatrix} \sigma_x \\ \sigma_y \\ \tau_{xy} \end{Bmatrix} \qquad 3.37$$

The strains may be written in terms of the stresses, including any initial strains, ε_o, in terms of Poisson's ratio, ν, and Young's modulus, E, as

$$\varepsilon_x = \frac{1}{E} (\sigma_x - \nu \sigma_y - \nu \sigma_z) + \varepsilon_{x_o}$$

$$\varepsilon_y = \frac{1}{E} (-\nu \sigma_x + \sigma_y - \nu \sigma_z) + \varepsilon_{y_o}$$

$$\gamma_{xy} = \frac{2 (1+\nu)}{E} \tau_x + \gamma_{xy_o}$$

For the two dimensional case of plane strain the stress in the z direction is

$$\varepsilon_z = \nu (\sigma_x + \sigma_y) - E \sigma_{z_o}$$

which upon substitution into equation 3.37 gives

$$\begin{Bmatrix} \varepsilon_x \\ \varepsilon_y \\ \gamma_{xy} \end{Bmatrix} = \frac{(1+\nu)}{E} \begin{bmatrix} 1-\nu & -\nu & 0 \\ -\nu & 1-\nu & 0 \\ 0 & 0 & 2 \end{bmatrix} \begin{Bmatrix} \sigma_x \\ \sigma_y \\ \tau_{xy} \end{Bmatrix} + \begin{Bmatrix} \varepsilon_{x_o} + \nu\varepsilon_{z_o} \\ \varepsilon_{y_o} + \nu\varepsilon_{z_o} \\ \gamma_{xy_o} \end{Bmatrix}$$

This equation can be inverted to give an expression for the stresses in terms of the strains

$$\{\sigma\} = [C](\{\varepsilon\} - \{\varepsilon_o\}) \qquad 3.38$$

where [C] is the elasticity matrix and is defined by

$$[C] = \frac{E}{(1+\nu)(1-2\nu)} \begin{bmatrix} 1-\nu & \nu & 0 \\ \nu & 1-\nu & 0 \\ 0 & 0 & \frac{(1-2\nu)}{2} \end{bmatrix} \qquad 3.39$$

and the initial strains, $\{\varepsilon_o\}$, are defined by

$$\{\varepsilon_o\} = \begin{Bmatrix} \varepsilon_{x_o} + \nu\varepsilon_{z_o} \\ \varepsilon_{y_o} + \nu\varepsilon_{z_o} \\ \gamma_{xy_o} \end{Bmatrix} \qquad 3.40$$

If initial stresses, $\{\sigma_o\}$, are present in the body equation 3.38 may be written

$$\{\sigma\} = [C](\{\varepsilon\} - \{\varepsilon_o\}) + \{\sigma_o\} \qquad 3.41$$

3.6.3 The stiffness matrix

The governing equilibrium equation for the continuum can be obtained by minimising the total potential energy of the whole body with respect to the displacements, $\{\delta\}$, induced by internal forces, {b}, and external boundary forces, {q}.

We therefore define the total potential energy, π, of the continuum as

$$\pi = W + U \qquad 3.42$$

where W, the work done by the applied loads, is defined

$$W = \int \{\delta\}^T \{b\}\, dV + \int \{\delta\}^T \{q\}\, dA$$

and U, the strain energy, is defined

$$U = \frac{1}{2} \int \{\varepsilon\}^T \{\sigma\}\, dV$$

To obtain the total potential of the continuum we sum the equations 3.21, 3.24 and 3.41 over all of the elements of the body and substitute the resulting equations into equation 3.42, which gives

$$\pi = \frac{1}{2} \int_V \{d\}^T [B]^T [C] [B] \{d\}\, dV - \int_V \{d\}^T [B]^T [C] \{\varepsilon_o\}\, dV$$

$$+ \int_V \{d\}^T [B]^T \{\sigma_o\}\, dV + \int_V \{d\}^T [L]^T \{b\}\, dV$$

$$+ \int_A \{d\}^T [L]^T \{q\}\, dA \qquad 3.43$$

which must be minimised with repect to the global displacements

$$\frac{\partial \pi}{\partial \{d\}} = 0 \qquad 3.44$$

Substituting equation 3.43 into 3.44 gives

$$\int_V [B]^T [C] [B] \{d\} \, dV - \int_V [B]^T [C] \{\varepsilon_o\} \, dV$$

$$+ \int_V [B]^T \{\sigma_o\} \, dV + \int_V [L]^T \{b\} \, dV$$

$$+ \int_A [L]^T \{q\} \, dA = 0$$

This may be rewritten in a simplified form as

$$[K] \{d\} = \{F\} \qquad 3.45$$

where [K], the global stiffness matrix, is defined for unit thickness in the z direction as

$$[K] = \int_A [B]^T [C] [B] \, dx \, dy \qquad 3.46$$

and the global force vector, {F}, is defined

$$\{F\} = \{f_{\varepsilon_o}\} - \{f_{\sigma_o}\} - \{f_b\} - \{f_q\} \qquad 3.47$$

where for unit thickness

$$\{f_{\varepsilon_o}\} = \int_A [B]^T [C] \{\varepsilon_o\} \, dx \, dy \qquad 3.48$$

$$\{f_{\sigma_o}\} = \int_A [B]^T \{\sigma_o\} \, dx \, dy \qquad 3.49$$

$$\{f_b\} = \int_A [L]^T \{b\} \, dx \, dy \qquad 3.50$$

$$\{f_q\} = \int_S [L] \{q\} \, dS \qquad 3.51$$

Therefore we may solve equation 3.45 for the displacements if we can evaluate the global stiffness matrix, [K].

The procedure which is generally adopted to obtain [K] is to evaluate the stiffness of each element of the body, $[K^e]$, which from equation 3.46 may be written (using equation 3.29) as

$$[K^e] = \int \int [B]^T [C] [B] \det J \; ds \; dt \qquad 3.52$$

This matrix can be evaluated using numerical integration.

The global stiffness matrix [K] can then be evaluated by summing the element stiffnesses, equation 3.52, over all the M elements of the body, i.e.

$$[K] = \sum_{e=1}^{M} [K^e]$$

A more detailed description of this assembly procedure is given in most texts on finite elements (e.g. Cook, 1978).

3.7 Nodal Representation Of Forces

The effect of distributed surface tractions and body forces can be incorporated into the finite element model by calculating equivalent forces which act at the nodes of the body. To make these forces compatible with the isoparametric finite element method it is necessary to calculate them by evaluating equations 3.50 and 3.51.

In this section expressions for the nodal loads due to body forces, surface tractions and isostatic restoring forces are obtained.

3.7.1 Body forces

The body force vector, $\{b\}$, due to gravity, g, (directed down the negative y axis) acting upon a material of density ρ is given by

$$\{b\} = \begin{Bmatrix} 0 \\ -\rho g \end{Bmatrix}$$

Therefore if we evaluate the global body force vector, $\{f_b\}$, given by equation 3.50, at each element of the body we may obtain the element body force vector, $\{f^e\}$, which is defined

$$\{f^e\} = \int \int [L]^T \begin{Bmatrix} 0 \\ -\rho g \end{Bmatrix} \det J \; ds \; dt \qquad 3.53$$

which must be evaluated by numerical integration.

The global body force vector $\{f_b\}$ can be evaluated by summing equation 3.53 over all the elements of the body.

3.7.2 Surface traction

In this section expressions for the nodal representation of forces due to surface loads are obtained. These forces, by definition, act only upon an edge of an element and it is convenient if we perform the required calculations in a special local co-ordinate system.

3.7.2.1 The local co-ordinate system

Consider the edge of an element formed by nodes 1, 2 and 3 which have the nodal co-ordinates (x_1, y_1), (x_2, y_2) and (x_3, y_3) respectively. Then we may let this edge define the local co-ordinate s-axis which has its origin at node 2 and its positive axis directed towards node 1 (figure 3.5).

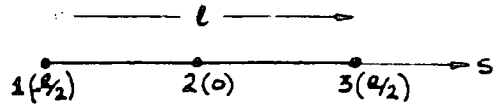

Figure 3.5: The local co-ordinate system for an isoparametric line element.

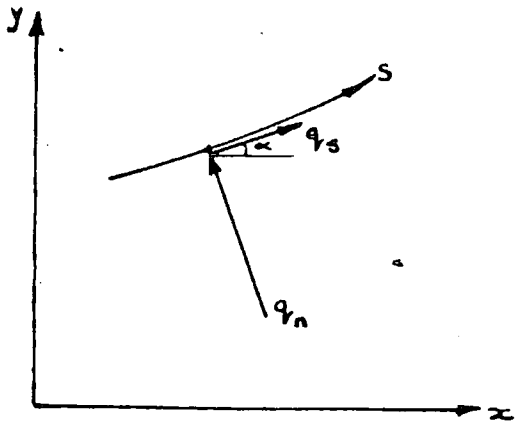

Figure 3.6: The normal and shear components of force acting at an edge of a finite element.

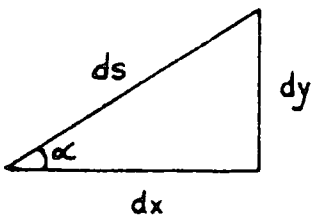

Figure 3.7: An infinitessimal segment of the edge of a finite element.

It is possible to define the quadratic shape functions of this system as

$$\bar{N}_1 = \frac{s}{\ell}\left(\frac{2s}{\ell} + 1\right)$$

$$\bar{N}_2 = 1 - \frac{4s^2}{\ell^2} \qquad 3.54$$

$$\bar{N}_3 = \frac{s}{\ell}\left(\frac{2s}{\ell} + 1\right)$$

where ℓ is the length of the side.

We may use these shape functions to express the cartesian co-ordinates (x,y) of a general point on the edge in terms of its nodal values as

$$\begin{Bmatrix} x \\ y \end{Bmatrix} = [\bar{L}] \{c\} \qquad 3.55$$

where the shape function matrix is

$$[\bar{L}] = \begin{bmatrix} \bar{N}_1 & 0 & \bar{N}_2 & 0 & \bar{N}_3 & 0 \\ 0 & \bar{N}_1 & 0 & \bar{N}_2 & 0 & \bar{N}_3 \end{bmatrix}$$

and {c}, the nodal co-ordinate vector, is

$$\{c\}^T = \{ x_1 \quad y_1 \quad x_2 \quad y_2 \quad x_3 \quad y_3 \}$$

It is also necessary to use a different numerical integration scheme when using this local co-ordinate system such that

$$\int \phi(s)\, ds = \sum_i W_i\, \phi(s_i) \qquad 3.56$$

where the location of the integration points and their weights are given in table 3.3.

no. of Gauss points	s_i	W_i
2	.5773502691	1.0
	-.5773502691	1.0
3	.7745966692	.5555555555
	-.7745966692	.5555555555
	0.0	.8888888888

Table 3.3: Numerical integration points for a line element.

3.7.2.2 Nodal representation of forces due to a surface traction

The nodal forces arising from a surface traction are defined by equation 3.51. This may be rewritten in terms of the local co-ordinate system as

$$\{f_q\} = \int [\bar{L}]^T \{q\} \, ds \qquad 3.57$$

where the global components of the nodal force vector, $\{f_q\}$, are

$$\{f_q\}^T = \{ f_{x_1} \; f_{y_1} \; f_{x_2} \; f_{y_2} \; f_{x_3} \; f_{y_3} \}$$

and the global components of the nodal tractions, $\{q\}$, are

$$\{q\}^T = \{ q_{x_1} \; q_{y_1} \; q_{x_2} \; q_{y_2} \; q_{x_3} \; q_{y_3} \}$$

In general $\{q\}$ is unknown, and therefore, it must be evaluated from the known values of the normal and shear traction at the boundary, $\{q_{sn}\}$, which are defined

$$\{q_{sn}\}^T = \{ q_{s_1} \; q_{n_1} \; q_{s_2} \; q_{n_2} \; q_{s_3} \; q_{n_3} \}$$

We must therefore find relationships between the global components of the traction and the local normal and shear components.

Using figure 3.7 we may write the relationship between these at a general point as

$$\begin{Bmatrix} q_x \\ q_y \end{Bmatrix} = \begin{bmatrix} \cos\alpha & -\sin\alpha \\ \sin\alpha & \cos\alpha \end{bmatrix} \begin{Bmatrix} q_s \\ q_n \end{Bmatrix} \qquad 3.58$$

From figure 3.8, however, we know that

$$dx = \cos\alpha \; ds$$

$$dy = \sin\alpha \; ds$$

and therefore we may rewite equation 3.58 as

$$\begin{Bmatrix} q_x \\ q_y \end{Bmatrix} = [R'] \begin{Bmatrix} q_s \\ q_n \end{Bmatrix} \qquad 3.59$$

in which

$$[R'] = \begin{bmatrix} \dfrac{dx}{ds} & -\dfrac{dy}{ds} \\ \dfrac{dy}{ds} & \dfrac{dx}{ds} \end{bmatrix}$$

Evaluating equation 3.59 at the three nodes on the boundary we obtain

$$\{q\} = [R] \; \{q_{sn}\} \qquad 3.60$$

in which

$$[R] = \begin{bmatrix} [R'] & 0 & 0 \\ 0 & [R'] & 0 \\ 0 & 0 & [R'] \end{bmatrix}$$

We therefore obtain the desired force equation by substituting equation 3.60 into equation 3.57, giving

$$\{f_q\} = \int [L]^T [R] \; \{q_{sn}\} \; ds \qquad 3.61$$

which must be evaluated by numerical integration.

3.7.2.3 Isostatic compensation

The situation where the body is bounded by a fluid is now considered. In this case the displacements of the body are resisted by hydrostatic restoring forces (Dean, 1973).

The pressure in a fluid, q, resisting a vertical displacement, v, is

$$q = -\rho g v$$

where ρ is the density of the fluid and g is the acceleration due to gravity. This restoring force acts normal to the boundary of the element, and therefore, we may write the normal and shear force vector, $\{q_{sn}\}$, as

$$\{q_{sn}\} = \rho g \{d\} \qquad 3.62$$

where

$$\{d\}^T = \{ 0 \quad v_1 \quad 0 \quad v_2 \quad 0 \quad v_3 \}$$

We therefore obtain the desired expression by substituting equation 3.62 into equation 3.61, giving

$$\{f_q\} = [K_I] \{d\} \qquad 3.63$$

where

$$[K_I] = \int [\bar{L}]^T [R] \, ds$$

which may be incorporated as a force in the global stiffness equation (equation 3.45)

$$\{ F + f_q \} = [K] \{d\}$$

so that by substitution of equation 3.61 we obtain

$$\{ F + [K_I]\{d\}) = [K] \{d\}$$

and therefore

$$\{F\} = [K - K_I] \{d\}$$

We can consequently incorporate isostatic restoring forces in the model by subtracting the isostatic matrix from the global stiffness matrix, [K].

3.8 Thermal Stresses

The effect of thermal volume changes can be incorporated into the finite element model using the initial strain approach (Cook, 1981). For plane strain we can therefore write the initial strain, $\{\varepsilon_o\}$, as

$$\{\varepsilon_o\} = \begin{Bmatrix} \varepsilon_{x_o} \\ \varepsilon_{y_o} \\ \gamma_{xy_o} \end{Bmatrix} = (1+\nu) \begin{Bmatrix} \alpha \Delta T \\ \alpha \Delta T \\ 0 \end{Bmatrix}$$

where α is the volume coefficient of thermal expansion and ΔT is the temperature change.

These initial strains can be incorporated into the finite element calculations by evaluating the initial strain force vector (equation 3.48). Solution of the stiffness equation then yields the strain in the body, so that the thermal stress can be calculated from

$$\{\sigma\} = [C] (\{\varepsilon\} - \{\varepsilon_o\})$$

where, for plane strain,

$$\sigma_z = \nu(\sigma_x + \sigma_y) - E\alpha\Delta T$$

3.9 Visco-elastic Analysis

Visco-elastic behaviour can be incorporated into the finite element method by using the initial strain aproach (Zienkiewicz et al, 1968).

The strain rate tensor, $\{\dot{\varepsilon}_{ij}\}$, at a general point in a Maxwell body with viscosity, η, is

$$\{\dot{\varepsilon}_{ij}\} = \frac{(1+\nu)}{E}\dot{\sigma}'_{ij} + \frac{1}{2\eta}\sigma'_{ij} \qquad 3.64$$

where σ'_{ij} is the devitoric stress tensor which is defined

$$\sigma'_{ij} = \sigma_{ij} - \delta_{ij}\left(\frac{\sigma_{kk}}{3}\right)$$

The second term on the right hand side of equation 3.64 is the viscous creep rate $\{\dot{\varepsilon}\}_c$ which is defined at a general point in the body as

$$\{\dot{\varepsilon}\}_c = \begin{Bmatrix} \{\dot{\varepsilon}_x\}_c \\ \{\dot{\varepsilon}_y\}_c \\ \{\dot{\gamma}_{xy}\}_c \\ \{\dot{\varepsilon}_z\}_c \end{Bmatrix} = \frac{1}{2\eta}\begin{Bmatrix} \sigma_x - \sigma_h \\ \sigma_y - \sigma_h \\ 2\tau_{xy} \\ \sigma_z - \sigma_h \end{Bmatrix}$$

where σ_h, the hydrostatic stress, is defined

$$\sigma_h = \frac{1}{3}(\sigma_x + \sigma_y + \sigma_z)$$

Because of the existence of the deviatoric stress the z component of creep $\{\varepsilon_z\}$ is not zero. Consequently to fulfill the condition of plane strain it is necessary that the total strain in the z direction equals zero, that is

$$\frac{(\sigma_z - \sigma_h)}{2} = -\frac{(1+\nu)}{E}\dot{\sigma}_{ij}$$

It is now possible to evaluate the total creep strain $\{\varepsilon\}_c$ over a timestep t by the simple integration

$$\{\varepsilon\}_c = \{\dot{\varepsilon}\}_c\, t$$

which may be written as an initial strain

$$\{\varepsilon_o\} = \{\varepsilon\}_c$$

and incorporated as a force due to the initial strains

$$\{f_{\varepsilon_o}\} = - \int [B]^T [C] \{\varepsilon_o\} \, dx \, dy$$

This must be evaluated by numerical integration and added to the global force vector. The stiffness equation can then be resolved using this new force vector, which gives the stress at the end of the time increment, and therefore a new estimate of the creep strains and the initial strain force vector. The stiffness equation is then resolved using this new force vector and the procedure is repeated until the creep stress at the end of the time increment falls to an acceptable level.

A more complete discussion of this algorithm is given in Park (1981).

CHAPTER 4

COMPARISON OF FINITE ELEMENTS

4.1 Introduction

In this thesis it is proposed to use the isoparametric finite element method to model lithospheric stress regimes. Previous attempts to model the stress in the lithosphere, however, have successfully used constant strain finite elements which are based upon simpler mathematics. It is therefore the aim of this chapter to compare the performance of these two finite element methods so that it can be assessed whether the use of the mathematically complex isoparametric finite element is justified. In order to investigate this problem the performance of the constant strain and isoparametric elements are compared with analytic solutions to elastic flexure, body forces, and the case of a pressurised visco-elastic cylinder.

4.2 Constant Strain Elements

Two types of constant strain finite elements have been used at Durham University to model the lithospheric stress regime;

1. The constant strain triangle

   This element, which has been extensively used (Dean, 1973; Kusznir, 1976; Woodward, 1976; Mithen, 1980; Park, 1981), is triangular with three nodes lying at its vertices (figure 4.1). Each triangular element is based upon a linear displacement function and therefore the strain is constant in each element. This element is consequently known as the constant strain triangle

(CST). The CST is the simplest of the two dimensional finite elements and its main advantage is that an explicit expression can be derived for its stiffness matrix. The solutions for the CST models which are shown in this chapter were obtained with the computer program of Park (1981).

2. The constant strain quadrilateral

This element, which was used by Linton (1982), is a quadrilateral which has four nodes located at its corners (figure 4.2). The stiffness matrix of each quadrilateral is assembled by a procedure known as condensation of internal degrees of freedom. The initial process in this approach is to divide each quadrilateral into four CST sub-elements which are formed by the four vertices of the the quadrilateral together with an assumed common node at the centroid of the element (figure 4.2). The stiffness of the quadrilateral is then found by calculating the stiffness of the four CST sub-elements and condensing internal degrees of freedom. This procedure eliminates the dependence of the stiffness matrix on the assumed internal node and consequently the displacements are only solved at each corner node. Finally, the stress is evaluated at the centroid of the quadrilateral by recovering the displacement of the internal node and averaging the stress in the four CST sub-elements. This results in a constant strain in each element and this technique is therefore known as the constant strain quadrilateral method (CSQ).

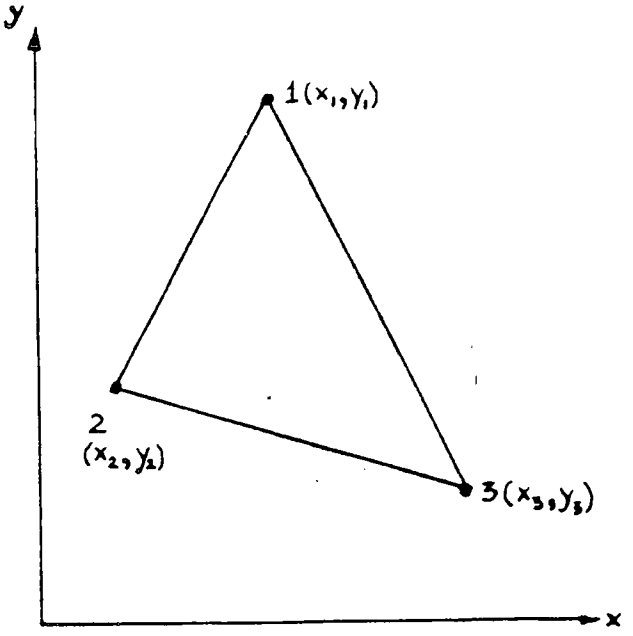

Figure 4.1: Geometry of the CST element.

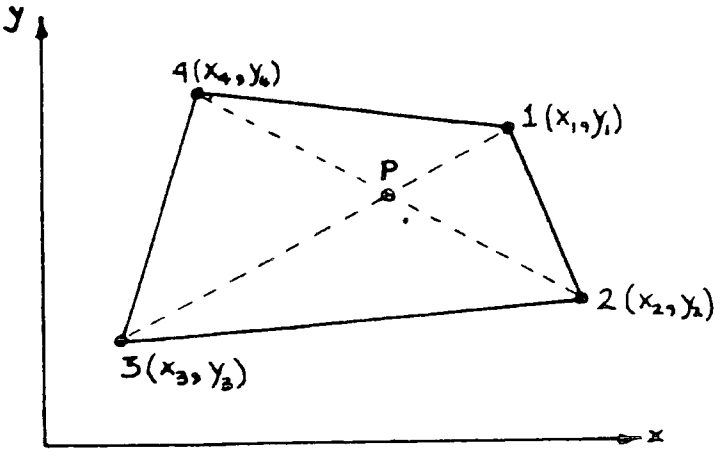

Figure 4.2: Geometry of the CSQ element. Node C is the condensed internal node.

4.3 Cantilever Bending

In this section the CST, CSQ and isoparametric finite element solutions to the problem of the flexure of a cantilever are compared to the analytic result.

4.3.1 Analytic solution

Consider a cantilever of unit width, length ℓ and thickness 2c which is fixed at its right hand edge and acted upon by a downwards oriented force of magnitude P at its free left hand edge (figure 4.3). It can be shown (Timoshenko and Goodier, 1970) that the vertical displacement, v, along the neutral fibre of the cantilever is given by

$$v = \frac{Px^3}{6EI} - \frac{P\ell^2 x}{2EI} + \frac{P\ell^3}{3EI}$$

where E is Young's Modulus and I is the moment of inertia which is defined as

$$I = \frac{2}{3} c^3$$

It can also be shown that the stress in the x direction is given by

$$\sigma_x = -\frac{3P}{2c^3} xy \qquad 4.1$$

Examination of this equation reveals that at a particular distance along the cantilever there is a linear variation of this stress in the y direction.

4.3.2 Finite element solutions

In the first part of this section the three finite element solutions will be compared using meshes of similar complexity, and therefore, each grid has been discretised so that it has 27 nodes. The isoparametric grid

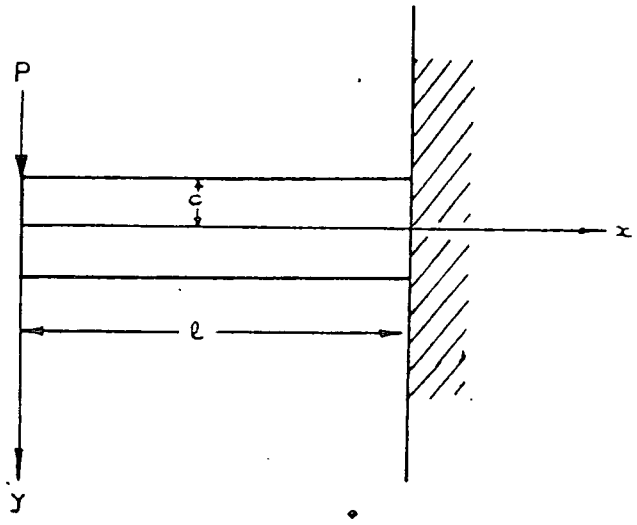

Figure 4.3: Geometry of the cantilever problem.

has 8 triangular elements with 6 Gaussian integration points (figure 4.4), the CST mesh has 32 elements (figure 4.5) and the CSQ mesh has 16 elements (figure 4.6). All the meshes are 10 inches long and 2.5 inches thick.

The material properties which were used in the calculations are representative of steel, which has a Young's modulus of 0.85×10^7 N m and a Poisson's ratio of 0.35. The boundary conditions are that the right hand edge of the model is fixed and a force of magnitude 5.0×10^4 psi acts vertically downwards at the free left hand edge of the model.

The vertical displacement profile of the neutral fibre of the finite element meshes are compared with the analytic solution in figure 4.6. The most accurate solution is obtained with the isoparametric finite element model, which predicts almost identical displacements to the analytic solution.

The solutions using the constant strain models are less accurate than the isoparametric one. The least accurate results are obtained with the CST model. The displacements predicted by this model are consistently less than the analytic solution, and the maximum displacement is only 58% of the exact value. This is because the finite element mesh is too stiff and consequently resists bending. The solution using the CSQ model is an improvement upon the CST one because its assembly procedure has the effect of making the mesh less stiff. The maximum displacement of the CSQ model, however, is only 83% of the analytic value.

Accurate solutions to flexural problems can therefore be obtained using simple isoparametric meshes. This is because the strain varies linearly within isoparametric elements, and therefore the linear strain profile within the flexed cantilever (equation 4.1) can be modelled with a

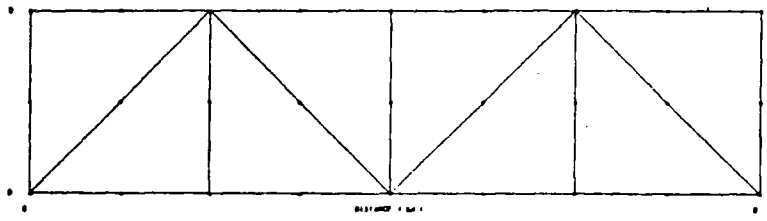

Figure 4.4: The geometry of the 27 noded isoparametric finite element mesh used in the cantilever flexure problem.

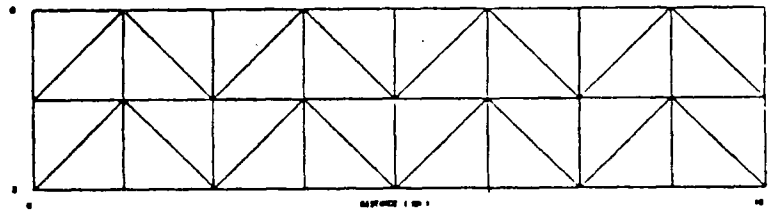

Figure 4.5: The geometry of the 27 noded CST mesh used in the cantilever flexure problem.

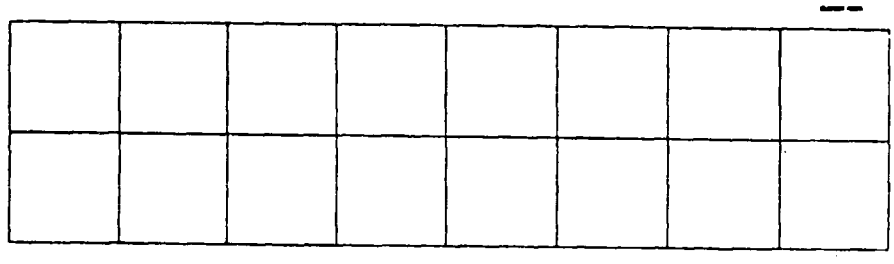

Figure 4.6: The geometry of the 27 noded CSQ mesh used in the cantilever flexure problem.

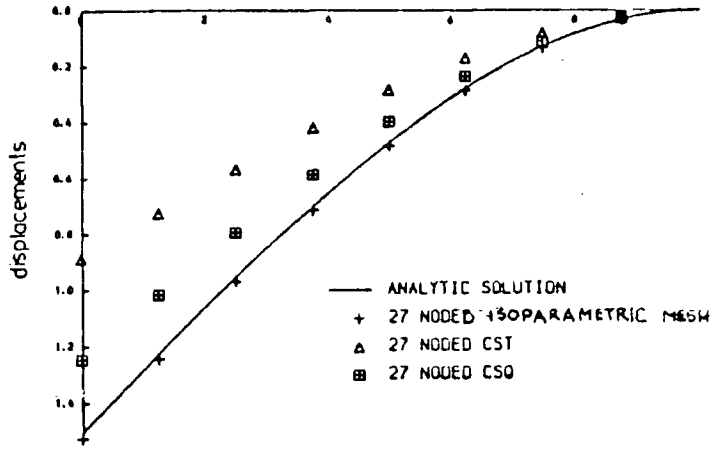

Figure 4.7: Comparison of the vertical displacement profile predicted by the 27 noded finite element models with the analytic solution.

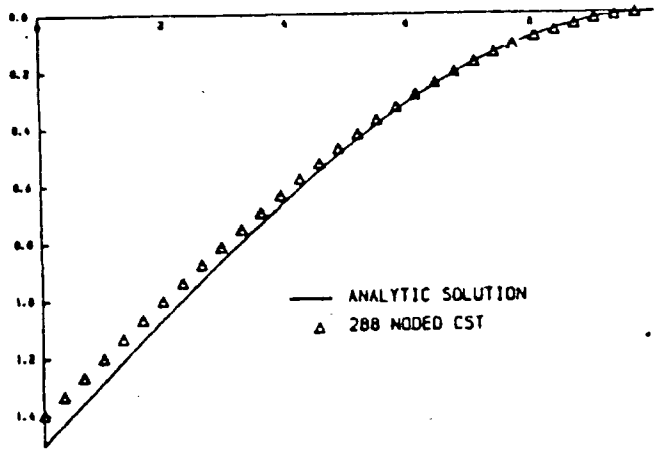

Figure 4.8: Comparison of the vertical displacement profile predicted by the 288 noded CST model with the analytic solution.

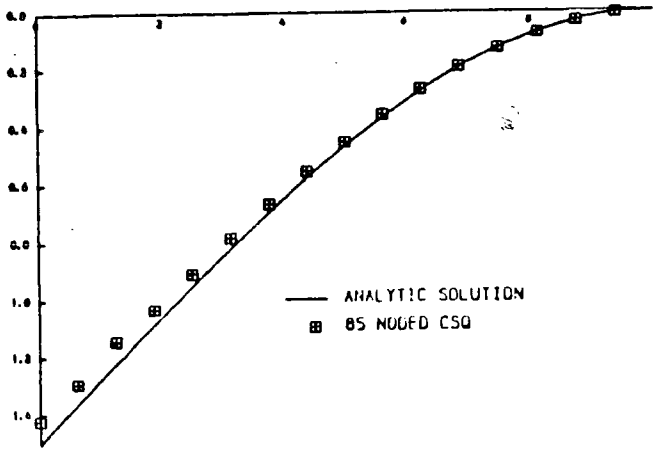

Figure 4.9: Comparison of the vertical displacement profile predicted by the 85 noded CSQ model with the analytic solution.

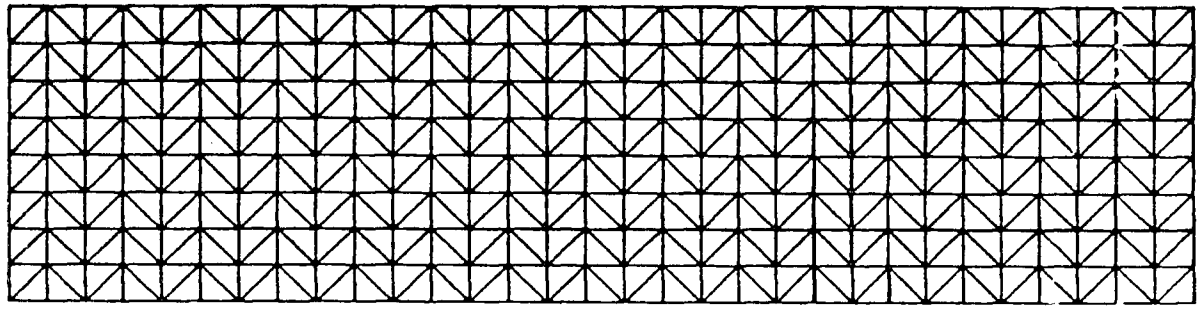

Figure 4.10: The geometry of the 288 noded CST mesh.

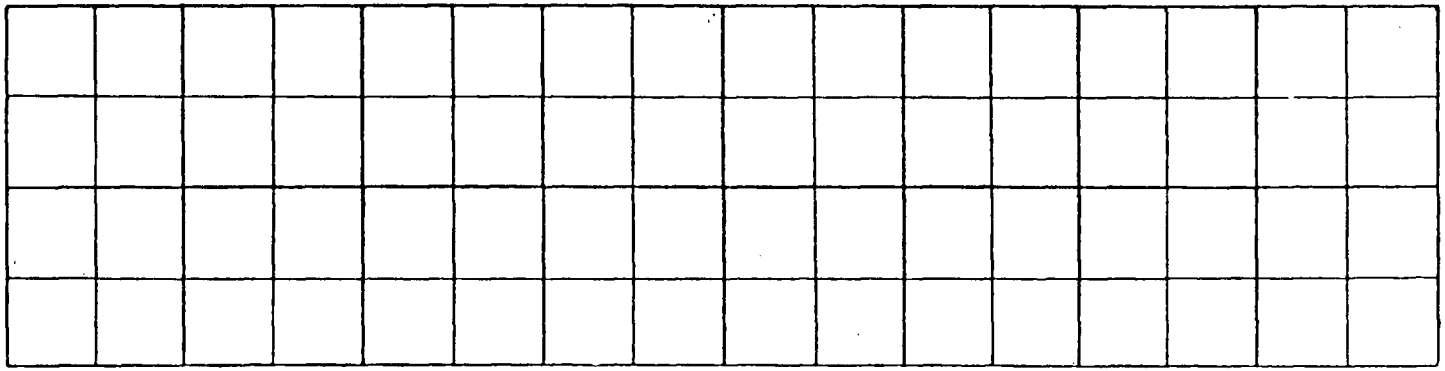

Figure 4.11: The geometry of the 85 noded CSQ mesh.

mesh which is only one element thick. The constant strain element meshes behave too stiffly because an insufficient number of elements were used to model the linear strain gradient. Accurate solutions to this problem can therefore only be obtained by increasing the complexity of the constant strain element meshes. They were therefore redesigned until they gave results which fell within 5% of the analytic solution.

The CST mesh (figure 4.10), which predicts displacements within 5% of the analytic solution (figure 4.8), has 288 nodes and 496 elements. The CSQ mesh (figure 4.11) which gives a comparable solution (figure 4.9) has 85 nodes and 64 elements.

These results demonstrate that the meshes which are required to obtain accurate solutions to flexural problems with constant strain elements are considerably more complex than isoparametric ones. There are consequently two practical disadvantages with using constant strain elements to model problems with a high strain gradient. Firstly, a relatively greater time is required to design, input to the computer, and eliminate any errors from the mesh. Secondly, a greater computational time is required to obtain an accurate solution (table 4.1).

METHOD	SOLUTION TIME (CPU seconds)
Isoparametric	1.269
QST	2.845
CST	12.192

Table 4.1: Comparison of the CPU time required to obtain displacements within 5% of the analytic solution with different finite element methods.

There is, however, a more important disadvantage in using the constant strain element to model lithospheric stress regimes. This is that we can only be sure the model is giving an accurate solution by iteratively redesigning the mesh until convergent solutions are obtained. This procedure, however, is rarely adopted in practise because it is very time consuming. It is therefore always possible that constant strain models will act too stiffly.

It is consequently desirable to use the isoparametric finite element method to model complex lithospheric stress distributions because it gives accurate results with a relatively simple mesh design.

4.4 Body Forces

The stresses in the lithosphere resulting from the action of body forces are generally of greater magnitude than those from other sources. It is therefore important that the finite element method which is adopted can accurately model these stresses.

In this section the solutions using the three finite element methods are compared with the analytic solution for the problem of body forces acting upon a flat constrained region.

4.4.1 Analytic solution

Consider a flat region, constrained for zero horizontal displacement, of uniform density, ρ, acted upon by gravity, g. Because there is no horizontal displacement anywhere in the body the strain in the x direction is zero, i.e.

$$\varepsilon_x = 0$$

Using this boundary condition it can be shown that the stress in the y direction is given by

$$\sigma_y = \rho g y \qquad 4.2$$

so that, for the case of plane strain, the stress in the x direction is

$$\sigma_x = \frac{\nu}{(1-\nu)} \sigma_y \qquad 4.3$$

Because there is no horizontal displacement anywhere in the body it can be shown that the maximum and minimum principal stresses are in the y and x direction and their magnitude is defined by equations 4.2 and 4.3.

For the case of plane strain we may express the strain in the y direction, using equation 4.2, as

$$\varepsilon_y = \frac{\partial v}{\partial y} = \frac{(1+\nu)\ (1-2\nu)}{E(1-\nu)} \rho g y$$

which may be integrated to obtain an expression for the vertical component of displacement at depth h

$$v = \frac{(1+\nu)\ (1-2\nu)}{E(1-\nu)} \rho g \frac{h^2}{2} \qquad 4.4$$

4.4.2 Finite element solutions

The finite element models were assumed to have a Poisson's ratio of 0.25, Young's modulus of 9.0×10^{10} N m^{-2}, and a density of 2800 kg m^{-3}. The acceleration due to gravity was assumed to be 9.81 m s^{-2}. All the finite element meshes are 10 km square and have 9 nodes. The boundary conditions were:

1. The left and right hand edges were constrained to move vertically.

2. The base was constrained to move horizontally.

The isoparametric finite element mesh has two triangular elements with 6 Gaussian integration points (figure 4.12). The stresses and vertical displacements of the nodes on the top surface of the model are shown in figure 4.13. The vertical displacements of all the nodes on the top surface of the model are 12.71 metres. This is in exact agreement with the analytic solution (obtained by substituting h = 10km in equation 4.4). The magnitude and orientation of the maximum and minimum principal stresses are also in exact agreement with the analytic solution.

The CST finite element mesh which was initially used to model this problem has nine nodes and eight elements (figure 4.14). The stress vectors and the vertical displacements of the top surface of the model are shown in figure 4.15. The displacement of the top node on the left hand edge of the model is 10% greater than the analytic solution and the displacement of the node on the top right hand edge of the model is 10% less than the analytic solution. The top surface of the finite element model is therefore 'skewed' about the analytic solution. The maximum and minimum principal stresses in this model are also skewed by up to 13 degrees from the analytic orientation and the magnitude of these stresses differ by up to 10% from the analytic values.

Solutions using nine noded CST meshes with different element topologies are shown in figure 4.16. Each model has a skewed stress and displacement surface. The orientation of the skewed displacement surface and stress vectors is dependant upon the topology of the finite element mesh. This non uniqueness of the solution is undesirable and is caused by

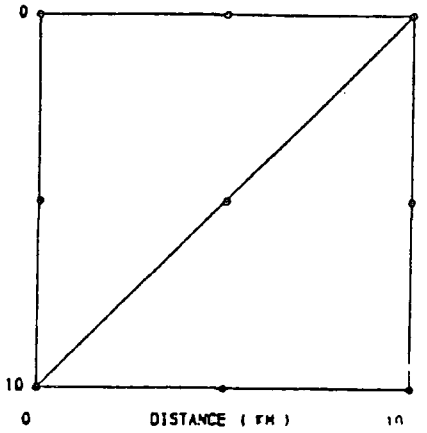

Figure 4.12: The geometry of the isoparametric finite element mesh used in the body force test.

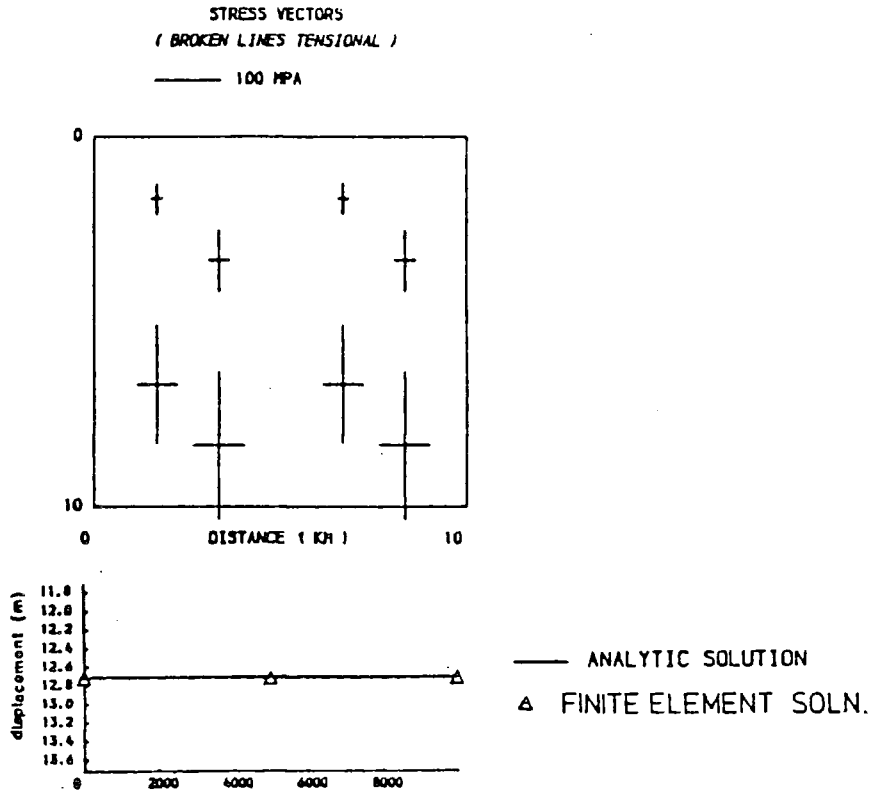

Figure 4.13: The principal stress vectors and the displacement of the top surface of the isoparametric model.

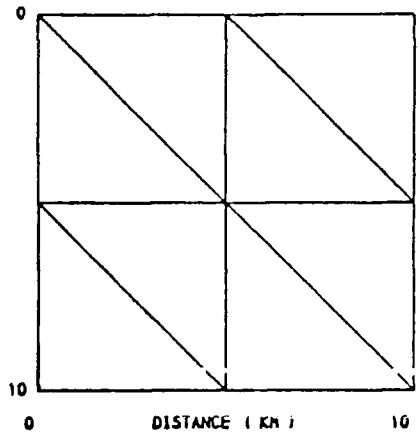

Figure 4.14: The geometry of the CST element mesh used in the body force test.

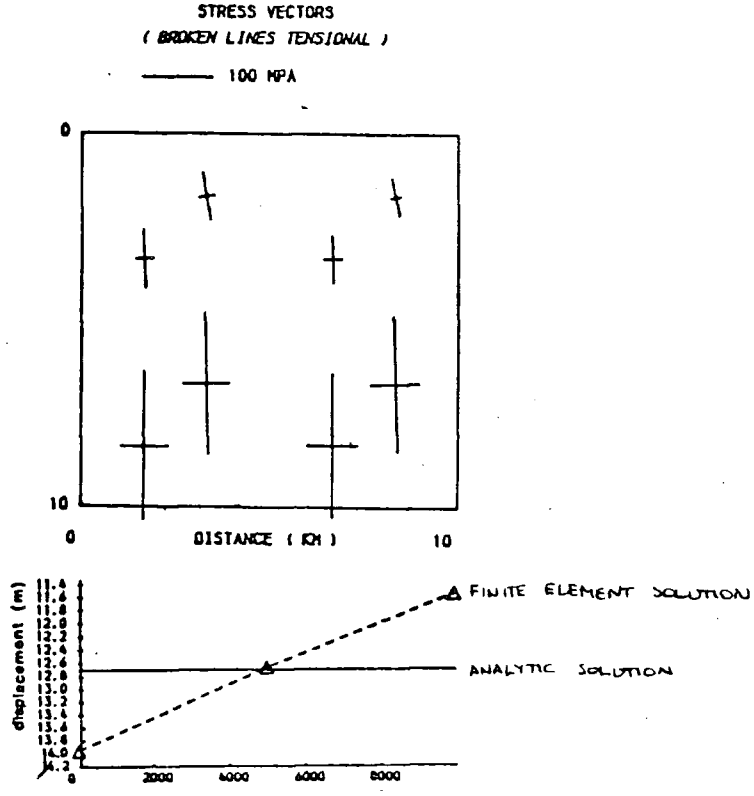

Figure 4.15: The principal stress vectors and the displacement of the top surface of the CST model.

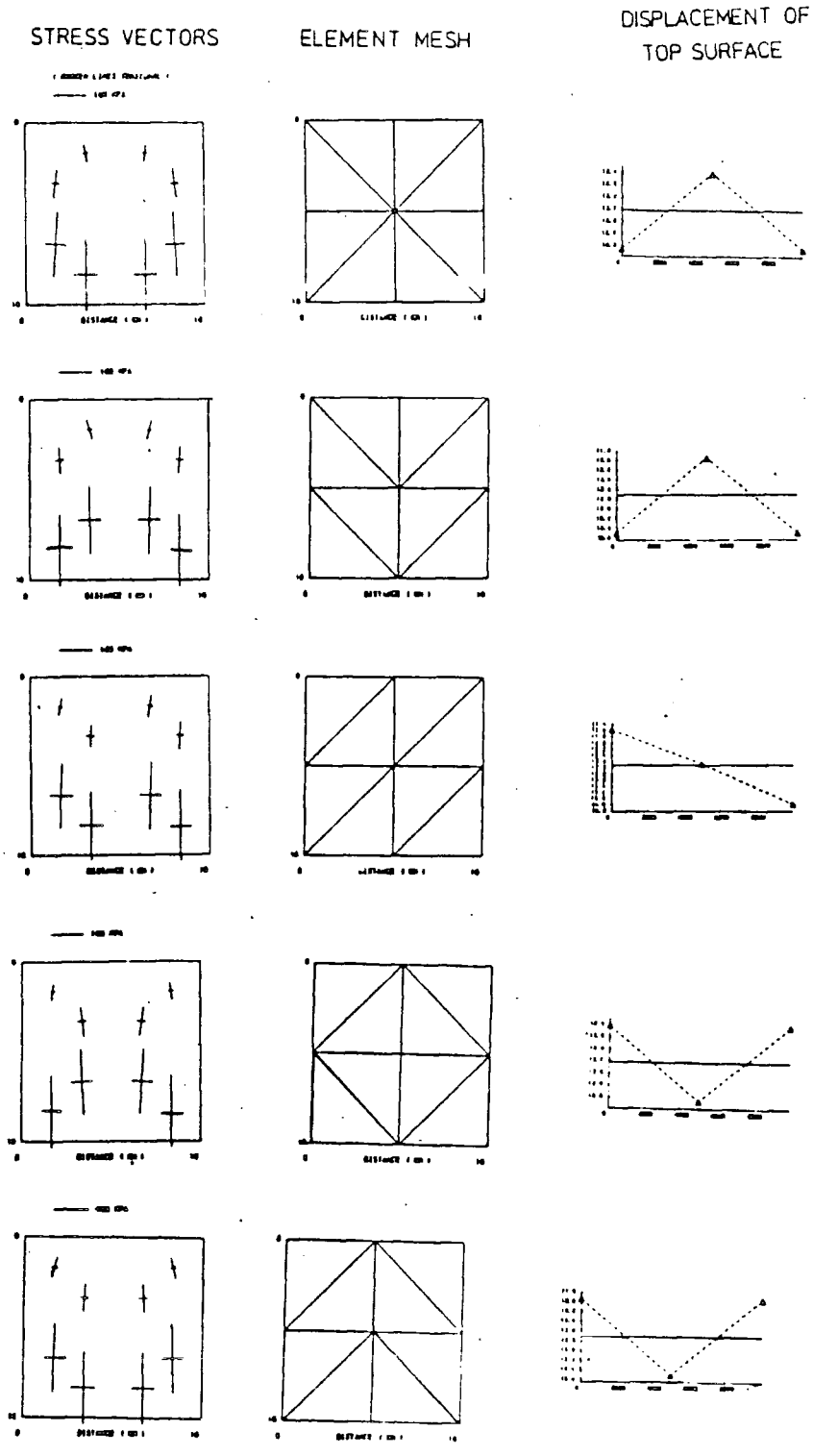

Figure 4.16: Comparison of the stress vectors and displacements predicted by CST meshes with different topologies.

irregularities in the stiffness of the finite element mesh. Doubling the number of CST elements in the mesh (figure 4.17) gives the correct surface dispacement but does not significantly improve the predicted stresses (figure 4.18). Skewed stress vectors are also common in other body force problems which have been modelled with CST elements (Mithen 1980, figure 4.3; Park 1981, figure 4.5). There are two problems with this behaviour which could potentially be encountered when attempting to model the more complex problems of geodynamics. The first is that the skew could obscure any true rotations of the stress vectors which are caused by lateral density variations. The second is that because the magnitude of the stress due to body forces is generally larger than that from other sources the skew will be present in the total or deviatoric stresses.

The CSQ mesh has nine nodes and four elements (figure 4.19) and the deformation predicted by this model (figure 4.20) is in exact agreement with the analytic solution. This result is surprising because the CSQ element is assembled from CST elements (section 4.2). The CSQ model, however, predicts accurate displacements because it is assembled from a set of four CST sub-elements (figure 4.17) which correctly model the displacements (figure 4.19). The stress vectors at the centroid of each quadrilateral element are also calculated correctly because they are obtained by averaging the stress in the four CST sub-elements. The CSQ element therefore performs better because its assembly procedure averages out the stiffness irregularities which occur in CST models.

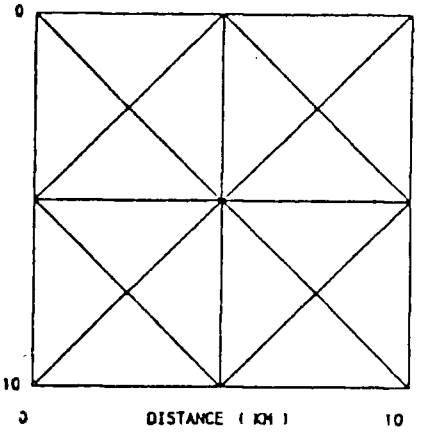

Figure 4.17: The geometry of the 13 noded CST mesh.

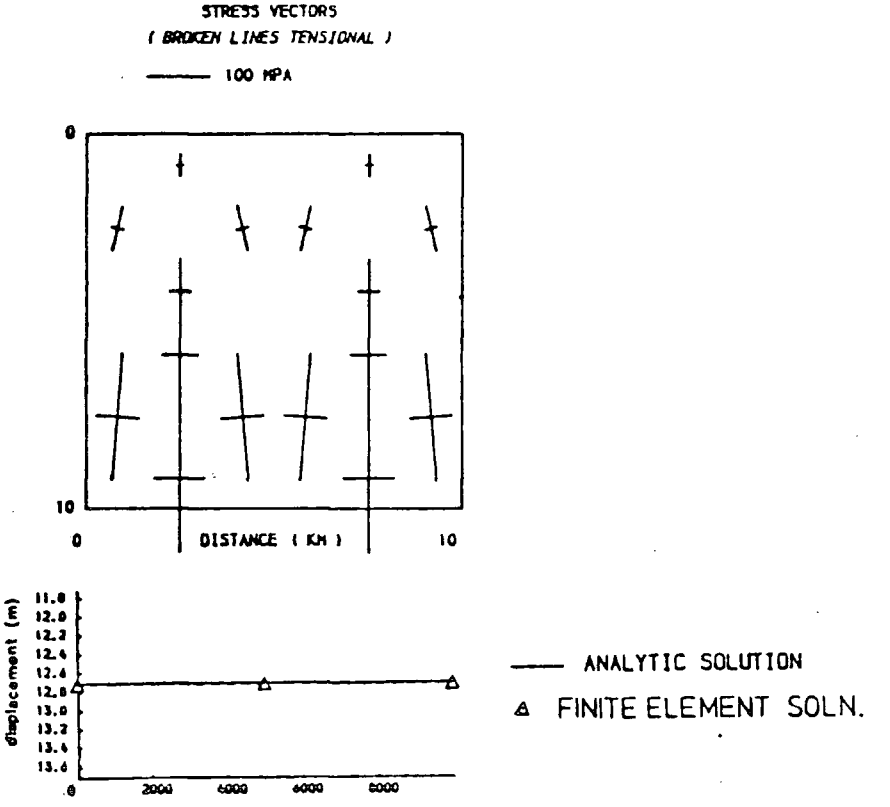

Figure 4.18: The principal stress vectors and the displacement of the top surface of the 13 noded CST mesh.

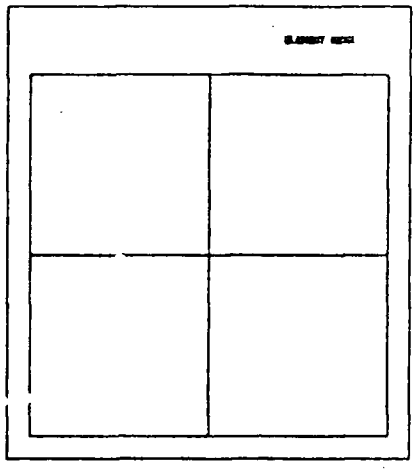

Figure 4.19: The geometry of the 9 noded CSQ finite element mesh used in the body force test.

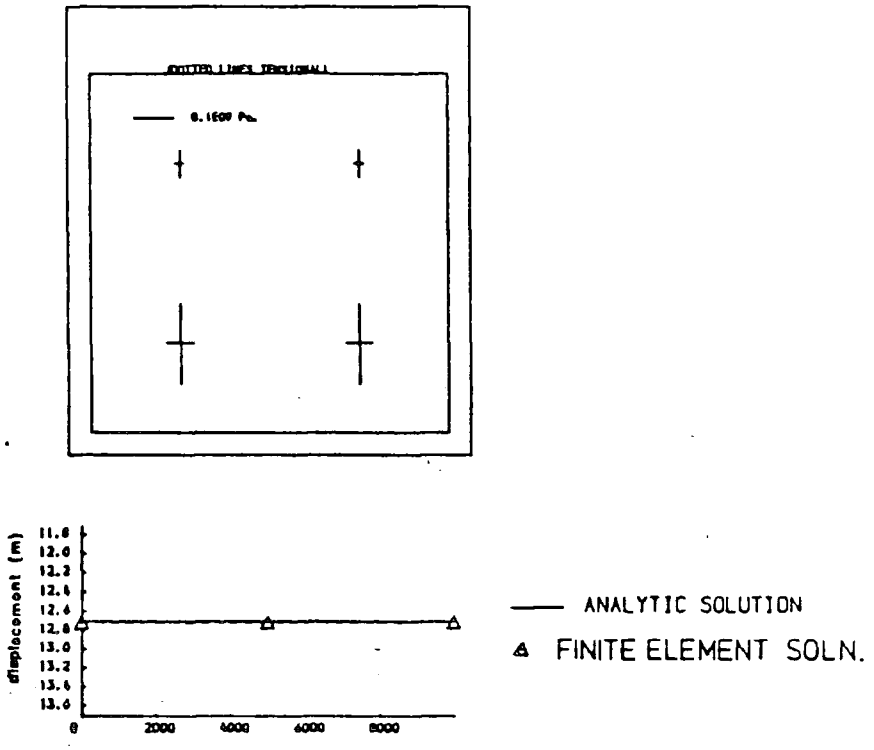

Figure 4.20: The principal stress vectors and displacements of the top surface of the CSQ model.

4.5 Visco-elastic Cylinder

It is important when modelling lithospheric stress regimes that the adopted finite element technique performs accurately in visco-elastic problems.

In this section the features of the CST and isoparametric finite element solutions are compared with the analytic solution to the case of a pressurised visco-elastic cylinder. The CSQ element can not be modelled in this section because the available program (Linton, 1982) does not have a visco-elastic capability.

4.5.1 Analytic solution

The time dependant nature of the stress distribution in an infinite hollow cylinder of visco-elastic material encased in a thin elastic shell, due to an applied internal pressure, has been solved analytically by Lee et al. (1959). They demonstrate that the principal stresses in the plane of a cross section through the cylinder are oriented radially, σ_r, and tangentially, σ_t, and that their magnitude is a function of time, t, and radial distance r. The radial and tangential stresses are defined as

$$\sigma_r(r,t) = -p\left(f(t) + \frac{r_o^2}{r^2}\, g(t)\right)$$

$$\sigma_t(r,t) = -p\left(f(t) - \frac{r_o^2}{r^2}\, g(t)\right)$$

where p is the internal pressure applied at time t=0, r_o is the outer radius of the visco-elastic cylinder, and f and g are functions which are related to the material properties of the cylinder.

4.5.2 Finite element solutions

In the computations the visco-elastic cylinder was assumed to have an inner radius of two inches and an outer radius of four inches. The elastic shell was assumed to be 4/33 of an inch thick. The material properties which were used in the calculations are summarised in table 4.2. The functions f(t) and g(t) for these material properties are

$$f(t) = 1.0 - 0.005363 \exp(-0.9849t) - 0.6331 \exp(-0.3528t)$$

$$g(t) = 0.001341 \exp(-0.9849t) - 0.1583 \exp(-0.3528t)$$

Material	Young's modulus (p.s.i)	Poisson's ratio	Viscosity (p.s.i)
Elastic	3.0×10^7	0.3015	-
Visco-elastic	1.0×10^5	0.3333	0.375×10^5

Table 4.2: Material properties of the visco-elastic cylinder.

Because of the symmetry of this problem it is only necessary to model a quadrant of the cylinder. The isoparametric mesh which was used to model this problem (figure 4.22) is composed of curved sided finite elements which reflect the cylindrical nature of the body. The CST mesh (figure 4.21) is composed of plane sided finite elements.

The displacement boundary conditions of the finite element models reflect the symmetry of the problem:

1. The left hand edge of the model is constrained to move vertically.

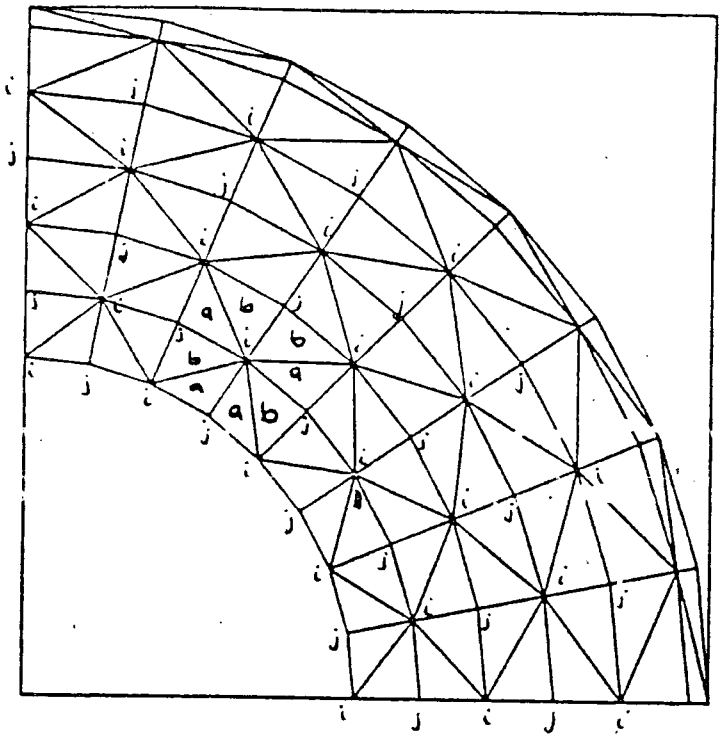

Figure 4.21: The geometry of the CST mesh used in the visco-elastic cylinder test.

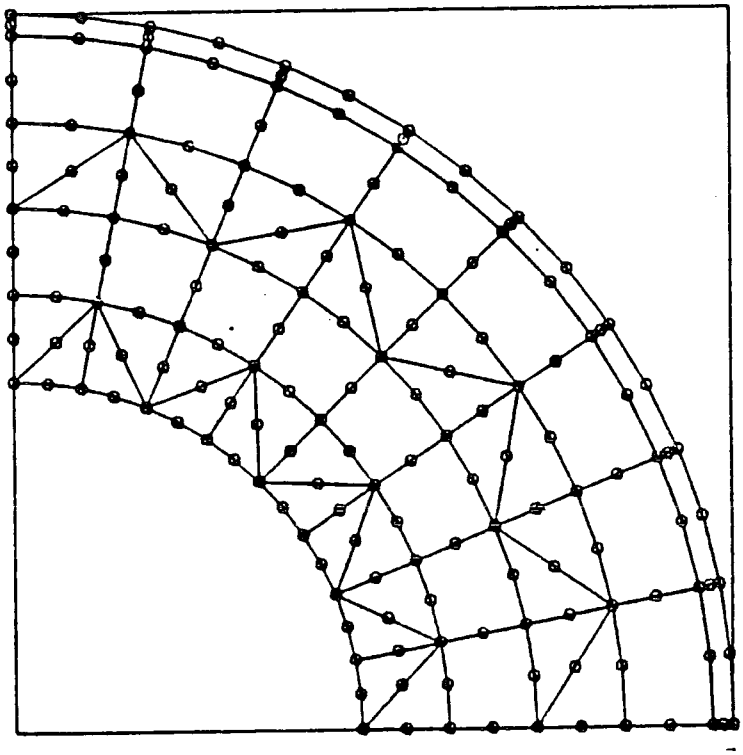

Figure 4.22: The geometry of the isoparametric element mesh used in the visco-elastic cylinder test.

2. The base of the model is constrained to move horizontally.

A uniform pressure of 1.0×10^3 psi was applied to the hollow interior of the model at time t=0 and the elastic solution was obtained. Subsequent solutions were obtained at some time following the application of the pressure so that the history of the stress distribution could be investigated.

The stress history predicted by the isoparametric model (figure 4.23) agrees well with the analytic solution and shows the approach of the radial and tangential stresses to a hydrostatic state with time.

In the CST solution (figure 4.24) the radial stresses are in close agreement with the analytic results. The tangential stresses, however, are regularly scattered about the analytic solution. The scatter is greatest in the elastic solution. It decreases to a negligible amount as the stresses become hydrostatic. The scatter in the magnitude of the stress vectors is related to the topology of the finite element mesh. Elements of topology a in figure 4.21 consistently predict stresses which are more compressive than those of the analytic solution, whilst elements of topology b predict stresses which are more tensional than the analytic solution. The reason for this is that the nodes at a given radius do not have the same radial component of displacement (e.g. at a radius of two inches, with t=0, the radial displacement at nodes i in figure 4.21 is 0.01386 inches whilst it is 0.01349 at nodes j) because some nodes are stiffer than others. The oscillation in the tangential stresses therefore occurs because the CST element mesh is unable to accurately model the high stress gradient close the inner boundary of the cylinder. Improved results to this problem could therefore only be obtained by increasing the

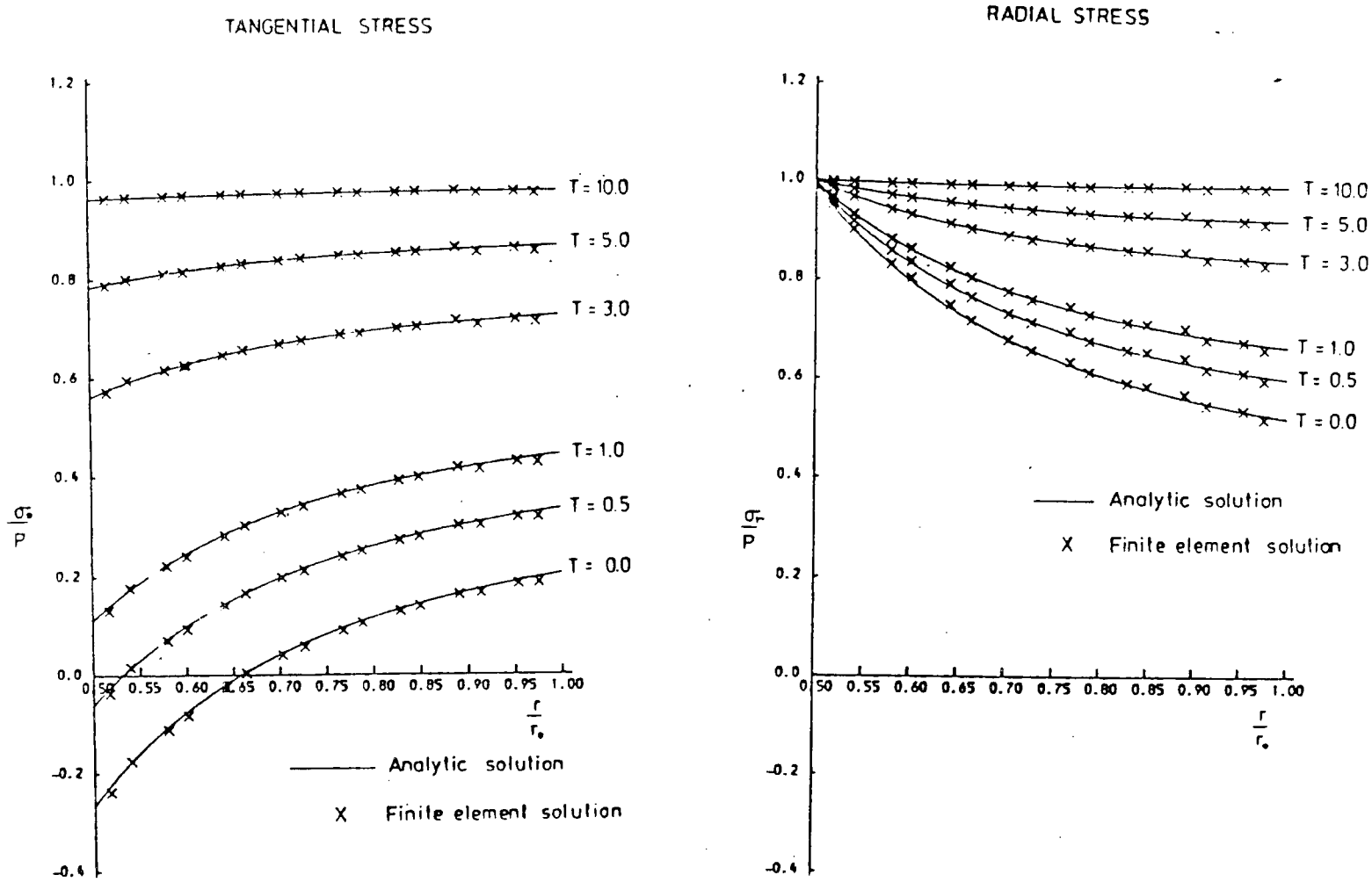

Figure 4.23: Comparison of the radial and tangential stresses predicted by the isoparametric model with the analytic solution.

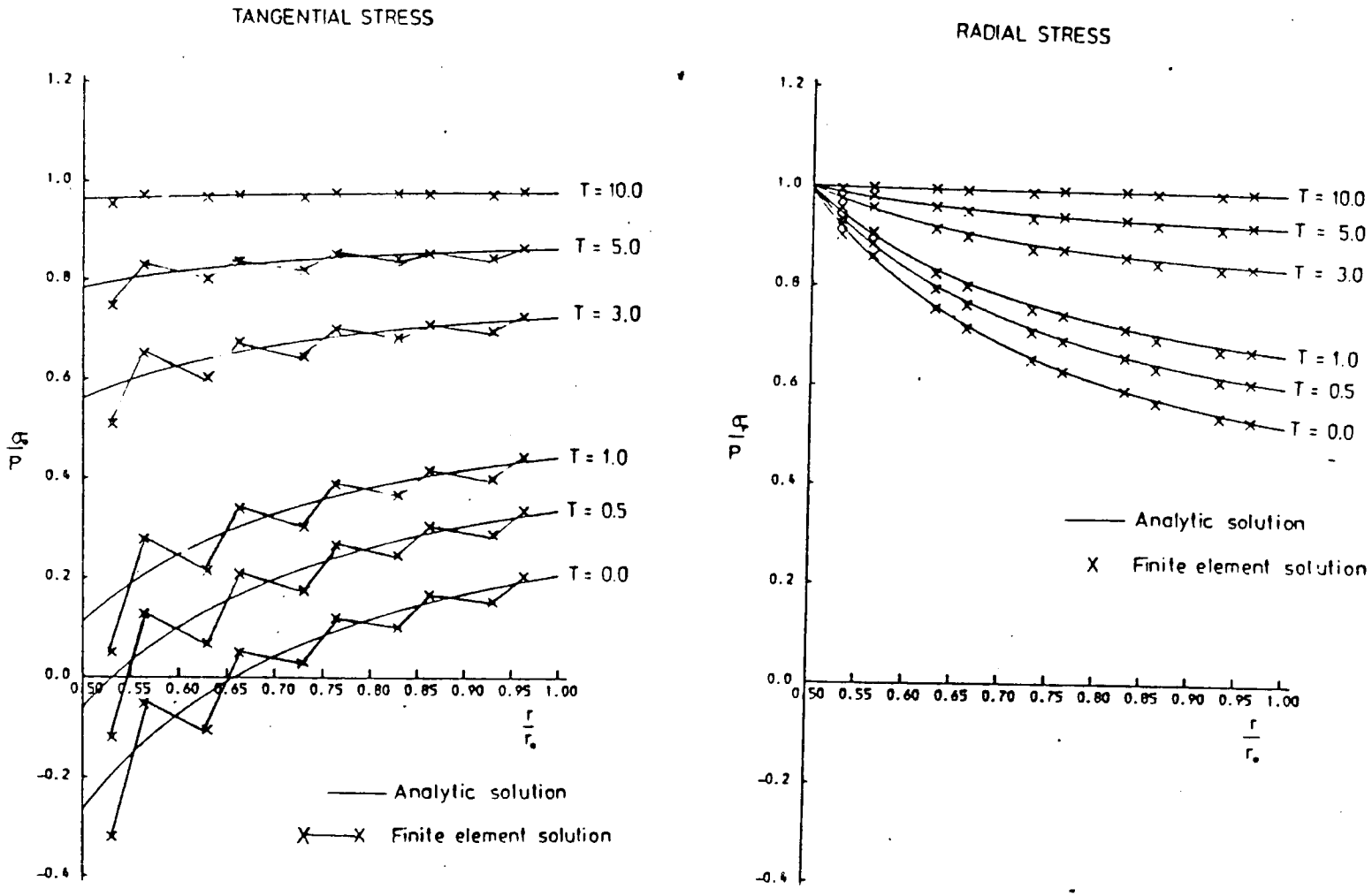

Figure 4.24: Comparison of the radial and tangential stresses predicted by the CST model with the analytic solution.

complexity of the finite element mesh.

Zienkiewicz et al (1968) pioneered the algorithm which has been used to model visco-elastic problems in this thesis. They tested this algorithm using an identical CST mesh to the one which has been used in this section. Their tangential stress vectors, however, agree with the analytic solution and do not exhibit any oscillation in magnitude. Detailed comparison of their results with those in figure 4.24, however, shows that the correct solution was obtained only because they averaged the stress in adjacent elements (a and b in figure 4.21). Their model therefore obscures the true oscillation in the stress vectors because the stiffness irregularities of the CST mesh have been averaged out.

A similar averaging procedure has been adopted by previous researchers who have modelled this test case (Kusznir, 1976; Woodward, 1976; Mithen, 1980; Park, 1981). This procedure, however, has not been adopted in their subsequent models, which explains why some of their visco-elastic solutions have oscillating stress vectors even after several million years relaxation (e.g figure 4.13 of Park, 1981; figure 4.4 of Mithen, 1980).

It is therefore desirable to adopt the isoparametric finite element method to model visco-elastic stress regimes because this method does not exhibit oscillation of the stress vectors.

4.6 Summary And Conclusions

The major requirement of the finite element method which is adopted to model lithospheric stress regimes is that it should be sufficiently versatile to give accurate and predictive solutions to a variety of elastic and visco-elastic problems.

It has been shown in this chapter that the CST element exhibits two undesirable features which restrict its accuracy and predictiveness;

1. It behaves too stiffly if the mesh is not optimally designed.

2. It has a tendancy to give skewed or oscillating stress vectors in regions where the strain gradient is high.

The isoparametric finite element, however, performs accurately in elastic and visco-elastic tests using relatively simple meshes.

It is therefore concluded that it is desirable to use the isoparametric finite element method to model lithospheric stress regimes.

CHAPTER 5

THE ISOPARAMETRIC FINITE ELEMENT FAULT MODEL

5.1 Introduction

A fault is a plane of discontinuity along which relative displacements have occurred. A fault originates as a fracture plane which develops when the lithospheric stress regime exceeds the elastic strength of the rocks. Slip subsequently occurs along the fracture plane. This causes relative displacements in the previously continuous rock mass and a redistribution of stress.

Following this period of instantaneous deformation the fault either continues to move as a result of creep or it becomes locked for a period of time, during which stresses are transmitted across the fault plane, until the stress becomes large enough to initiate another period of instantaneous slip.

Consequently, when faulting occurs along a major fault plane it modifies the stress regime which existed prior to fracture. To build realistic models of the lithospheric stress regime, it is therefore necessary to have a method for modelling the deformation associated with faults.

In this chapter a method to model the first order effects of faulting, which have been described above, is developed using the isoparametric finite element method. This technique is a modification of the dual node method which was developed by Mithen (1980) to model frictional sliding in constant strain finite elements. The advantage of a fault model based upon

the isoparametric finite element method is that it allows the frictional sliding on curved faults to be modelled.

The first section of this chapter reviews previous methods which have been proposed to model faults using finite elements, following which a method to obtain the stiffness and model the frictional sliding along the fault plane is described.

5.2 Review Of Finite Element Fault Models

Service and Douglas (1973) have suggested that a fault may be modelled in finite element computations by introducing elements with weak elastic properties. Mithen (1980) has pointed out that this approach suffers from two disadvantages. Firstly, the amount by which the elastic parameters should be reduced by is not known. Secondly, it can not be justified that a fault actually behaves in this way. Consequently, this technique will not be used in this thesis.

A simple and effective method for introducing faults into finite element calculations has been described by Melosh and Raefsky (1981). This technique is known as the split node technique and requires that the relative displacements of the nodes lying on the fault plane are known. These displacements are then introduced as prescribed relative displacements by modifying the force vector. Consequently, solution of the stiffness equation allows the stresses due to the prescribed displacements to be evaluated.

The split node technique has the adavantage that a fault can be introduced at any node of the body without having to make any alterations to the finite element mesh or to the stiffness matrix. The disadvantage of the method is that it can not be used to model the deformation on deep

faults where the displacements are generally unknown. Consequently, this method will not be used in this thesis.

An alternative approach to model the deformation associated with faulting has been proposed by Mithen (1980), and is known as the dual node method. This technique is an adaptation of the method developed by Goodman et al (1968) to model rock joints. The dual node method assumes that the location of the fault plane is known, so that initially two separate bodies can be considered to exist to the right and left hand sides of the fault plane. The finite element mesh is then discretised for these two bodies during which it is ensured that the nodes which fall on the fault plane are dual nodes, that is, they are formed by two nodes which are present at the same spatial locations, but which belong to the elements on opposite sides of the fault plane (figure 5.1). The stiffness of the bodies on either side of the fault are then calculated and incorporated into the global stiffness matrix in the normal way. The stiffness matrix therefore contains the elastic properties of the two separate bodies and it is consequently necessary to link them by defining the elastic properties of the fault. Solution of the stiffness equation therefore yields the displacements of the fault and the surrounding material under a particular set of boundary conditions. From these displacements the shear stress on the fault plane can be calculated and, if it is greater than the frictional strength of the fault, slip is allowed to occur on the fault plane until equilibrium is achieved.

The dual node method is compatible with the approach which is to be adopted in this thesis because it allows the displacement of the fault and the resulting stresses to be computed for various types of boundary conditions. Consequently, the dual node method will be modified in this

chapter to make it compatible with the isoparametric approach.

5.3 Local Co-ordinate System For A Fault Element

It is convenient when dealing with an isoparametric fault element to perform the necessary mathematical operations in a local co-ordinate system. This will be defined in this section.

Consider the line element formed by the three dual nodes which lie on a section of the fault plane formed by nodes 1, 2 and 3 of an element on the left hand side of the fault and nodes 4, 5 and 6 of an element on the right hand side of the fault (Figure 5.1). The local co-ordinate system is then defined such that its origin is at the mid point dual node, its s-axis lies along the fault and its n-axis lies normal to it (Figure 5.2).

We define the shape functions for the nodes in this local co-ordinate system as

$$\begin{aligned} \bar{N}_1 &= \bar{N}_4 = \frac{s}{\ell}\left(\frac{2s}{\ell} + 1\right) \\ \bar{N}_2 &= \bar{N}_5 = 1 - \frac{4s^2}{\ell^2} \\ \bar{N}_3 &= \bar{N}_6 = \frac{s}{\ell}\left(\frac{2s}{\ell} + 1\right) \end{aligned} \qquad 5.1$$

where ℓ is the length of the fault section.

The x co-ordinate of a general point on the line element can therefore be defined by an interpolation of its nodal values, i.e. as

$$x = \sum_{i=1}^{3} \bar{N}_i x_i = \sum_{i=4}^{6} \bar{N}_i x_i$$

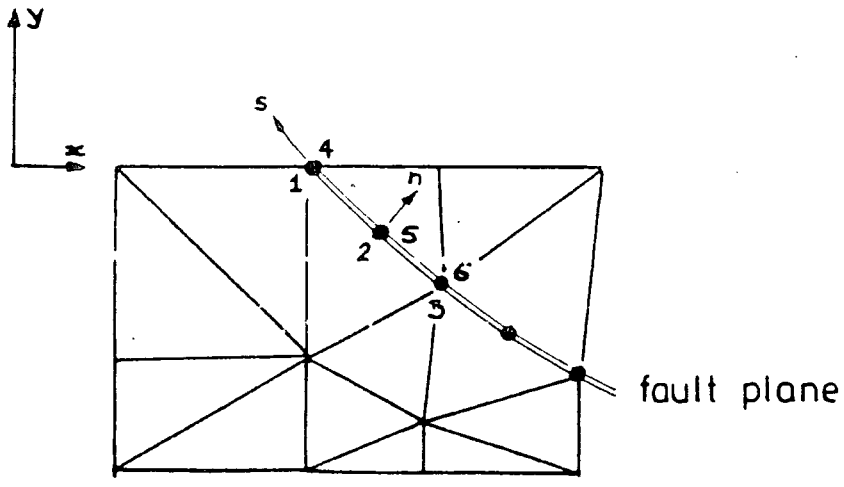

Figure 5.1: The geometry of the isoparametric fault model.

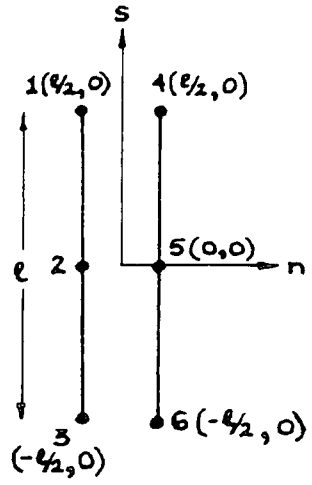

Figure 5.2: The local (s,n) co-ordinate system of an isoparametric fault element.

Similar relations hold for the y co-ordinate and the components of displacement. The numerical integration scheme for this system is given in equation 3.56 and the location of the integration points are given in table 3.3.

5.4 Stiffness Of An Isoparametric Fault Element

We now proceed to evaluate the stiffness of the fault using the concept of a linkage element (Ngo and Scordelis, 1967). It is necessary to use this approach as the method developed in chapter 3 is inapplicable because the fault has zero area.

Using the variational approach of chapter 3 we may write the stored energy W of a fault element of unit thickness as

$$W = \frac{1}{2} \int_{-\ell/2}^{\ell/2} \{w\}^T \{p\} \, ds \qquad 5.2$$

where, following Mithen (1980), $\{p\}$ is the force per unit length vector which is defined as

$$\{p\} = \begin{Bmatrix} p_s \\ p_n \end{Bmatrix} = \frac{1}{\ell} [K] \{w\} \qquad 5.3$$

where

$$[K] = \begin{bmatrix} k_s & 0 \\ 0 & k_n \end{bmatrix}$$

in which k_n and k_s are the normal and shear stiffnesses of the fault element.

The relative displacement vector, $\{w\}$, in equations 5.2 and 5.3 is defined at a general point as

$$\{w\} = \begin{Bmatrix} w_s \\ w_n \end{Bmatrix} = \begin{bmatrix} u_s(\text{RHS}) & - u_s(\text{LHS}) \\ u_n(\text{RHS}) & - u_n(\text{LHS}) \end{bmatrix} \qquad 5.4$$

where u_n and u_s are the local displacements in the normal and shear directions. We can rewrite equation 5.4 to express the relative displacement of a general point through an interpolation of the nodal values of the local displacement. This gives

$$\{w\} = [L]\{d'\} \qquad 5.5$$

where the local nodal displacement vector, $\{d'\}$ is defined as

$$\{d'\}^T = \{ u_{s_1}\ u_{n_1}\ u_{s_2}\ u_{n_2}\ u_{s_3}\ u_{n_3}\ u_{s_4}\ u_{n_4}\ u_{s_5}\ u_{n_5}\ u_{s_6}\ u_{n_6} \}$$

and the shape function matrix, $[\bar{L}]$, is defined as

$$[\bar{L}] = \begin{bmatrix} -\bar{N}_1 & 0 & -\bar{N}_2 & 0 & -\bar{N}_3 & 0 & \bar{N}_4 & 0 & \bar{N}_5 & 0 & \bar{N}_6 & 0 \\ 0 & -\bar{N}_1 & 0 & -\bar{N}_2 & 0 & -\bar{N}_3 & 0 & \bar{N}_4 & 0 & \bar{N}_5 & 0 & \bar{N}_6 \end{bmatrix} \qquad 5.6$$

in which the nodal shape functions have been defined in equation 5.1.

Substituting equations 5.3 and 5.5 into equation 5.2, and using the fact that the local displacements are nodal quantities and are therefore constants of the integration, we may write,

$$W = \frac{1}{2} \{d'\}^T \int_{-\ell/2}^{\ell/2} [K'_F]\, ds \; \{d'\} \qquad 5.7$$

where the local fault stiffness matrix, $[K'_F]$, is defined by

$$[K'_F] = \frac{1}{\ell} [L]\,[K]\,[L]$$

which can be evaluated and expressed as a partitioned matrix

$$[K'_F] = \left[\begin{array}{c|c} [A] & -[A] \\ \hline -[A] & [A] \end{array}\right]$$

where

$$[A] = \begin{bmatrix} \bar{N}_1^2 k_s & 0 & \bar{N}_1 \bar{N}_2 k_s & 0 & \bar{N}_1 \bar{N}_3 k_s & 0 \\ 0 & \bar{N}_1^2 k_n & 0 & \bar{N}_1 \bar{N}_2 k_n & 0 & \bar{N}_1 \bar{N}_3 k_n \\ \bar{N}_1 \bar{N}_2 k_s & 0 & \bar{N}_2^2 k_s & 0 & \bar{N}_2 \bar{N}_3 k_s & 0 \\ 0 & \bar{N}_1 \bar{N}_2 k_n & 0 & \bar{N}_2^2 k_n & 0 & \bar{N}_2 \bar{N}_3 k_n \\ \bar{N}_1 \bar{N}_3 k_s & 0 & \bar{N}_2 \bar{N}_3 k_s & 0 & \bar{N}_3^2 k_s & 0 \\ 0 & \bar{N}_1 \bar{N}_3 k_n & 0 & \bar{N}_2 \bar{N}_3 k_n & 0 & \bar{N}_3^2 k_n \end{bmatrix}$$

To obtain the global fault stiffness matrix it is necessary to express equation 5.7 in terms of the global displacements, {d}, and we now seek relationships between these and the local displacements {d'}.

Using figure 5.3 we may write the global displacement at a general point in terms of the local displacements as

$$\begin{Bmatrix} u \\ v \end{Bmatrix} = \begin{bmatrix} \cos\alpha & -\sin\alpha \\ \sin\alpha & \cos\alpha \end{bmatrix} \begin{Bmatrix} u_s \\ u_n \end{Bmatrix} \qquad 5.8$$

but since

$$dx = \cos\alpha \; ds$$

$$dy = \sin\alpha \; ds$$

we may invert equation 5.8 and rewrite it as

$$\begin{Bmatrix} u_s \\ u_n \end{Bmatrix} = [R'_F] \begin{Bmatrix} u \\ v \end{Bmatrix}$$

where

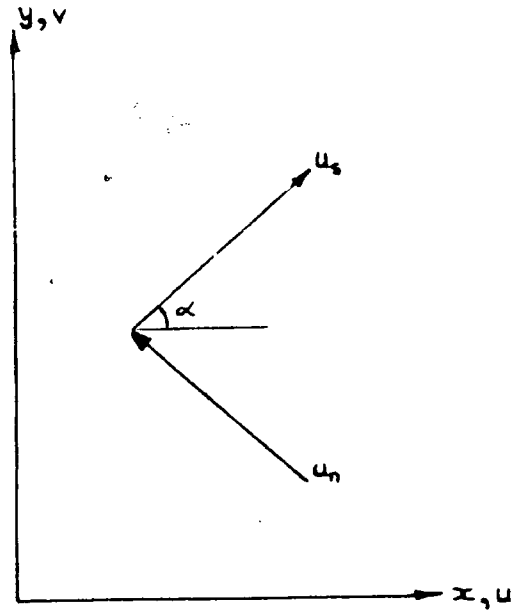

Figure 5.3: The local components of displacement at a point on the edge of an isoparametric fault element.

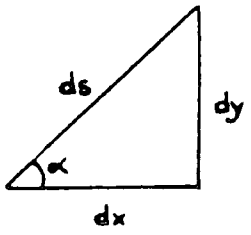

Figure 5.4: An infinitessimal segment of the fault element.

$$[R'_F] = \begin{bmatrix} \frac{dx}{ds} & \frac{dy}{ds} \\ -\frac{dy}{ds} & \frac{dx}{ds} \end{bmatrix}$$

The global nodal displacement can therefore be obtained by evaluating equation 5.8 at the nodes, giving

$$\{d'\} = [R]\{d\} \qquad 5.9$$

where [R] is defined

$$[R] = \begin{bmatrix} [R'_F] & 0 & 0 & 0 & 0 & 0 \\ 0 & [R'_F] & 0 & 0 & 0 & 0 \\ 0 & 0 & [R'_F] & 0 & 0 & 0 \\ 0 & 0 & 0 & [R'_F] & 0 & 0 \\ 0 & 0 & 0 & 0 & [R'_F] & 0 \\ 0 & 0 & 0 & 0 & 0 & [R'_F] \end{bmatrix}$$

Substituting equation 5.9 into 5.7 we may write,

$$W = \frac{1}{2}\{d\}^T [K_F]\{d\}$$

where the global fault stiffness matrix, $[K_F]$, is defined

$$[K_F] = \int_{-\ell/2}^{\ell/2} [R][K'_F][R]^T \, ds$$

which must be evaluated by numerical integration.

Minimising the energy of the system with respect to the nodal displacements we obtain

$$\frac{\partial W}{\partial \{d\}} = [K_F]\{d\}$$

which can be added into the global stiffness equation to give

$$[K + K_F]\{d\} = \{F\} \qquad 5.10$$

Consequently, the elastic properties of the fault can be introduced into the computations by adding the fault stiffness to the global stiffness matrix.

5.5 Modelling Of Frictional Sliding

Solution of the stiffness equation (equation 5.10) yields the elastic displacements of the model and includes the displacements which occur as a result of the elastic properties of the fault. This solution, however, does not include any displacements which are induced in the body as a result of frictional sliding on the fault plane. The contribution of frictional sliding to fault deformation is likely to be larger than that which is due to the elastic properties of the fault, and therefore, it is necessary to have a technique for modelling this process.

Mithen (1980) proposed a method for modelling frictional sliding in constant strain finite elements and his approach is modified in the following sections so that it may be used with the isoparametric elements of this thesis.

5.5.1 Calculation of the stress on the fault plane

To model frictional sliding it is necessary to be able to calculate the stress on the fault plane. This cannot be found directly in the finite element method because the stress between adjacent elements is discontinuous, and therefore, the stress on the fault plane, which is formed by the boundary of two elements, is also discontinuous. The simplest way of calculating the stress at an element boundary is to average

the stress in adjacent elements. This approach was used by Mithen (1980) who represented the stress on the fault plane by averaging the stress in the two constant strain elements which lie on opposite sides of the fault.

In the isoparametric method the quadratic displacement function results in a linear variation of strain within each element, and therefore, the stress can be calculated at any position within the element. The most obvious way to represent the stress on the fault plane in an isoparametric element is therefore as a linear function which is calculated by obtaining the stress at each node on either side of the fault and then averaging the stress at each dual node. This method, however, proved unsatisfactory in practise because the stress is poorly defined at the edges of any linear strain element (Zienkiewicz, 1979; Barlow, 1976). An alternative technique must therefore be developed for evaluating the stress on the fault plane.

The stress in an isoparametric finite element is most accurately defined at its centroid, because it represents the average stress in a linear strain element. The method which has been used to represent the stress on the fault plane is therefore to average the stress at the centroid of the elements on the left and right hand sides of the fault. This stress must be assumed to be constant along this section of the fault plane.

We therefore write the stress at the centroid of the element on the left hand side of the fault, $\underline{\sigma}_c(\mathrm{LHS})$, as

$$\underline{\sigma}_c(\mathrm{LHS}) = \begin{Bmatrix} \sigma_x(\mathrm{LHS}) \\ \sigma_y(\mathrm{LHS}) \\ \tau_{xy}(\mathrm{LHS}) \end{Bmatrix} = [C]\,[B]\,\{d(\mathrm{LHS})\}$$

(which is evaluated at s=1/3, t=1/3). A similar expression can be written

for the stress at the centroid of the element on the right hand side of the fault plane, σ_c(RHS). We may therefore write the stress on the fault plane, $\{\sigma_F\}$, as the average of these components

$$\{\sigma_F\} = \begin{Bmatrix} \sigma_x \\ \sigma_y \\ \tau_{xy} \end{Bmatrix} = \frac{1}{2} \begin{Bmatrix} \sigma_x(\text{LHS}) + \sigma_x(\text{RHS}) \\ \sigma_y(\text{LHS}) - \sigma_y(\text{RHS}) \\ \tau_{xy}(\text{LHS}) + \tau_{xy}(\text{RHS}) \end{Bmatrix}$$

We can now find expressions for the normal stress, σ, and shear stress, τ, on the fault plane

$$\begin{aligned} \sigma &= \sigma_x \cos^2\theta + \sigma_y \sin^2\theta + 2\tau_{xy}\cos\theta \sin\theta \\ \tau &= (\sigma_y - \sigma_x)\sin\theta\cos\theta + \tau_{xy}(\cos^2\theta - \sin^2\theta) \end{aligned} \qquad 5.11$$

where θ is the hade of the fault and is defined

$$\theta = \arctan\left(-\frac{dx}{dy}\right)$$

where

$$\frac{dx}{dy} = \frac{\dfrac{dx}{ds}}{\dfrac{dy}{ds}} = \frac{d\sum_{i=1}^{3} \bar{N}_i x_i}{d\sum_{i=1}^{3} \bar{N}_i y_i}$$

which is evaluated at the midpoint dual node on the fault segment as this represents the average hade of the fault element.

If body forces have not been included in the model it is necessary to modify the normal stress component, and for a lithostatic stress distribution this may be written

$$\sigma = \sigma + \rho g\, y_m$$

where ρ is the density, g is the acceleration due to gravity and y_m is the

y co-ordinate of the midpoint node of the fault element which can be found by evaluating the following expression at s=0

$$y_m = \bar{N}_1 y_1 + \bar{N}_2 y_2 + \bar{N}_3 y_3$$

If the fault is assumed to be percolated by water it is necessary to subtract the pore pressure from the normal component of stress which is defined above.

5.5.2 Slip conditions

To determine whether frictional sliding will occur on the fault plane we must define the frictional strength of the fault, τ_F. The simplest expression for this (Mithen, 1980) is

$$\tau_F = \mu\sigma$$

where μ is the coefficient of friction and σ is the normal stress defined by equation 5.11 or 5.12.

Frictional sliding will therefore occur when the shear stress on the fault plane exceeds the frictional strength, i.e. if

$$\tau > \tau_F \qquad 5.12$$

No frictional sliding will occur, however, if the shear stress on the fault plane is less than the frictional strength, i.e. if

$$\tau \leq \tau_F \qquad 5.13$$

5.5.3 Calculation of the excess shear stress and fault force vector

If slip is predicted by equation 5.12 then we must have a method for calculating the amount of slip which must occur until equilibrium (equation 5.13) is attained. One method to estimate this is to evaluate the excess shear stress, τ_{xs}, on the fault (Mithen, 1980), which is defined

$$\tau_{xs} = \tau - \tau_F$$

For the isoparametric formulation it is assumed that the excess shear stress is constant along the fault plane, which allows an expression for the equivalent nodal forces that result from the excess shear stress. Therefore, for the model developed here, we define these forces, using equation 3.61, as

$$\{f_q\} = -\tau_{xs} \int_{-q/2}^{q/2} [\bar{L}]^T \begin{Bmatrix} \frac{dx}{ds} \\ \frac{dy}{ds} \end{Bmatrix} ds \qquad 5.14$$

where $[\bar{L}]$ is the shape function matrix, defined in equation 5.6 and $\{f_q\}$ is the fault force matrix which is defined

$$\{f_q\}^T = \{ f_{x_1} \; f_{y_1} \; f_{x_2} \; f_{y_2} \; f_{x_3} \; f_{y_3} \; f_{x_4} \; f_{y_4} \; f_{x_5} \; f_{y_5} \; f_{x_6} \; f_{y_6} \}$$

These forces must be evaluated by numerical integration.

5.5.4 Iteration to remove the excess shear stress

The fault force vector, equation 5.14, must be added into the global force vector $\{F\}$. The stiffness equation can then be resolved to obtain the displacements and the stresses in the model following frictional sliding. From these a new estimate of the excess shear stress, and thus the forces which are required to attain equilibrium, can be obtained. This procedure is repeated until the shear stress on the fault becomes less than the frictional strength.

CHAPTER 6

FRICTIONAL SLIDING ON PLANE AND LISTRIC FAULTS

In this chapter the isoparametric fault model (chapter 5) is used to analyse the deformation which results from frictional sliding on plane and listric faults.

There are three aims to this chapter. The first is to examine the characteristics of the model by examining its response to frictional sliding on plane normal faults. The second aim is to extend this analysis to predict the deformation which occurs on listric normal faults. The final aim is to examine the deformation which occurs on thrust faults.

6.1 Frictional Sliding On A Plane Sided Normal Fault

The deformation following frictional sliding on a plane-sided normal fault has been previously modelled by Mithen (1980) using constant strain finite elements. The aim of this section is to compare and contrast the deformation of Mithen's models with those obtained using the isoparametric formulation.

6.1.1 Description of the finite element mesh

The finite element mesh (figure 6.1) represents a 1000 km long section through the upper 20 km of the elastic lithosphere. The fault, which is located at the centre of the mesh, dips at 63.43 degrees.

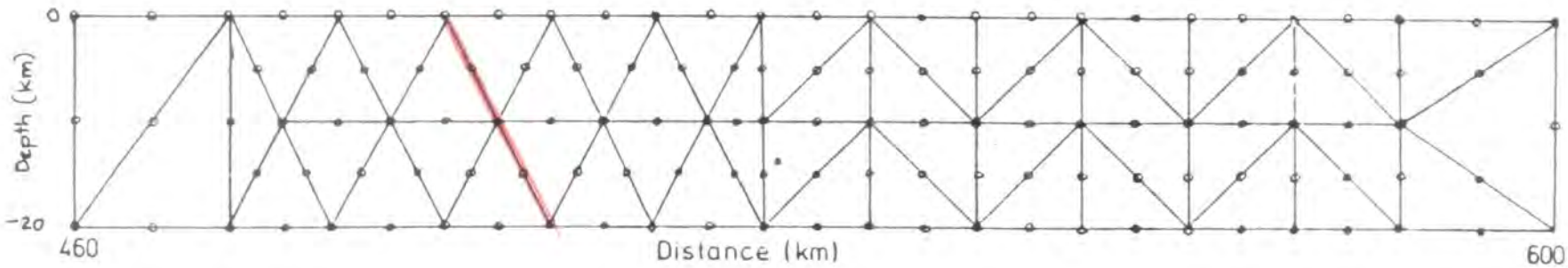

Figure 6.1: Central section of the 1000 km long plane normal fault finite element mesh. Location of the fault plane shown in red.

The mesh is formed from 100 triangular isoparametric elements, each having six Gaussian integration points. The elastic properties are summarised in table 6.1. The following boundary conditions were applied:

1. The right hand edge was constrained to move vertically.

2. The left hand edge was free, so that various tensile stresses could be applied.

3. The base was assumed to be underlain by a fluid with a density of 2900 kg m^{-3}.

This finite element mesh has identical dimensions and physical parameters to that used by Mithen (1980).

PARAMETER	VALUE
Young's modulus	0.85×10^{11} N m^{-2}
Poisson's ratio	0.25
Density	2750.0 kg m^{-3}

Table 6.1: Values assigned to elastic parameters of the finite element model.

6.1.2 Response of the finite element model to flexure

The models of Mithen (1980) predict that the deformation produced by frictional sliding on a plane-sided fault is dominated by lithospheric flexure. It is consequently desirable to compare the response of the finite element model (section 6.1.1) with the analytic solution for the flexure of a thin elastic beam underlain by a fluid substratum. The analytic solution to this problem is well known (e.g. Mithen, 1980).

So that the analytic and finite element solutions could be compared the following additional boundary conditions were initially applied to the model:

1. The left and right hand edges of the model were constrained to move vertically.

2. The normal and shear stiffness of the fault were set to a high value of 1.0×10^{15} N m^{-1} so that the model approximates a continuum.

3. A vertical force of 2.0×10^{12} MPa was applied to the central node (P in figure 6.1) of the finite element mesh.

The vertical displacement profiles for the two solutions are compared in figure 6.2. The displacements are almost identical. This shows that the finite element mesh is correctly designed and is suitable for predicting the deformation associated with lithospheric flexure. It also shows that the value of 1.0×10^{15} N m^{-1} assigned to the normal and shear stiffness of the fault has the desired effect of making the model behave as an elastic continuum.

This test was applied to all of the finite element meshes of this chapter to check that no errors had been introduced in the computational description of the model and to verify that the model was sufficiently well defined to give accurate solutions to flexural problems.

6.1.3 Initial elastic deformation of the model

It was assumed in the development of the fault model (Chapter 5) that deformation would proceed in two phases. Firstly, by an initial elastic displacement arising from the contrasting elastic properties of the fault

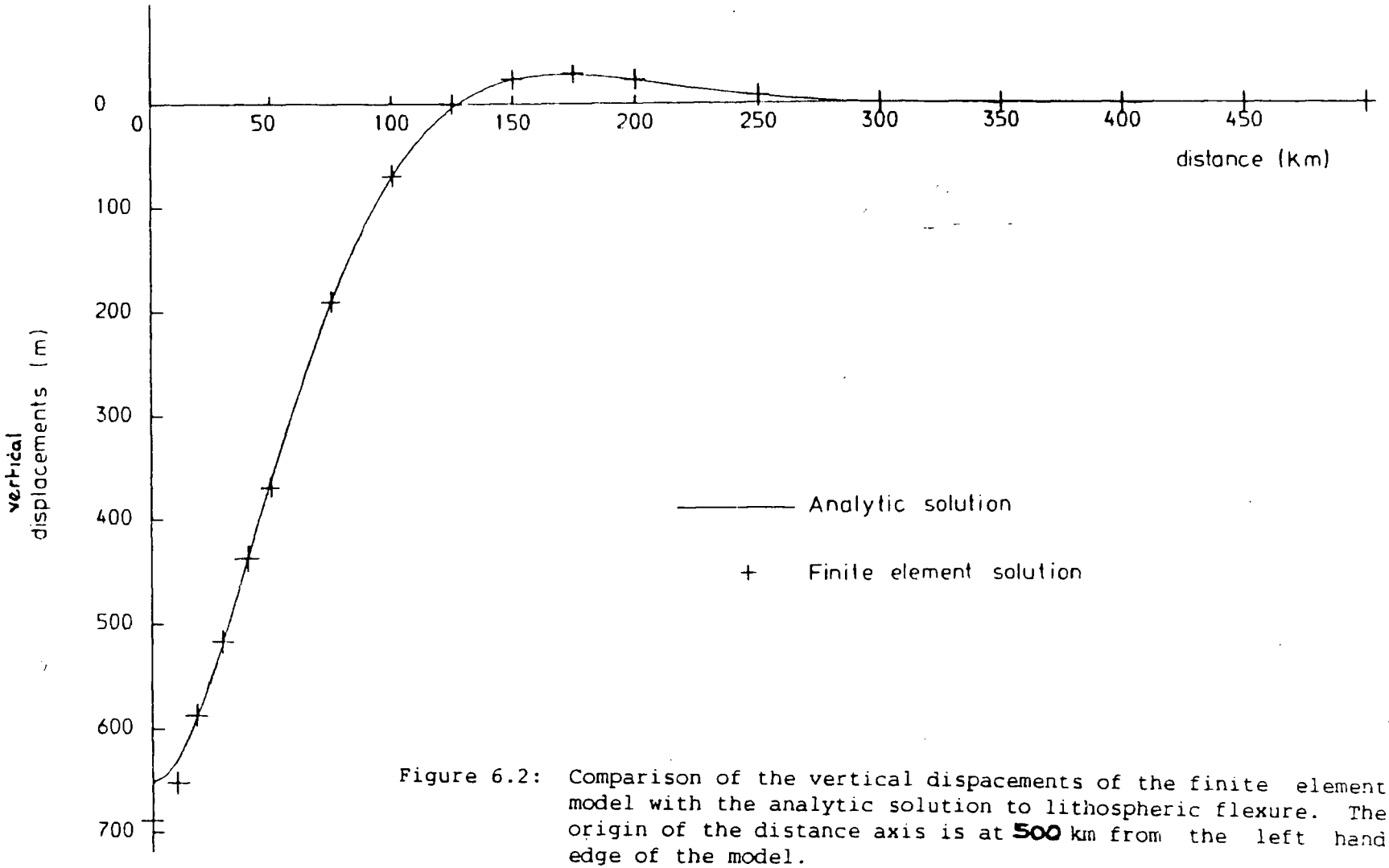

Figure 6.2: Comparison of the vertical dispacements of the finite element model with the analytic solution to lithospheric flexure. The origin of the distance axis is at 500 km from the left hand edge of the model.

and the surrounding lithosphere, and secondly, by frictional sliding in order to reduce any excess shear stress on the fault. This section illustrates the primary stage of fault deformation, the initial elastic response, and contrasts the solutions with those of Mithen (1980).

Before it is possible to model any fault deformation, however, it is necessary to assign values to the normal and shear stiffnesses of the fault. These parameters cannot be measured at depth in the earth and consequently the values assigned to them must be chosen to conform with observed fault behaviour.

The walls of the fault would be expected to be closed at depth because of the lithostatic pressure. The value chosen for the normal stiffness should therefore simulate this behaviour. The value of 1.0×10^{15} N m^{-1} assigned to the stiffness of the fault in the previous section had the effect of closing the sides of the fault and making the model behave as an elastic continuum. The normal stiffness of the fault was therefore assigned a value of 1.0×10^{15} N m^{-1}.

Because the fault would be expected to be initially locked by asperities, Mithen (1980) proposed that the value of the shear stiffness of the fault should be approximately the same as the stiffness of the surrounding lithosphere. He therefore modelled deformation on the fault using a shear stiffness of 5.0×10^{10} N m^{-1}. In order to compare the isoparametric model with the CST model, the same value has been used in this section. The effect of changing the shear stiffness is considered later.

Figure 6.3 shows the vertical displacement and stress in the central section of the model when a 50 MPa tensional stress is applied to its left

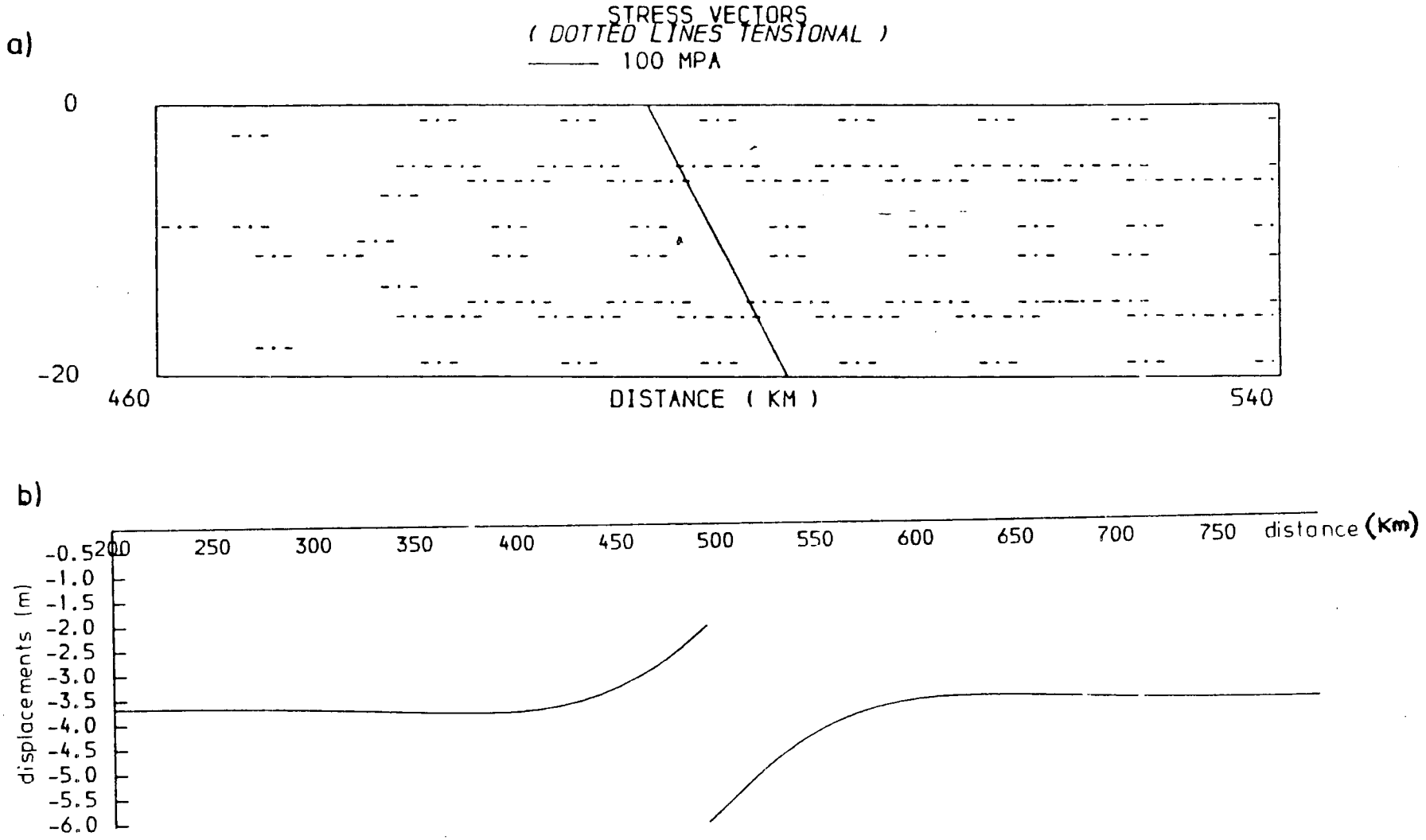

Figure 6.3: The initial elastic deformation of the plane normal fault model, with a shear stiffness of 5.0×10^{10} N m^{-1}, in response to a 50 MPa tensional stress.

a) Principal stresses around the fault.

b) Vertical displacements of the top surface.

hand edge. The deformation which the model undergoes can be summarised as follows:

1. The contrast between the elastic properties of the fault and the surrounding lithosphere causes relative displacements along the fault discontinuity.

2. The left and the right hand sides of the fault are upthrown and downthrown respectively. The fault is consequently a normal fault. This type of fault would be expected to develop in response to horizontal tensional stress (Anderson, 1951; Mithen, 1980).

3. The local displacements along the fault result in flexure of the adjacent lithosphere. The top of the lithosphere on the upthrown and downthrown sides is flexed upwards and downwards respectively.

4. The lithosphere at the edges of the model is unaffected by flexure and has subsided by 3.7 metres. This dilatation is controlled by the value of Poisson's ratio assigned to the model.

The effect of reducing the shear stiffness of the fault from 1.0×10^{11} N m^{-1} to 1.0×10^{10} N m^{-1} on the vertical displacements of the top surface of the model is shown in figure 6.4. These models demonstrate that reducing the shear stiffness increases the relative displacements at the fault and in the surrounding lithosphere. The value assigned to the shear stiffness of the fault therefore scales the deformation of the model. Because the aim of this chapter is only to illustrate the general effects of fault deformation it was considered appropriate to assign a value of 5.0×10^{10} N m^{-1} to the shear stiffness of the fault.

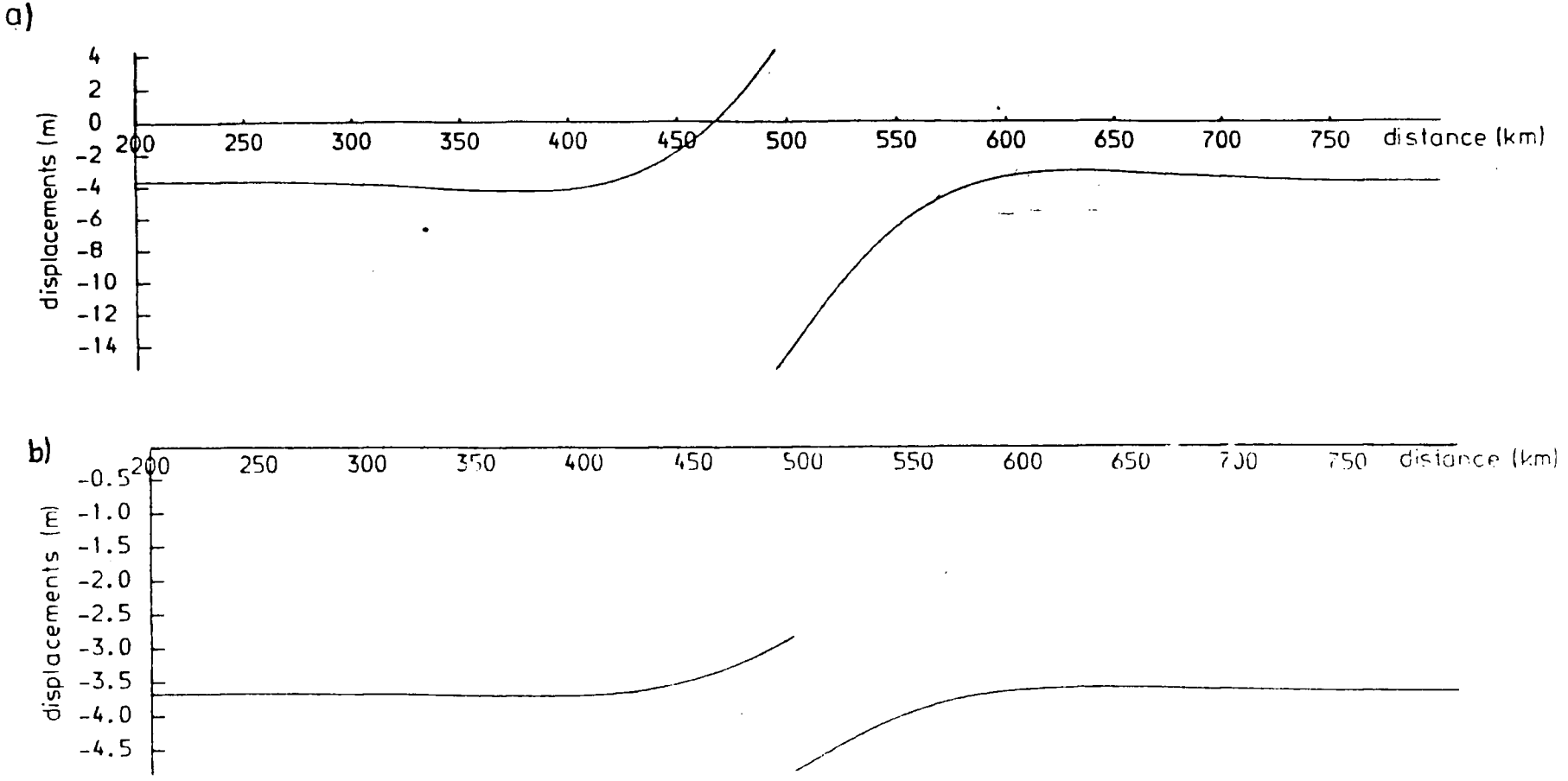

Figure 6.4: The effect of the shear stiffness of the fault on the displacements of the top surface of the model in response to a 50 MPa tensional stress.

a) Shear stiffness of 1.0×10^{10} N m^{-1}

b) Shear stiffness of 1.0×10^{11} N m^{-1}

The only difference between these solutions and those of Mithen (1980) is that larger relative vertical displacements occur in the isoparametric models. A possible explanation of this is that the CST element mesh is too stiff and therefore resists bending. A fuller discussion of this effect, however, is given in section 6.1.7.

6.1.4 Frictional sliding in response to a 50 MPa tension

The aim of this section is to describe the second phase of fault deformation; frictional sliding. The properties which have been assigned to the elastic parameters of the fault are summarised in table 6.2. The deformation following frictional sliding in response to a 50 MPa tensional stress is shown in figure 6.5. The following differences can be observed between this model and that of the initial elastic deformation of the fault:

1. The relative vertical displacement on the fault has increased by 600 metres.

2. The principal stresses above the fault have been modified by frictional sliding. There is now compression parallel to the fault plane on its downthrown side and tension on its upthrown side.

3. The amplitude of the flexure in the model adjacent to the fault has also increased.

4. The horizontal tensional stress adjacent to the fault is modified by the flexure. The horizontal tensional stresses at the top of the downthrown side has increased by 40 MPa, and decreased by the same amount at its base, because of the flexural uparching of this

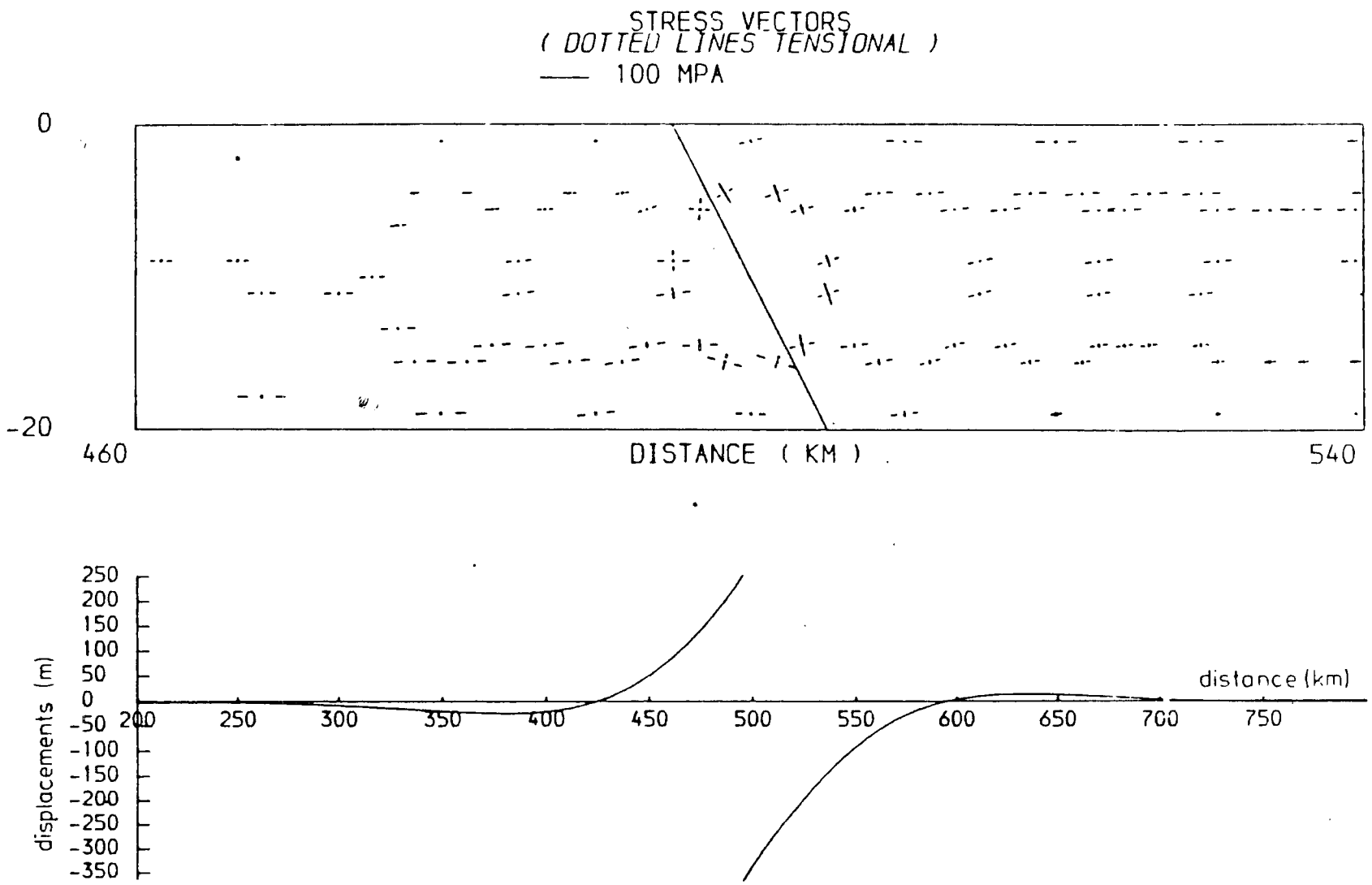

Figure 6.5: The deformation following frictional sliding in response to a 50 MPa tensional stress.

a) Principal stresses around the fault.

b) Vertical displacements of the top surface.

region. The opposite pattern is observed on the upthrown side of the fault.

PARAMETER	VALUE
Shear stiffness	5.0×10^{10} N m^{-1}
Normal stiffness	1.0×10^{15} N m^{-1}
Coefficient of friction	0.1

Table 6.2: Values assigned to the fault model.

6.1.5 Convergence factor

The model described in section 6.1.4 required 1023 iterations before the excess shear stress on the fault plane was redistributed and equilibrium attained. Because of the large amount of CPU time required to obtain this solution it is desirable to speed the convergence of the model.

Mithen (1980) found that multiplication of the fault force vector by a convergence factor speeded the solution. When a similar scheme was adopted the following effects were observed:

1. The optimum convergence factor depends on the value assigned to the shear stiffness of the fault.

2. The optimum convergence factor for a shear stiffness of 5.0×10^{10} N m^{-1} is 15. Using this value the number of iterations is reduced from 1023 to 76.

3. Convergence factors greater than this produced divergence and oscillation, whilst lower values increased the number of iterations required to attain equilibrium.

A convergence factor was consequently used in this thesis to speed up the solution. There are, however, a number of limitations with this approach. Firstly, the optimum convergence factor can only be found by trial and error. Secondly, considerable CPU time is still required to attain a solution. The simple technique which has been adopted is therefore not necessarily the optimum method and convergence might be further speeded using an advanced algorithm.

6.1.6 Frictional sliding in response to 40 and 30 MPa tension

The deformation following frictional sliding after reducing the tensional stress to 40 and 30 MPa is shown in figures 6.6 to 6.7. The following generalisations can be made from an analysis of these results:

1. Reducing the tensional stress from 50 to 30 MPa decreases the depth to which frictional sliding occurs from 20 km to 10 km. This is because the depth at which the excess shear stress on the fault exceeds the frictional strength is reduced when the tensional stress is lower.

2. Consequently, the relative vertical displacement on the fault decreases from 620 to 26 metres. This is because the magnitude of the excess shear stress on the fault is lower in the 30 MPa model and consequently less deformation has to occur in order to redistribute these stresses.

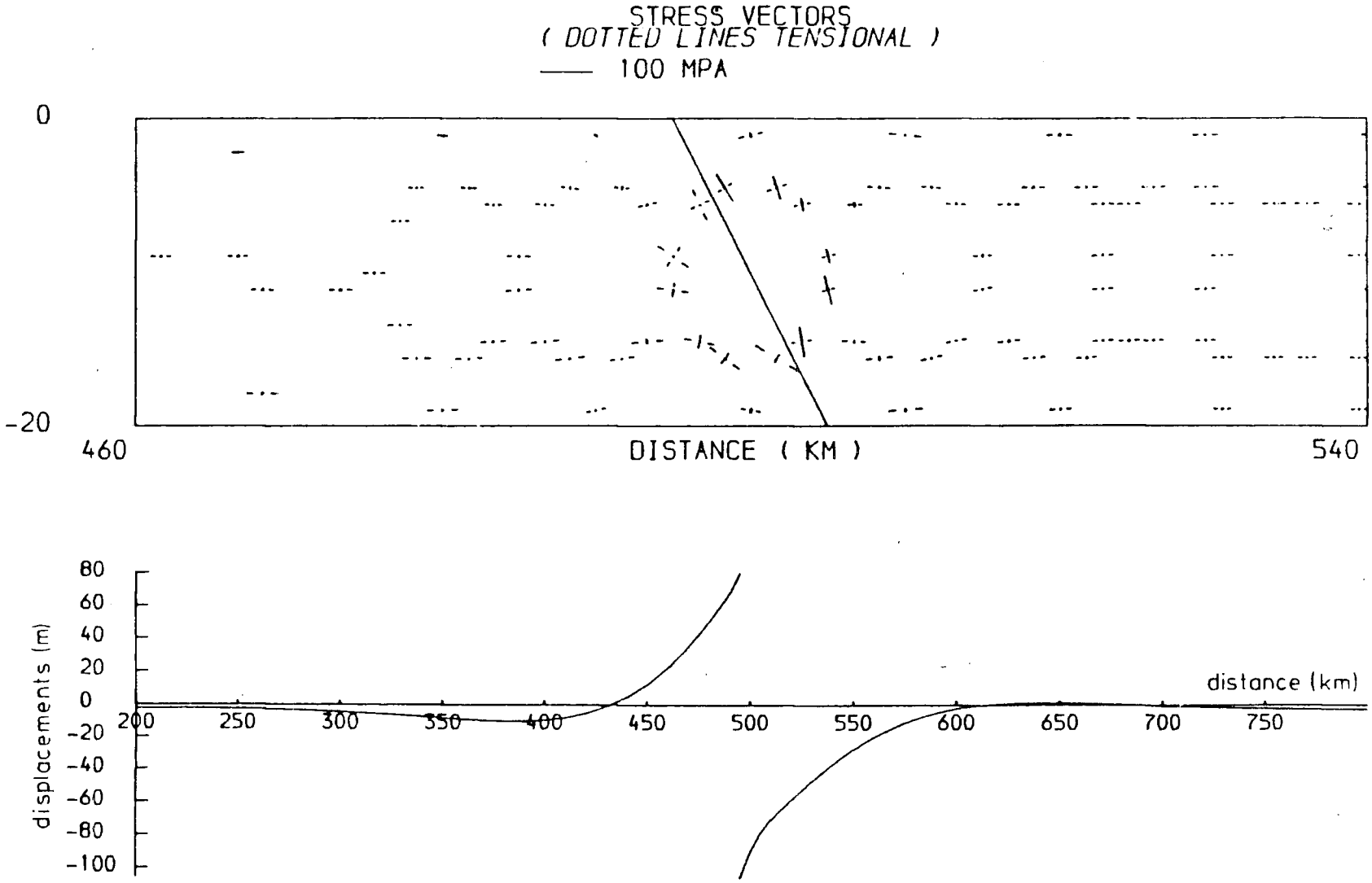

Figure 6.6: The deformation following frictional sliding in response to a 40 MPa tensional stress.

a) Principal stresses around the fault.

b) Vertical displacements of the top surface.

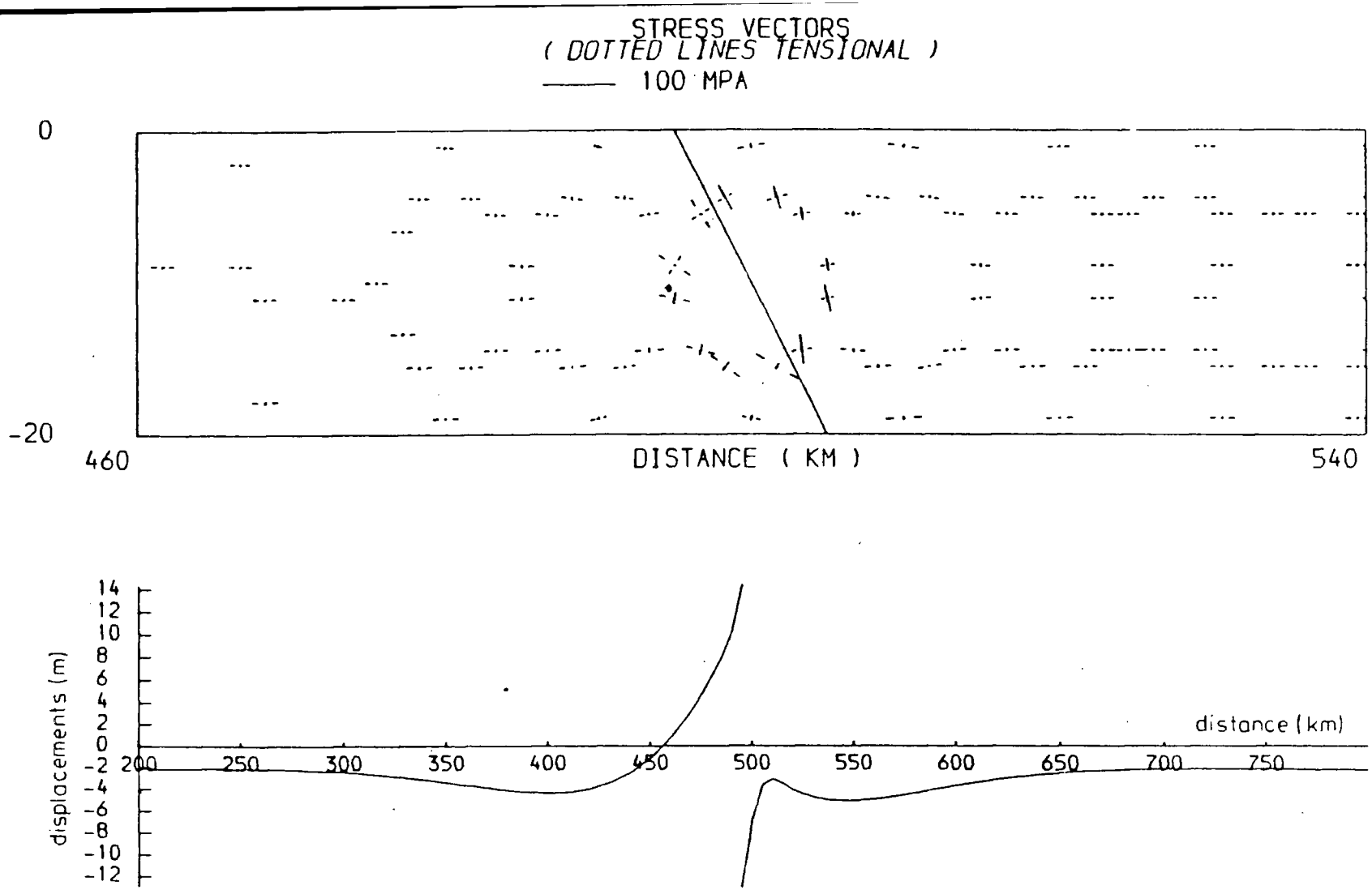

Figure 6.7: The deformation following frictional sliding in response to a 30 MPa tensional stress.

a) Principal stresses around the fault.

b) Vertical displacements of the top surface.

3. The amplitude of the flexure in the model adjacent to the fault is reduced. This decreases the magnitude of the horizontal tensional stress at the top of the model on the downthrown side of the fault.

4. At low tensional stresses a short wavelength upwards flexure occurs on the downthrown side of the fault. This flexure, which has its axis at 15 km from the fault plane, has previously been noted by Mithen (1980). This flexure occurs when frictional sliding has not penetrated throughout the elastic layer and it is the result of flexure above a continuous elastic substratum.

These results are qualitatively similar to those obtained by Mithen (1980) who performed identical tests with CST elements. The major difference is that the relative displacements of the isoparametric model are consistently higher than than those of the CST model: for 50 MPa the throw of the fault in the isoparametric models is 100 metres greater. Larger tensions consequently occur at the top of the downthrown side of the fault in the isoparametric model. The implications and origins of these differences are discussed in the next section.

6.1.7 Predicted graben widths

The models presented in section 6.1.6 demonstrate that large near surface horizontal tensional stress occurs on the downthrown side of the fault because of the flexure produced by frictional sliding. A consequence of this is that tensional failure is likely to occur on the downthrown side of the fault. The modified Griffith theory is therefore used in this section to predict the distance from the fault where failure is most likely to occur. This distance will be referred to as the predicted graben width.

ELASTIC THICKNESS (km)	TENSIONAL STRESS (MPa)	GRABEN WIDTH (km)
10	20	22.5
	30	26.5
	40	27.2
	50	27.2
20	20	15.0
	40	15.0
	60	45.5
	80	45.5
30	40	10.5
	60	17.0
	80	57.5

Table 6.3: Graben width predicted for different elastic thicknesses and tensional stresses.

The predicted graben widths for a 10, 20 and 30 km thick lithosphere are compared in table 6.3. Some generalisations can be made from an analysis of these results:

1. Two graben widths are predicted for a given elastic thickness. The maximum width is predicted when the applied tensional stress is sufficiently large for frictional sliding to penetrate throughout the elastic layer and the deformation on the downthrown side of the fault is dominated by the long wavelength flexure. The minimum width, which is predicted at lower applied tension,

occurs when frictional sliding has not penetrated through the elastic layer and the deformation is dominated by the short wavelength flexure.

2. Increasing the thickness of the elastic layer increases the maximum graben width.

The graben widths for different thicknesses of the elastic layer calculated by thin elastic beam theory (Mithen, 1980) are summarised in table 6.4. These analytic solutions predict that increasing the thickness of the elastic layer increases the graben width. The graben width predicted by the isoparametric finite element models agree with the lower bound of these analytic solutions. Both the analytic and isoparametric solutions predict that wider grabens occur as the thickness of the elastic layer increases.

ELASTIC THICKNESS (km)	PREDICTED WIDTH (km)
10	25.2 <w< 50.4
20	42.4 <w< 84.0
30	57.5 <w<115.0

Table 6.4: Graben widths predicted by analytic theory (Mithen, 1980)

Mithen (1980), who performed identical analyses with CST elements, predicted a constant graben width of 50-55 km for all thicknesses of the elastic layer. These models consequently disagree with the analytic

solutions. Mithen (1980) proposed that this discrepancy arose because the approximations made in the thin elastic beam solutions oversimplify the true complexity of the problem.

The agreement between the graben widths predicted by the analytic solutions and the isoparametric models of this thesis, however, suggests an alternative explanation; the CST meshes which were used by Mithen (1980) are too stiff to accurately model lithospheric flexure. This conclusion is supported by the observations in previous sections of this chapter that the displacements of the CST models are consistently less than those of the isoparametric solutions. As shown in Chapter 4 this commonly occurs in flexural problems when the CST finite element mesh is too stiff because an insufficient number of elements have been used to model the linear strain gradient. Mithen (1980), however, used relatively coarse CST element meshes to extend his analysis to predict graben widths in much more complex situations. Those of Mithen's conclusions which are dependent upon the flexural response of CST meshes should therefore be treated cautiously until verified by isoparametric solutions.

6.1.8 Isostatic compensation on the upper surface of the model

Some of the models in the previous sections show large vertical displacements of the top surface of the model. In reality isostatic restoring forces oppose the development of large vertical upward or downward displacements. An isostatic restoring force equivalent to the topographic load on the top surface of the model is therefore introduced in this section. This compensation procedure is identical to that applied at the base of the finite element models.

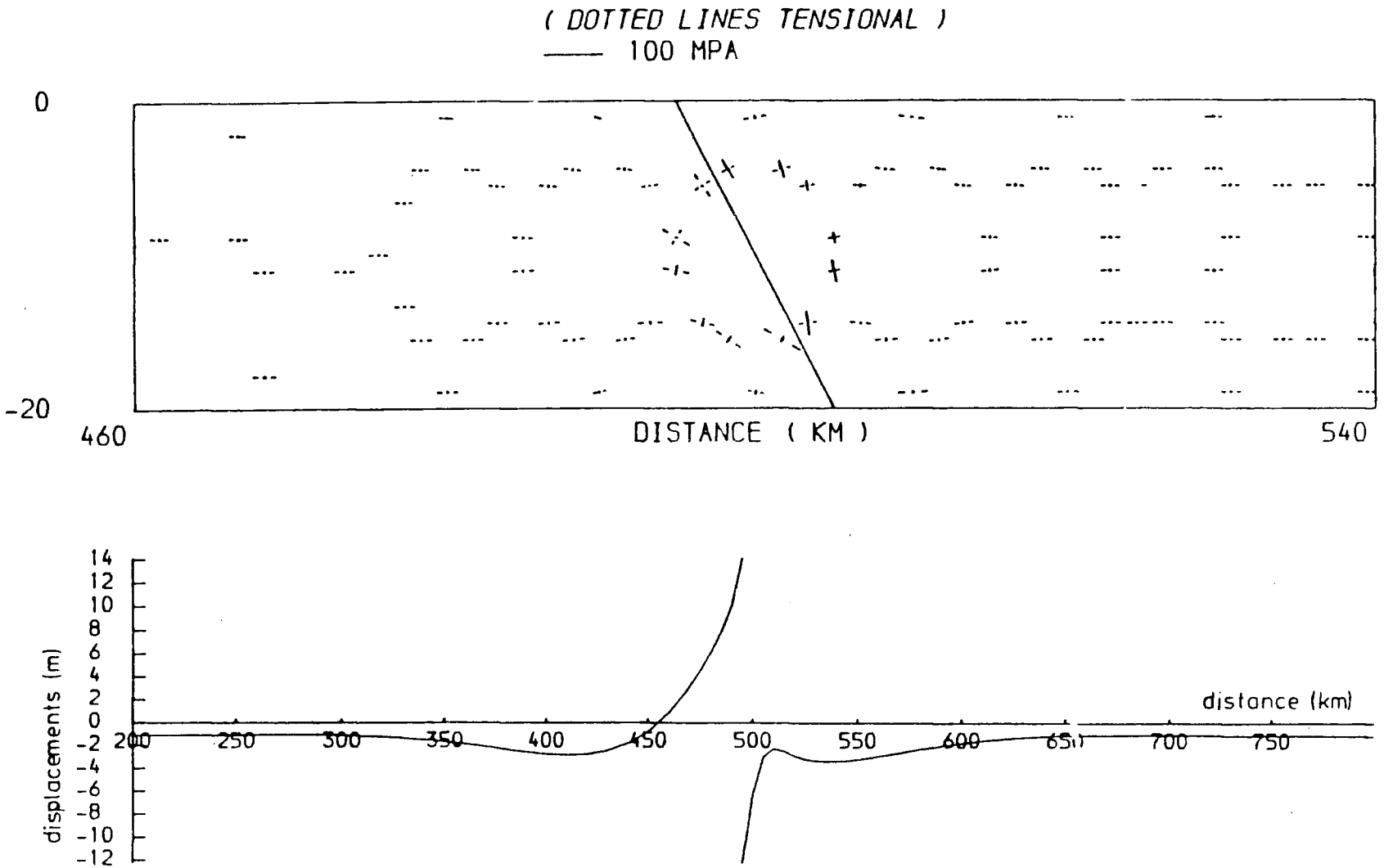

Figure 6.8: The deformation following frictional sliding in response to a 30 MPa tensional stress with isostatic restoring forces on the top surface.

a) Principal stresses around the fault.
b) Vertical displacements of the top surface.

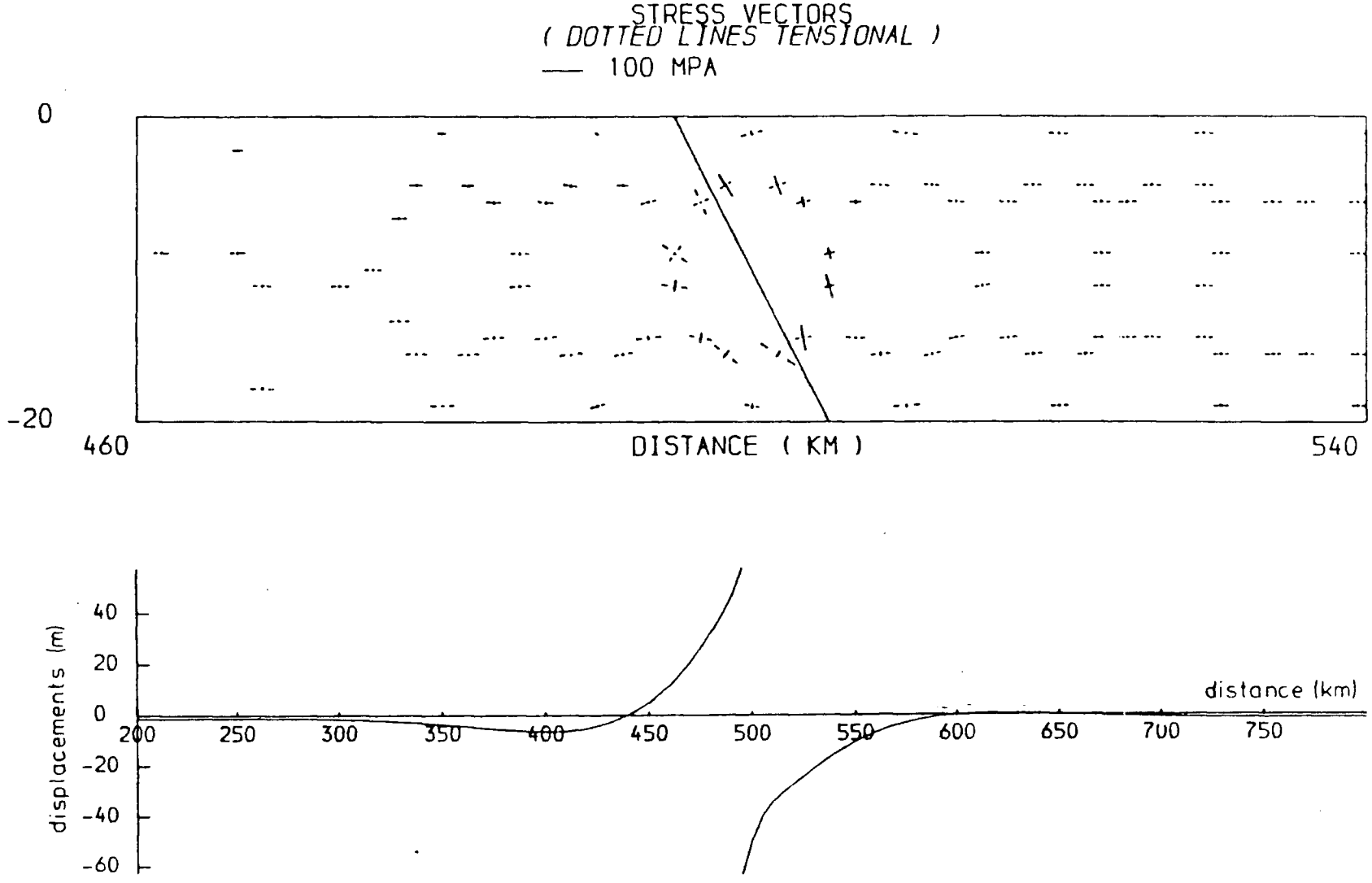

Figure 6.9: The deformation following frictional sliding in response to a 40 MPa tensional stress with isostatic restoring forces on the top surface.

a) Principal stresses around the fault.
b) Vertical displacements of the top surface.

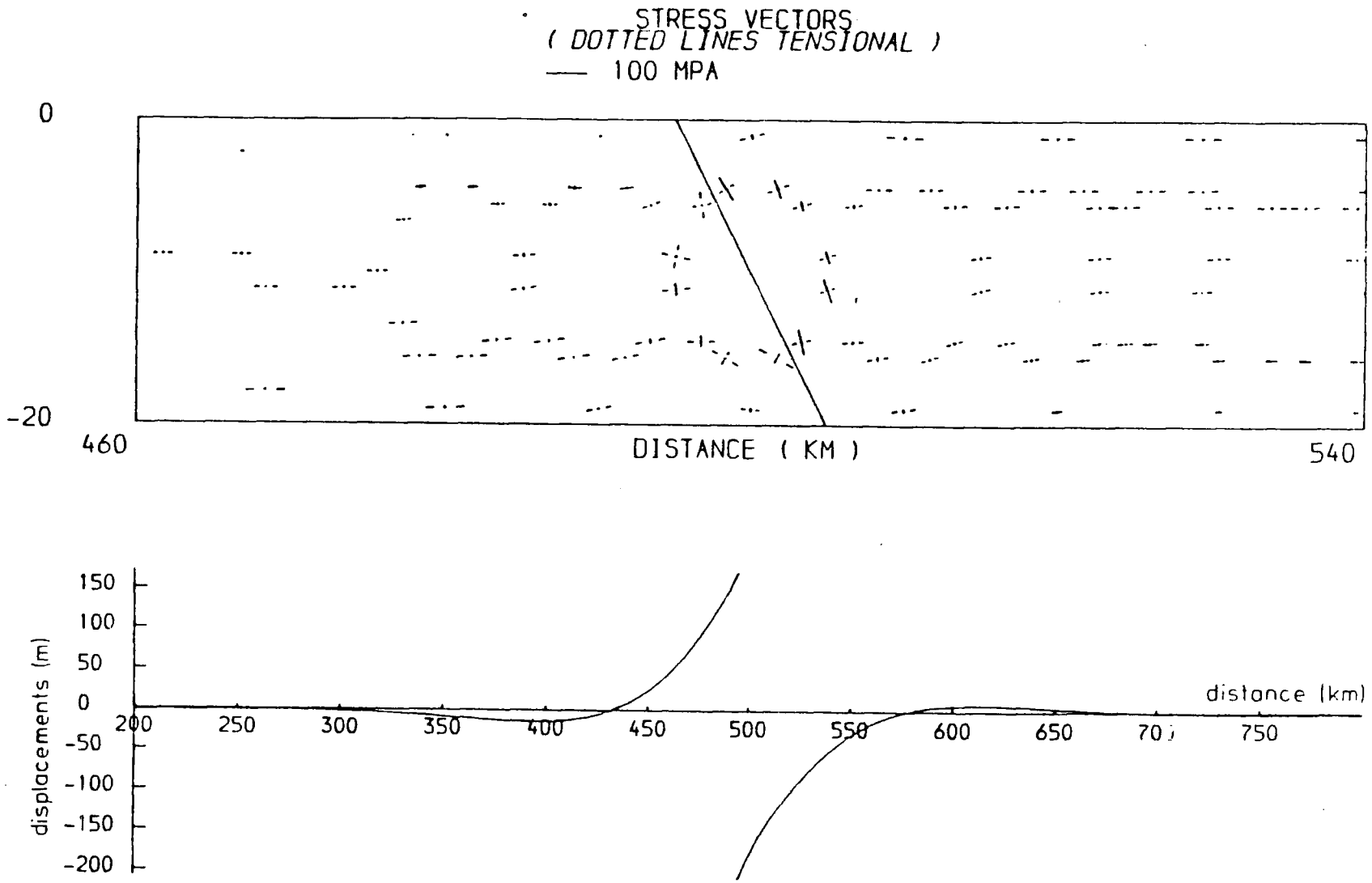

Figure 6.10: The deformation following frictional sliding in response to a 50 MPa tensional stress with isostatic restoring forces on the top surface.

a) Principal stresses around the fault.

b) Vertical displacements of the top surface.

The effect of introducing this boundary condition to the models which have 30, 40 and 50 MPa tension applied to them is shown in figures 6.8 to 6.10. Comparing these results with the previous solutions (section 6.1.5) demonstrates that the introduction of the isostatic restoring forces on the top surface reduces the large vertical displacements in the 50 and 40 MPa models, but has little effect on the smaller displacements in the 30 MPa solution. The overall shape of the displacement profile in the surrounding lithosphere, however, is unchanged. Consequently, the predicted graben widths do not differ from the previous solution.

Because this boundary condition is considered to be realistic it is applied to the models which are presented in later sections of this chapter.

6.2 Listric Normal Fault

The results of section 6.1 demonstrate that the model of frictional sliding accurately simulates the deformation on a plane normal fault. This analysis is now extended to predict the deformation on listric normal faults. This section compares and contrasts the modelled deformation on a listric normal fault with that on plane normal faults.

6.2.1 Description of the finite element mesh

The central section of the 800 km long finite element mesh and the position of the listric fault are shown in figure 6.11. The fault has the following geometry:

1. Between the surface and 10 km it is plane and has a dip of 63.43 degrees.

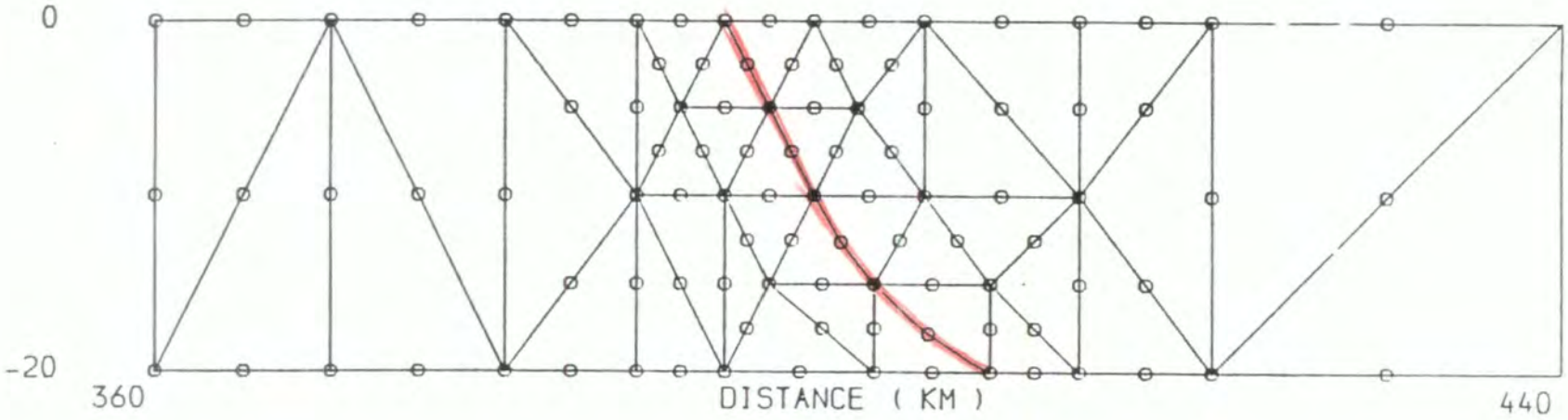

Figure 6.11: Central section of the listric normal fault finite element mesh. Position of the fault shown in red.

2. Between 10 and 20 km it is defined by a circle with a radius of 21.25 km and its centre (x,y) at (417.5,0.0).

The elastic properties of the finite element mesh and the fault are summarised in tables 6.1 and 6.2. The boundary conditions are identical to those used in the plane normal fault model; the right hand side was constrained to move vertically, the left hand edge is free and isostatic restoring forces are applied to the top and base of the model using densities of 2700 kg m^{-3} and 2900 kg m^{-3} respectively. The convergence factor which was used to model the frictional sliding was 15.0.

6.2.2 Discussion of results

The deformation of the model in response to 30, 40 and 50 MPa tensional stresses is shown in figures 6.12 to 6.14. The deformation is generally similar to that of the plane normal fault model:

1. The left and right hand sides of the fault have been displaced upwards and downwards respectively. The fault is consequently a normal fault.

2. Increasing the magnitude of the applied tension increases the throw of the fault.

3. The principal stresses are modified close to the fault. Following frictional sliding tension and compression occurs parallel to the fault plane on its upthrown and downthrown sides respectively.

4. The vertical displacements at the fault plane induce a long wavelength flexure. At low stress an additional short wavelength upward flexure of the lithosphere occurs on the downthrown side of

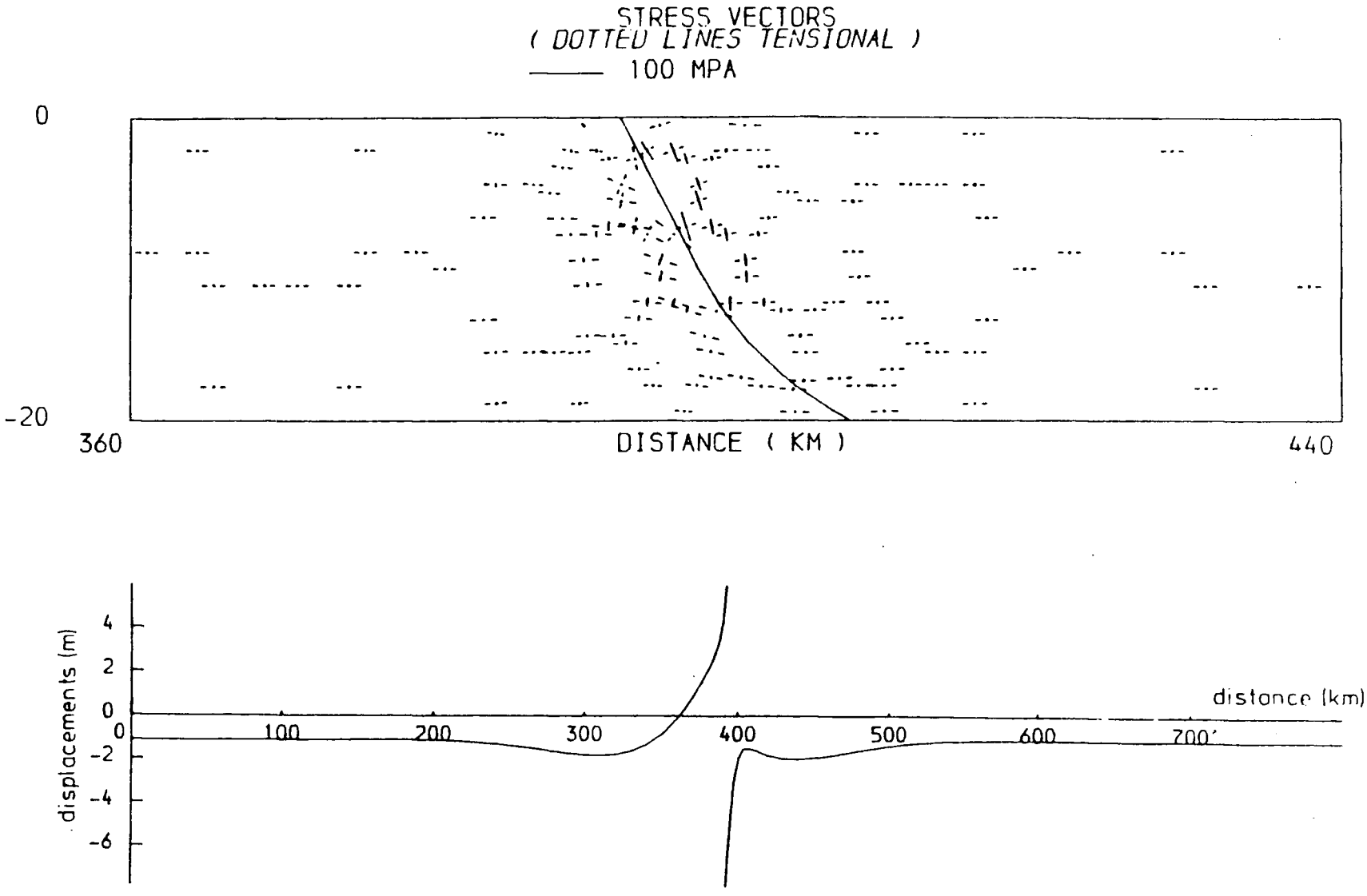

Figure 6.12: The deformation of the listric normal fault model following frictional sliding in response to a 30 MPa tensional stress.
a) Principal stresses around the fault.
b) Vertical displacements of the top surface.

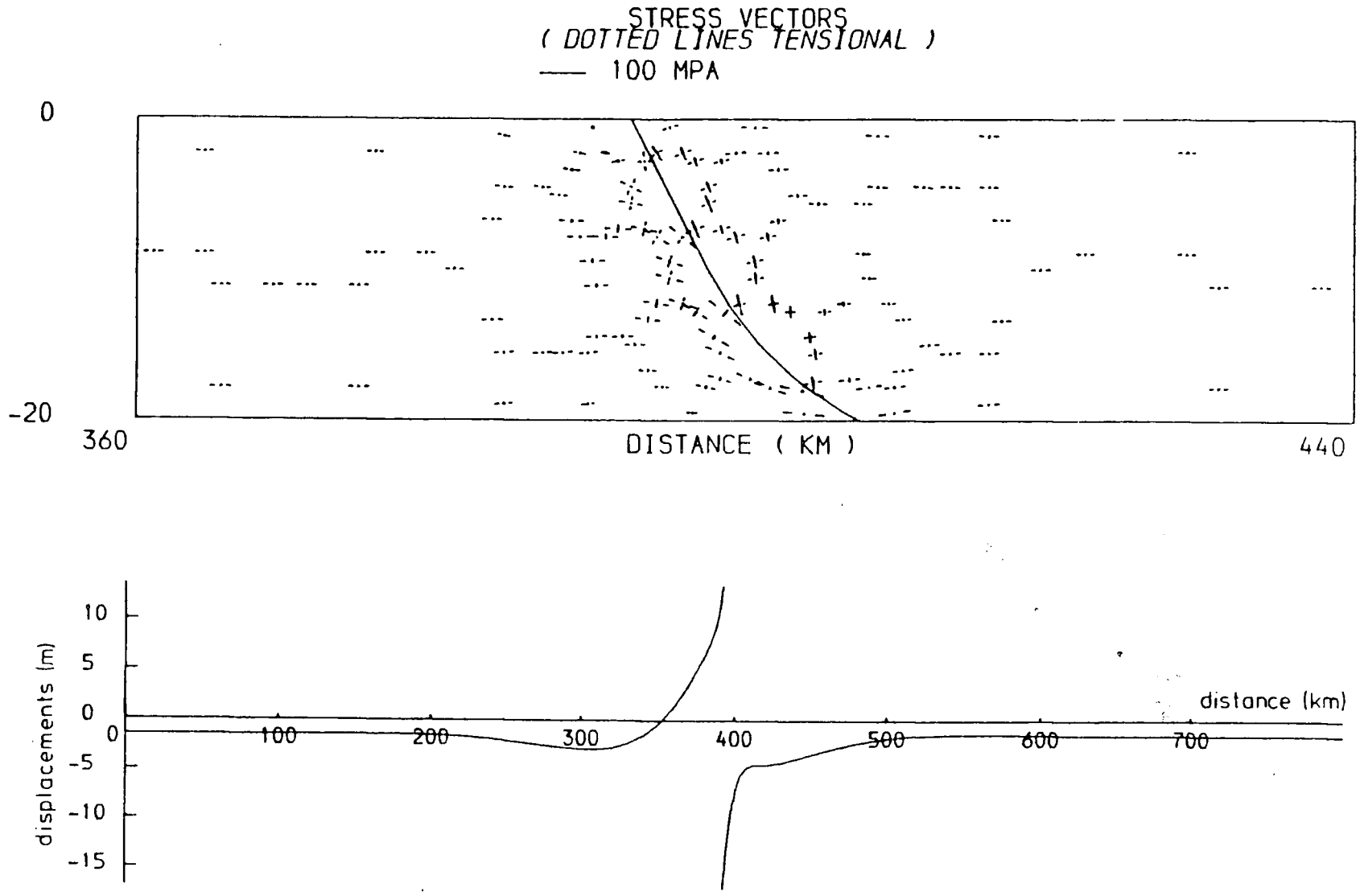

Figure 6.13: The deformation of the listric normal fault model following frictional sliding in response to a 40 MPa tensional stress.
a) Principal stresses around the fault.
b) Vertical displacements of the top surface.

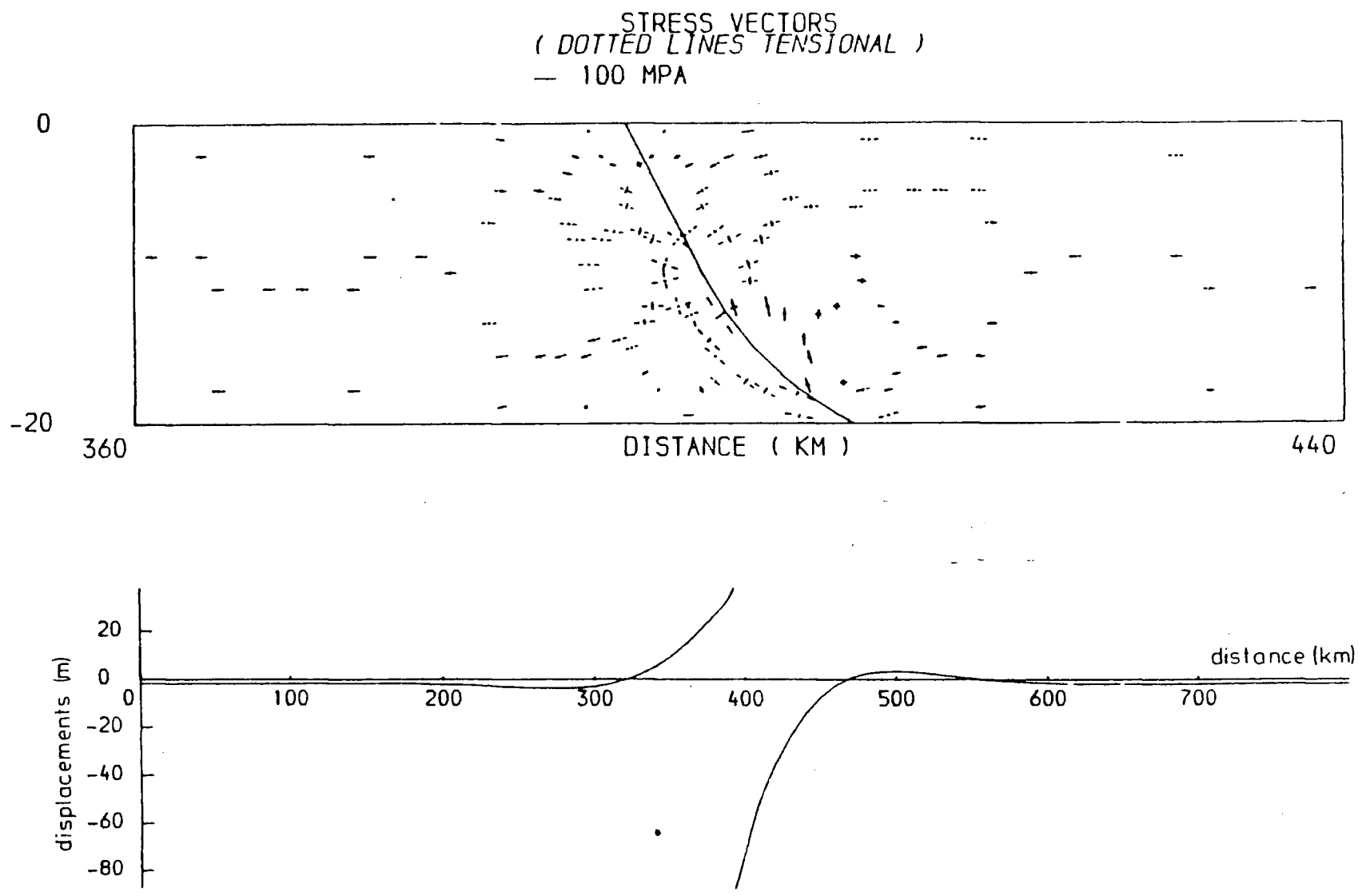

Figure 6.14: The deformation of the listric normal fault model following frictional sliding in response to a 50 MPa tensional stress.
a) Principal stresses around the fault.
b) Vertical displacements of the top surface.

the fault. This flexure, which has its axis 15 km from the fault plane, disappears as the applied tensional stress is increased.

5. Increasing the tensional stress increases the depth to which frictional sliding occurs. At 30 MPa frictional sliding occurs down to 10 km, whilst at 50 MPa it extends throughout the elastic layer. This means that increasingly more deformation occurs on the listric section of the fault as the tension increases.

The vertical displacements in the listric fault model are consistently less than those of the corresponding plane normal fault model. This is because rotation has to occur on the listric fault plane to maintain its geometry.

6.3 Thrust Faults

The previous sections of this chapter have shown that the model of frictional sliding can simulate the deformation on plane and listric normal faults. In this section this analysis is extended to model the deformation on plane and listric thrust faults.

6.3.1 Plane thrust faults

The central section of the 1000 km long finite element mesh and the position of the plane thrust fault are shown in figure 6.15. The thrust fault has a dip of 26.57 degrees. The elastic properties of the finite element mesh and the fault are summarised in tables 6.1 and 6.2. The boundary conditions which were applied to this body were identical to those used in the normal fault models (section 6.2.1).

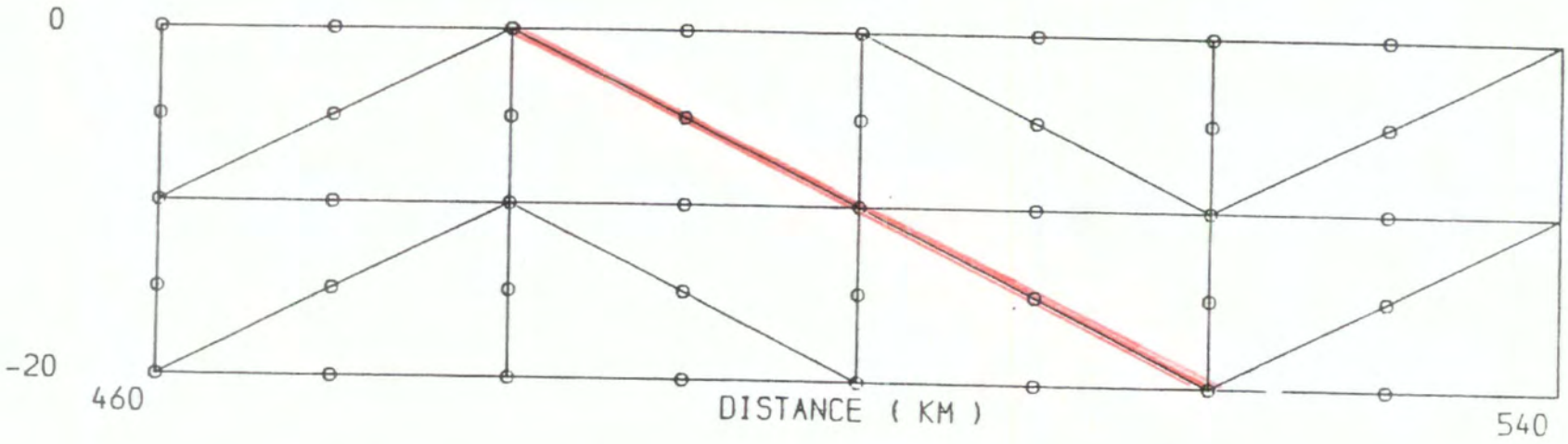

Figure 6.15: Central section of the plane thrust fault finite element mesh. Position of the fault shown in red.

The initial elastic deformation of the model in response to a 30 MPa compressive stress is shown in figure 6.16. The top surface of this model to the left and right hand sides of the fault is displaced upwards and downwards respectively. The fault is consequently a thrust fault. This type of fault would be expected to develop in response to horizontal compressive stress (Anderson, 1951). The effect of these local displacements along the fault plane is to induce a long wavelength flexure in the adjacent lithosphere. This effect has been previously observed in the normal fault models.

The deformation following frictional sliding on the fault is shown in figure 6.17. The following generalisations can be made from an analysis of these results:

1. The relative vertical displacements at the fault plane are increased by frictional sliding.

2. The stress close to the fault is modified by the frictional sliding. Tension occurs parallel to the fault plane on its overthrust side and compression occurs on its downthrust side.

3. A short wavelength downwards flexure of the lithosphere occurs on the downthrown side of the fault. This short wavelength flexure, which has its axis 15 km from the fault, is superimposed upon the long wavelength flexure which affects both sides of the fault. A similar short wavelength flexure was observed at low stress in the normal fault models. This flexure occurs above the fault plane because frictional sliding is limited to the upper part of the thrust plane.

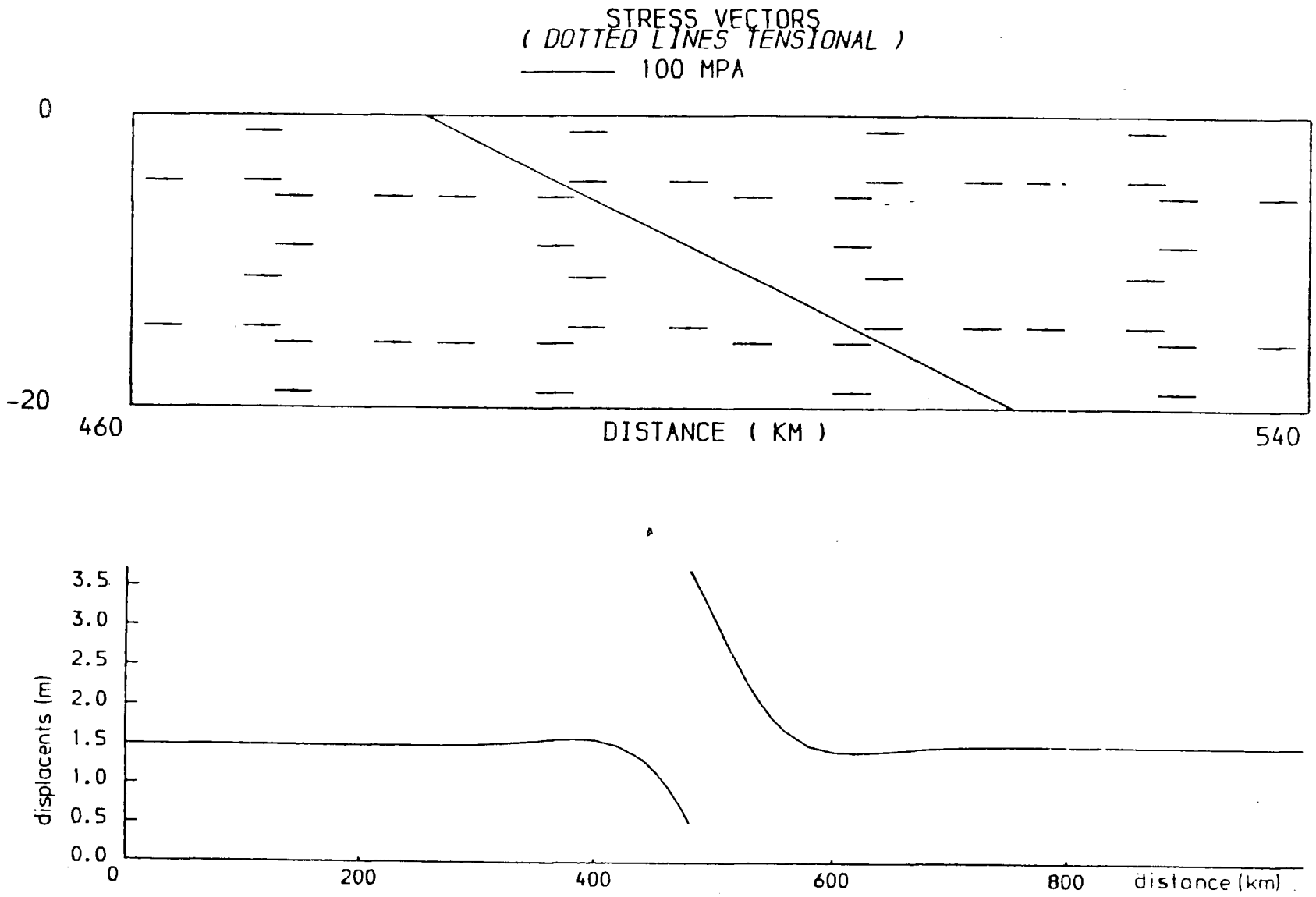

Figure 6.16: Initial elastic deformation of the plane thrust fault model in response to a 30MPa compressive stress.
a) Principal stresses around the fault.
b) Vertical displacements of the top surface.

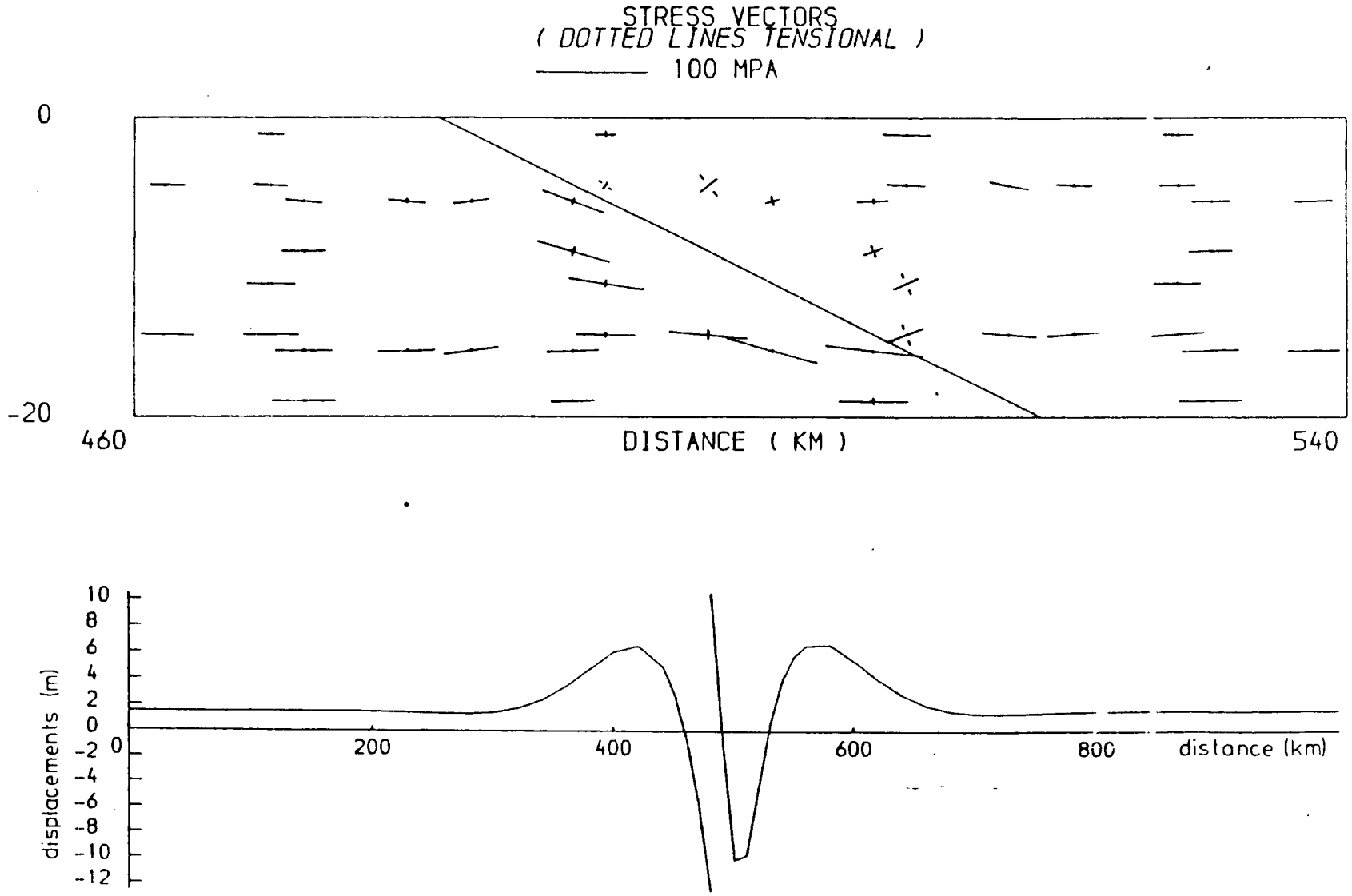

Figure 6.17: The deformation of the plane thrust fault model following frictional sliding in response to a 30 MPa compressive stress.

a) Principal stresses around the fault.
b) Vertical displacements of the top surface.

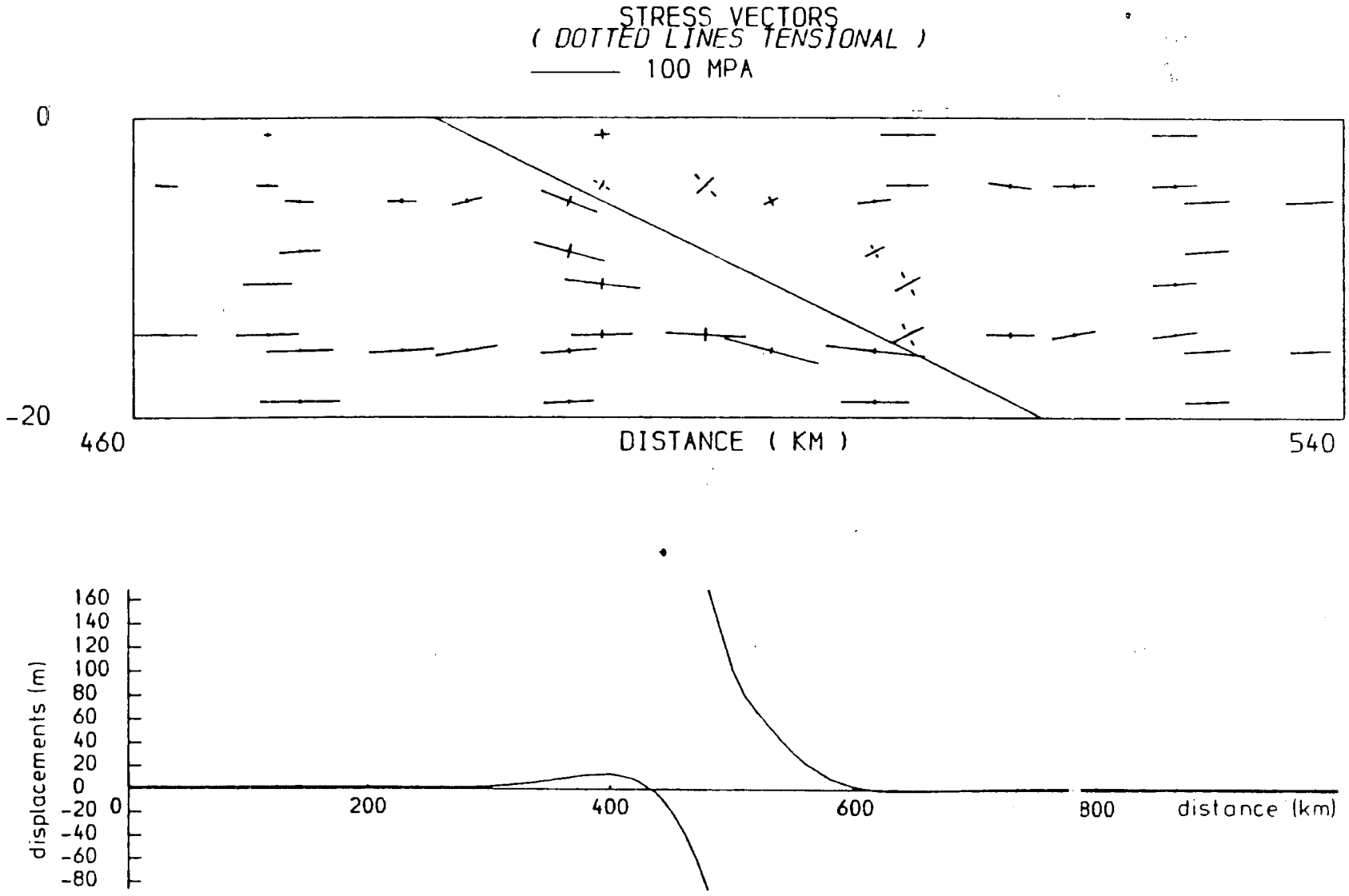

Figure 6.18: The deformation of the plane thrust fault model following frictional sliding in response to a 50 MPa compressive stress.

a) Principal stresses around the fault.
b) Vertical displacements of the top surface.

The effect of increasing the horizontal compression from 30 to 50 MPa is shown in figures 6.17 to 6.18. The deformation in response to increasing stress follows the same pattern as that for the normal fault models. Firstly, increased displacement occurs on the fault plane as frictional sliding penetrates through the entire elastic layer to redistribute the larger magnitude excess shear stresses on the fault plane. Secondly, the short wavelength flexural feature on the overthrust side of the fault disappears as the applied stress is increased.

An important implication of these models is that although compressive stresses cannot cause a buckling of a homogeneous elastic layer (Ramberg and Stephansson, 1964), they can produce significant deformation when a fault is present.

6.3.2 Listric thrust faults

The central section of the 700 km long finite element mesh and the position of the listric thrust fault are shown in figure 6.19. The listric fault plane is described by a circle which has its origin (x,y) at (315 km, -70 km) and a radius of 71 km. The same elastic properties and boundary conditions which have been used in previous sections were applied to this model (e.g. section 6.3.1).

The deformation produced by increasing the compressive stress from 30 to 50 MPa is shown in figures 6.20 and 6.21. The deformation of these models is generally similar to that of the plane thrust fault. The major differences between these solutions are in the shape of the vertical displacement profile on the overthrust side of the fault which can be summarised as follows:

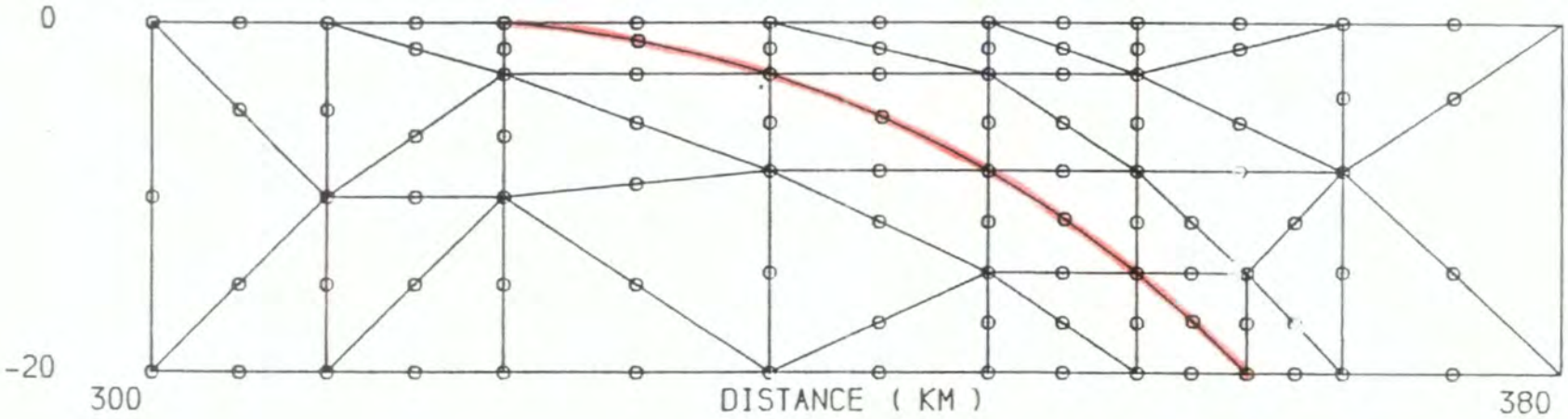

Figure 6.19: Central section of the curved thrust fault finite element mesh. Position of the fault shown in red.

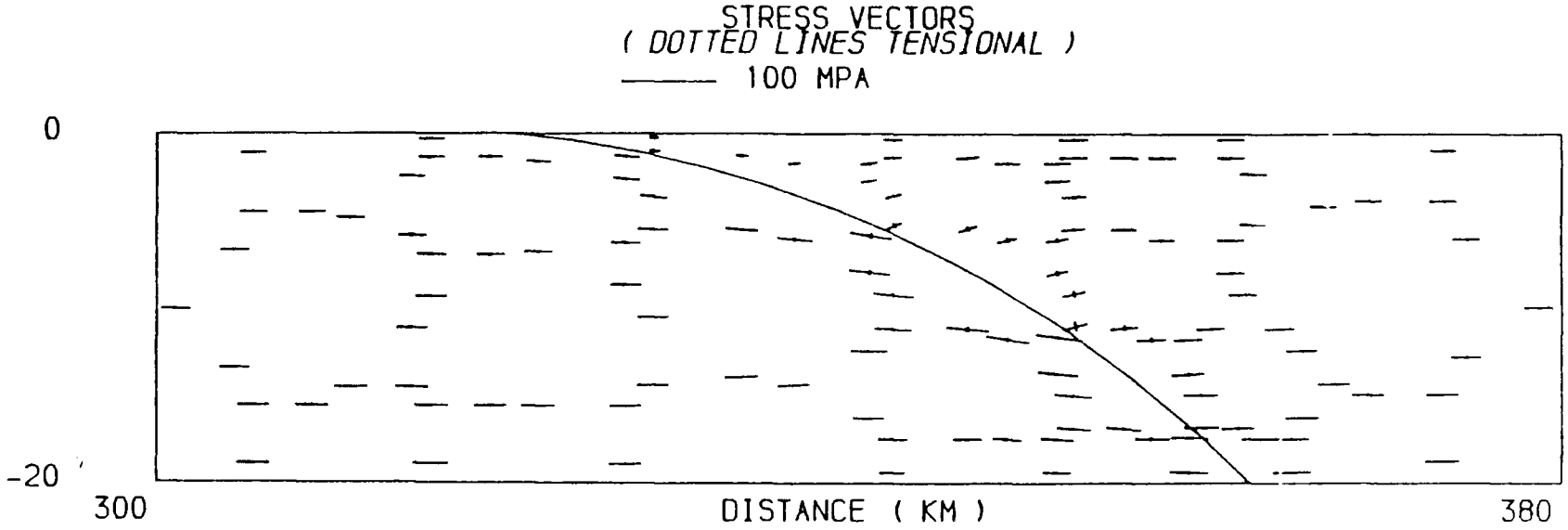

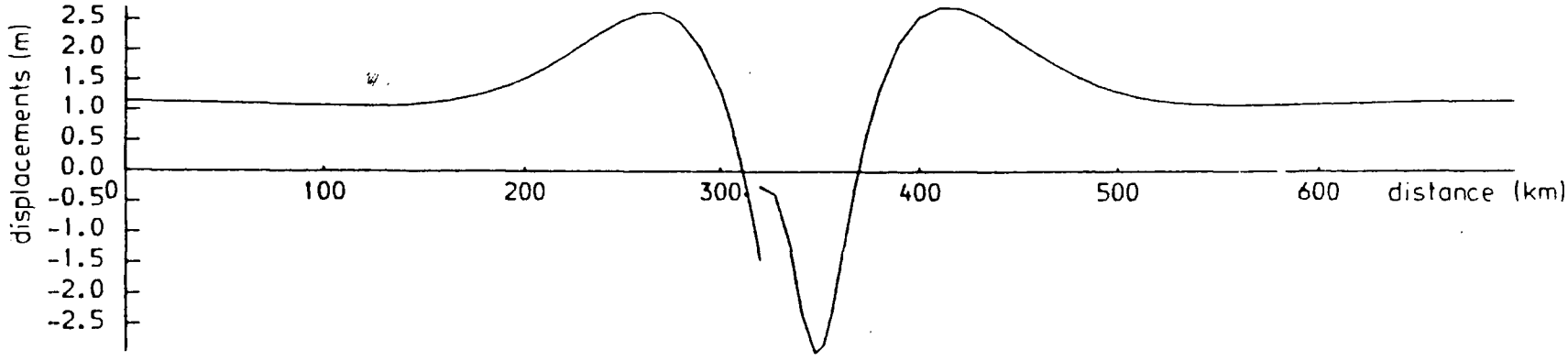

Figure 6.20: The deformation of the listric thrust fault model following frictional sliding in response to a 30 MPa compressive stress.

a) Principal stresses around the fault.
b) Vertical displacements of the top surface.

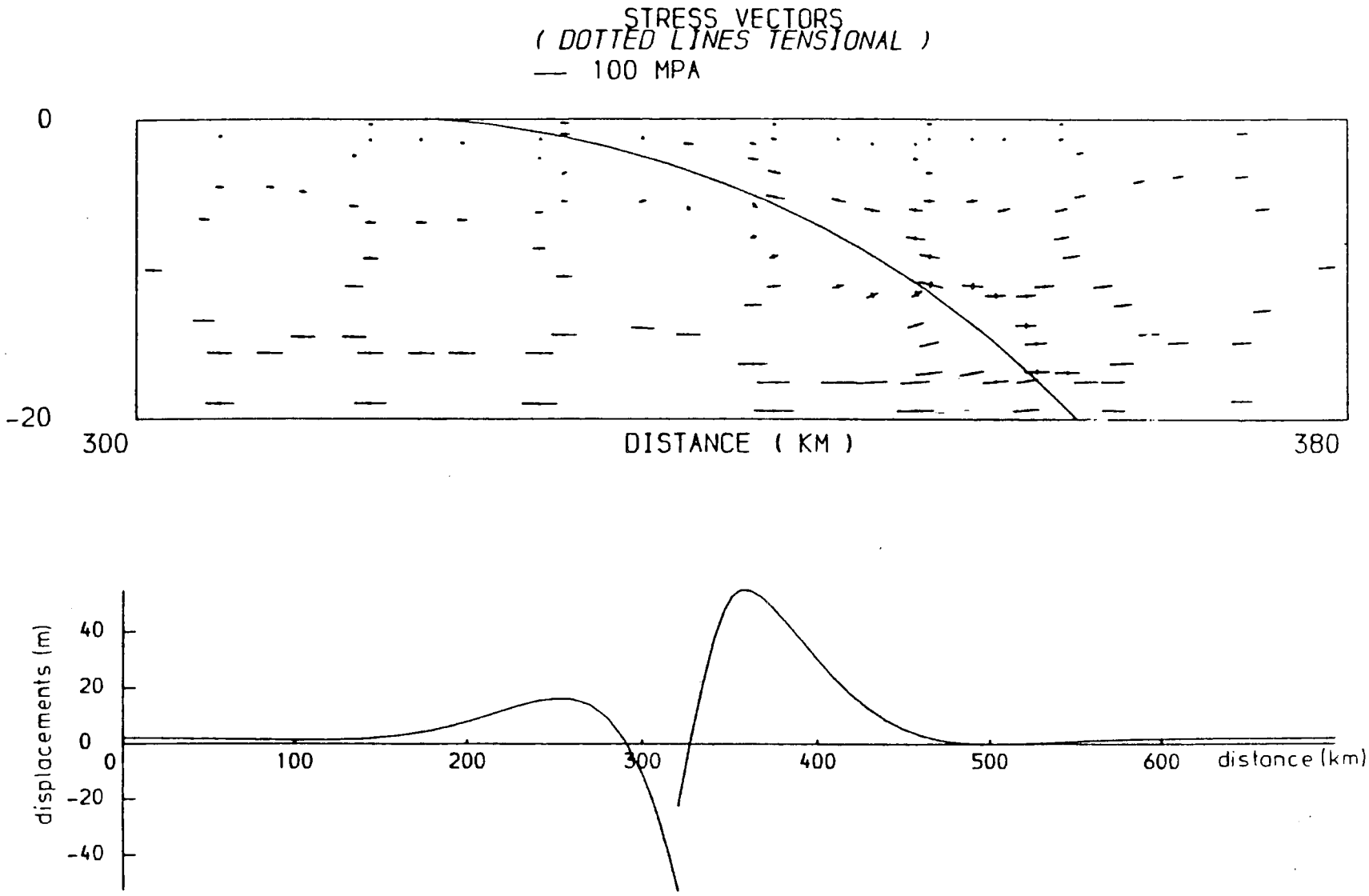

Figure 6.21: The deformation of the listric thrust fault model following frictional sliding in response to a 50 MPa compressive stress.

a) Principal stresses around the fault.
b) Vertical displacements of the top surface.

1. Only several metres of vertical displacement occurs at the top of the listric fault because of its very low angle near the surface.

2. An upwards flexure occurs above the steeply dipping section of the listric fault which makes the stresses more tensional at the top of the overthrust lithosphere.

These models demonstrate that listric thrust faults can be modelled using the methods of chapter 5. The frictional sliding model is therefore suitable for analysing the deformation which occurs on the subduction zone fault.

6.4 Summary And Conclusions

In this chapter the performance of the model of frictional sliding (chapter 5) has been evaluated. The most important points can be summarised as follows:

1. The tests have demonstrated that the dual node model is suitable for predicting the type of fault and the deformation which is produced by frictional sliding in response to applied horizontal stress. These results show that thrust faults are predicted in response to compression and normal faults are predicted in response to horizontal tension. The model is consequently suitable for predicting the deformation which will occur in response to any stress regime if the geometry of the fault and its mechanical properties are known or can be assumed.

2. The model is capable of analysing the deformation on both plane and listric faults.

3. The model predicts graben widths which are comparable with the results which are derived from analytic thin elastic beam theory. The failure to obtain similar results with CST elements (Mithen, 1980) arises because the finite element mesh is too stiff as an insufficient number of elements were used to give accurate solutions to flexural problems. The conclusions of Mithen's thesis concerning the failure arising from lithospheric flexure should therefore be used with caution until they have been verified by comparison with results from isoparametric models.

Despite the general success of the model several limitations have been identified. Firstly, the iterative algorithm which has been used to model frictional sliding on faults is not optimally designed. Future analyses should therefore attempt to improve this part of the model. Secondly, the predictiveness of the model is limited because the value of the shear stiffness, which controls the scale of the fault deformation, is not constrained by experimental indications. Future analyses should therefore attempt to constrain the shear stiffness of faults by estimating it from real world examples.

In conclusion, the model which has been developed in chapter 5 is capable of modelling fault deformation in a variety of tectonic settings. This model will consequently be used in the next chapter to analyse the stress regime at subduction zones.

CHAPTER 7

THE STRESS REGIME AT SUBDUCTION ZONES

7.1 Introduction

In previous chapters of this thesis an isoparametric finite element method has been developed which is capable of modelling the deformation which occurs at subduction zones. In this chapter this method is used to model the stress regime which is produced at subduction zones by lateral density variations, the slab pull force, the mechanical coupling of the plates and the slab induced convection. The stress regime predicted by these models is then compared with the observed state of stress at subduction zones to investigate why:

1. A lateral variation in stress is observed across the strike of all subduction zones.

2. The state of stress in the back arc area of the overlying plate is so variable between different subduction zones.

7.2 Description Of The Finite Element Mesh

The finite element mesh which has been used to model the stress regime at subduction zones is shown in figure 7.1. It represents an idealised two dimensional cross section through the upper 95 km of an active continental margin subduction zone. The finite element mesh has been simplified by omitting the deep structure of the subducting plate from the model. The forces which are transmitted to the surface plates by the subducted oceanic

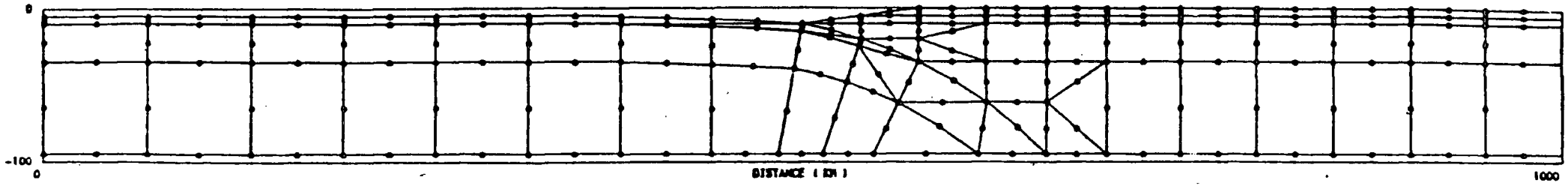

Figure 7.1: Finite element mesh of an active continental margin subduction zone.

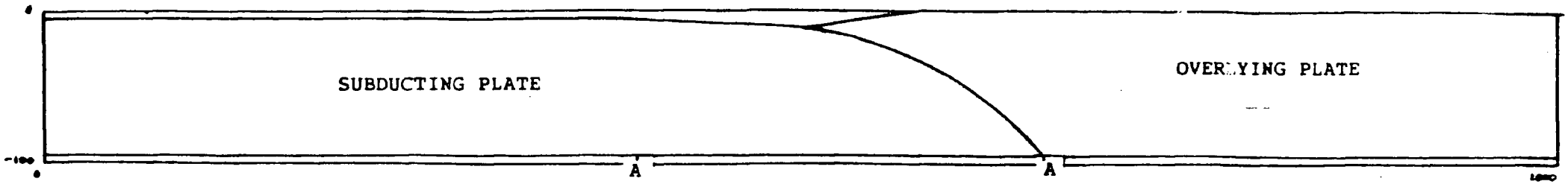

Figure 7.2: Position of the subducting and overlying plates in the finite element model.

lithosphere will therefore be represented by applying appropriate normal and shear stresses to the base of the model where the subducting slab is truncated (position A-A in figure 7.2).

The finite element mesh is formed from 23 triangular and 62 quadrilateral isoparametric finite elements. The finite element calculations have been performed using 6 Gaussian integration points in the triangular elements and 4 integration points in the quadrilateral elements.

The assumed positions of the subducting oceanic and the overlying continental plate are shown in figure 7.2. The interface between the two plates is represented in the model by a curved fault plane which is defined by four isoparametric fault elements. The fault plane is defined by a circle of 300 km radius which has its origin (x,y) at (445.456 km, -305.0 km). These parameters, which are representative of subduction zones, were chosen so that the subducting plate has a dip of 45 degrees at the base of the model.

	Young's modulus ($N\ m^{-2}$)	Poisson's ratio	Tensile strength (MPa)	Density ($kg\ m^{-3}$)
Crust	0.85×10^{11}	0.25	12.0	2922.0
Mantle	1.90×10^{11}	0.25	50.0	3300.0

Table 7.1: Elastic parameters assigned to the crust and mantle.

The subducting oceanic lithosphere at the left hand edge of the model is 90 km thick and is overlain by 5 km of water which is assumed to have a density of 1030 kg m^{-3}. The oceanic lithosphere is subdivided into a 5 km thick crustal layer which overlies 85 km of upper mantle (Figure 7.3). The values assigned to the elastic parameters and densities of these layers are

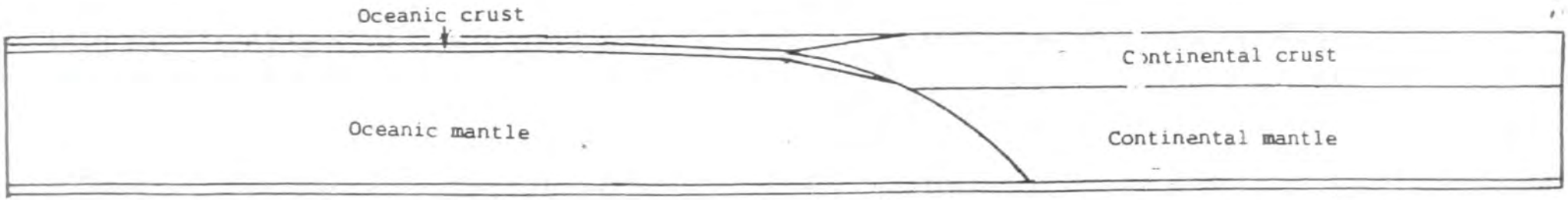

Figure 7.3: Position of the crust and mantle of the subducting and overlying plates in the finite element model.

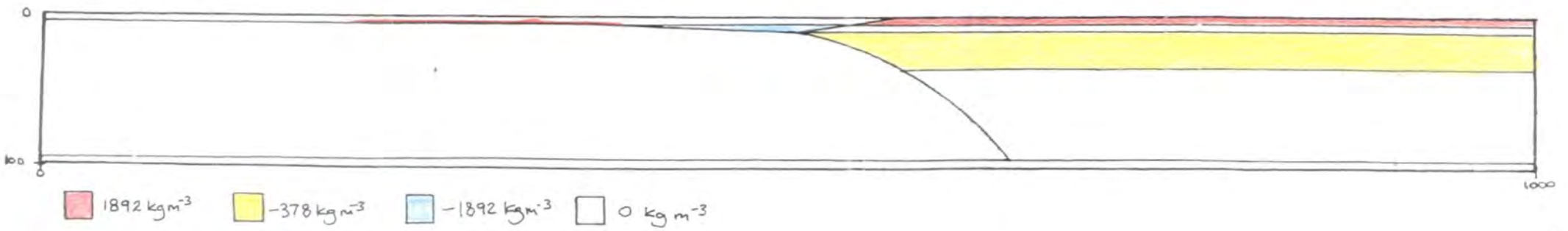

Figure 7.4: Stripped density distribution applied to the subduction zone model

summarised in table 7.1. The thickness of the elastic oceanic lithosphere is assumed to be 30 km and the lower oceanic lithosphere is assumed to be visco-elastic with a viscosity of 1.0×10^{23} Pa s.

The trench, which is assumed to be 10 km deep, has its axis at 500 km from the left hand edge of the model. The characteristic flexural profile of the oceanic lithosphere seawards of the trench was calculated from the universal elastic trench profile of Caldwell et al (1976). This relates the deflection of the sea floor, w, to the amplitude of the bulge, w_b, and horizontal distance, x, as

$$w = w_b \sqrt{2} \sin\left(\frac{\pi x}{4x_b}\right) \exp\left[\frac{\pi}{4}\left(1 - \frac{x}{x_b}\right)\right]$$

where

$$x_b = \frac{\pi}{4}\left(\frac{4 E h^3}{12g(\rho_m - \rho_w)(1-\nu^2)}\right)^{1/4}$$

in which the symbols, and the values assigned to them, are defined in table 7.2.

Symbol	Definition	Value assigned
E	Young's modulus	0.85×10^{11} N m^{-2}
ν	Poisson's ratio	0.25
g	acceleration due to gravity	9.81 m s^{-2}
ρ_m	mantle density	3300 kg m^{-3}
ρ_w	water density	1030 kg m^{-3}
h	elastic thickness	30 km
w_b	amplitude of bulge	300 m

Table 7.2: Parameters used to calculate the universal elastic trench profile.

The continental lithosphere, which is assumed to be 95 km thick, is divided into a 35 km crustal layer which overlies a 60 km thick mantle (Figure 7.3). The values assigned to the elastic parameters and densities of these layers are summarised in table 7.1. The mantle is assumed to have a viscosity of 1.0×10^{23} Pa s. The lower 25 km of the continental crust is also assumed to be visco-elastic and to have a viscosity of 1.0×10^{24} Pa s.

The density of the oceanic and continental crust was assumed to be 2922 kg m^{-3}. This value was chosen so that the undisturbed oceanic lithosphere at the left hand side of the model and the continental lithosphere are in isostatic equilibrium. The location of the crustal layers are shown in figure 7.3.

7.3 Lateral Density Variations

Lateral variations in crustal thickness and density produce important deviatoric stresses in the lithosphere. The aim of this section is to model the stresses which are produced by the lateral density variations across subduction zones.

There are two major loads which result from lateral density variations. The first of these arises from the isostatically compensated loading of the continental or island arc lithosphere relative to the undisturbed oceanic lithosphere. This effect is analogous to the differential loading which occurs at passive continental margins (Bott and Dean, 1972). The second arises from the isostatically uncompensated flexure of the lithosphere which produces variation in the water and sediment thickness over the trench and the outer rise.

The stresses produced by these two loads will be modelled using the density stripping procedure (Bott and Dean, 1972; Dean, 1973; Kusznir, 1976; Bott and Kusznir, 1979) because it allows the deviatoric stresses to be seen more clearly than using the actual lithospheric densities.

7.3.1 Description of the finite element model.

The geometry and material properties of the finite element mesh have been described in section 7.2.

The density distribution of the model (figure 7.4) was calculated by subtracting the density-depth profile of the undisturbed oceanic lithosphere from the model. The density distribution of the model is therefore relative to the undisturbed oceanic lithosphere. The consequence of this density stripping procedure is that the isostatically uncompensated loading at the trench and outer rise appears as a relative upthrust and downthrust respectively, whilst the upper 5 km of the continental crust and its compensating 'root' appear as an equal relative downthrust and upthrust respectively. The stresses which are calculated from this stripped density distribution are therefore relative to those in the undisturbed oceanic lithosphere.

The nodal forces which result from the stripped density distribution of the continental lithosphere were evaluated using the body force procedure described in chapter 3. The loads arising from the isostatically uncompensated loading at the trench and outer rise, however, were input as boundary forces with a magnitude equivalent to the pressure on the surface (ρgh). These forces are orientated perpendicular to the top of the lithosphere.

The other boundary conditions which were applied to this finite element mesh were as follows; the left and right hand edges were constrained to move vertically and the base was constrained to move horizontally. The normal and shear stiffness of the subduction zone fault were assigned high values of 1.0×10^{15} N m^{-1}. These values have the effect of making the model behave as an elastic continuum (Chapter 6).

7.3.2 Discussion of results.

The elastic solution using the model which has been described in the previous section is shown in figure 7.5. Two distinct stress regimes can be identified. The first of these affects the continental crust. The second affects the subducting oceanic lithosphere beneath the trench.

The continental crust is in compression relative to the undisturbed oceanic lithosphere (figure 7.7). The axes of maximum and minimum compression are aligned vertically and horizontally. The deviatoric stresses in the continental crust, however, are vertical compression and horizontal tension (figure 7.8). The horizontal deviatoric tension has a maximum magnitude of 22.5 MPa at 5-10 km depth. This stress regime is the elastic response of the lithosphere to the isostatically compensated surface loading which has squeezed the continental crust and caused it to displace laterally into the low pressure region formed by the trench (figure 7.9). The effect of the lateral variation in loading is therefore similar to the trench suction force (Elsasser, 1971) because it causes a seawards migration of the trench axis which induces horizontal deviatoric tensions in the overlying plate.

The subducting plate beneath the trench is in vertical tension relative to the undisturbed oceanic lithosphere (figure 7.6). The tension

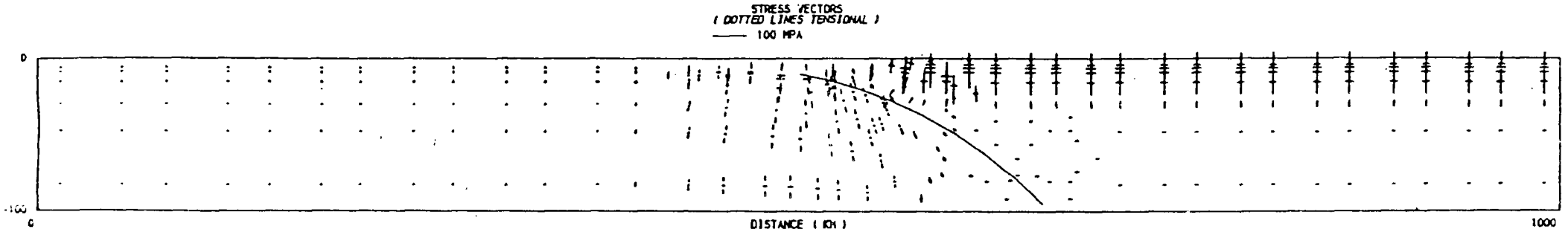

Figure 7.5: The elastic principal stresses in the lateral density variation model.

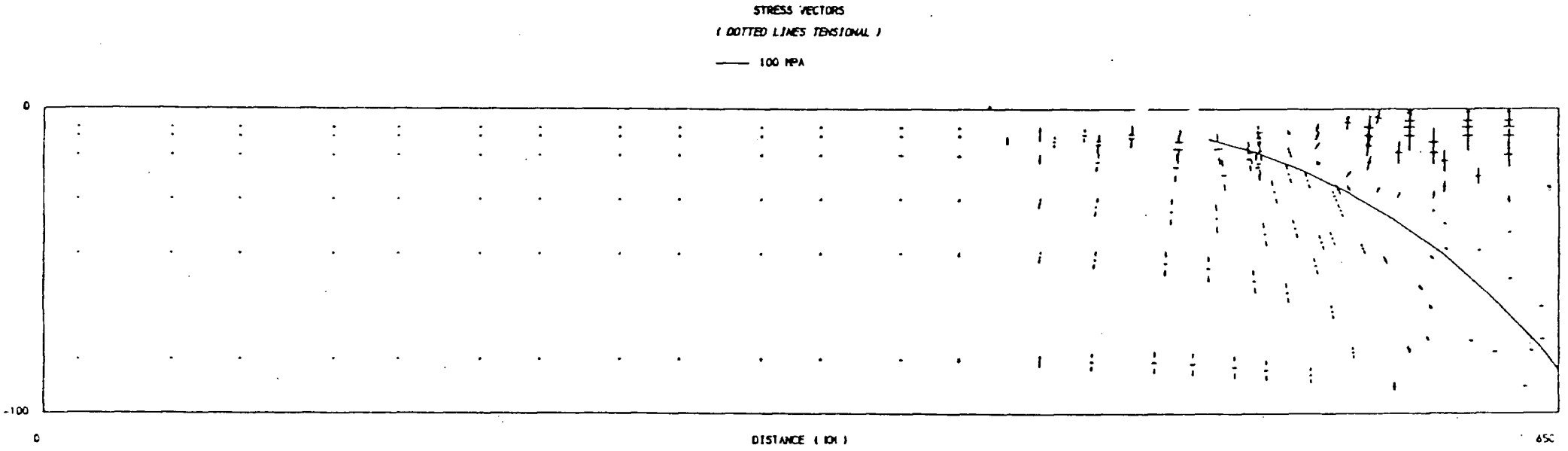

Figure 7.6: The elastic principal stresses in the subducting plate in the lateral density variation model.

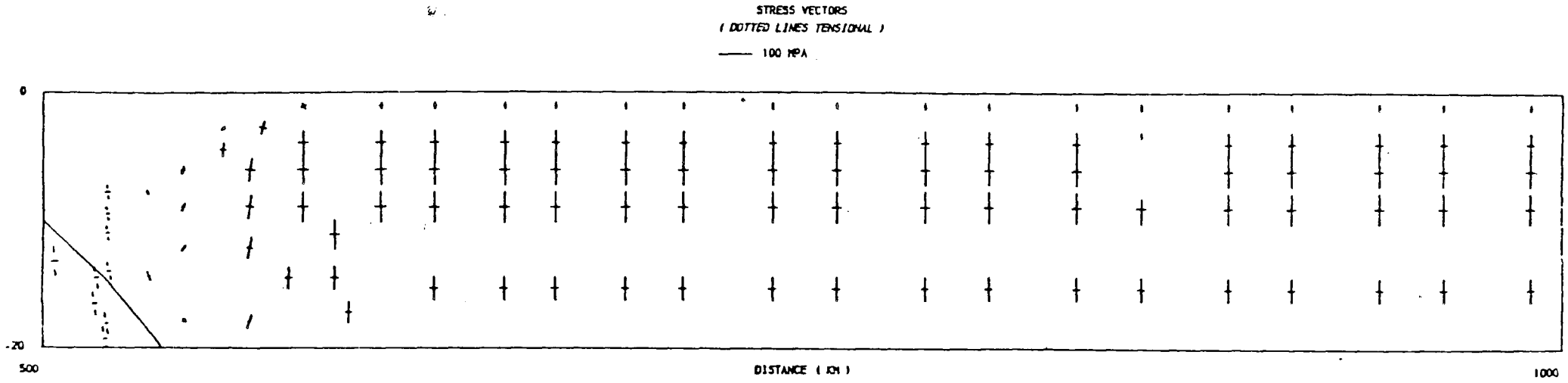

Figure 7.7: The elastic principal stresses in the top 20 km of the overlying plate in the lateral density variation model.

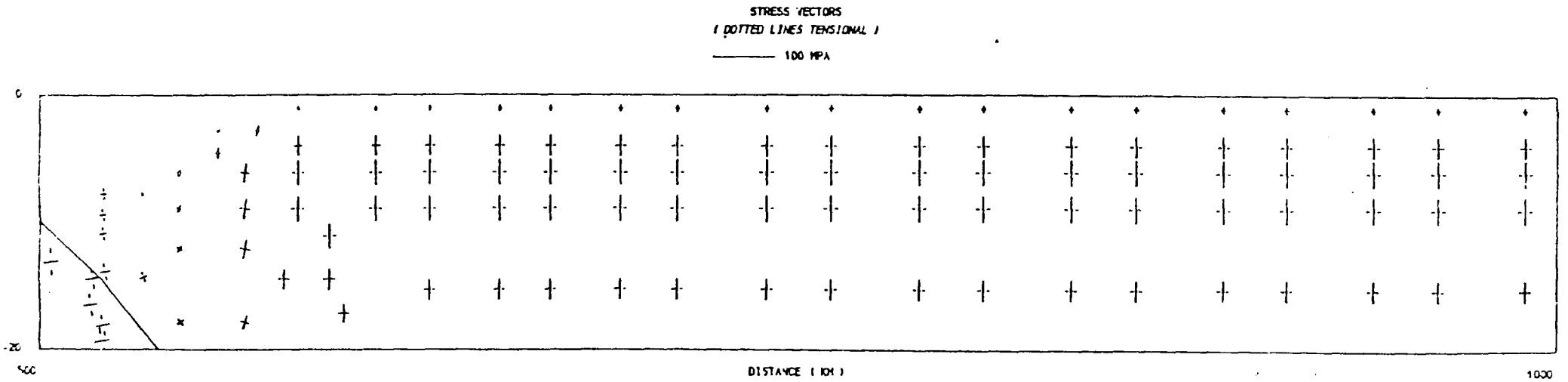

Figure 7.8: The elastic deviatoric principal stresses in the top 20 km of the overlying plate in the lateral density variation model.

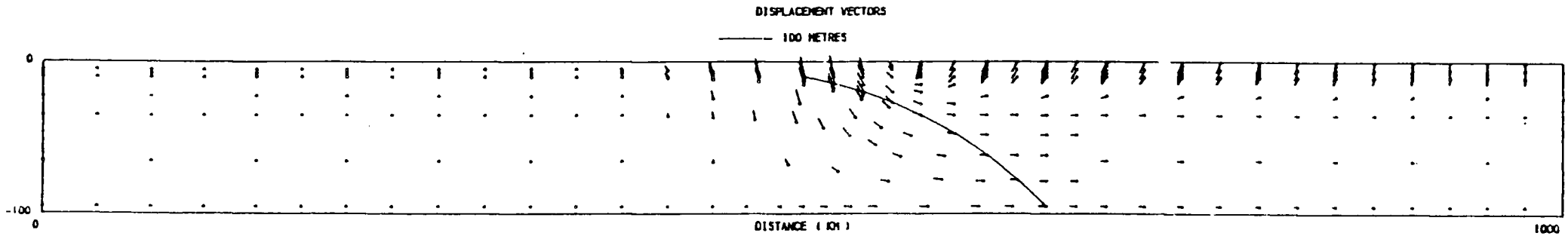

Figure 7.9: The elastic displacements of the lateral density variation model.

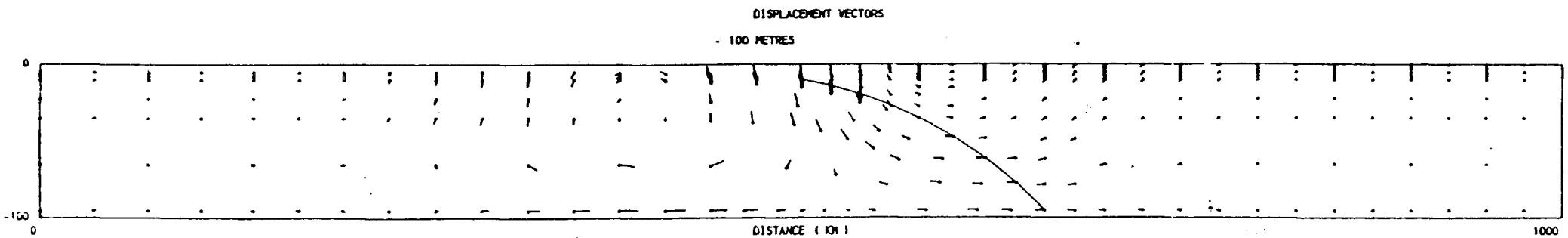

Figure 7.10: The displacements of the lateral density variation model after 5 million years of visco-elastic relaxation.

has a maximum magnitude of 100 MPa and is produced by the relative upthrust of the low pressure trench. A small vertical compression of 10 MPa is developed in the subducting plate beneath the outer rise. These vertical stresses affect the whole thickness of the subducting plate because of the zero vertical displacement boundary condition at the base of the model.

The stress regime after allowing this model to relax visco-elastically for 5 million years is shown in figure 7.11. The most obvious difference between this and the previous solution is that the horizontal stresses have decayed in the visco-elastic part of the model and have become concentrated in the elastic part of the lithosphere.

The stresses in the continental crust are shown in figure 7.13. The maximum principal stresses are vertical compressions which have the same magnitude as those in the elastic solution. The minimum principal stresses are horizontal compressions which are more tensional than those in the elastic model. This enhanced horizontal tension can be clearly seen in the deviatoric stresses (figure 7.14). The horizontal deviatoric tension at the right hand edge of the model has increased to a maximum of 38 MPa at 5-10 km depth. This increased horizontal deviatoric tension in the elastic lithosphere is produced by the stress amplification resulting from the creep of the ductile lower lithosphere (Kusznir and Bott, 1977). These results indicate that the stresses produced by the lateral density variation are renewable, and therefore, may contribute to the tensional stress which is observed in the back arc area of some active continental margin subduction zones.

The stress regime in the subducting plate (figure 7.12) differs considerably from the elastic solution. In the elastic lithosphere beneath the trench there are near surface horizontal tensions with complementary

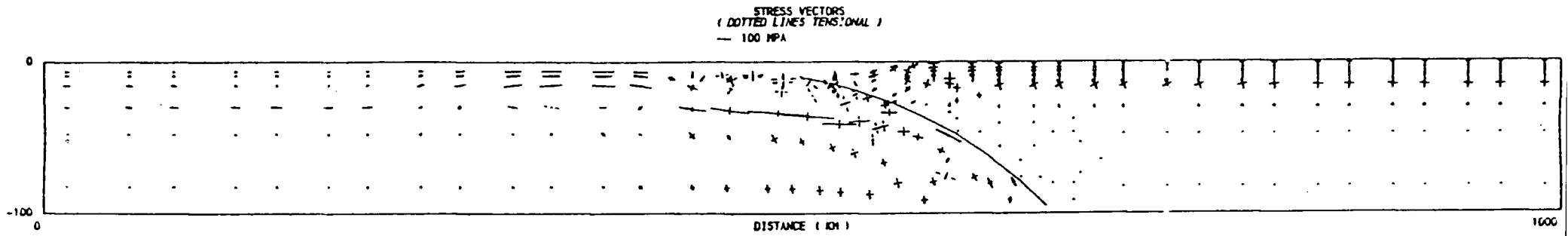

Figure 7.11: The principal stresses in the lateral density variation model after 5 million years of visco-elastic relaxation.

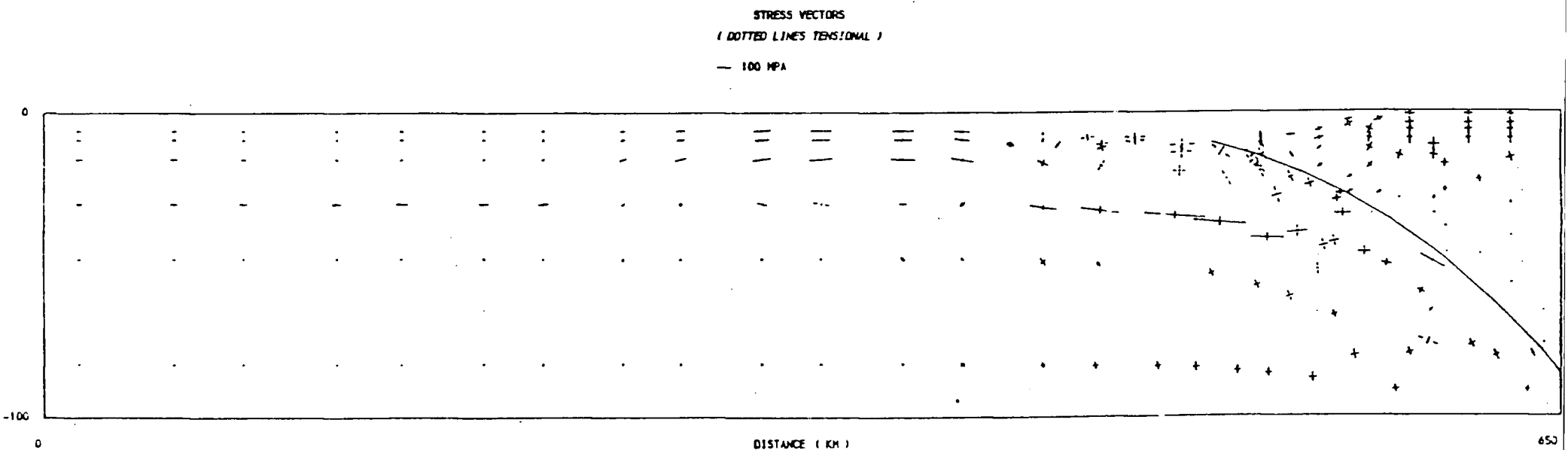

Figure 7.12: The principal stresses in the subducting plate in the lateral density variation model after 5 million years of visco-elastic relaxation.

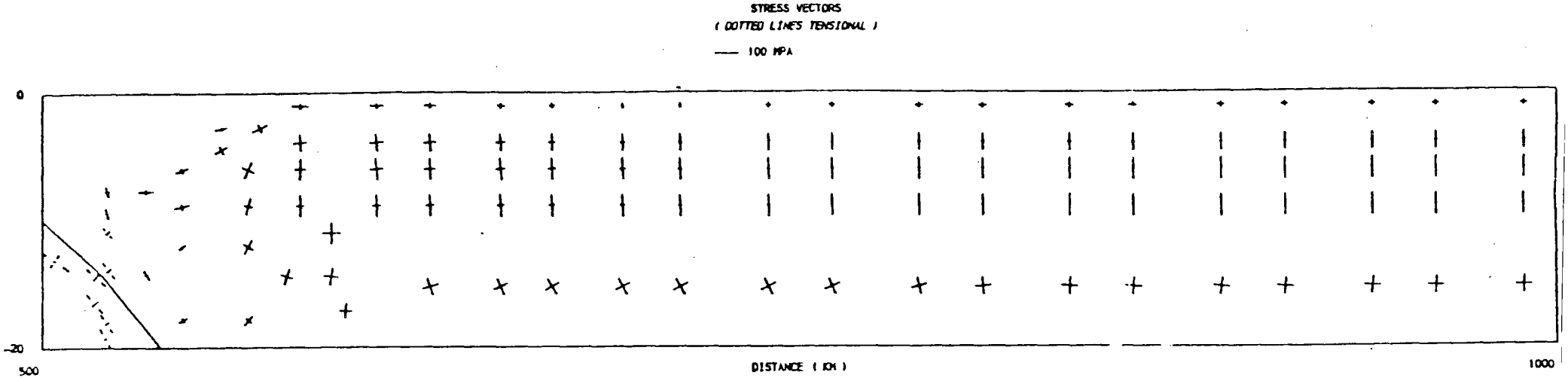

Figure 7.13: The principal stresses in the top 20 km of the overlying plate in the lateral density variation model after 5 million years of visco-elastic relaxation.

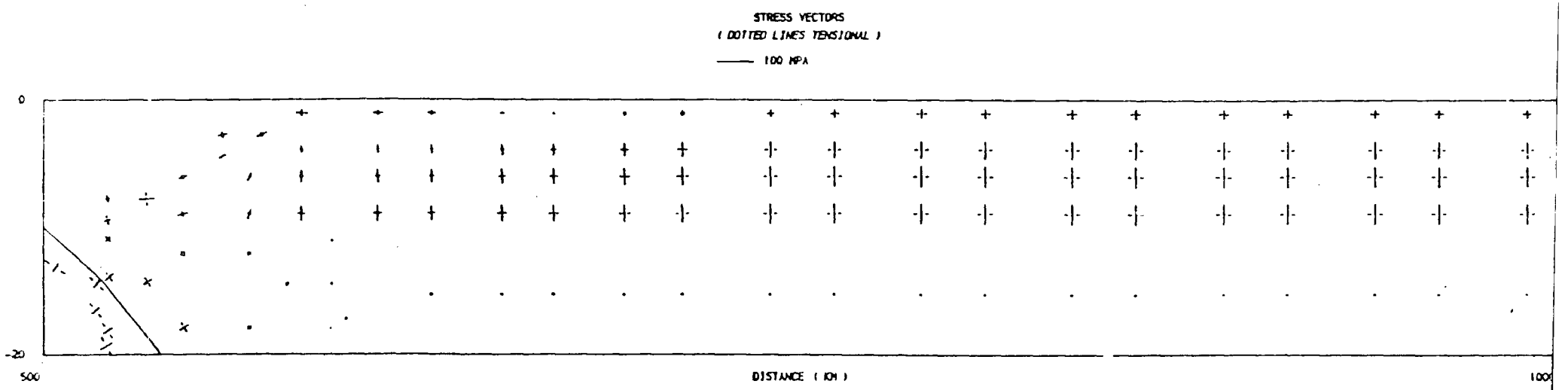

Figure 7.14: The deviatoric principal stresses in the top 20 km of the overlying plate in the lateral density variation model after 5 million years of visco-elastic relaxation.

horizontal compressions below. The opposite pattern is observed beneath the outer rise. This stress regime is the result of flexure of the lithosphere (figure 7.10), and is caused by the viscous flow of ductile material away from the high pressure region beneath the outer rise and into the low pressure region below the trench. This stress regime is the response of a static subducting oceanic lithosphere to the continuous application of the forces at the trench and outer rise over a period of 5 million years. This stress regime cannot exist in practise because the subducting plate is not static for such long periods of time. The stress regime in the subducting plate in a visco-elastic solution is therefore unrealistic because the static finite element methods which have been used in this thesis cannot model the true dynamic nature of the subduction process. It was not, however, possible to develop a dynamic finite element model to study this behaviour in the time available to complete this thesis.

7.3.3 Further considerations: Other lateral density variations at subduction zones

The models in this section have analysed the stress regime which is produced by the two most obvious lateral density variations at subduction zones. There are, however, several other lateral density variations which affect subduction zones. It was not possible to model these in the time available to complete this thesis, and therefore, the aim of this section is to state the origin of these lateral density variations and speculate on their effect upon the stress regime at subduction zones.

The first, and probably most important of these lateral density variations, affects the back arc area of the overlying plate at subduction zones. In these regions slab induced convection causes surface loading

which is isostatically compensated by a hot, low density region in the underlying lithosphere. This load would be expected to produce horizontal deviatoric tensions which would be amplified in a way analogous to those in regions of plateau uplift (Bott and Kusznir, 1979). Since these stresses are renewable this loading is potentially important in producing the observed tensional stresses in back arc regions.

The second lateral density variation affects the crust beneath the volcanic arc. In this region the short wavelength surface load of the volcanic arc is compensated by an underlying, hot low density region. The effect of this load would be to produce horizontal deviatoric tensions in the crust beneath the volcanic edifice (Bott, 1971). This load could therefore be important in locally modifying the regional stress regime, and consequently, it may be an important factor in explaining the observation that tensional failure occurs at the volcanic arc during the initiation of back arc spreading.

The third lateral density variation which has been neglected affects the back arc area of the overlying plate at active continental margins. This is produced by the surface loading of a cordilleran mountain range and the upthrust of the low density root which compensates the load. The effect of this loading would be to produce additional horizontal deviatoric tensions in the crust beneath the mountain range, and these would be superimposed upon the stresses which have been modelled in this section.

7.3.4 Limitations of the models

There are several limitations of the models which have been developed. These are:

1. The models have used the density stripping approach rather than the full lithospheric densities. The major limitation of this approach is that it neglects the contrast in the elastic properties between the horizontal layers which are stripped (Park, 1981). This limitation, however, is unlikely to have a major influence upon the results which have been obtained.

2. The deformation arising from the lateral density variations at island arc subduction zones has not been modelled. The results which have been obtained in this section, however, are applicable to island arcs. This is because although the overlying plate in these regions is mainly oceanic there is an isostatically compensated crustal load in the vicinity of the volcanic arc. This load would be expected to induce horizontal deviatoric tensions in the island arc crust. These tensions, however, would not extend into the oceanic lithosphere of the back arc plate at island arc subduction zones.

3. The base of the model has been constrained by the zero vertical displacement boundary condition. The vertical component of the load applied at the upper surface of the trench-outer rise has therefore been implicity balanced by equivalent vertical boundary forces distributed along the base of this region. At subduction zones, however, it would be expected that the loads at the top surface of the subducting plate would be balanced by a more localised system of vertical forces arising from slab pull. The zero vertical displacement boundary condition therefore does not correctly model the force distribution arising from the vertical component of the slab pull force and it also inhibits bending.

4. A further limitation of the models is that they predict that horizontal deviatoric tension is present throughout the crust of the overlying plate. This is incompatible with the observed stress regime at many subduction zones and suggests that other forces act on the overlying plate.

The limitations discussed in points 3 and 4 can be mainly overcome by introducing a slab pull force to the base of the model This situation is considered in the next section.

7.4 Slab Pull

The subducting oceanic plate has a large negative buoyancy because it is cooler, and consequently denser, than the surrounding mantle and also because phase transitions to denser mineralogies are elevated in the subducting plate (McKenzie, 1969; Turcotte and Oxburgh, 1969; Minear and Toksoz, 1970a,b; Hasebe et al, 1970; Toksoz et al, 1971, 1973; Turcotte and Schubert, 1971, 1973; Griggs, 1972; Schubert et al, 1975). The possibility that a component of this negative buoyancy force is transmitted along the subducting oceanic lithosphere to drive the horizontal motions of the surface plates was suggested by Elsasser (1969). Since then various independent approaches have demonstrated the importance of this force, known as slab pull, in driving the observed plate motions (Forsyth and Uyeda, 1975; Harper, 1975; Chapple and Tullis, 1977; Richardson et al, 1979). All of these studies have demonstrated that only a fraction of the gravitational potential of the dense subducting plate is transmitted to drive the motions of the surface plates, and therefore that a substantial part of the negative buoyancy force must be balanced by resisting forces. The resisting forces arise from friction at the interplate shear zone and

from viscous drag at the contact of the subducting lithosphere with the asthenosphere (Davies, 1980). The net slab pull force which is transmitted to drive the surface plate motions is therefore estimated to be of a similar magnitude to the ridge push force (Davies, 1983).

Despite the demonstration that the slab pull force is important in driving plate motions, there have been no direct attempts to model the stress regime which this force produces in the near surface plates at a subduction zone. This is because the aim of most previous models of the slab pull force has been to analyse the stress at deep and intermediate depths in the subducting plate (Smith and Toksoz, 1972; Neugebauer and Brietmayer, 1975).

The aim of this section is therefore to model the stress regime which is produced by the slab pull force in the upper 95 km of the plates at a subduction zone.

7.4.1 Description of the finite element model

The finite element model is described in section 7.2. The left and right hand sides of this model were constrained to move vertically. The base of the model is assumed to be underlain by a fluid asthenosphere with a density of 3300 kg m^{-3} It is necessary to introduce this boundary condition so that the slab pull force can be applied to the nodes at the base of the model. The subduction zone fault was 'locked' by assigning values of 1.0×10^{15} N m^{-1} to its normal and shear stiffnesses.

The stripped density distribution (section 7.3.1) was applied to this model to simulate the loads which are produced by the lateral density variations at a subduction zone. Applying these forces to a model with the base underlain by a fluid has two effects. Firstly, the vertical forces

applied to the continental lithosphere are balanced. This is because the surface load acts downwards and is balanced by the equal upthrust from the low density 'root' which compensates this region. Secondly, the vertical forces which are applied at the trench-outer rise are unbalanced. The unbalanced vertical component of this force has a magnitude of 8.95×10^{12} N and is directed upwards.

Because the vertical forces acting at a subduction zone would be expected to be balanced, the vertical component of the slab pull force was assigned a magnitude of 8.95×10^{12} N and directed downwards so that it balances the forces arising from the isostatically uncompensated load at the trench and outer rise. This force therefore represents the effective vertical component of the slab pull force which is transmitted to the subducting plate and which holds the trench out of isostatic equilibrium.

The slab pull force can be resolved into vertical and horizontal components. The vertical component of the slab pull force, F_y, has been simulated in the models by applying appropriate normal forces to the nodes at location A-A in figure 7.2, as they represent the position where the subducted plate has been truncated by the finite element mesh. Applying this force to these nodes produces a vertical component of stress which is equal to 51.05 MPa.

The horizontal component of the slab pull force, F_x, has been modelled by applying an appropriate shear stress to the nodes along the base. The vertical component of the slab pull force was maintained at the same magnitude in these models to ensure that the vertical forces at the subduction zone are balanced. Thus

$$\frac{F_y}{F_x} = \tan I$$

where I is the dip of the slab pull force.

7.4.2 The stress regime produced by a vertical slab pull force

In this section the deformation produced by the vertical component of the slab pull force, together with the lateral density variation (section 7.3), is modelled. The elastic solution is shown in figure 7.15. There are two superimposed stress regimes which can be identified in this model. The first affects the lithosphere in the vicinity of the trench and the second affects the crust of the overlying plate.

The most obvious stress system in the model affects the subducting plate beneath the trench and the overlying plate above the base of the subduction zone fault. In the subducting plate (figure 7.16) there are near surface horizontal tensions with complementary horizontal compressions at the base of the lithosphere. The opposite pattern is observed above the base of the subduction zone fault. These horizontal stresses have a maximum magnitude of 110 MPa and are produced because the lithosphere has been flexed upwards at 75 km seawards of the trench axis and has been flexed downwards above the base of the subduction zone fault. This flexure, which can be observed in the nodal displacements of the model (figure 7.19), arises from the bending moment which is produced by the system of boundary and body forces which act at the outer rise, trench and the base of the subducting plate.

The second stress system is produced by the isostatically compensated surface loading of the continental crust (figure 7.17). This effect is similar to that which has been discussed in section 7.3 but it has been modified because of the superimposed bending stresses. The horizontal deviatoric tensions can therefore only be seen clearly at the right hand

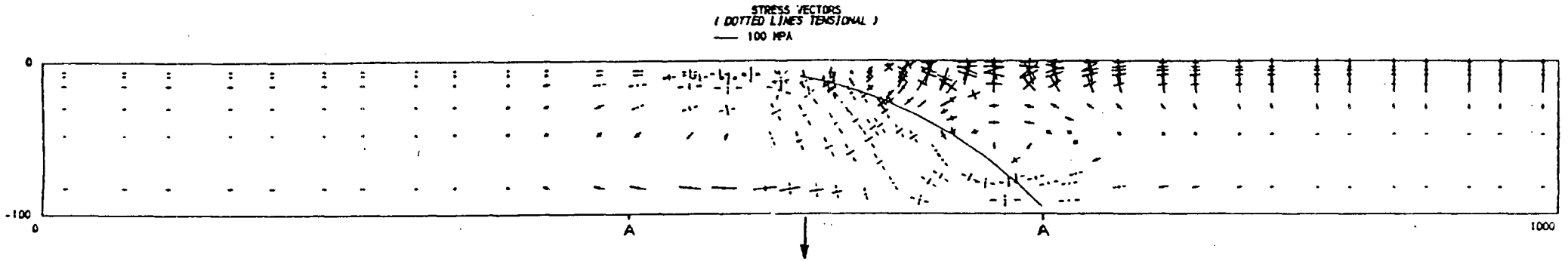

Figure 7.15: The elastic principal stresses in the 90 degree slab pull model. The orientation of the slab pull force is indicated by the arrow and acts over the distance A-A.

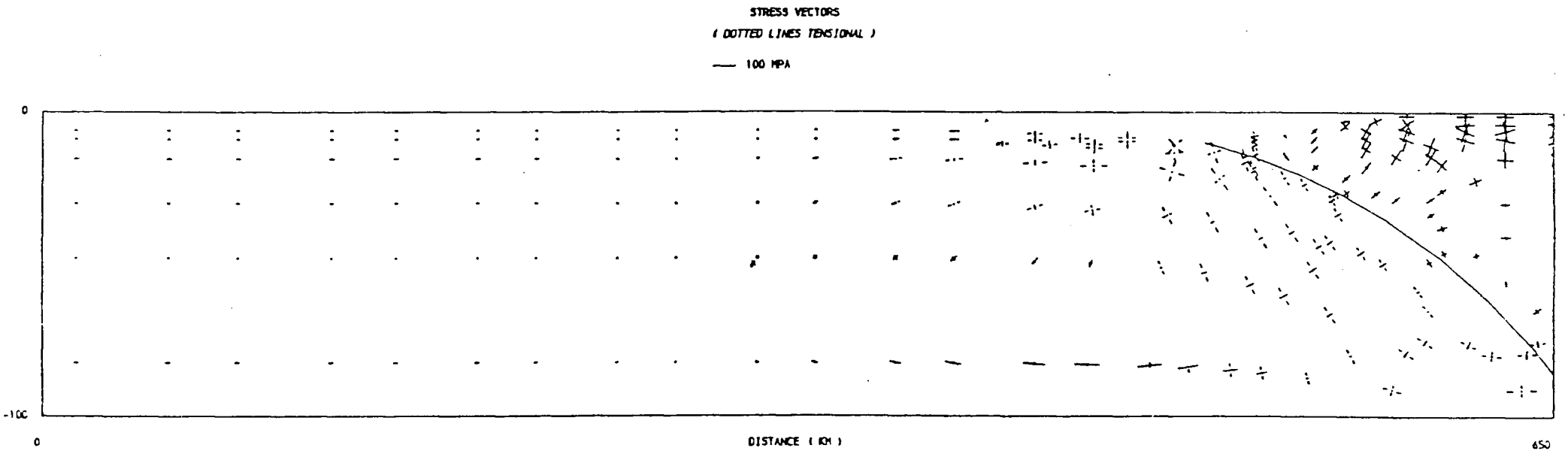

Figure 7.16: The elastic principal stresses in the subducting plate in the 90 degree slab pull model.

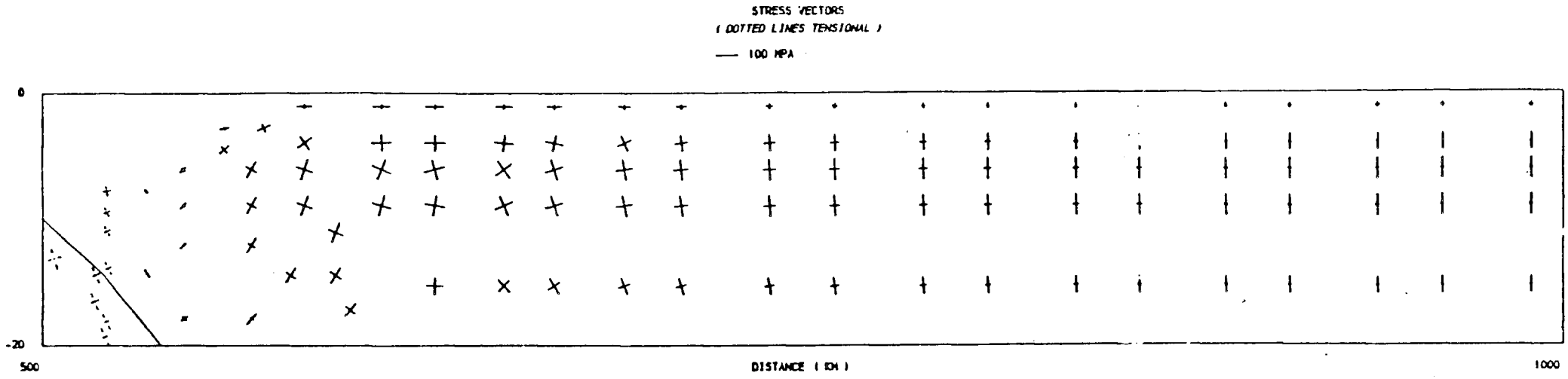

Figure 7.17: The elastic principal stresses in the top 20 km of the overlying plate in the 90 degree slab pull model.

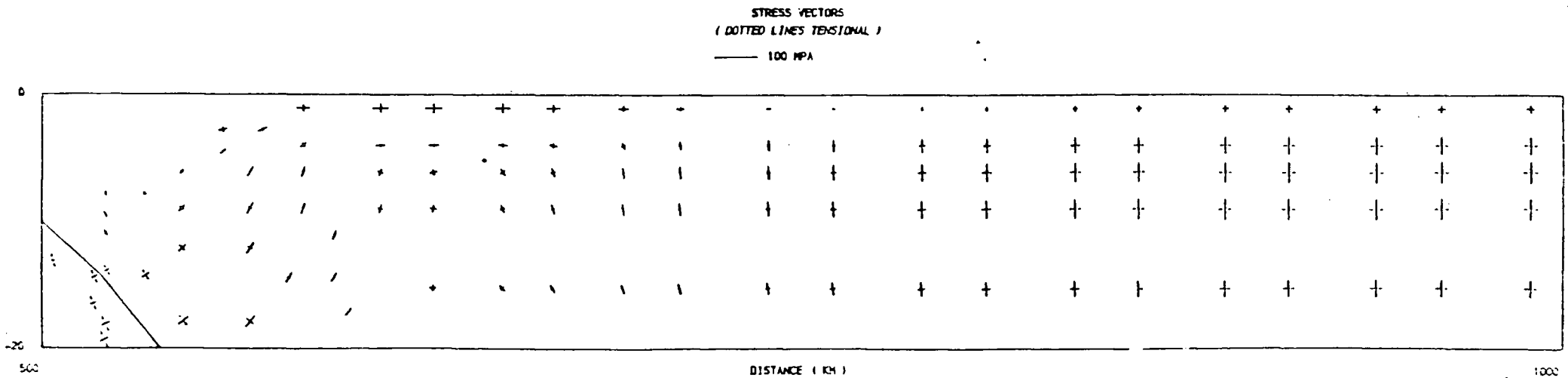

Figure 7.18: The elastic deviatoric principal stresses in the top 20 km of the overlying plate in the 90 degree slab pull model.

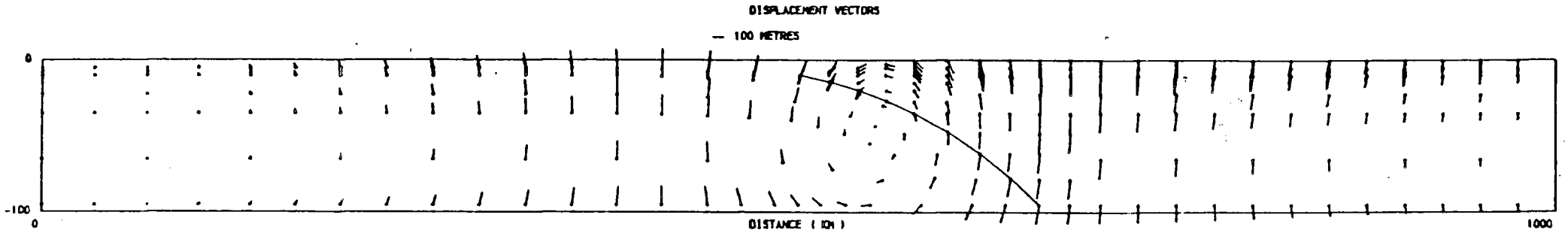

Figure 7.19: The elastic displacements of the 90 degree slab pull model.

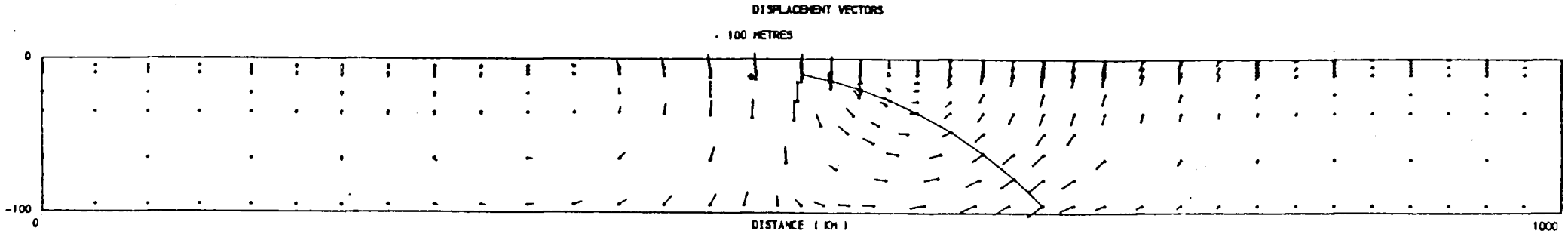

Figure 7.20: The displacements of the 90 degree slab pull model after 5 million years of visco-elastic relaxation.

edge of the model where the bending stresses are small (figure 7.18). At this position the maximum horizontal deviatoric tension is 31.5 MPa at 5-10 km depth. This tension is about 10 MPa larger than those in the density stripping model (section 7.3) because it has been superimposed upon the bending stresses produced by the downwards flexure of this end of the model.

The stress regime after running this model visco-elastically for 5 million years is shown in figure 7.21. The stresses in the overlying plate have been concentrated in the elastic lithosphere with the result that large horizontal deviatoric compressions occur above the base of the subduction zone fault and gradually become horizontal deviatoric tensions in the back arc region (figure 7.21). The stress distribution in the overlying plate is therefore similar to the previous elastic solution and the major difference is that the magnitude of the horizontal stress has been increased by the effect of stress amplification. The stresses in the subducting plate (figure 7.22), however, are considerably different to those which were observed in the elastic solution. The stresses are dominated by a downwards flexure of the lithosphere at the outer rise and an upwards flexure at the trench axis (figure 7.20). This effect, which has been previously described in a visco-elastic run of the density stripped model (section 7.3.2), probably arises because the dynamic motion of the subducting plate has not been taken into account.

It has been shown in this section that the introduction of a vertical slab pull force gives a stress pattern which comes closer to agreement with the observed state of stress at subduction zones. A more realistic situation will be considered in the next section by introducing a dipping slab pull force.

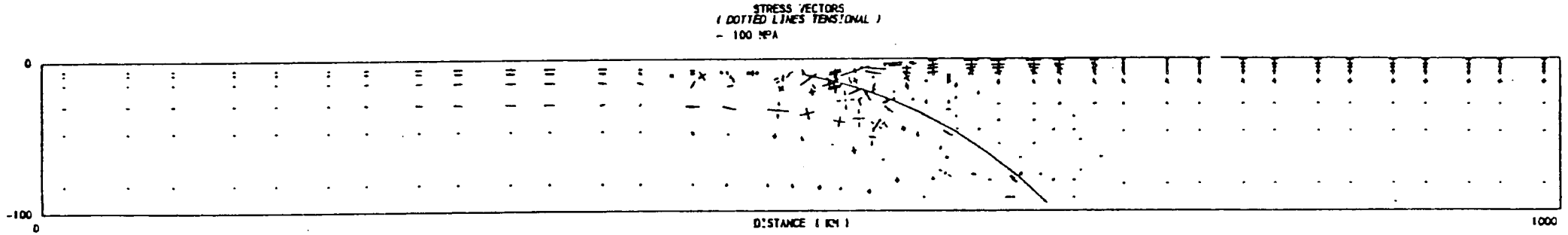

Figure 7.21: The principal stresses in the 90 degree slab pull model after 5 million years of visco-elastic relaxation.

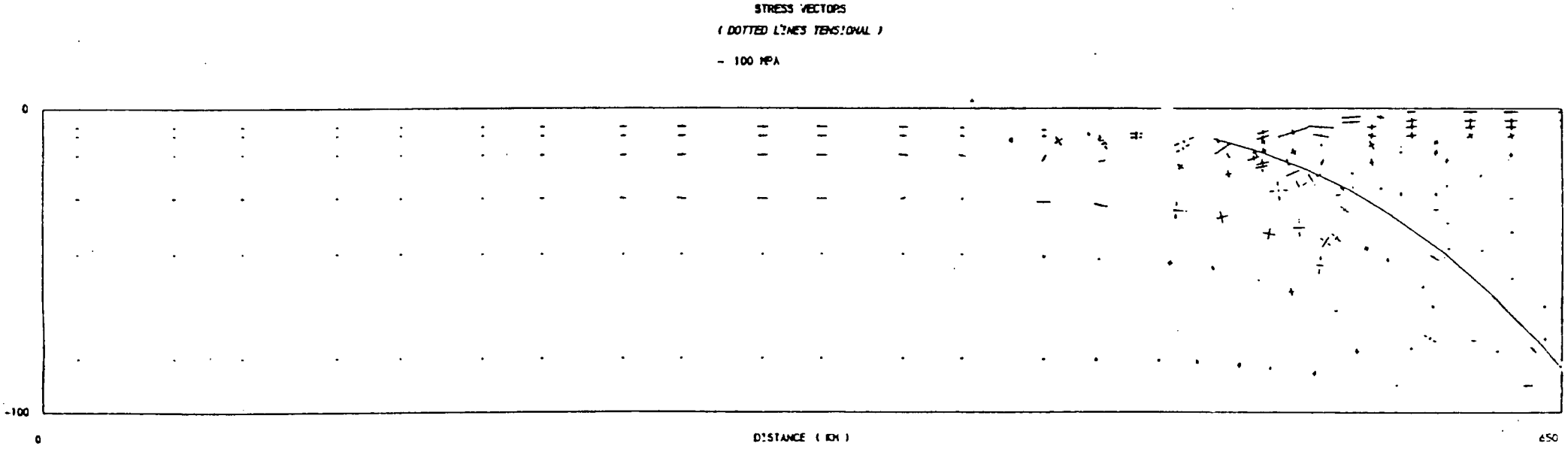

Figure 7.22: The principal stresses in the subducting plate in the 90 degree slab pull model after 5 million years of visco-elastic relaxation.

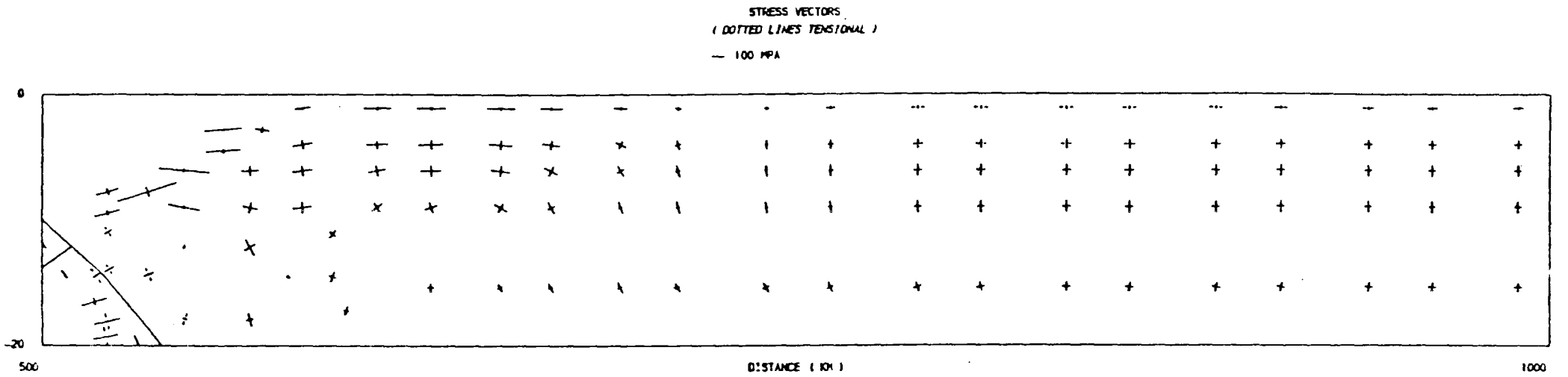

Figure 7.23: The principal stresses in the top 20 km of the overlying plate in the 90 degree slab pull model after 5 million years of visco-elastic relaxation.

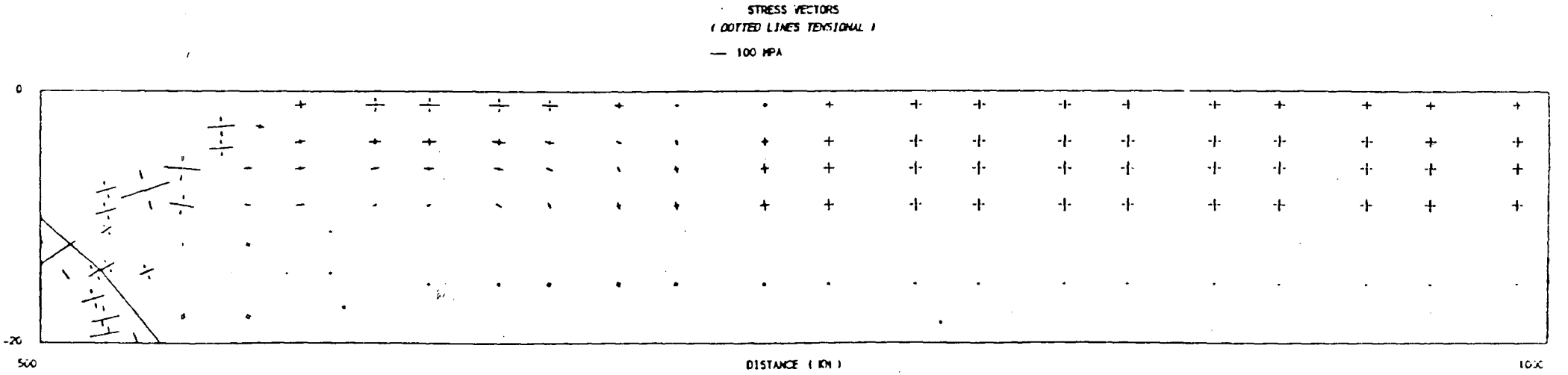

Figure 7.24: The deviatoric principal stresses in the top 20 km of the overlying plate in the 90 degree slab pull model after 5 million years of visco-elastic relaxation.

7.4.3 Effect of a dipping slab pull force

The effect of decreasing the dip of the slab pull force from 90 degrees to 63, 45 and 26 degrees towards the overlying plate is shown in figures 7.25 to 7.53. The only differences between these models and those of the previous section is that a shear component has been added to the vertical slab pull force. The stresses produced by this shear component will therefore be superimposed upon the stresses which have been described in the previous section.

The following generalisations can be made from a study of these results:

1. The effect of introducing a dipping component to the slab pull force is to produce a regional horizontal tension in the subducting plate and a regional horizontal compression of a similar magnitude in the overlying plate. This stress regime arises because the shear component of the slab pull force has the effect of displacing the centre of the model towards the overlying plate.

2. The effect of decreasing the dip of the slab pull force from 63 to 26 degrees is to increase the magnitude of the regional horizontal tensions and compressions which are developed in the subducting and overlying plates by 115 MPa. This stress regime is produced because decreasing the dip of the slab pull force increases the displacement of the centre of the model towards the overlying plate. This increase in displacement arises because the magnitude of the shear component of the slab pull force increases as the dip of the slab is decreased.

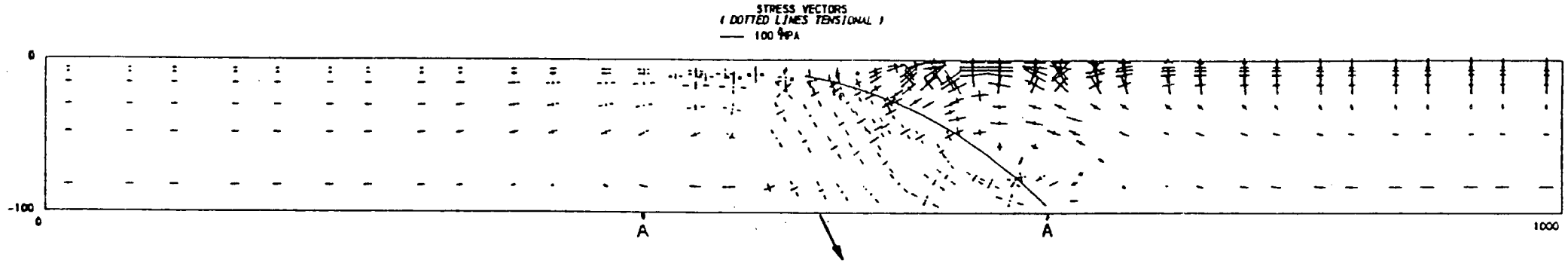

Figure 7.25: The elastic principal stresses in the 63 degree slab pull model. The orientation of the slab pull force is indicated by the arrow and acts over the distance A-A.

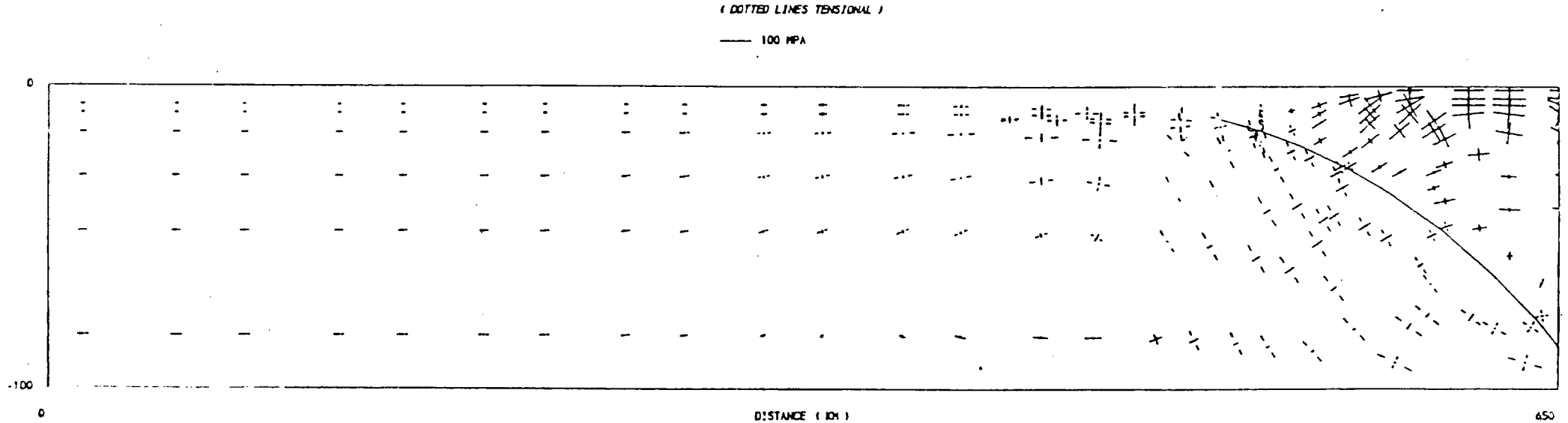

Figure 7.26: The elastic principal stresses in the subducting plate in the 63 degree slab pull model.

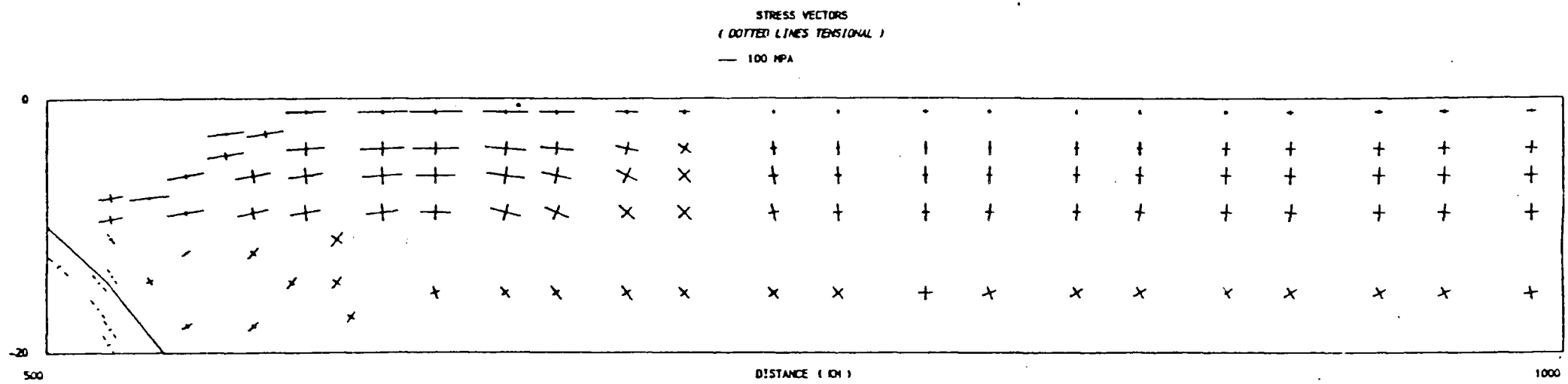

Figure 7.27: The elastic principal stresses in the top 20 km of the overlying plate in the 63 degree slab pull model.

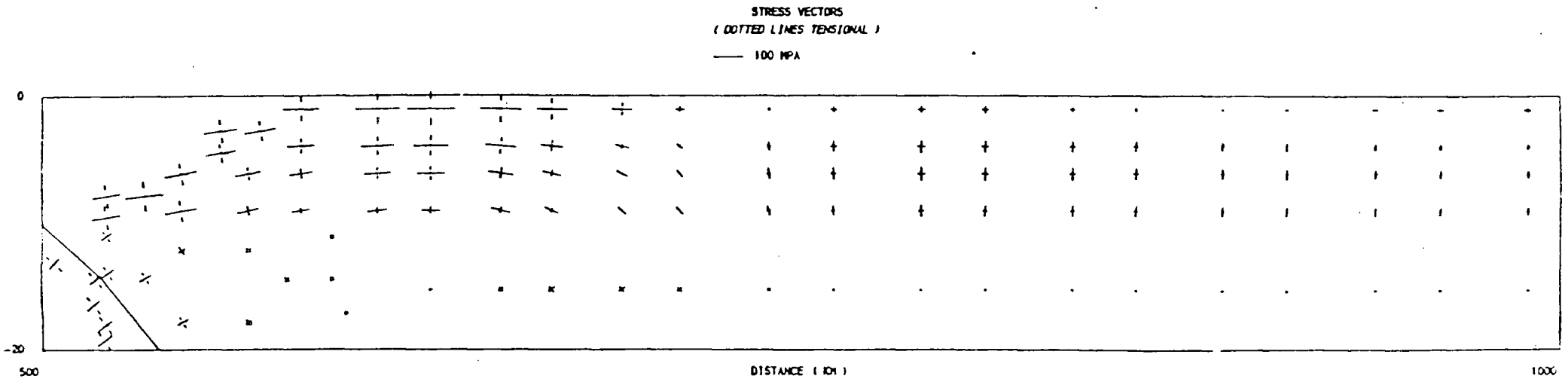

Figure 7.28: The elastic deviatoric principal stresses in the top 20 km of the overlying plate in the 63 degree slab pull model.

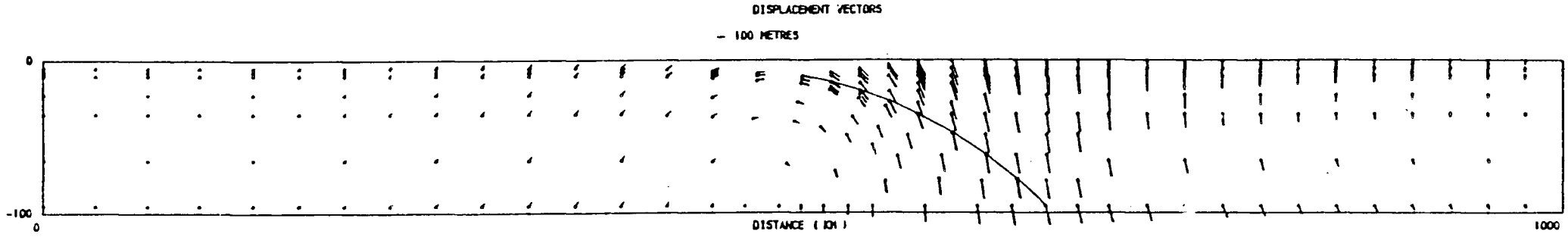

Figure 7.29: The elastic displacements of the 63 degree slab pull mod l.

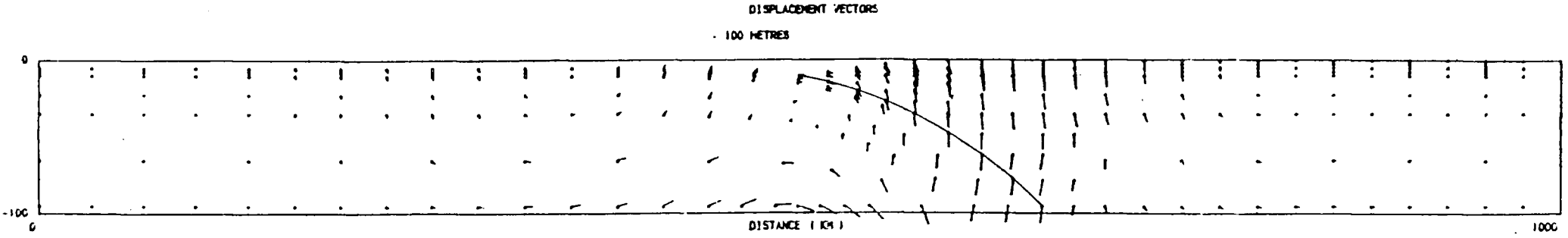

Figure 7.30: The displacements of the 63 degree slab pull model after 5 million years of visco-elastic relaxation.

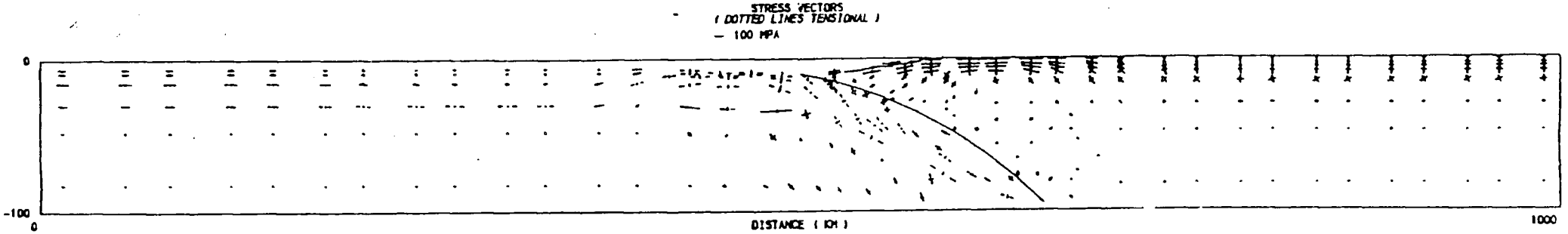

Figure 7.31: The principal stresses in the 63 degree slab pull model after 5 million years of visco-elastic relaxation.

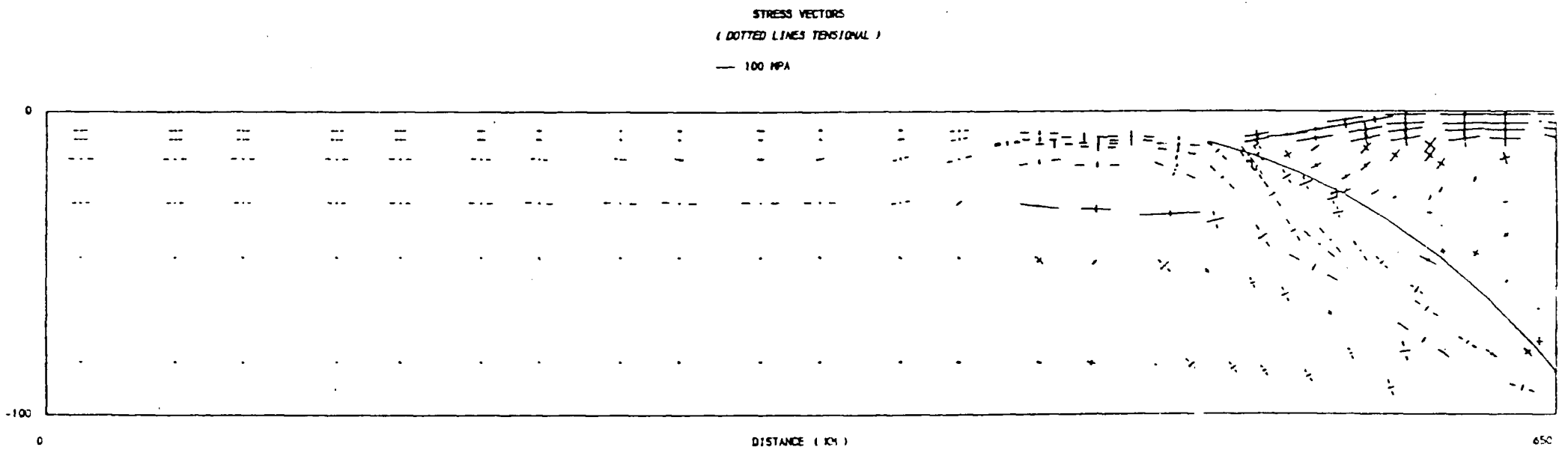

Figure 7.32: The principal stresses in the subducting plate in the 63 degree slab pull model after 5 million years of visco-elastic relaxation.

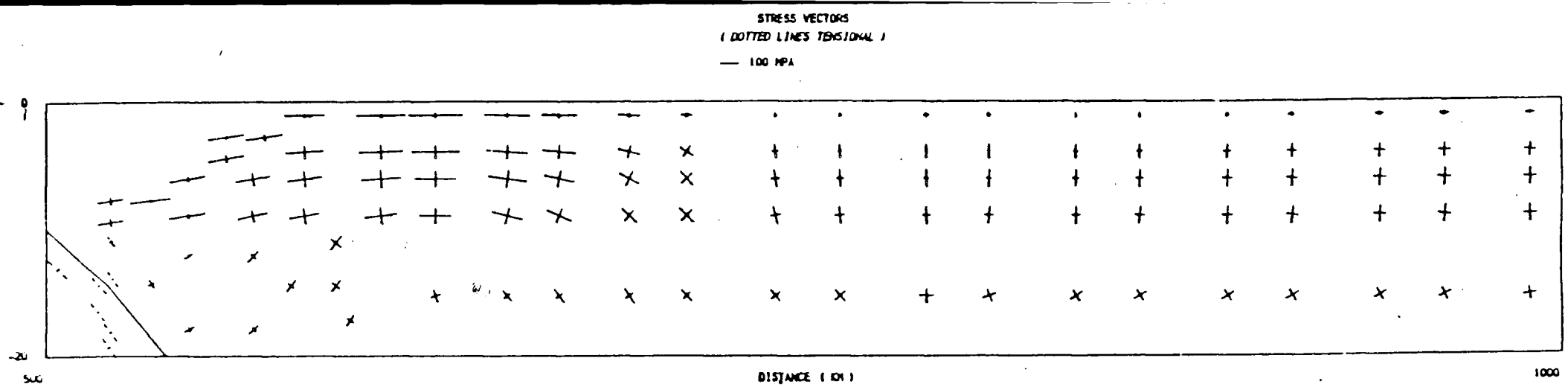

Figure 7.33: The principal stresses in the top 20 km of the overlying plate in the 63 degree slab pull model after 5 million years of visco-elastic relaxation.

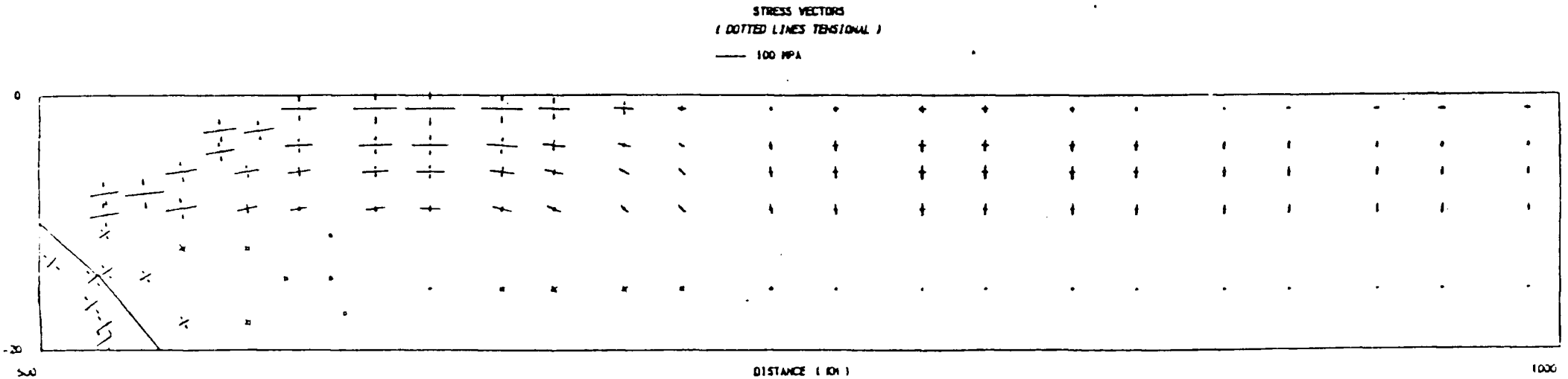

Figure 7.34: The deviatoric principal stresses in the top 20 km o the overlying plate in the 63 degree slab pull model after 5 million years of visco-elastic relaxation.

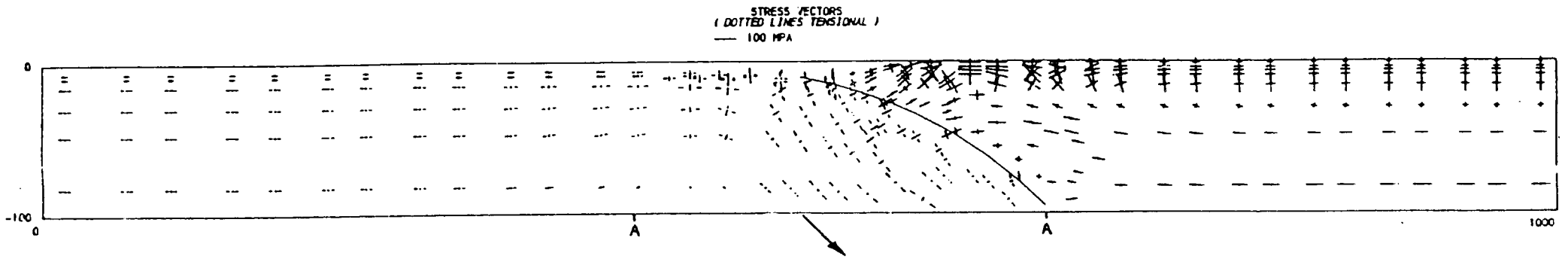

Figure 7.35: The elastic principal stresses in the 45 degree slab pull model. The orientation of the slab pull force is indicated by the arrow and acts over the distance A-A.

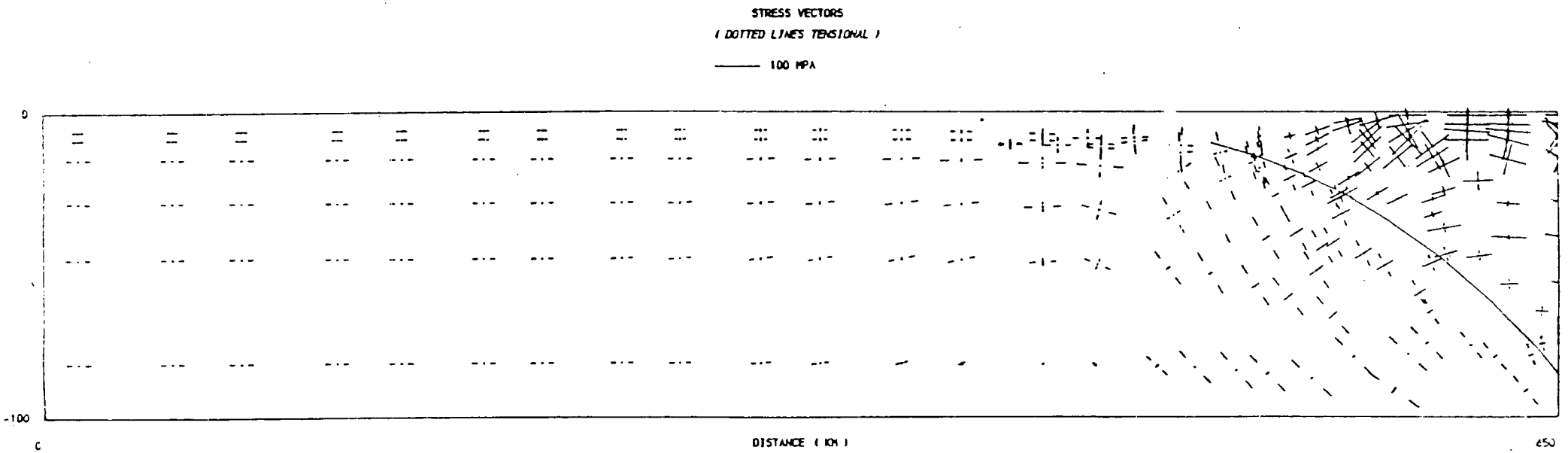

Figure 7.36: The elastic principal stresses in the subducting plate in the 45 degree slab pull model.

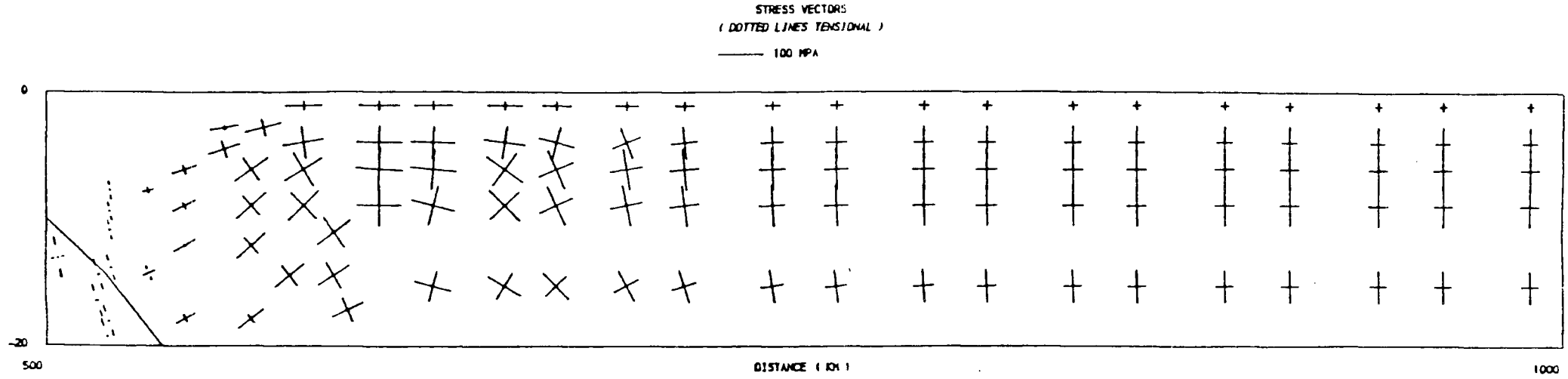

Figure 7.37: The elastic principal stresses in the top 20 km of the overlying plate in the 45 degree slab pull model.

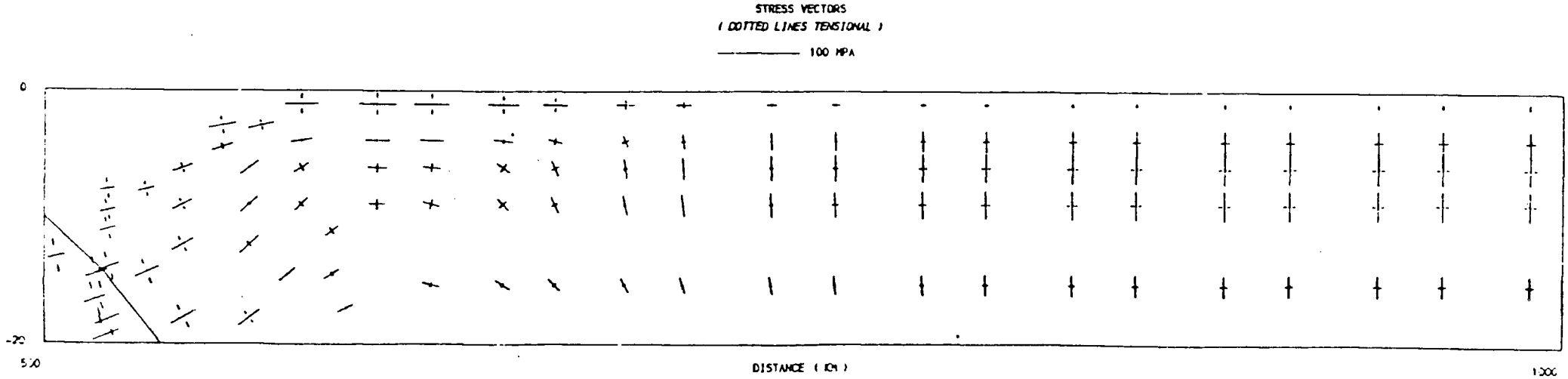

Figure 7.38: The elastic deviatoric principal stresses in the top 20 km of the overlying plate in the 45 degree slab pull model.

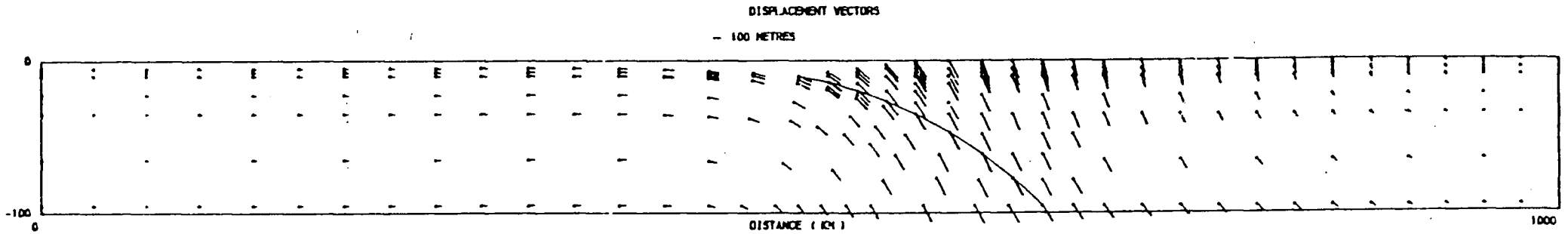

Figure 7.39: The elastic displacements of the 45 degree slab pull model.

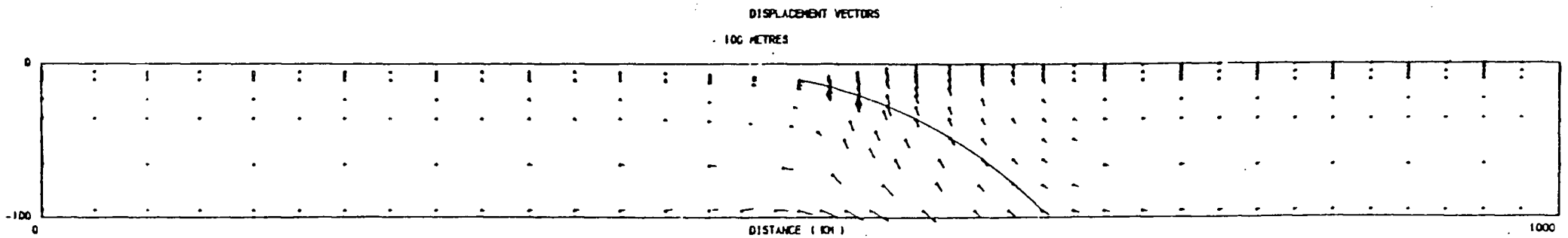

Figure 7.40: The displacements of the 45 degree slab pull model after 5 million years of visco-elastic relaxation.

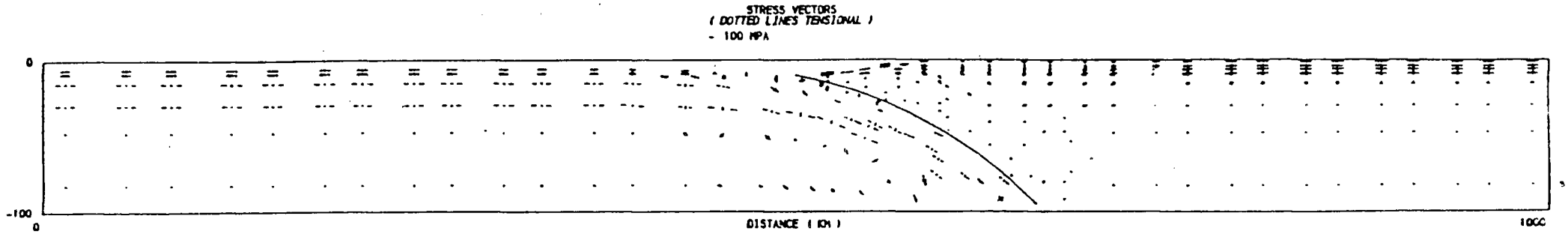

Figure 7.41: The principal stresses in the 45 degree slab pull model after 5 million years of visco-elastic relaxation.

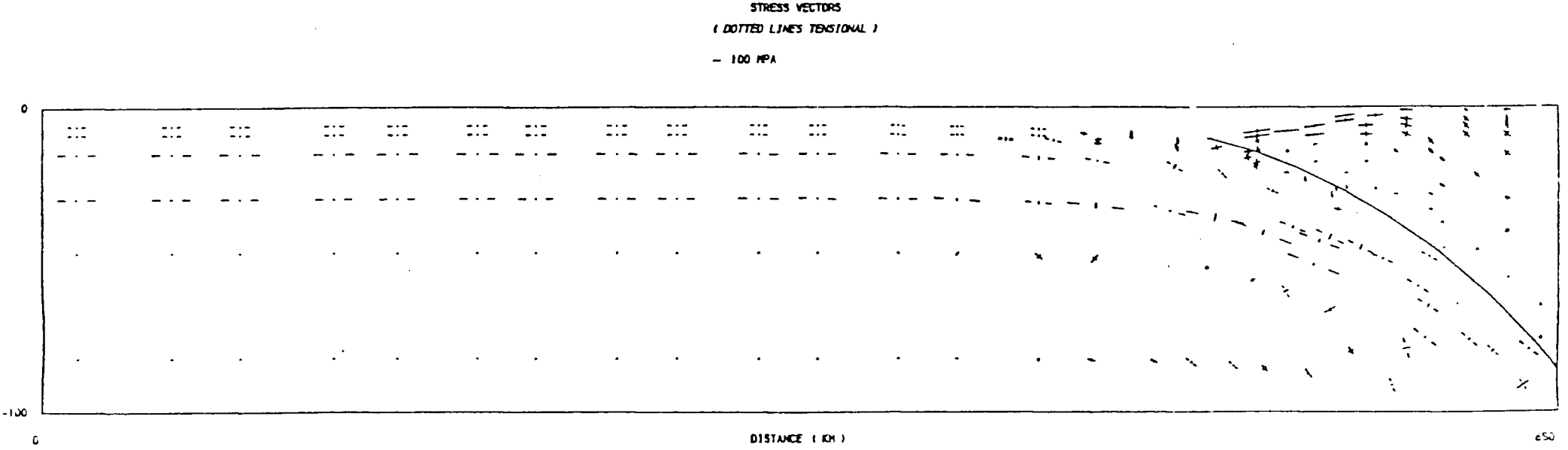

Figure 7.42: The principal stresses in the subducting plate in the 45 degree slab pull model after 5 million years of visco-elastic relaxation.

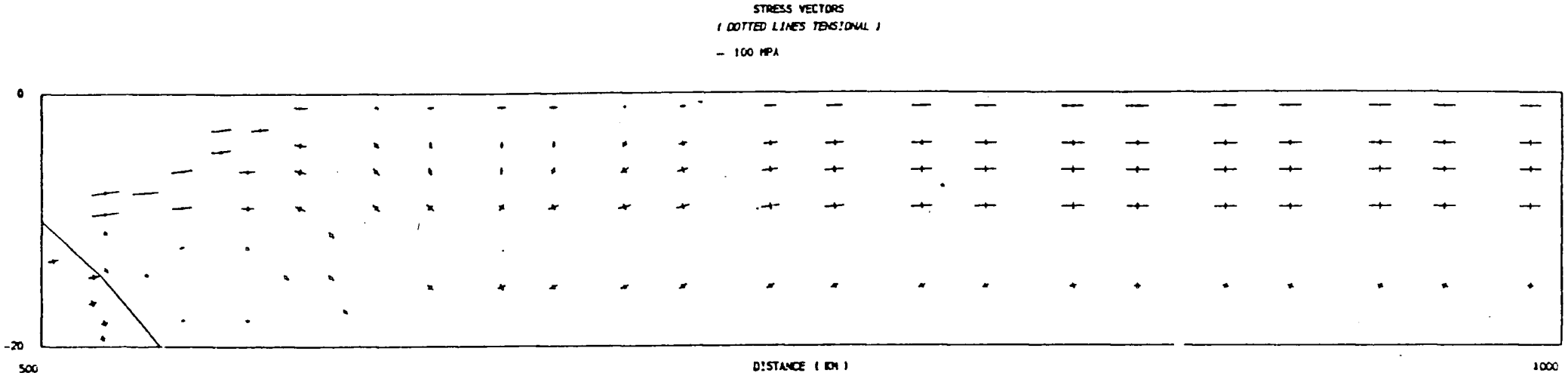

Figure 7.43: The principal stresses in the top 20 km of the overlying plate in the 45 degree slab pull model after 5 million years of visco-elastic relaxation.

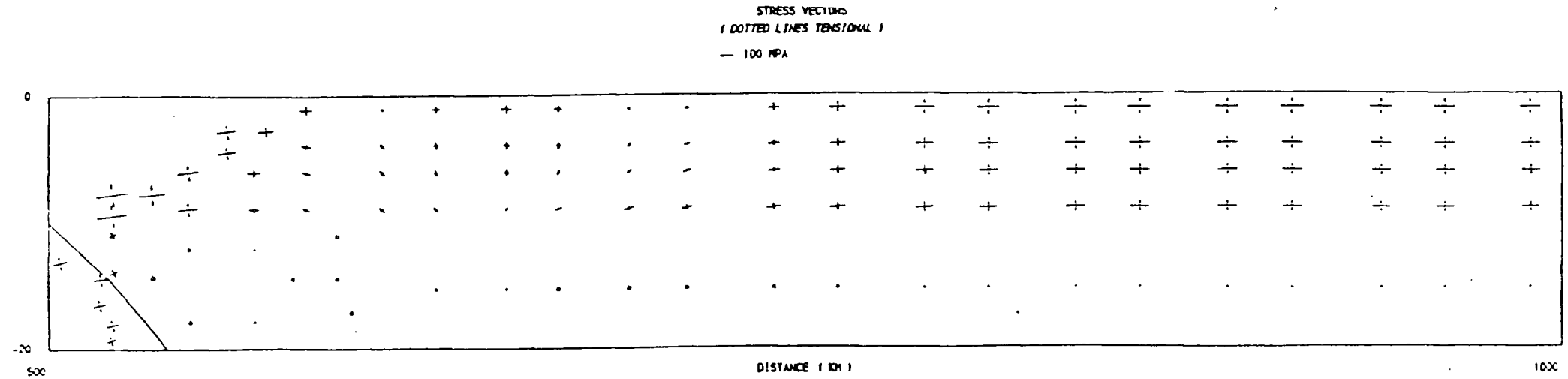

Figure 7.44: The deviatoric principal stresses in the top 20 km of the overlying plate in the 45 degree slab pull model after 5 million years of visco-elastic relaxation.

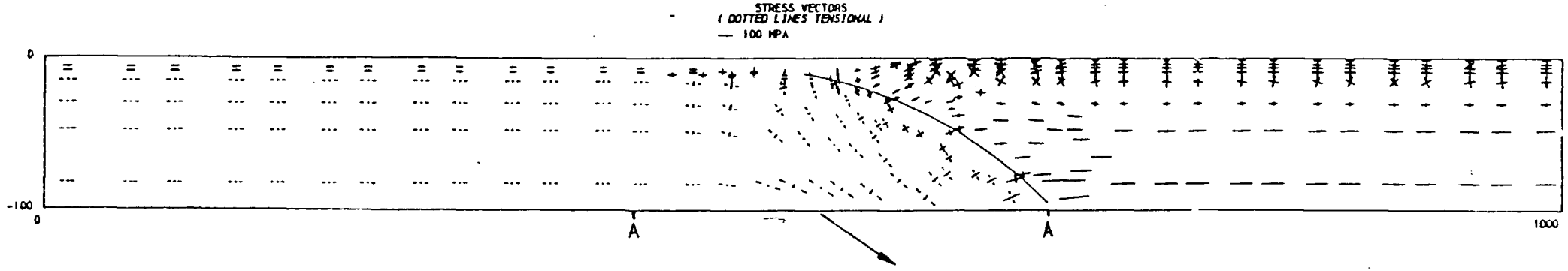

Figure 7.45: The elastic principal stresses in the 26 degree slab pull model. The orientation of the slab pull force is indicated by the arrow and acts over the distance A-A.

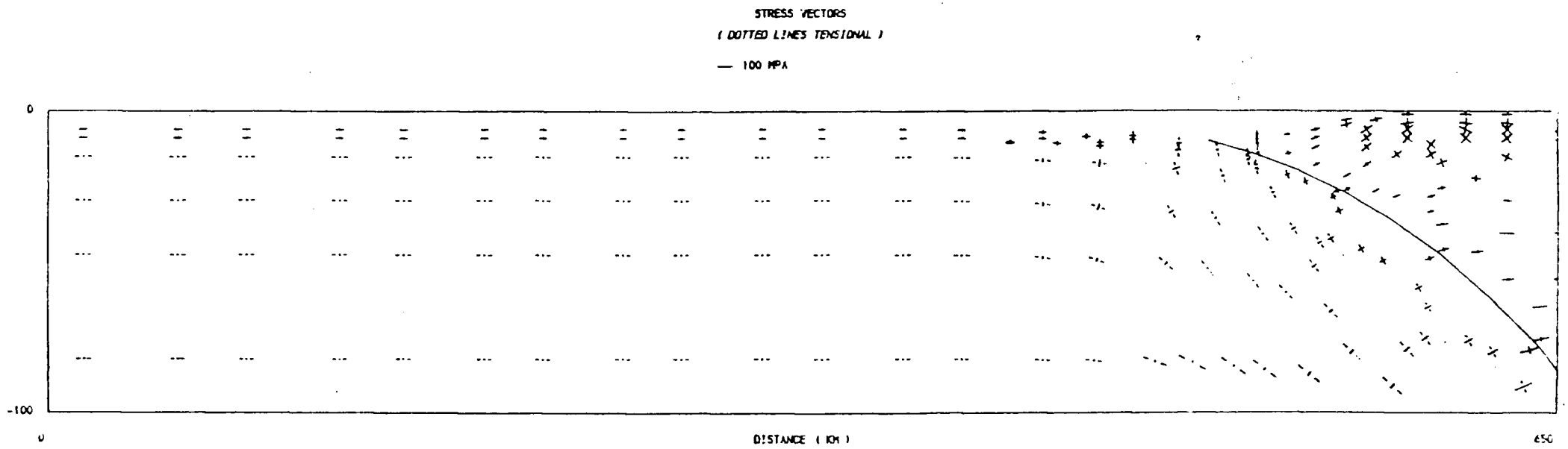

Figure 7.46: The elastic principal stresses in the subducting plate in the 26 degree slab pull model.

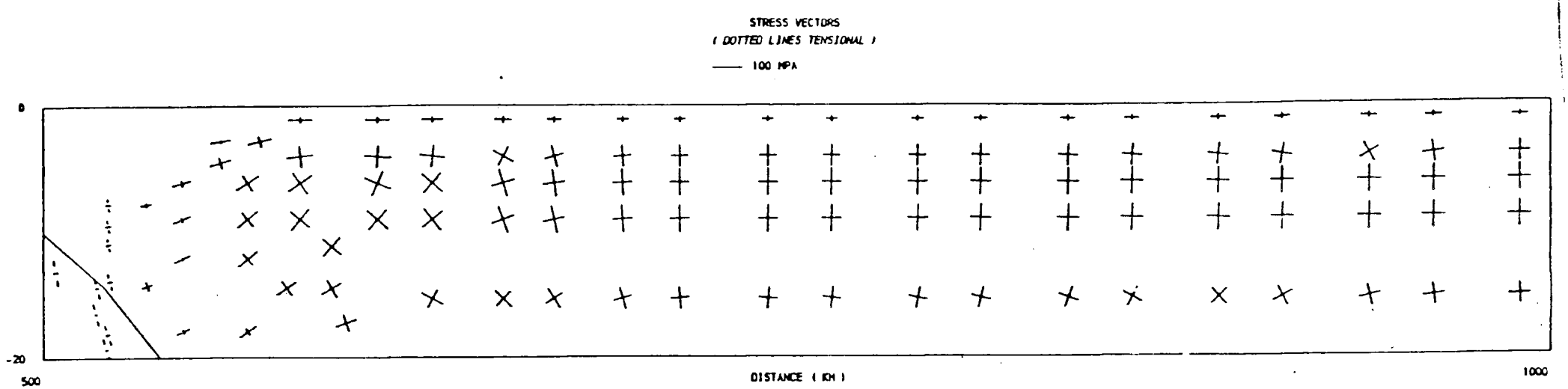

Figure 7.47: The elastic principal stresses in the top 20 km of the overlying plate in the 26 degree slab pull model.

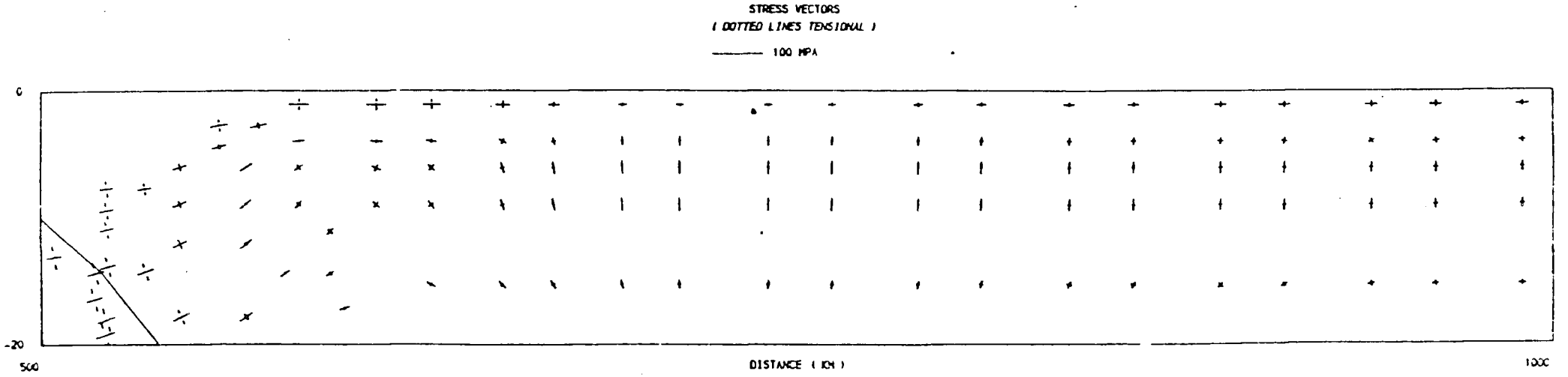

Figure 7.48: The elastic deviatoric principal stresses in the top 20 km of the overlying plate in the 26 degree slab pull model.

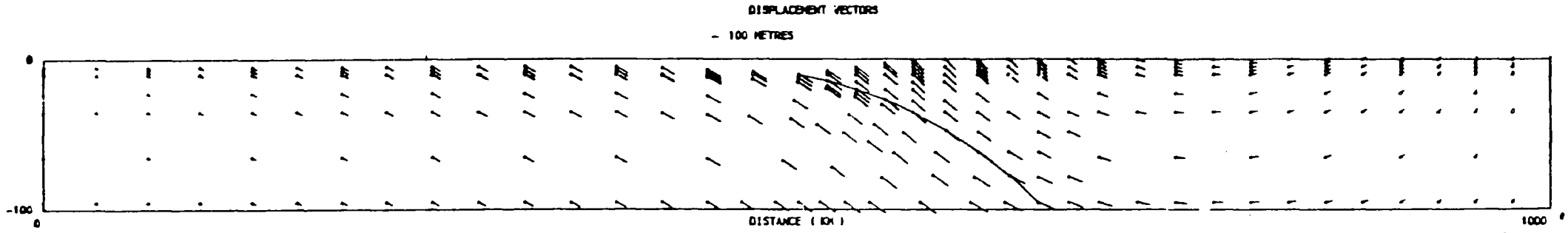

Figure 7.49: The elastic displacements of the 26 degree slab pull model.

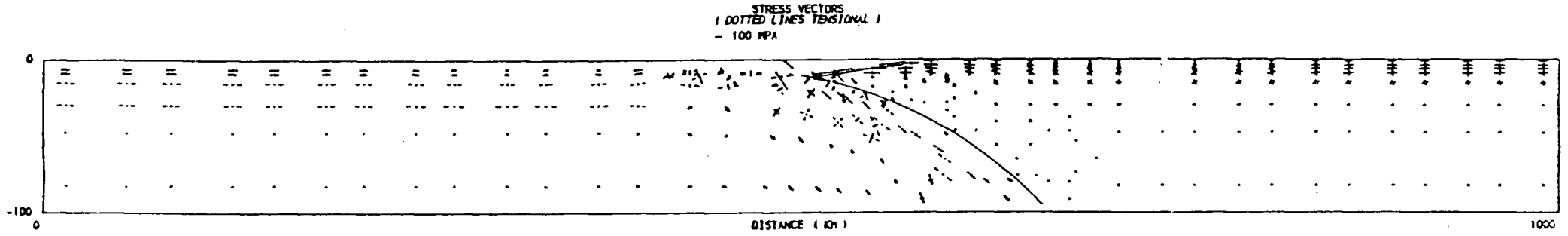

Figure 7.50: The principal stresses in the 26 degree slab pull model after 5 million years of visco-elastic relaxation.

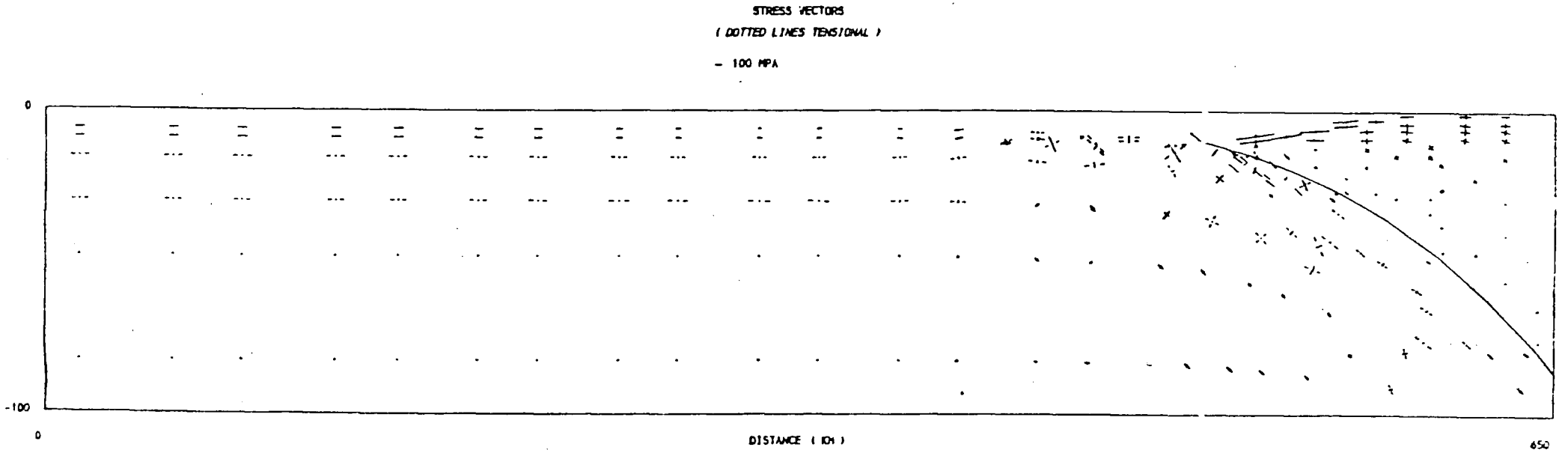

Figure 7.51: The principal stresses in the subducting plate in the 26 degree slab pull model after 5 million years of visco-elastic relaxation.

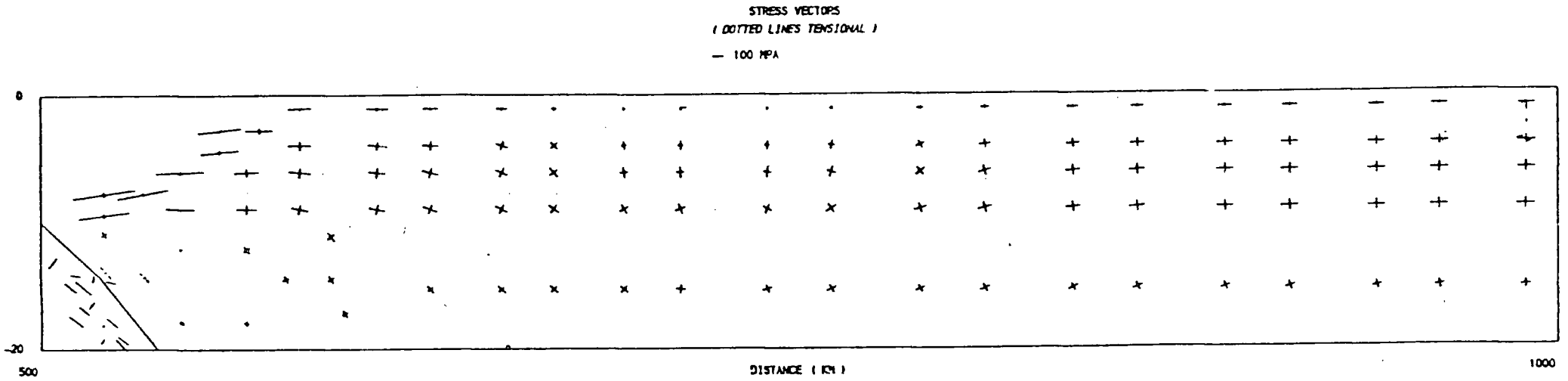

Figure 7.52: The principal stresses in the top 20 km of the overlying plate in the 26 degree slab pull model after 5 million years of visco-elastic relaxation.

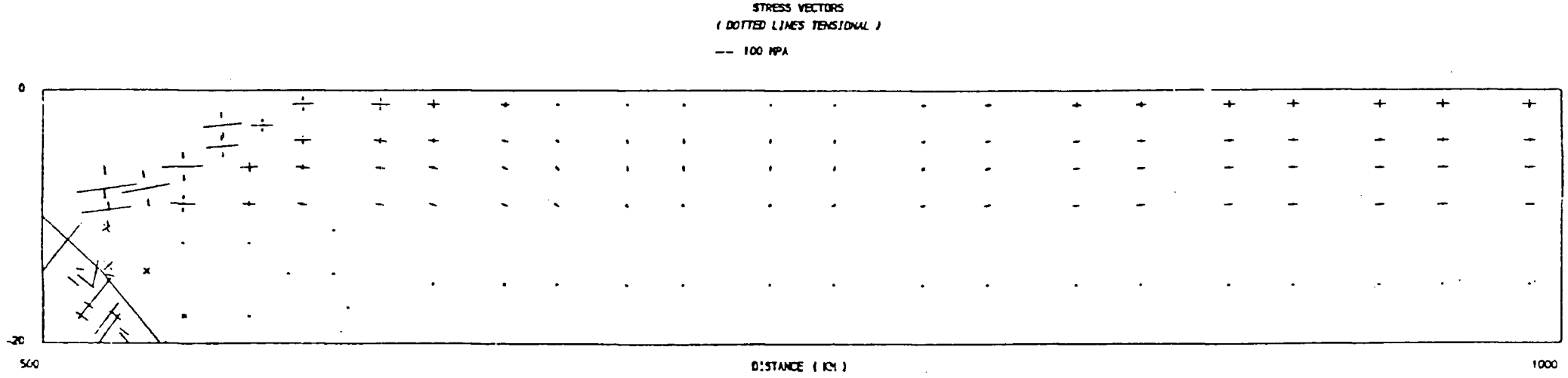

Figure 7.53: The deviatoric principal stresses in the top 20 km of the overlying plate in the 26 degree slab pull model after 5 million years of visco-elastic relaxation.

The deformation after allowing these models to relax visco-elastically for 5 million years is shown in figures 7.30 to 7.34, 7.40 to 7.44, and 7.50 to 7.53. The effect of this visco-elastic model is to concentrate and amplify the stresses observed in the elastic solution into the elastic layers of the lithosphere.

7.4.4 Discussion

The models which have been presented in this section predict that the effect of the vertical component of the slab pull force is to induce horizontal tension in the subducting plate and horizontal compression in the overlying plate between the trench axis and the volcanic arc. This lateral variation of the horizontal stress is observed at all subduction zones. The models therefore suggest that the slab pull force contributes to the observed lateral variation of stress across the strike of subduction zones.

The models show that a horizontal component of slab pull force produces a regional horizontal tension in the subducting plate and a regional horizontal compression in the overlying plate. Because the slab pull force probably acts approximately down the dip of the subducting slab, it may explain the observed variation in the stress regime between the back arc areas of different subduction zones. The models predict that subduction zones with a shallow dip should have compression in the back arc areas whilst those with high dips should be less compressive. This prediction is in reasonable agreement with observations.

7.4.5 Limitations of the models

The models in this section have three main limitations.

Firstly, the magnitude of the vertical component of the slab pull force is an upper limit. This is because it has been estimated from a 5 km deep trench which is the largest observed depth of any trench (Grellet and Dubois, 1982). The magnitude of the stresses in the models are therefore an upper limit on those which the slab pull force produces. The models therefore demonstrate the general implications of the slab pull force rather than make specific predictions for the magnitude of the stresses at any particular subduction zone. The models imply, however, that for a lower slab pull force the magnitude of the stress would be reduced.

The second limitation is that mantle drag, which resists the motion of the subducting plate, has been neglected. It is, however, unlikely that this force could have an important effect on the stress regime which has been modelled. This is because the resistance produced by mantle drag over the 500 km long base of the subducting plate would be small.

The third limitation is that the subduction zone fault has been assumed to be locked. Stresses in these models have therefore been transmitted perfectly across the fault zone. This is unrealistic because it neglects any effect of the elastic properties of the subduction zone fault. To overcome this limitation the effect of freeing the fault is considered in the next section.

7.5 Effect Of The Subduction Zone Fault

The effect of locking the subduction zone fault is to constrain each dual node to have identical displacements. The previous models have

consequently behaved as a single elastic continuum in which stress is transmitted perfectly across the fault plane. They have therefore assumed that the plates are perfectly elastically coupled at the subduction zone fault.

Kanamori (1977) suggested that the coupling between the plates at subduction zones is spatially variable. He demonstrated that the seismic slip rate at subduction zones which have great thrust earthquakes (e.g. Chile) is comparable with the subduction rate predicted by plate motion models. Elsewhere, where there are no great thrust earthquakes (e.g. Marianas), the subduction rate is many times greater than the seismic slip rate. Kanamori explained this observation by proposing that the degree of mechanical coupling of the plates varies between different subduction zones. Kanamori, and more recently Uyeda and Kanamori (1979), also demonstrated that the subduction zones at which plates are strongly coupled have compression in the back arc region whilst those which are weakly coupled have tensional stresses which give rise to active back arc spreading.

These observations suggest that the stress regime in the overlying plate may be controlled by the degree of mechanical coupling between the plates at a subduction zone. The aim of this section is therefore to investigate the effect of varying the elastic properties of the subduction zone fault.

7.5.1 Description of the finite element model

The effect of different properties of the subduction zone fault has been investigated by reducing the shear stiffness of the 45 degree slab pull model (section 7.4.2) to values of 1.0×10^{10} N m^{-1}, 5.0×10^{9} N m^{-1} and

1.0×10^{9} N m^{-1}. The fault was assumed to have a coefficient of friction equal to 0.1 and frictional sliding was allowed to occur. To ensure that both sides of the fault plane remain in contact during frictional sliding the normal stiffness of the fault has been assigned a value of 1.0×10^{15} N m^{-1}.

7.5.2 Effect of reducing the shear stiffness of the subduction zone fault

The stress regime which has been calculated after reducing the shear stiffness of the subduction zone fault from 1.0×10^{15} N m^{-1} to 1.0×10^{10} N m^{-1}, 5.0×10^{9} N m^{-1} and 1.0×10^{9} N m^{-1} is shown in figures 7.35 to 7.39, 7.54 to 7.57, 7.58 to 7.61 and 7.62 to 7.65 respectively. The variation of the horizontal deviatoric stress with depth at the right hand edge of the overlying plate and the left hand edge of the subducting plate is shown in figures 7.66 and 7.67.

These results demonstrate that reducing the shear stiffness of the subduction zone fault from 1.0×10^{15} N m^{-1} to 1.0×10^{9} N m^{-1} has two effects upon the regional stress regime which is produced by the horizontal component of the slab pull force. Firstly, it reduces the regional horizontal compression in the overlying plate by 40 MPa in the mantle and 17.5 MPa in the crust (the difference being due to the contrasting Young's moduli of these layers). The magnitude of the regional horizontal compression which is transmitted into the overlying plate by the horizontal component of the slab pull force is therefore strongly controlled by the shear stiffness of the subduction zone fault. Secondly, the regional horizontal tension in the subducting plate is increased by a commeasurate amount. The effect of reducing the shear stiffness of the subduction zone fault is therefore to make the horizontal stresses more tensional throughout the model.

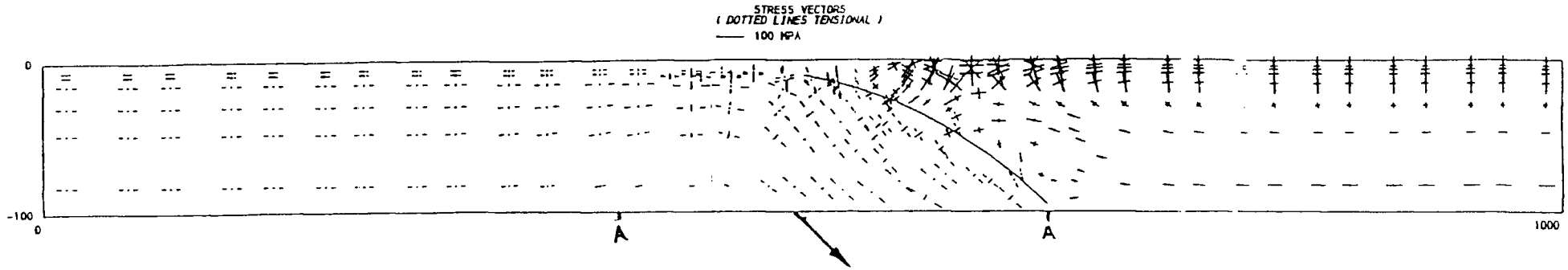

Figure 7.54: The elastic principal stresses in the 45 degree slab pull model with the shear stiffness of the subduction zone fault equal to 1.0×10^{10} N m^{-1}. The orientation of the slab pull force is indicated by the arrow and acts over the distance A-A.

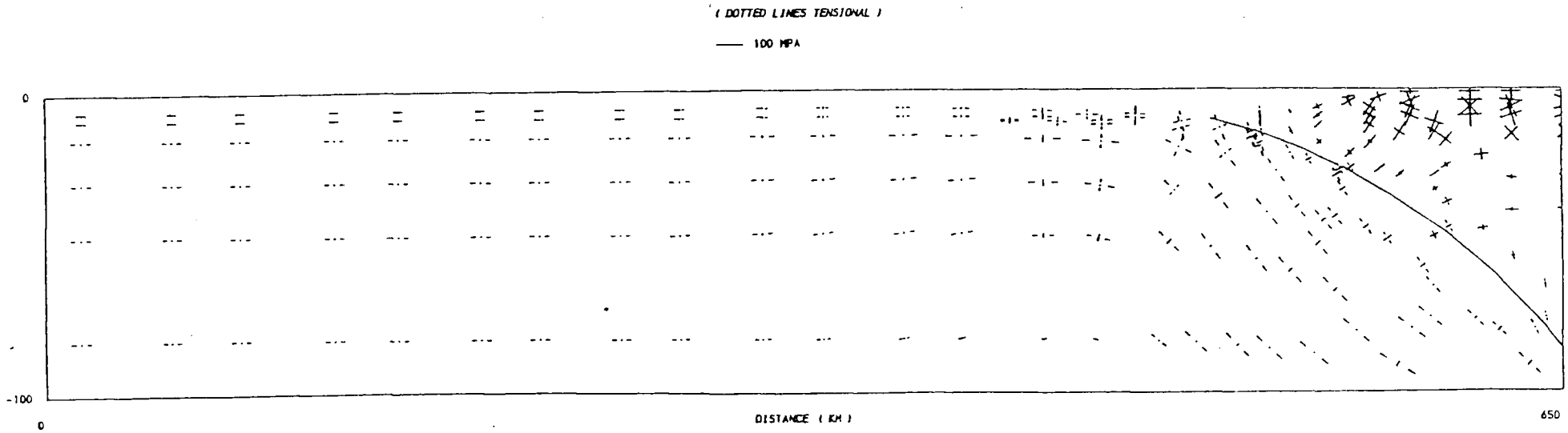

Figure 7.55: The elastic principal stresses in the subducting plate in the 45 degree slab pull model with the shear stiffness of the subduction zone fault equal to 1.0×10^{10} Nm^{-1}.

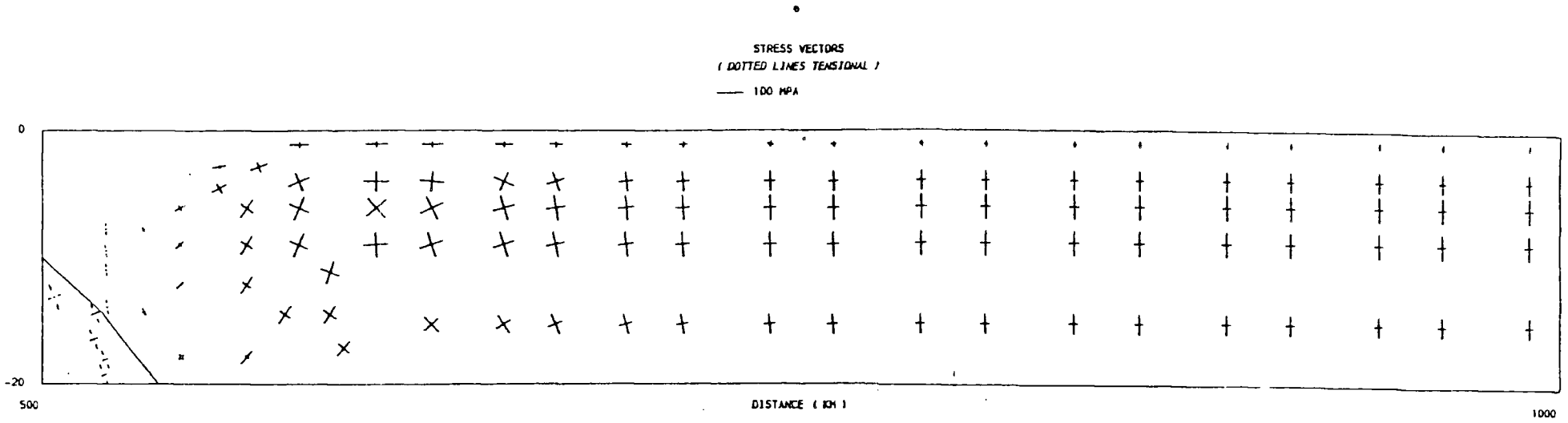

Figure 7.56: The elastic principal stresses in the top 20 km of the overlying plate in the 45 degree slab pull model with the shear stiffness of the subduction zone fault equal to 1.0×10^{10} N m^{-1}.

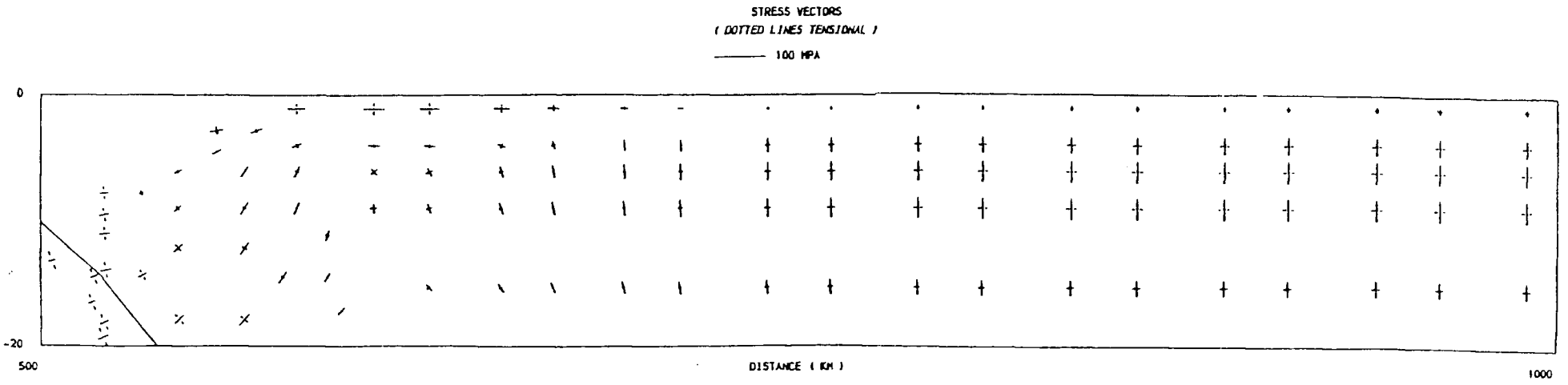

Figure 7.57: The elastic deviatoric principal stresses in the top 20 km of the overlying plate in the 45 degree slab pull model with the shear stiffness of the subduction zone fault equal to 1.0×10^{10} N m^{-1}.

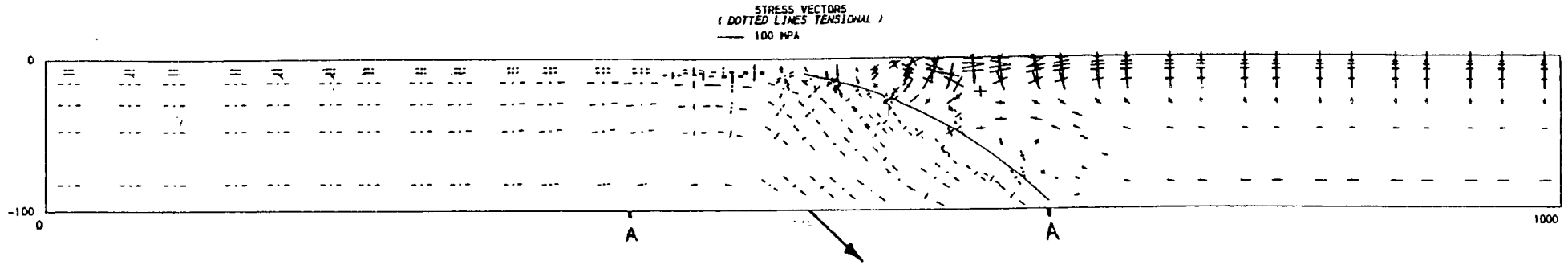

Figure 7.58: The elastic principal stresses in the 45 degree slab pull model with the shear stiffness of the subduction zone fault equal to 5.0×10^{9} N m^{-1}. The orientation of the slab pull force is indicated by the arrow and acts over the distance A-A.

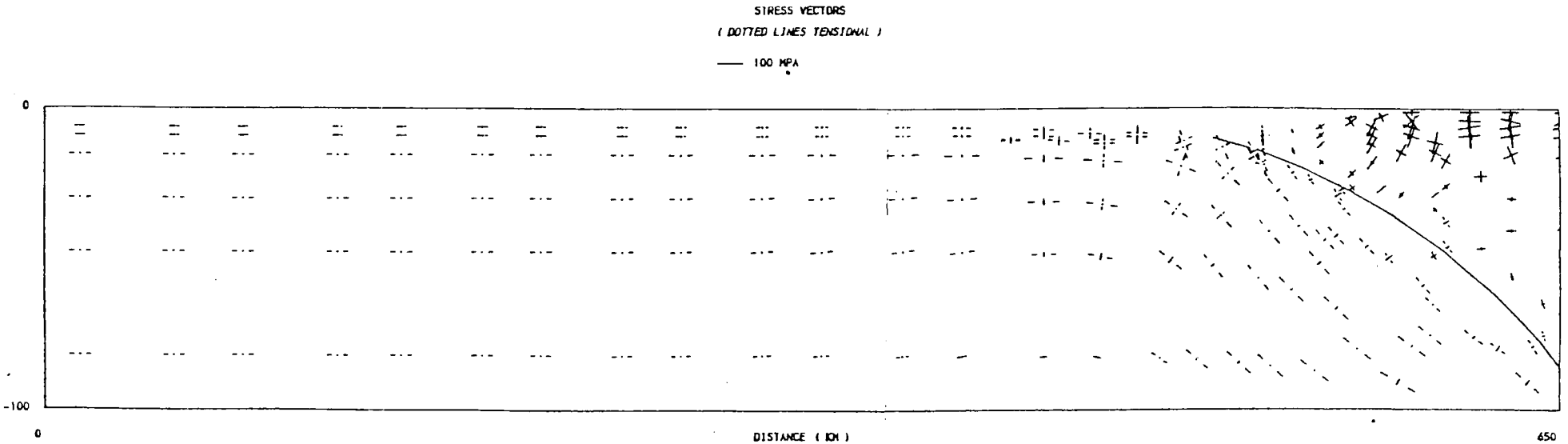

Figure 7.59: The elastic principal stresses in the subducting plate in the 45 degree slab pull model with the shear stiffness of the subduction zone fault equal to 5.0×10^{9} Nm^{-1}.

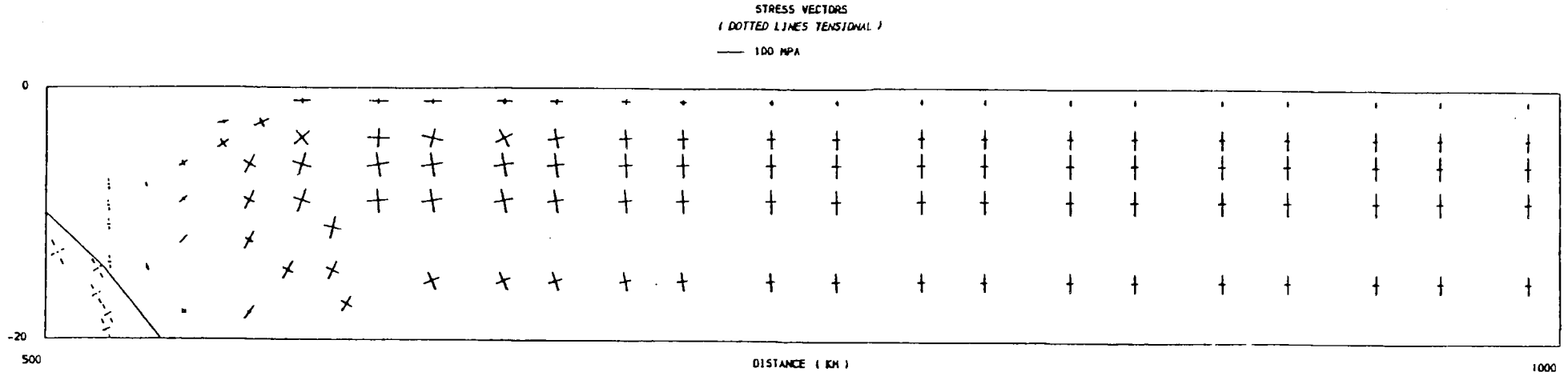

Figure 7.60: The elastic principal stresses in the top 20 km of the overlying plate in the 45 degree slab pull model with the shear stiffness of the subduction zone fault equal to 5.0×10^9 N m^{-1}.

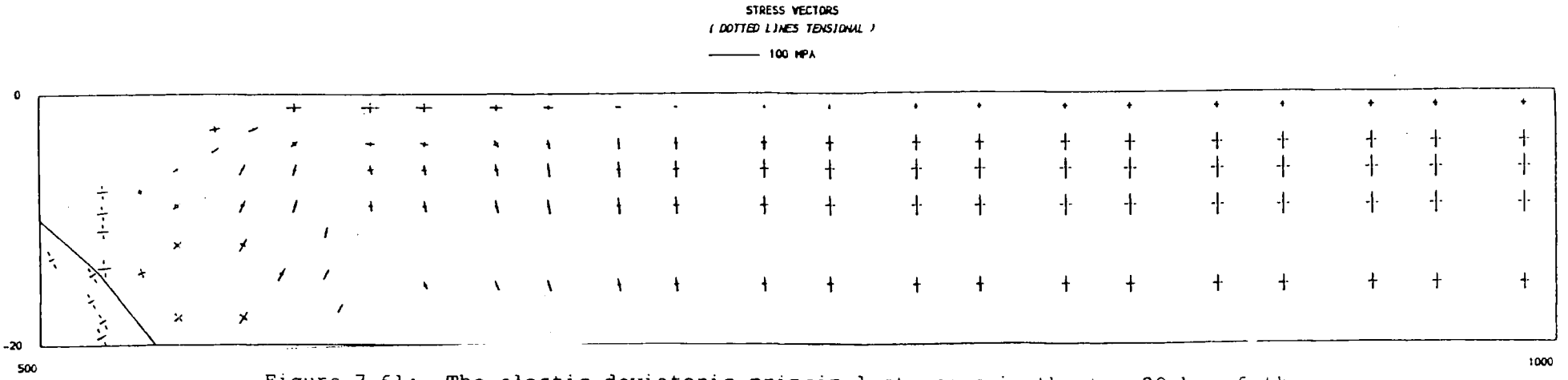

Figure 7.61: The elastic deviatoric principal stresses in the top 20 km of the overlying plate in the 45 degree slab pull model with the shear stiffness of the subduction zone fault equal to 5.0×10^9 N m^{-1}.

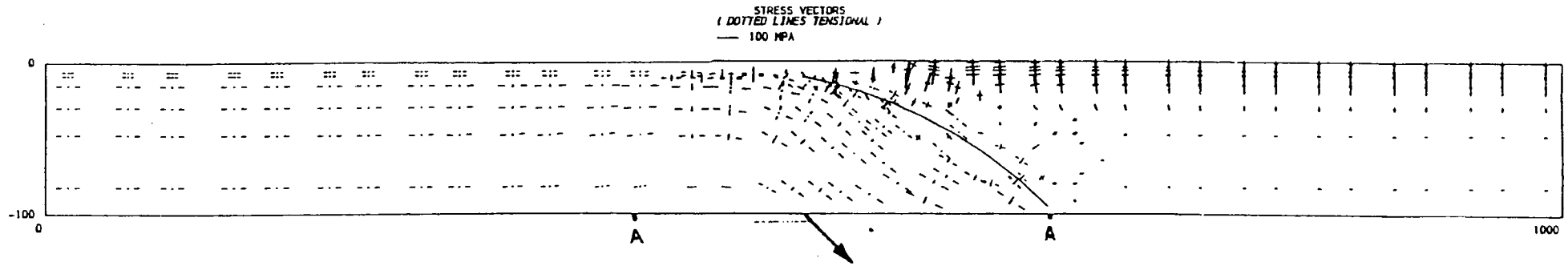

Figure 7.62: The elastic principal stresses in the 45 degree slab pull model with the shear stiffness of the subduction zone fault equal to 1.0×10^{9} N m^{-1}. The orientation of the slab pull force is indicated by the arrow and acts over the distance A-A.

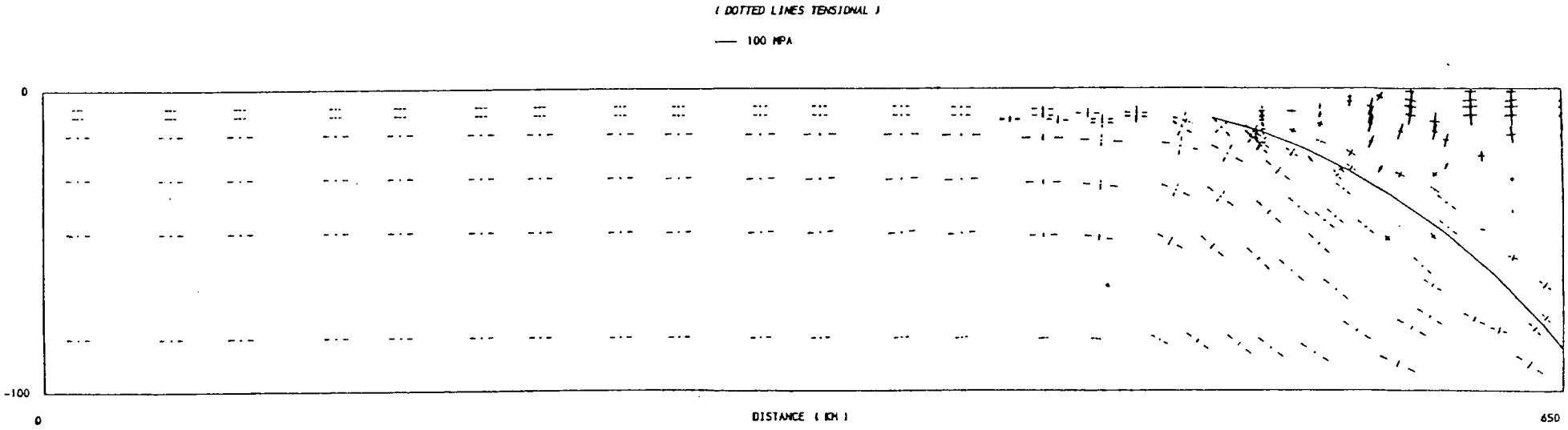

Figure 7.63: The elastic principal stresses in the subducting plate in the 45 degree slab pull model with the shear stiffness of the subduction zone fault equal to 1.0×10^{9} Nm^{-1}.

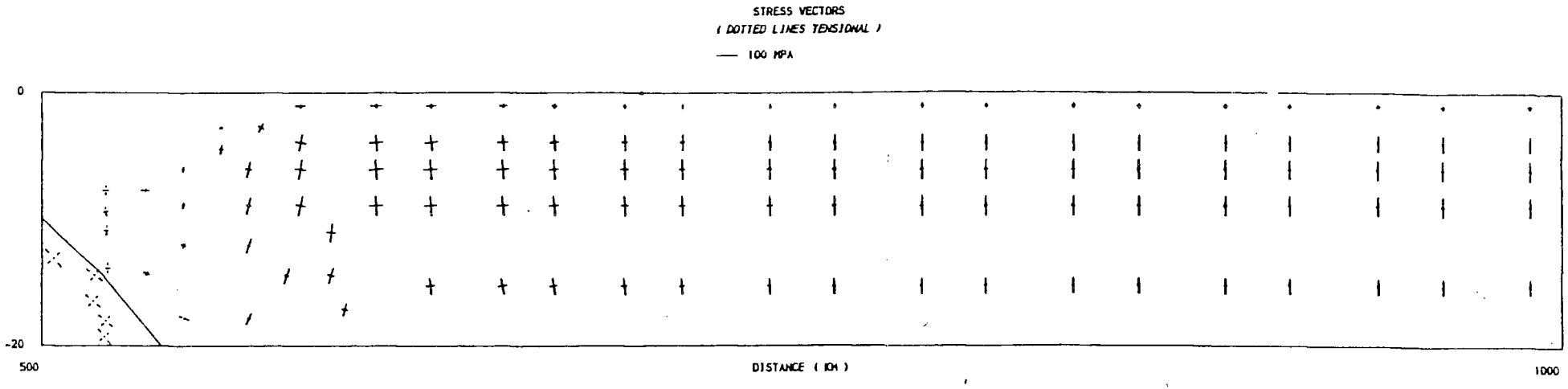

Figure 7.64: The elastic principal stresses in the top 20 km of the overlying plate in the 45 degree slab pull model with the shear stiffness of the subduction zone fault equal to 1.0×10^9 N m^{-1}.

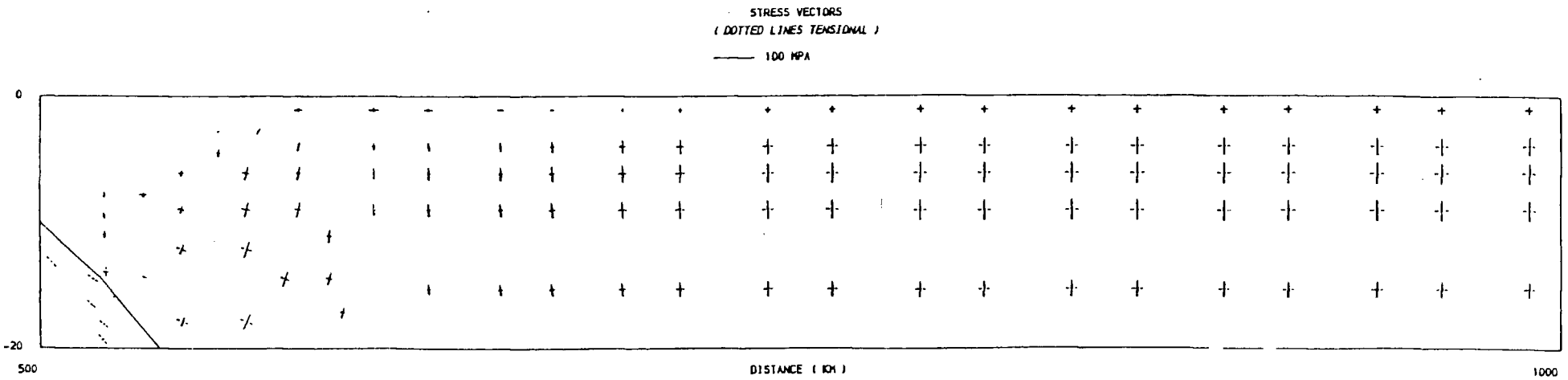

Figure 7.65: The elastic deviatoric principal stresses in the top 20 km of the overlying plate in the 45 degree slab pull model with the shear stiffness of the subduction zone fault equal to 1.0×10^9 N m^{-1}.

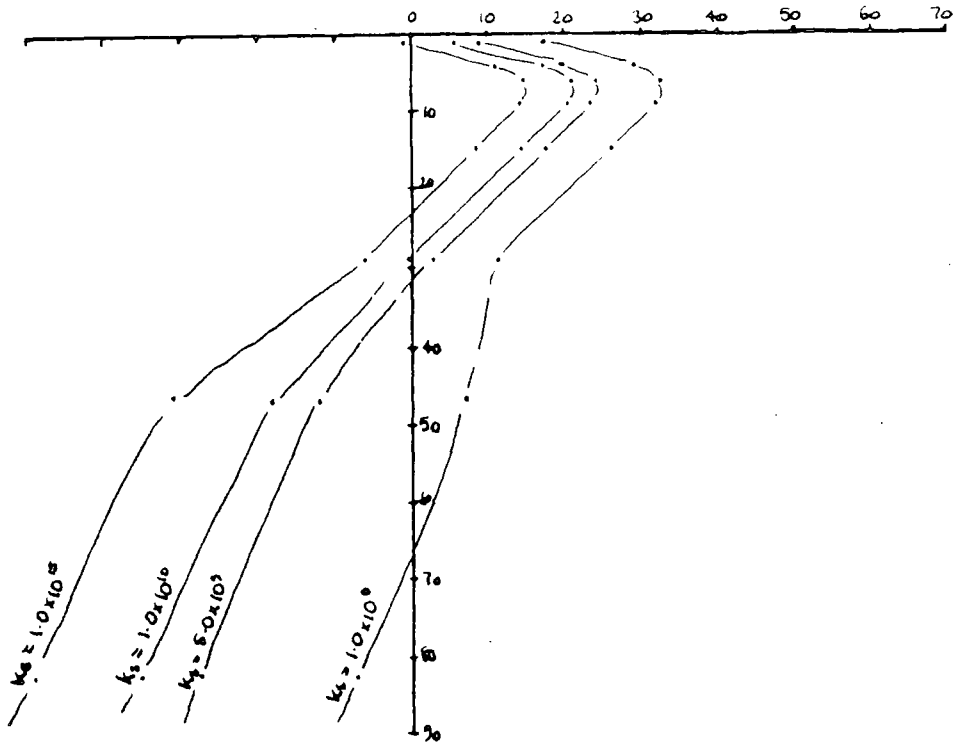

Figure 7.66: The horizontal deviatoric stresses at the right hand edge of the overlying plate in the 45 degree slab pull model with various shear stiffnesses of the subduction zone fault.

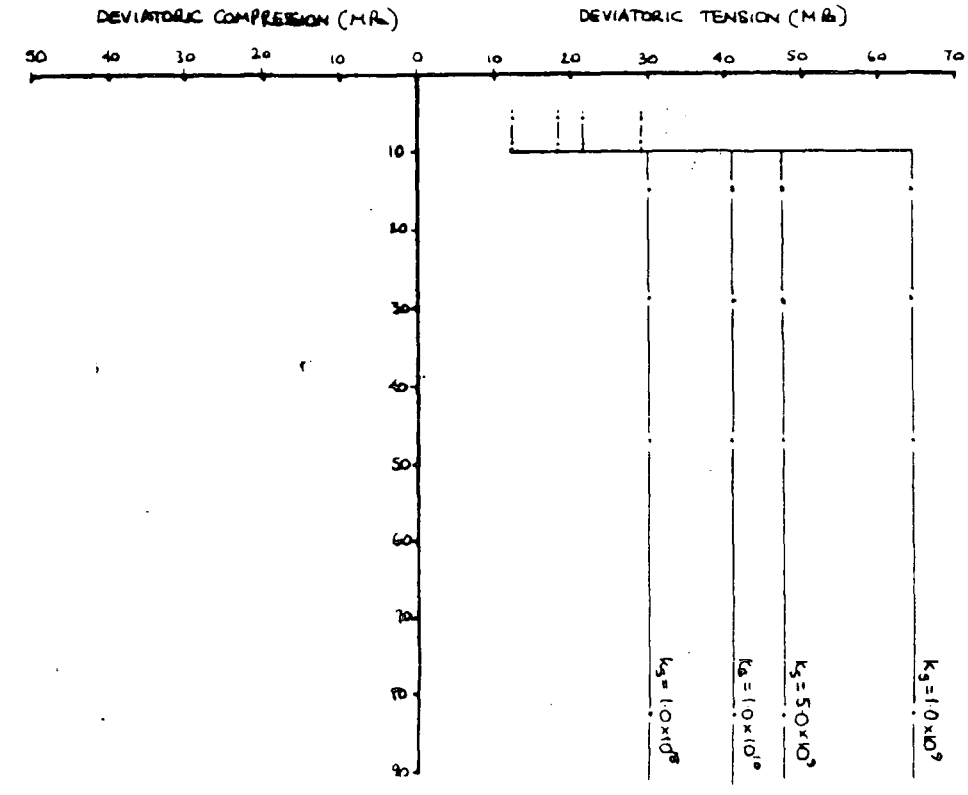

Figure 7.67: The horizontal deviatoric stresses at the left hand edge of the subducting plate in the 45 degree slab pull model with various shear stiffnesses of the subduction zone fault.

The reason for this response can be seen in the nodal displacements. When the fault is locked (figure 7.39) each dual node is constrained to have the same displacement and consequently the slab pull force acts equally to deform both the overlying and subducting plates. The result of this strong coupling of the plates is that the 45 degree slab pull force pushes the centre of the model to the right, which compresses the overlying plate and produces tensions in the subducting plate. Reducing the shear stiffness of the fault increases the relative displacement on the dual nodes so that the two plates slide past one another (figures 7.68 to 7.70). This occurs because the horizontal component of the slab pull force acts unequally on the two plates; more of it is used to pull the subducting plate into the mantle and less is transmitted to compress the overlying plate. Reducing the shear stiffness consequently decouples the displacement and the stresses of the two plates. The models therefore suggest that the degree of mechanical coupling between the plates at a subduction zone determines the amount of compression which the shear component of the slab pull force transmits into the overlying plate.

In the final model (figure 7.62), in which the shear stiffness of the subduction zone fault has been reduced to 1.0×10^{9} N m^{-1}, the regional horizontal compressive stress produced by the shear component of the slab pull force has been reduced to less than 5 MPa. In this model, however, near surface horizontal compression of 25 MPa still occurs in the overlying plate between the trench axis and the volcanic arc. This is because the overlying plate is still bending in response to the vertical component of the slab pull force (figure 7.70). This deformation occurs because the high value which has been assigned to the normal stiffness of the subduction zone fault allows a component of the slab pull force to be transmitted normally across the fault plane to deform the leading edge of

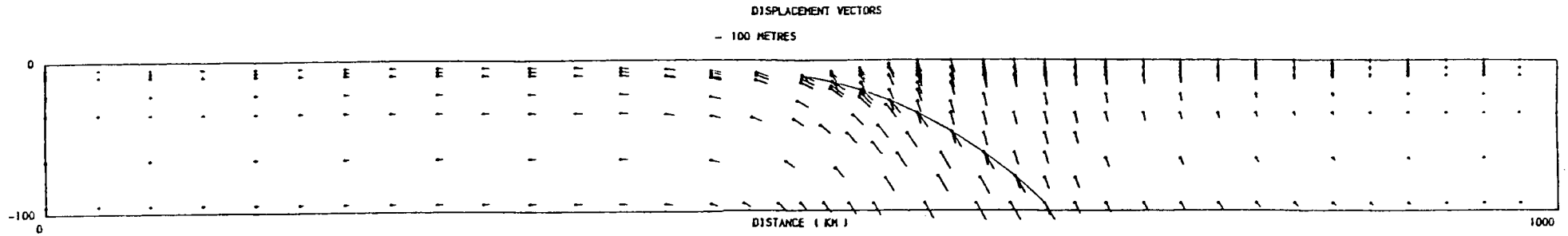

Figure 7.68: The elastic displacements of the 45 degree slab pull model with the shear stiffness of the subduction zone fault equal to 1.0×10^{10} Nm^{-1}.

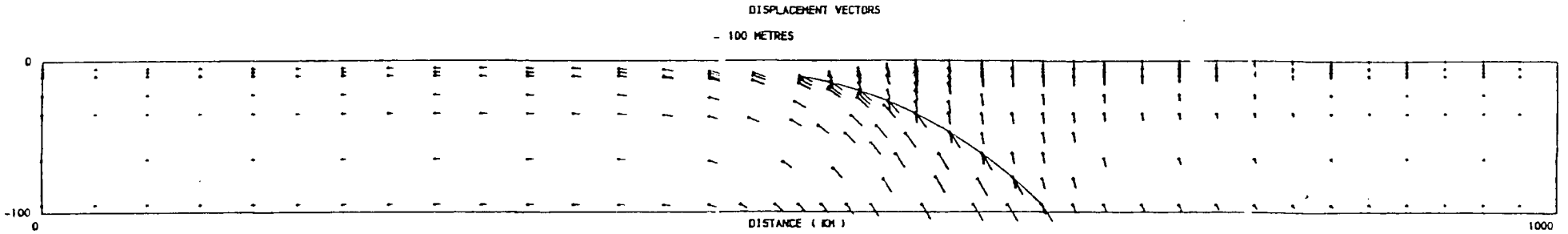

Figure 7.69: The elastic displacements ofthe 45 degree slab pull model with the shear stiffness of the subduction zone fault equal to 5.0×10^{9} Nm^{-1}.

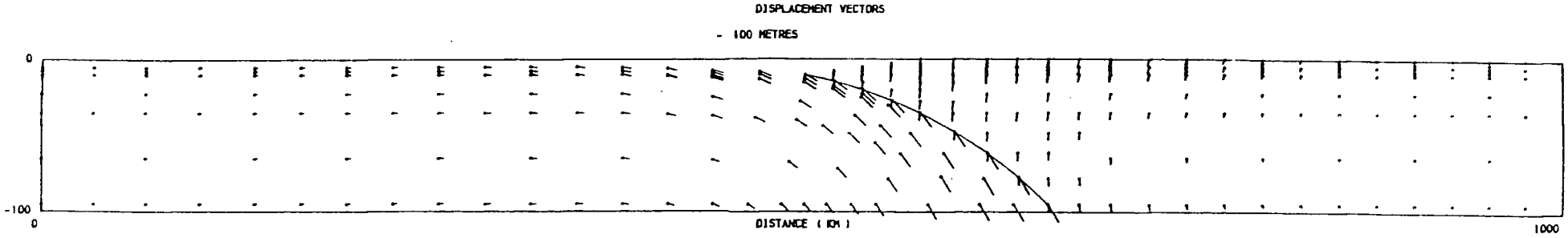

Figure 7.70: The elastic displacements of the 45 degree slab pull model with the shear stiffness of the subduction zone fault equal to 1.0×10^{9} Nm^{-1}

the overlying plate. Reducing the shear stiffness of the subduction zone fault therefore does not decrease the local horizontal compression which the vertical component slab pull force produces at the leading edge of the overlying plate.

7.5.3 Discussion

The models presented in this section demonstrate that the regional horizontal compression which is transmitted into the back arc region by the slab pull force is strongly controlled by the mechanical coupling between the plates at the subduction zone fault. The models predict that the stress regime in the back arc regions of subduction zones which are strongly coupled will be more compressive than at subduction zones which are weakly coupled. The models therefore explain that the degree of mechanical coupling is an additional factor in explaining why the stress regime in the back arc regions is variable between different subduction zones. These models quantitatively demonstrate that the decoupling hypothesis of Kanamori (1971; 1977) is plausible.

An important implication of these models is that whatever the coupling of the plates, near surface horizontal compression occurs at the leading edge of the subducting plate. This may explain why the stress in this region is consistently observed to be compressive, whatever the state of stress is in the back arc basins. These models demonstrate, however, that the magnitude of the compression is increased when the coupling between the plates is higher. This implies that great thrust earthquakes are more likely to occur at subduction zones which are strongly coupled than at those which are weakly coupled. This prediction helps to explain why the tectonic deformation of the overlying plate is so variable between different subduction zones (Kanamori, 1977).

The models therefore explain why crustal shortening can occur at subduction zones without producing regional horizontal compression.

7.6 Convection In The Asthenospheric Wedge

The possibility that the subducting plate induces a viscous drag convective flow in the overlying asthenospheric wedge which heats and shears the overlying plate was initially proposed by McKenzie (1969) to explain the high heat flow which is observed in the back arc areas of subduction zones. Following this proposal, Karig (1970; 1971a, b) demonstrated that in the island arcs of the Western Pacific the high heat flow coincides with presently or recently active sites of back arc spreading. This observation stimulated the development of increasingly sophisticated numerical models of the slab induced convection (Sleep and Toksoz, 1971; Andrews and Sleep, 1974; Toksoz and Bird, 1977; Toksoz and Hsui, 1978) which propose that back arc spreading is initiated and driven by the combination of shearing and heating of the overlying plate produced by the viscous flow.

The hypothesis that slab induced convection initiates back arc spreading, however, has recently been challenged because the model cannot explain the observed spatial and temporal episodicity of back arc spreading (Chase, 1978; Uyeda and Kanamori, 1979). Hsui and Toksoz (1981), however, concluded that the one available focal mechanism solution for back arc areas agrees with their hypothesis (Toksoz and Hsui, 1978) that back arc spreading is initiated and driven by slab induced convection. This assertion is obviously based upon an extremely limited data set and therefore the role of slab induced convection in driving back arc basins remains uncertain.

One of the reasons for this uncertainty about the role of slab induced convection in driving back arc spreading is that the stress regime which is produced by this mechanism has only been qualitatively assessed. The sophisticated models of slab induced convection, however, make quantitative predictions about the heating and shearing of the overlying plate. The model of Toksoz and Hsui (1978), for example, predicts that for a slab dipping at 45 degrees and subducting at 8 cm/yr the slab induced convection cell will exert a shear stress of 3.5 MPa on the base of the overlying plate and will raise the temperature of the base of the lithosphere by 250°C at 75 million years after the initiation of subduction. These predictions can therefore be used to quantify the stress regime which is produced by slab induced convection.

In this section the stress regime produced by the shearing and thermal volume changes which are predicted by the model of Toksoz and Hsui (1978) are evaluated. The results will be used to test two hypotheses. Firstly, does the slab induced convection generate sufficient tension to initiate back arc spreading by failure at the volcanic arc ? Secondly, is the slab induced convection able to produce the tensional stress observed in many back arc basins, and which may drive active back arc spreading in some areas ?

7.6.1 Effect of shear stress

The model of Toksoz and Hsui (1978) predicts that the slab induced convection cell exerts a shear stress of 3.5 MPa on the base of the overlying plate at subduction zones. The stress regime produced by the action of this basal shear stress is evaluated in this section.

The finite element mesh is described in section 7.2. The sides of this model were constrained for zero horizontal displacement and the base was assumed to be underlain by a fluid asthensophere with a density of 3300 kg m^{-3}. A basal shear stress of 3.5 MPa was applied to the 260 km long base of the overlying plate shown in figure 7.71. The subduction zone fault was assumed to be locked.

The elastic solution is shown in figures 7.72 to 7.75. The basal shear stress has two effects. The first is that it displaces the centre of the model to the left which produces a regional horizontal compression of 4 MPa in the subducting plate and a regional horizontal compression of a similar magnitude in the overlying plate. The second is that it induces a bending moment which causes an upwards flexure of the model about an axis above the base of the subduction zone fault, and a downwards flexure at the right hand edge of the model (figure 7.76). The upward flexure produces near surface horizontal tensions of 4 MPa with underlying compressions of 10 MPa, and the downward flexure produces near surface stresses of zero with underlying horizontal tensions of 14 MPa. The effects of the bending moment therefore dominates the stress regime in the overlying plate. The stress associated with it, however, is insufficient to cause failure anywhere in the model.

The shear stress produced by slab induced convection is a renewable source of stress, as long as subduction continues, and therefore the above model was allowed to relax visco-elastically for 5 million years. The results of this analysis are shown in figures 7.78 to 7.81. The major difference between this and the elastic solution is that the regional compression and tension has been amplified in the elastic layers, but the superimposed flexural stresses are unaltered and are consequently less

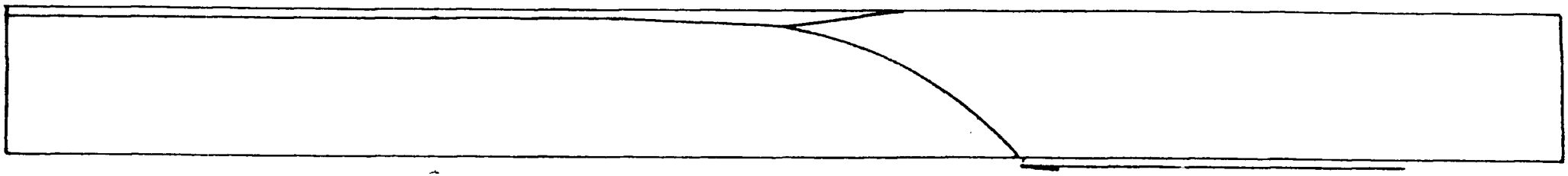

Figure 7.71: Position where the 3.5 MPa basal shear stress was applied to the model.

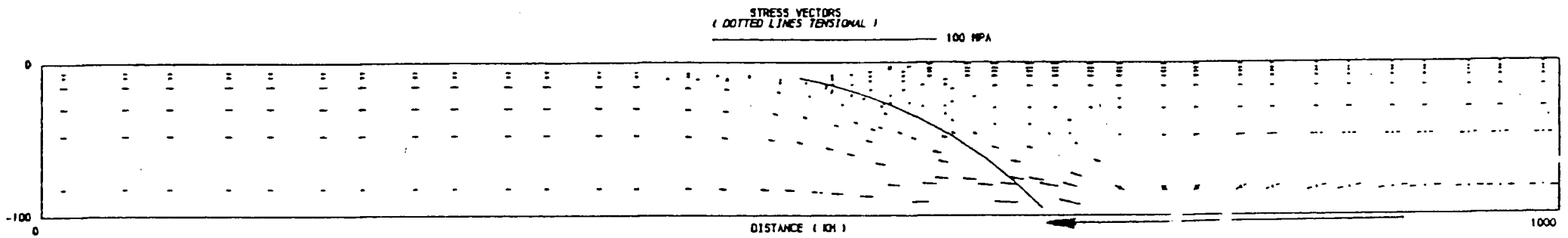

Figure 7.72: The elastic principal stresses in the 3.5 MPa basal shear stress model. The location of the shear stress is indicated by the arrow.

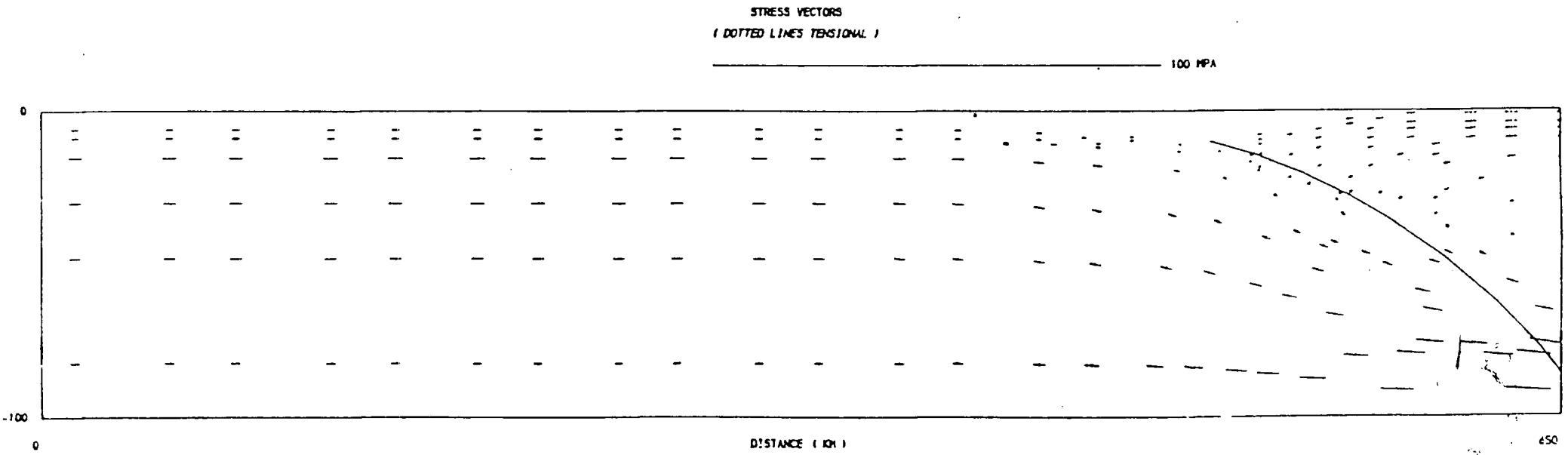

Figure 7.73: The elastic principal stresses in the subducting plate in the 3.5MPa basal shear stress model.

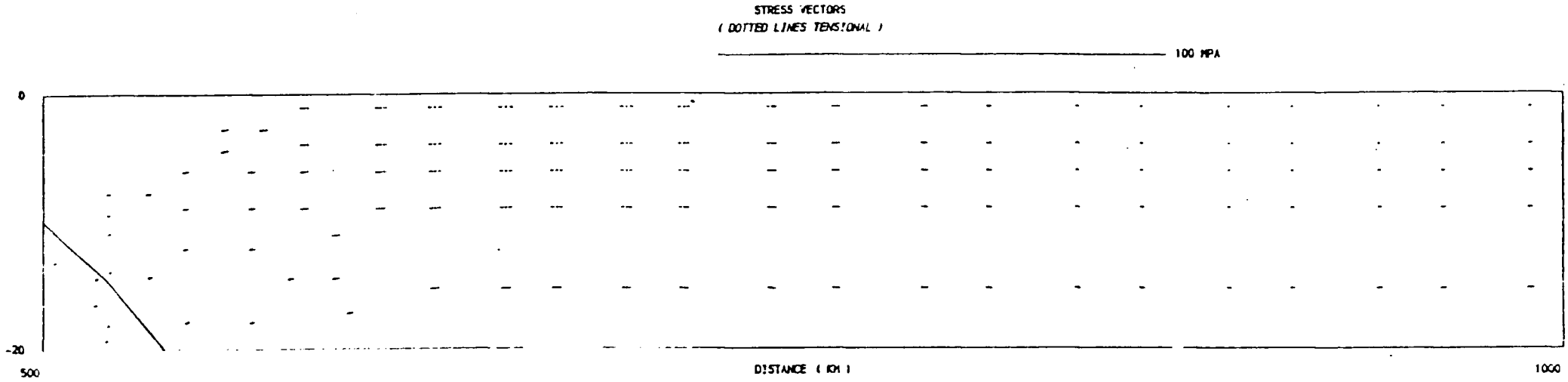

Figure 7.74: The elastic principal stresses in the top 20 km of the overlying plate in the 3.5 MPa basal shear stress model.

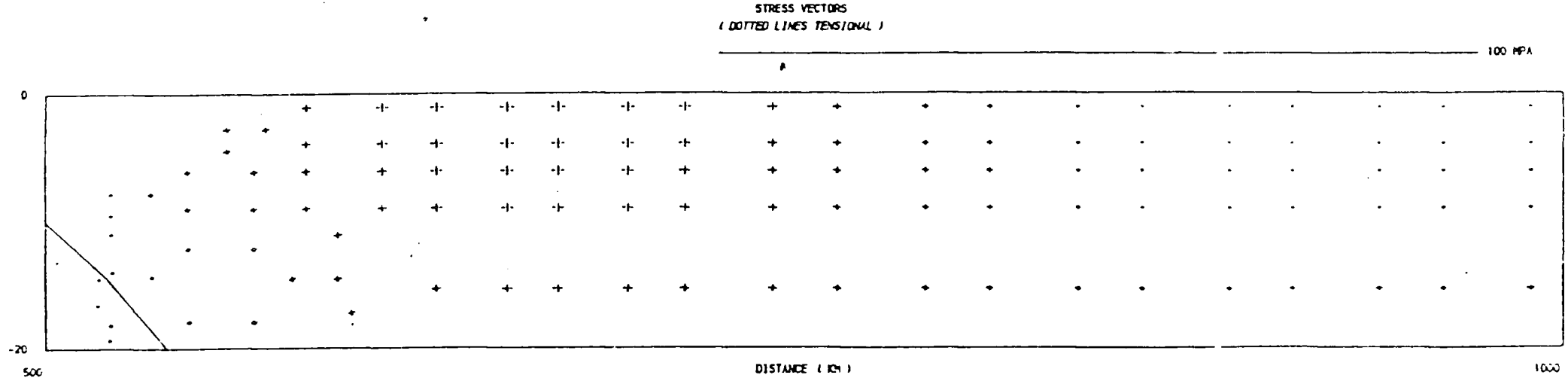

Figure 7.75: The elastic deviatoric principal stresses in the top 20 km of the overlying plate in the 3.5 MPa basal shear stress model.

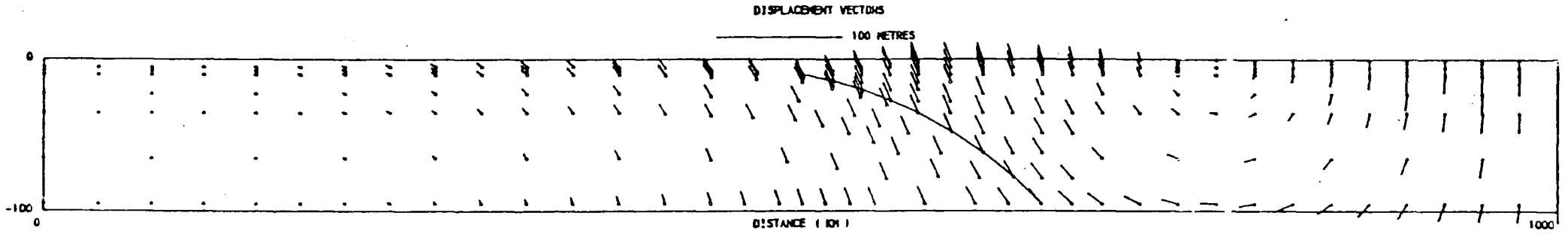

Figure 7.76: The elastic displacements of the 3.5 MPa basal shear stress model.

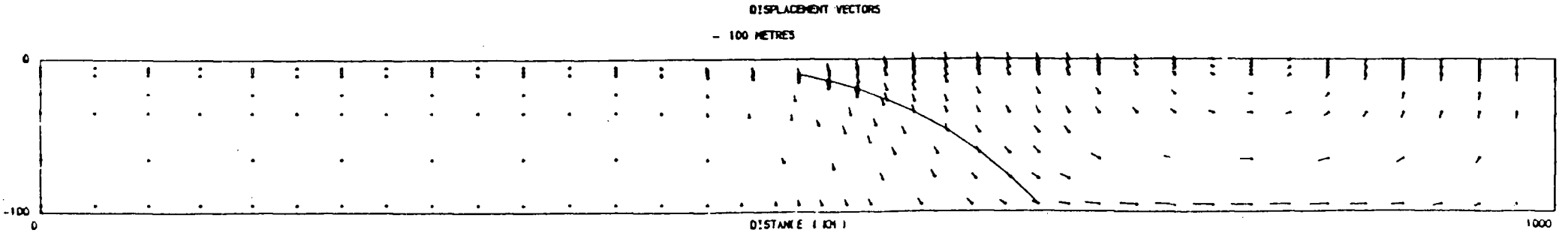

Figure 7.77: The displacements of the 3.5 MPa basal shear stress model after 5 million years of visco-elastic relaxation.

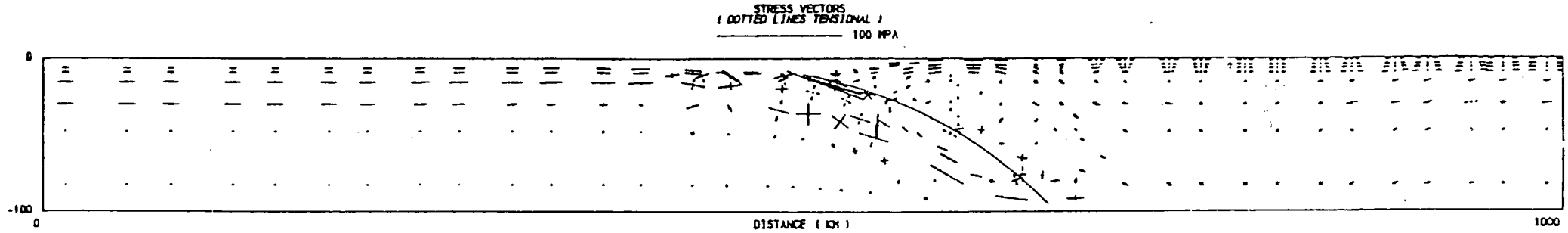

Figure 7.78: The principal stresses in the 3.5 MPa basal shear stress model after 5 million years of visco-elastic relaxation.

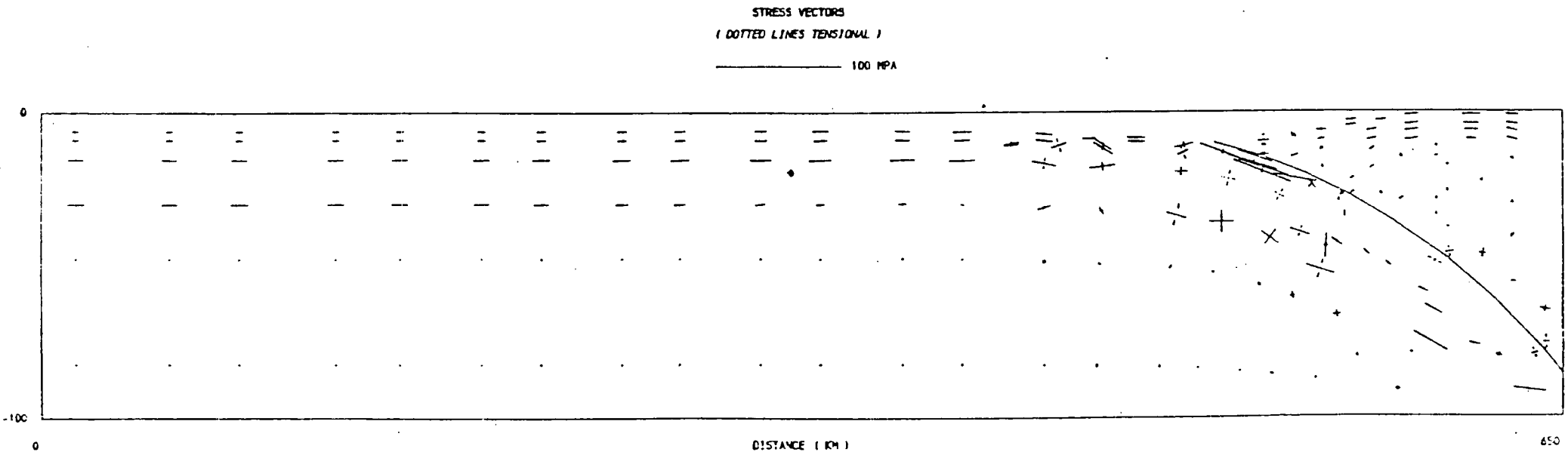

Figure 7.79: The principal stresses in the subducting plate in the 3.5 MPa basal shear stress model after 5 million years of vis o-elastic relaxation.

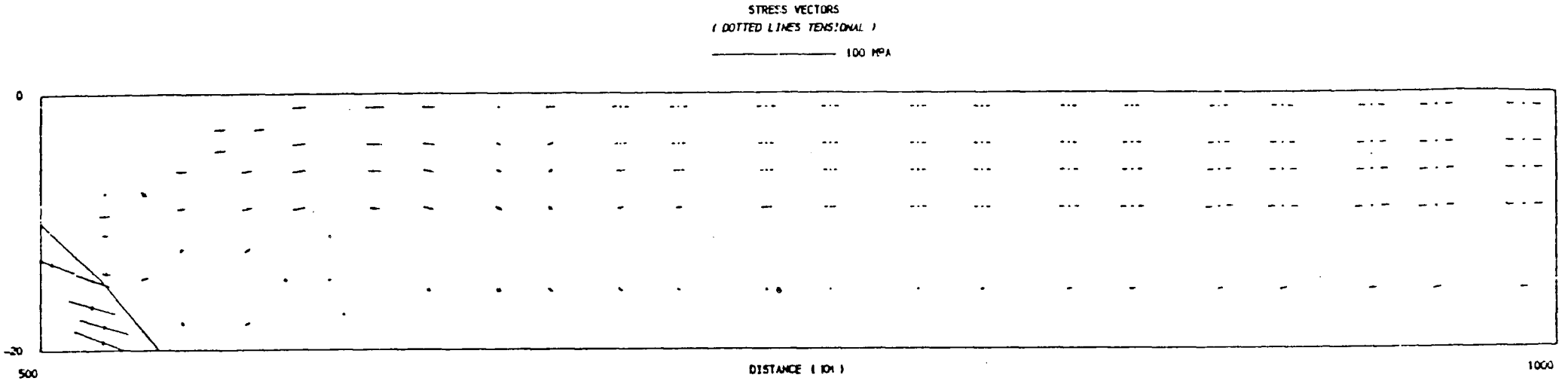

Figure 7.80: The principal stresses in the top 20 km of the overlying plate in the 3.5 MPa basal shear stress model after 5 million years of visco-elastic relaxation.

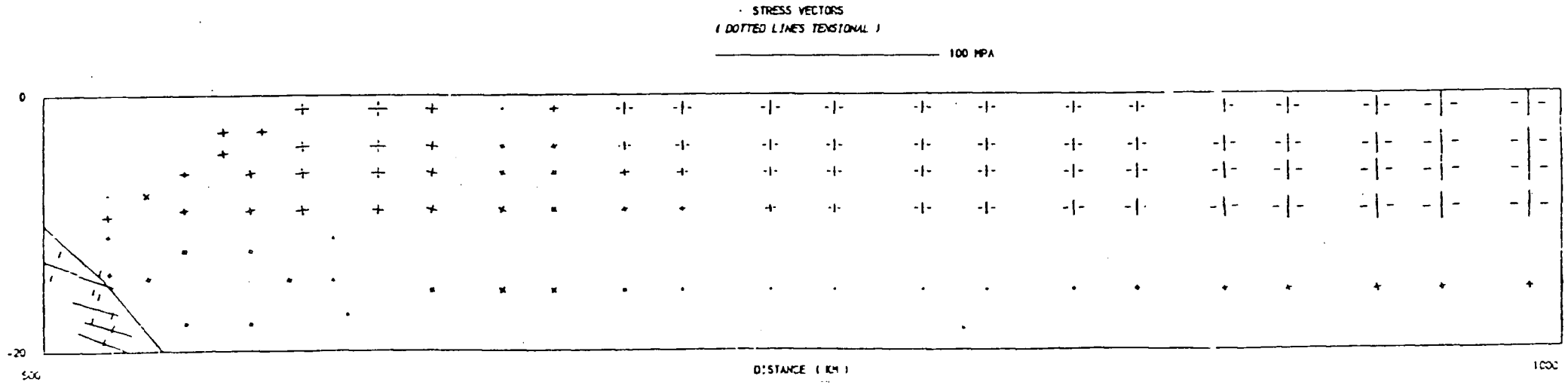

Figure 7.81: The deviatoric principal stresses in the top 20 km of the overlying plate in the 3.5 MPa basal shear stress model after 5 million years of visco-elastic relaxation.

prominent. Despite this stress amplification, however, failure is not predicted anywhere in the model.

These results demonstrate that the shear stress predicted by the slab induced convection model of Toksoz and Hsui (1978) produces horizontal tensional stresses in the back arc area of subduction zones. The model therefore agrees with the suggestion of these authors that this force can help to drive back arc spreading and can account for the tension commonly observed in these regions. The magnitude of the tensional stress, however, is insufficient to cause failure of the lithosphere and therefore cannot solely account for initiation of back arc spreading. In order for the basal shear stress to cause failure it would therefore either have to be of a larger magnitude or act over a greater distance. A much more fundamental problem, however, is that the volcanic arc is in compression and therefore this mechanism cannot account for why the back arc spreading is initiated by fracture at the volcanic arc.

The slab induced convection causes the overlying plate to be displaced towards the trench, i.e. to override the subducting plate. This supports the proposal of Richter (1973) that this force contributes towards the trench suction effect. The model, however, indicates that the contribution would be relatively small unless the basal shear stress is much larger.

7.6.2 Effect of thermal volume changes

The model of Toksoz and Hsui (1978) predicts that after 75 million years the slab induced convection cell causes a 250°C heating of the base of the overlying plate. The stress regime produced by the resulting thermal volume changes are modelled in this section.

The finite element mesh is described in section 7.2. The sides of this model were constrained for zero horizontal displacement and the base was assumed to be underlain by a fluid asthenosphere with a density of 3300 kg m^{-3}.

The temperature anomaly (figure 7.82) which was used in the finite element calculations is cylindrical, with its axis perpendicular to the strike, and has its centre (x_c, y_c) at (780.0 km, -123.289 km). The temperature rise, T, at a point (x_p, y_p) in the overlying plate was calculated from the function

$$T = \frac{(y_c - r_p)\Delta T_b}{\ell}$$

where ℓ, the thickness of the lithosphere was taken as 95 km, ΔT_b, the temperature rise of the base was assumed to be 250°C, and r_p, the radial distance to the point p was calculated from the expression

$$r_p = \sqrt{(x_p - x_c)^2 + (y_p - y_c)^2}$$

This temperature anomaly approximates that in the model of Toksoz and Hsui (1978). The thermal stresses were calculated using the initial strain method (section 3.8) assuming that the volume coefficient of expansion, α, is 1.0×10^{-5}.

The elastic solution using this model is shown in figures 7.83 to 7.86. These results demonstrate that the thermal volume changes which are produced by a heating of the overlying plate by a slab induced convection cell has two effects. The first is to induce a flexure of the overlying plate with an axis at the centre of the temperature anomaly (figure 7.87).

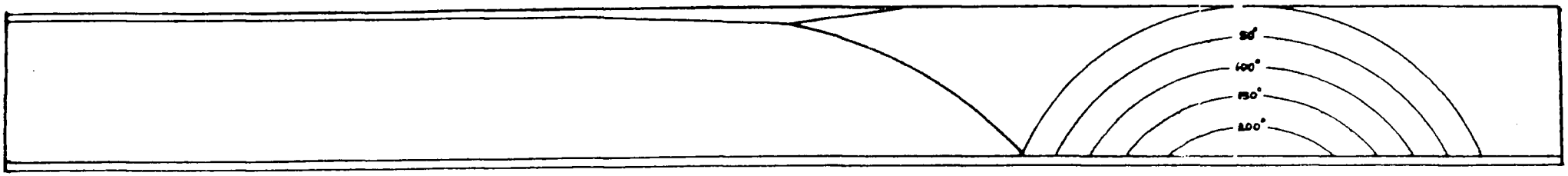

Figure 7.82: The position of the thermal anomaly which was applied to the finite element model.

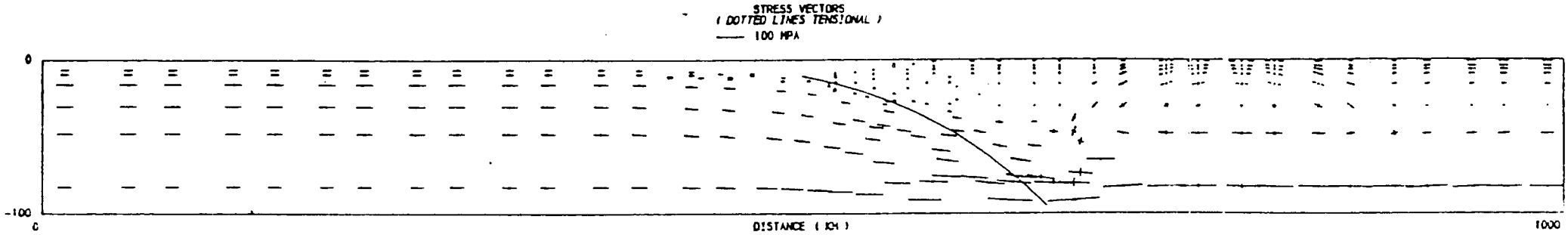

Figure 7.83: The elastic principal stresses in the thermal anomaly model.

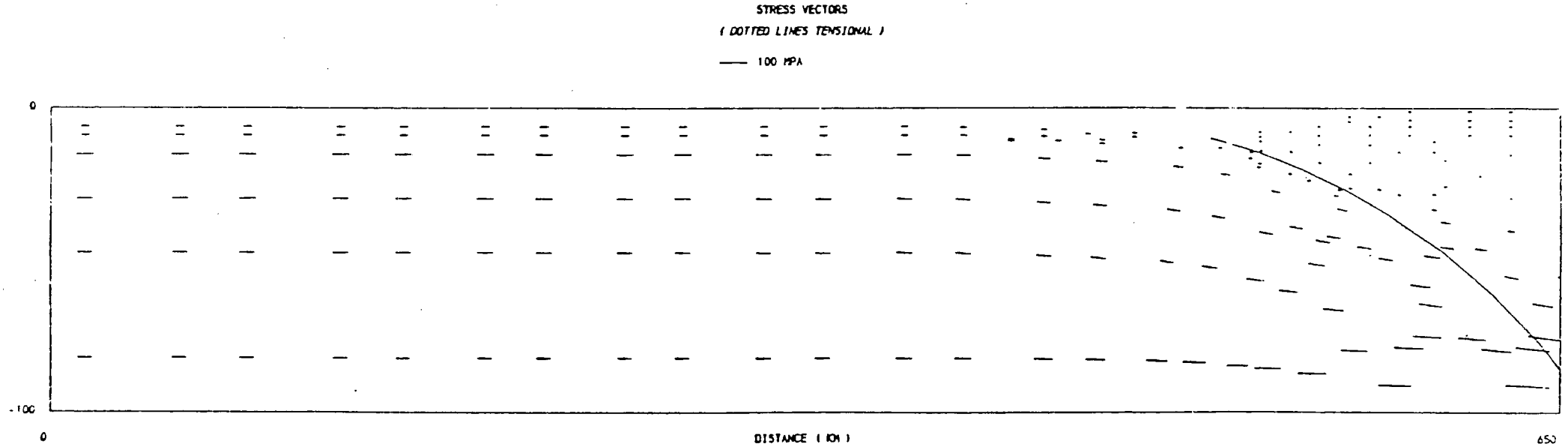

Figure 7.84: The elastic principal stresses in the subducting plate in the thermal anomaly model.

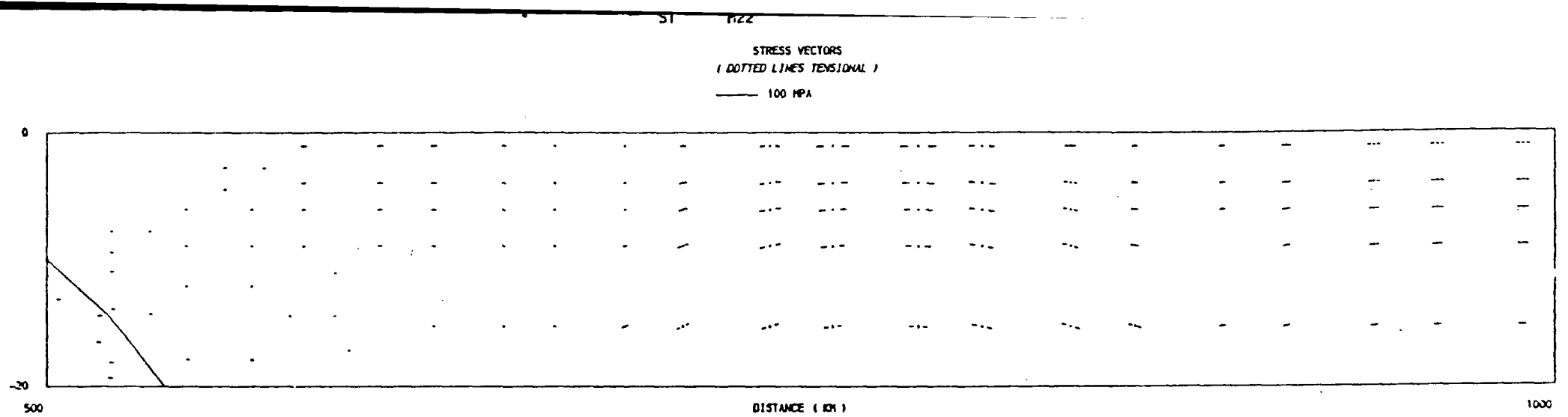

Figure 7.85: The elastic principal stresses in the top 20km of the overlying plate in the thermal anomaly model.

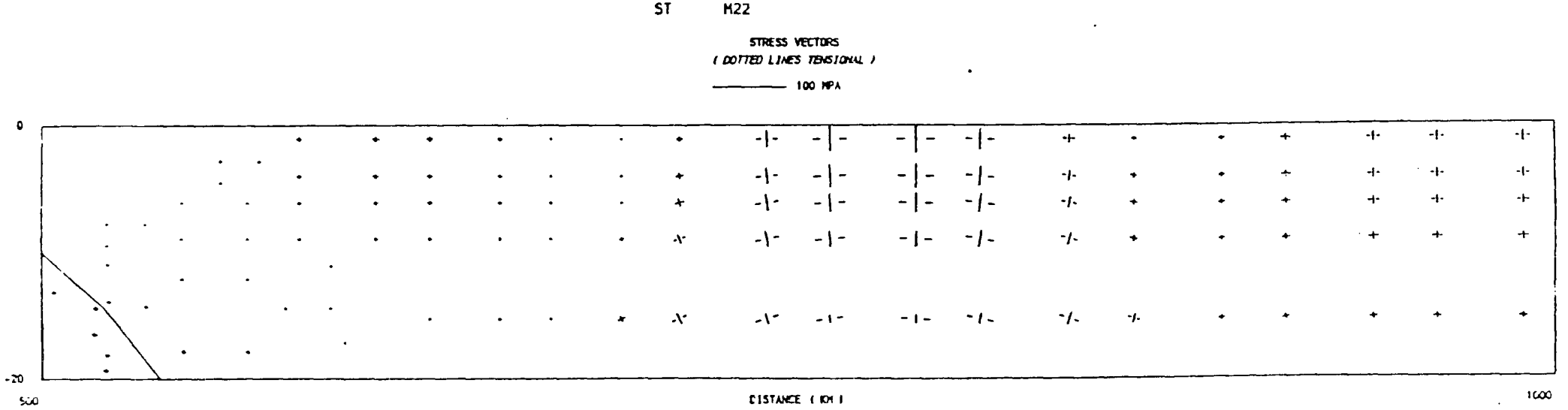

Figure 7.86: The elastic deviatoric principal stresses in the top 20km of the overlying plate in the thermal anomaly model.

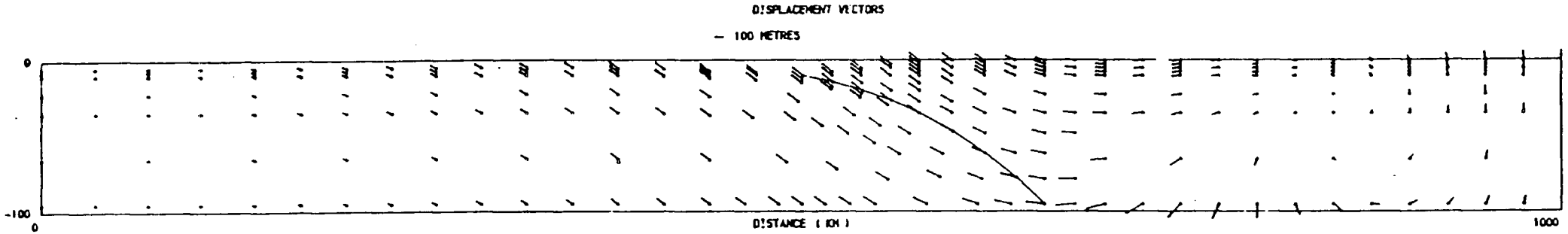

Figure 7.87: The elastic displacements of the thermal anomaly model.

This flexure produces a horizontal tension of 62 MPa at the top of the crust and a horizontal compression of 130 MPa at the base of the lithosphere. It is predicted from these stresses that failure will occur at 1 km depth in the element above the centre of the temperature anomaly. Failure is not predicted anywhere else in the model. The second effect is that the thermal expansion of the overlying plate produces a regional horizontal compression of 60 MPa in the subducting plate and the region of the overlying plate above the subduction zone fault. This compression results from the zero horizontal displacement boundary condition applied to the left hand edge of the model. Because compressive stress of this magnitude is not observed at subduction zones it is concluded that this boundary condition is unrealistic.

These results demonstrate that the temperature anomaly which is produced by the slab induced convection model of Toksoz and Hsui (1978) causes thermal volume changes which produce near surface horizontal tensional stresses in the back arc area of subduction zones. The model predicts that these stresses will be a maximum above the centre of the temperature anomaly and therefore agrees with the hypothesis that the tension driving back arc spreading can be produced by the thermal effects of slab induced convection. The model, however, does not agree with the the hypothesis that back arc spreading is initiated by the thermal effects of slab induced convection because tensional stresses are not predicted in the region of the volcanic arc.

7.6.3 Discussion

The models which have been presented in this section show that both the basal shear stress and the thermal volume changes produce near surface horizontal tensional stresses in the back arc area of subduction zones.

The model therefore supports the hypothesis that slab induced convection can cause tensional tectonics in the overlying plate and consequently may provide the tension to drive back arc spreading.

Both the basal shear stress and the thermal volume changes, however, give rise to either compression or low magnitude tension in the vicinity of the volcanic arc. These results therefore suggest that back arc spreading is not initiated by the slab induced convection cell, contrary to the hypothesis of Toksoz and Hsui (1978). Back arc spreading must therefore be initated by some other mechanism as has been proposed by other authors (Chase, 1978; Uyeda and Kanamori, 1979). Once back arc spreading has been initiated, however, the slab induced convection cell can provide additional tension to drive the spreading.

The models which have been presented in this section assume a subduction rate of 3 cm/yr and a dip of 45 degrees. Although these values are representative of several subduction zones there are some important deviations from this, notably the Marianas where the dip is 80 degrees and the Chile area where the dip is about 20 degrees. It was, however, not possible to quantitatively examine the effect of varying these parameters.

An additional limitation of the models of the thermal anomaly is that it has been assumed that the thermal stresses after 75 million years can be evaluated using an elastic solution. Thermal strains, however, may be relieved by creep over a much shorter period because they are non-renewable. The model of section 7.6.2 consequently represents the maximum stress which could be produced by the temperature anomaly.

Another limitation is that using the zero displacement boundary condition at the edges of the model results in the development of

unrealistically large compressions in the subducting plate. A more realistic solution could possibly be obtained if the left hand boundary was unconstrained.

The final limitation of the models is that they neglect the stress produced by isostatically compensated loading over the hot, low density region in the back arc areas. This may be a significant source of tension in back arc basins.

7.7 Summary And Conclusions

A consistent stress regime is predicted in the subducting plate and in the portion of the overlying plate between the trench axis and the volcanic arc in all of the models which have a slab pull force applied to them. This stress regime is horizontal tension in the subducting plate and horizontal compression in the overlying plate. It has been shown that this stress system is predicted whatever the angle of the slab pull force, the degree of mechanical coupling of the plates or the magnitude of the slab pull force are assumed to be. The consistency of these stresses implies that the lateral variation in the horizontal stress which is observed in these regions at all subduction zones is produced by the slab pull force. It has, however, been shown that the magnitude of the horizontal stress which is produced by the slab pull force is dependent upon the magnitude of the slab pull force, its dip and the degree of mechanical coupling of the plates. The observed variation in the dip of the slab and the degree of mechanical coupling between the plates, therefore, probably explains the observed variation in the tectonic deformation at the leading edge of the overlying plate at different subduction zones.

The state of stress in back arc areas, however, has been shown to be variable. Both horizontal tension and compression can occur. Horizontal tension is produced at active continental margins by the isostatically compensated loading of the crust. Local horizontal tension is also produced by heating and shearing associated with slab induced convection wherever the subducted slab penetrates deeper than a few hundred kilometres. Renewable horizontal tension may also be generated by isostatically compensated loading resulting from the hot, low density mantle associated with slab induced convection. The tensional stress from these sources would not be expected to vary greatly in magnitude between different subduction zones. Regional horizontal compressive stress arising from the slab pull force may be superimposed upon these tensional stresses. Their magnitude, however, is dependent upon the dip and the magnitude of the slab pull force. Unlike the tensional stresses, however, the amount of compression which is transmitted into this region is strongly controlled by the degree of mechanical coupling of the plates at the subduction zone fault. The models therefore demonstrate that the state of stress in back arc areas is critically dependent upon the local interplay between the processes producing tension and compression. This may explain why the stress regime is observed to be so variable in back arc areas.

An important implication of the models is that the largest magnitude tensional stresses, and therefore the most favourable conditions for the development of actively spreading back arc basins, will be developed where the dip of the slab pull force is high and/or the plates are decoupled at the subduction zone fault. This prediction is in good agreement with observations (Uyeda and Kanamori, 1979). The models do not, however, provide a clear explanation of how back arc spreading can be initiated by failure at the volcanic arc. One possibility is that the compression in

this region is reduced as a result of a decoupling of the plates at the subduction zone fault so that the tensional stresses produced by the short wavelength load of the volcanic arc can produce fracture in the crust. An alternative explaination is that the dynamics of the subduction process, which include roll-back (Chase, 1978; Molnar and Atwater, 1978) and the underthrusting resulting from subduction zone earthquakes (Melosh and Fleitout, 1982) could initiate the fracture. The factors which cause the initiation of back arc spreading therefore remain a major outstanding problem.

The models also make two proposals about the origin of the trench suction force. Firstly, they suggest that this arises from the lateral pressure variations at a subduction zone. This occurs because the trench is a low pressure region and the overlying crust a high pressure region. This pressure gradient causes diplacement of the high pressure overlying plate into the low pressure trench. The effect of this displacement is to induce horiontal deviatoric tensions in the crust of the overlying plate. These stresses would be expected to be renewable as long as the trench remains and therefore could explain why this factor is required in all of the models of the plate tectonic driving force. An additional, although much lower magnitude, effect is the renewable shear stress produced by the slab induced convection cell.

The demonstration that the lateral density variations at active continental margins produces a similar effect to the trench suction force has an important implication for the continental splitting mechanism. This is because it is generally considered that Pangea was almost completely surrounded by active continental margin subduction zones. The subducted plate in these regions would probably have a steep dip because it would not

be actively overriden by the supercontinent. In this situation the compression transmitted into the overlying plate would be of a low magnitude so that the trench suction force could cause the tension required to inititiate continental splitting (Bott, 1982b).

In conclusion, the models are important in demonstrating that crustal shortening can occur at subduction zones without necessarily producing regional compression in the overlying plate. They explain that the observed lateral variation in stress across the subducting plate and the overlying plate is caused by the combined effect of lateral density variations and the slab pull force. The variation in stress across the back arc region of subduction zones, however, has been explained in terms of the local balance of the forces producing tension and compression and the mechanical coupling of the plates at the subduction zone fault.

The models developed in this chapter have therefore gone some way towards establishing the major sources of stress at a general subduction zone. Future analyses should concentrate on analysing the stress produced by these forces at particular examples of subduction zones.

Despite the general success of the models which have been presented in this chapter there are some shortcomings of the present analysis. These are:

1. The bending stress arising from the flexure of the subducting plate have not been modelled. These stresses would be superimposed upon the stress regime modelled in the subducting plate and would therefore locally modify the stress regime.

2. The downpull effect of the viscous drag flow in the asthenospheric wedge between the subducting and overlying plate (Tovish et al, 1978) has not been modelled. This effect may contribute to the compression at the leading edge of the overlying plate.

3. The dynamic forces arising from the subduction process have not been modelled. The principal dynamic forces are the roll back of the subducting plate (Elsasser, 1971; Chase, 1978; Molnar and Atwater, 1978; Kanamori and Uyeda, 1979) and the underthrusting occuring during earthquakes (Melosh and Fleitout, 1982). These forces may contribute towards the trench suction effect and may cause the initiation of back arc spreading by failure at the volcanic arc.

Future analyses should therefore give attention to these effects.

CHAPTER 8

SUMMARY AND CONCLUSIONS

The isoparametric finite element method has been used in this thesis to model the stress regime at subduction zones. There have been two aims to this study. The first has been to investigate why a lateral variation of stress is observed between the subducting plate and the leading edge of the overlying plate at all subduction zones. The second has been to determine why the stress regime in back arc regions is so variable between different subduction zones.

Several problems are posed when attempting to model the stress regime in such tectonically complex areas as subduction zones, and consequently, much of this thesis has been an attempt to resolve these difficulties.

The initial problem was to chose a realistic rheological model of the lithosphere upon which the mathematical models can be based. A simplified rheological model has been used in which the lithosphere is assumed to be subdivided into an upper elastic layer, which deforms non-elastically by brittle fracture, and an underlying visco-elastic layer which creeps in response to long term loads.

The second problem has been to chose a suitable mathematical technique which can realistically model the stress regime in such complex regions as subduction zones. One technique which has been popular and successful in modelling lithospheric stress regimes is the constant strain triangle (CST) finite element method. It has been demonstrated in this thesis, however,

that this method has two disadvantages. Firstly, it acts too stiffly if the finite element mesh is not optimally designed. Secondly, it gives skewed stress and displacement vectors in elastic and visco-elastic problems when the strain gradient is high. These two limitations degrade the predictiveness and accuracy of CST models. A higher order quadratic isoparametric finite element, which does not exhibit any of these undesirable features, has consequently been used in this thesis. An additional advantage of this method is that it enables curved-sided finite elements to be introduced.

The final problem has been to develop a method which is capable of modelling the deformation on the subduction zone fault. The solution adopted in this thesis was to adapt Mithen's (1980) CST model of frictional sliding to the isoparametric method. This method was used to model the deformation following frictional sliding on plane normal faults and predicted graben widths which agree with analytic solutions. This suggests that Mithen's CST models failed to agree with analytic solutions because they were too stiff, and consequently, that the isoparametric method should be used to re-investigate his subsequent analysis of graben development. Two additional advantages of the isoparametric fault model are that it can be used to study the deformation on thrust faults, and also on listric faults. This method is consequently suitable for modelling the deformation on the curved subduction zone fault.

These isoparametric finite element methods have been incorporated into a computer program which is suitable for modelling static lithospheric stess distributions in a variety of tectonic settings.

Analysis of the stress regime at subduction zones has shown that the slab pull force causes tension in the subducting plate and compression at the leading edge of the overlying plate. This force may possibly be the dominant cause of the lateral variation in stress which is observed in this region at all subduction zones. The magnitude of the stress produced by the slab pull force, however, is dependent upon the dip, age and depth extent of the subducted plate. The stress distribution is also dependent upon the degree of mechanical coupling between the plates at the subduction zone fault. Local differences in these factors may therefore explain the observed variation in the tectonic deformation of this region at different subduction zones.

Several forces produce different stress regimes in the back arc region of subduction zones. Tension is produced by lateral density variations and also by the heating and shearing arising from the slab induced convection. The magnitude of the tensional stress arising from these mechanisms should be approximately constant at all subduction zones. Compressive stress, arising from the slab pull force, is superimposed upon the tensional stress. The magnitude of the compressive stress, however, is dependent upon two factors. Firstly, the dip and the magnitude of the slab pull force. Secondly, upon the degree of mechanical coupling between the plates at the subduction zone fault. It has been shown that if the coupling is weak, no compression will be transmitted into the back arc region by the slab pull force. Local differences in these two factors may therefore explain why the state of stress is so variable in the back arc regions of different subduction zones, and also why tension is more common than compression. Roll-back of the subducting plate, which has not been included in the models, may be an additional cause of the dominance of tensional stress in the overlying plate. Future investigations should

therefore evaluate the stress regime which is produced by this mechanism.

The models which have been produced have accounted for some of the principal features of the observed stress regime at subduction zones. There are, however, three major limitations of the present analysis:

1. A visco-elastic rheology has been used to model creep in the lower seismic lithosphere rather than the power law creep rheology which is suggested by rock mechanic experiments. Although this represents a major simplification, previous analyses have demonstrated that the stress following relaxation is independent of which rheology is used, and it is therefore unlikely that using a power law creep rheology would substantially modify the conclusions of this analysis.

2. Bending stresses arising from the flexure of the subducting plate have not been included in the models. Stresses from this source would be superimposed upon those which have been modelled and could cause important local variations in the stress in the subducting plate.

3. The effect of the dynamic forces associated with the subduction process have not been modelled. This is because the finite element methods which have been used can only model static stress distributions. This is a major limitation of the present analysis because dynamic forces, particularly those arising from the roll-back of the subducting plate, may be an important cause of the trench suction effect and consequently important in generating the stress regime in the overlying plate. This may explain why the present analysis has been unable to explain how back arc

spreading is initiated by a fracture at the volcanic arc.

Our understanding of the origin of the stress regime at subduction zones could consequently be improved by developing more sophisticated models of these regions.

APPENDIX

COMPUTER PROGRAMS

A.1 Introduction

The computer programs which have been written to analyse lithospheric stress regimes are based upon the isoparametric finite element formulation which has been described in chapters 3 and 5. They are capable of modelling the elastic or visco-elastic stresses which are produced by body forces, boundary forces, thermal volume changes and frictional sliding on a fault.

The programs are written in a modular form in IBM FORTRAN IV and are stored in two files called ISOFELP and ISOLIB. ISOLIB is a library file which contains one subroutine to perform each finite element operation, such as assembling or inverting the stiffness matrix. ISOFELP is a calling program through which the user may call any combination of the available modules in ISOLIB.

There are three steps which must be followed when using these programs to run a finite element model. The first is to modify ISOFELP so that it calls the desired finite element routines. The second is to input data describing the finite element model. The final step is to link and run the programs. The aim of this appendix is to document each of these procedures so that the programs can be used to model lithospheric stress regimes.

A.2 ISOLIB: Description Of Subroutines

To keep the programs as flexible as possible each finite element operation has been coded as a separate subroutine and stored in a library file called ISOLIB. In addition to these several external subroutines are called. The aim of this section is to describe the function of each of these subroutines so that the user can construct a calling sequence (section A.3).

A.2.1 Finite element subroutines

The aim of this section is to describe the operations which are performed by each of the finite element subroutines which can be called by ISOFELP.

READ : reads in all the data which are required to set up a particular finite element model. The input specification for this subroutine is described in section A.3.

ECHO : prints the data read in by READ on device 5. The function of this module is to allow the user to check that there are no errors in the data file which was read in by READ.

FORMK : assembles the global stiffness matrix of the finite element model. It should be called every time an elastic or visco-elastic stress distribution is to be evaluated.

TANOM : calculates the body forces arising from thermal volume changes.

BODY4S: calculates the body forces arising from the density distribution of the model.

ISOS : calculates isostatic restoring forces at specified nodes of the

model.

BOUNDS: introduces the prescribed displacements of the model by modifying the force vector and stiffness matrix (Park, 1981). This routine should be called in every finite element job.

ELVIS : evaluates the elastic or visco-elastic displacements of the model by inverting the stiffness matrix.

FSHEAR: evaluates the displacements produced by frictional sliding on the fault.

STRESS: calculates the principal stresses in the model.

FAIL : uses the modified Griffith theory to test if brittle fracture has occured in the model.

DISOUT: prints the displacements of each node to device 7.

STOUT : prints the principal stresses of each element to device 7.

PAMS : initialises the plotting parameters. It should be called every time that plotted output is required.

GRID : plots the finite element mesh.

VECPLT: plots the principal stresses in the model.

SURF : plots the vertical displacement profile of specified nodes in the model.

DISVEC: plots the displacement vectors of the model.

DEVST : calculates the deviatoric stress vectors of the model.

A.2.2 External subroutines

Three external subroutine libraries are internally referenced in ISOLIB. The first is the MTS system subroutine TIME which evaluates the CPU time which elapses between specified instructions. The second is the *HARWELL subroutine MA07BD which inverts a banded coefficient matrix. The third is the *GHOST plotting system. There are numerous calls to routines in this library (e.g. FRAME and GREND).

A.3 ISOFELP: The Construction Of A Calling Sequence

ISOFELP (ISOparametric Finite ELement Package) is the main FORTRAN written programming segment. This program contains a call to each of the finite element subroutines which have been described in section A.2.1. In most finite element jobs it will not be desired to call all of the available subroutines. The user must therefore define those modules which are not to be called by inserting a C in the first column of the relevant line(s). This has the effect of making the call a comment, which is non-executable during running of the program.

This approach therefore provides the user with a set of subroutines which can be used to model a wide range of problems simply by modifying the subroutines which are called.

A.4 Utilisation

Once the user has modified ISOFELP there are two further steps to complete. The first is to generate a set of input data which describes the geometry, physical properties and boundary conditions of the model. The second step is to link and run the programs. These two steps are

documented in this section.

A.4.1 Input specification: Device 4

The data describing the geometry, material properties and boundary conditions of the model are input on device 4. The parameters are as follows:

NNOD	NTRI	NQUAD	NMAT	NFIX	NDIR	NSEG	NSI	NST	NFS

JNOD	XCORD	YCORD

EM	PM	RHOM	TM	ETAM

JEL	NODE1	NODE2	NODE3	NODE4	NODE5	NODE6	ITYP	NGAUSS

JEL	NODE1	NODE2	NODE3	NODE4	NODE5	NODE6	NODE7	NODE8	ITYP	NGAUSS

NOD4S	FX	FY

NODS

NDIS	FNORM	FTAN

NOFIX	IXFIX	XFIX	IYFIX	YFIX

NITS

KN	KS

MU	FAC

NELL	NODL	NELR	NODR

NSEG

NODIC	RHO

NODI

Card 1: General model information

field	1-5	6-10	11-15	16-20	21-25	26-30	31-35	36-40	41-45	46-50
	NNOD	NTRI	NQUAD	NMAT	NFIX	NDIR	NSEG	NSI	NST	NFS

This card defines the general information on the model. It must be specified for every finite element job which is run. The parameter definitions are as follows:

NNOD [I5]: The number of nodes in the finite element grid. NNOD must be greater than or equal to 6. Up to 350 nodes can be defined.

NTRI [I5]: The number of triangular finite elements. Up to 300 triangular elements can be defined.

NQUAD [I5]: The number of quadrilateral finite elements. Up to 300 quadrilateral elements can be defined.

NMAT [I5]: The number of material types. NMAT must be greater than 0. Up to 10 different material types can be defined.

NFIX [I5]: The number of nodes at which displacement boundary conditions are to be applied. NFIX must be greater than 0. Up to 100 fixed displacements can be defined.

NDIR [I5]: The number of nodes at which direct nodal forces are to be applied.

NSEG [I5]: The number of surfaces over which distributed forces are to be applied.

NSI [I5]: Flag indicating the units of the nodal co-ordinates.
NSI = 0 Units are kilometres
NSI = 1 Units are metres

NST [I5]: Flag indicating whether the model is to be calculated assuming plane strain or plane stress.
NST = 0 Plane strain
NST = 1 Plane stress

NFS [I5]: Number of dual nodes. Up to 50 dual nodes can be defined.

Card 2: Node definition

Field	1-5	6-15	16-25
	JNOD	X	Y

This card defines the node number and its co-ordinates in MSI units. There should be NNOD of these cards. The parameter definitions are as follows:

JNOD [I5]: The node number.

X [F10.3]: The x co-ordinate of the node.

Y [F10.3]: The y co-ordinate of the node. This should be negative for depths beneath sea level.

Card 3: Material Properties.

Field	1-10	11-20	21-30	31-40	41-50
	EM	PM	RHOM	TM	ETAM

This card defines the elastic and visco-elastic properties of the material types. There should be NMAT of these cards. The definition of the parameters is as follows:

EM [D10.3]: Young's modulus in Nm.

PM [F10.3]: Poisson's ratio.

RHOM [F10.3]: Density in kg m.

TM [D10.3]: Tensile strength in MPa.

ETAM [D10.3]: Viscosity of layer in Pa s. If this is 0.0 the layer is assumed to be elastic.

Card 4: Topology of triangular elements

Field	1-5	6-10	11-15	16-20	21-25	26-30	31-35	36-40	41-45
	JEL	NODE1	NODE2	NODE3	NODE4	NODE5	NODE6	ITYP	NGAUS

This card defines the topology of the triangular finite elements. There should be NTRI of these cards. The nodes must be supplied in a clockwise or anticlockwise direction. The definition of these parameters is as follows:

JEL [I5]: The element number.

NODE1 [I5]: The number of the first node. This must be a node at one of the corners of the element.

NODE2 [I5]: The number of the second node.

NODE3 [I5]: The number of the third node.

NODE4 [I5]: The number of the fourth node.

NODE5 [I5]: The number of the fifth node.

NODE6 [I5]: The number of the sixth node.

ITYP [I5]: The number of the material type for this element.

NGAUS [I5]: The number of Gaussian integration points in this element. This should be either 3, 4 or 6.

Card 5: Topology of quadrilateral elements

Field	1-5	6-10	11-15	16-20	21-25	26-30	31-35	36-40	41-45	46-50	51-55
	JEL	NODE1	NODE2	NODE3	NODE4	NODE5	NODE6	NODE7	NODE8	ITYP	NGAUS

This card defined the topology of the quadrilateral finite elements. There should be NQUAD of these cards. The nodes must be supplied in a clockwise or anticlockwise direction. The definition of these parameters is as follows:

JEL [I5]: The element number.

NODE1 [I5]: The number of the first node. This must be a node at one of the corners of the element.

NODE2 [I5]: The number of the second node.

NODE3 [I5]: The number of the third node.

NODE4 [I5]: The number of the fourth node.

NODE5 [I5]: The number of the fifth node.

NODE6 [I5]: The number of the sixth node.

NODE7 [I5]: The number of the seventh node.

NODE8 [I5]: The number of the eigth node.

ITYP [I5]: The number of the material type for this element.

NGAUS [I5]: The number of Gaussian integration points in this element. This should be either 4 or 9.

Card 6: Direct nodal forces

Field	1-5	9-20	24-35
	NOD4S	FX	FY

This card defines the magnitude of the direct x and y forces which are to be applied to nodes of the model. There should be NDIR of these cards. The parameters have the following definitions.

NOD4S [I5]: The node number.

FX [F11.3]: The magnitude of the x component of the direct force in N.

FY [F11.3]: The magnitude of the y component of the direct force in N.

Cards 7 and 8: Distributed nodal forces

Field	1-5	9-20	24-35
	NODS		
	NDIS	FNORM	FTAN

This card defines the magnitude of the normal and shear components of the distributed forces which act upon the surface of the model. The parameter descriptions are as follows:

NODS [I5]: The number of nodes at which distributed forces are to be applied. There should be NSEG of these cards.

NDIS [I5]: The node number.

FNORM [F11.3]: The magnitude of the normal component of the force.

FTAN [F11.3]: The magnitude of the tangential component of the force.

Card 9: Prescribed displacements

Field 1-5 6-10 11-20 21-25 26-35

NOFIX	IXFIX	XFIX	IYFIX	YFIX

This card defines the dislacement boundary conditions which are to be applied to nodes of the finite element models. There should be NFIX of these cards. The parameter definitions are as follows:

NOFIX [I5]: The node number.

IXFIX [I5]: Flag which must equal 1 if the x co-ordinate of displacement is to be fixed.

XFIX [F10.3]: The value of the fixed x displacement in metres.

IYFIX [I5]: Flag which must equal 1 if the y co-ordinate of displacement is to be fixed.

YFIX [F10.3]: The value of the fixed y displacement in metres.

Cards 10 to 12: Fault information

Field 1-5 6-10 11-20

NITS		
KN	KS	
MU	FAC	

These cards define the elastic properties and location of the fault element. The parameters are defined as follows:

NITS [I5]: The maximium number of iterations to perform in order to reduce the excess shear stress on the fault.

KN [F10.3]: The normal stiffness of the fault element in N m.

KS [F10.3]: The shear stiffness of the fault element in N m.

MU [F10.3]: The coefficient of friction on the fault.

FAC [F10.3]: The convergence factor to multiply the fault force vector by.

Card 13: Fault geometry

Field 1-5 6-10 11-15 16-20

NELL	NODL	NELR	NODR

These parameters are a list of the number of the dual nodes and the element which they belong to. There should be NFS of these cards.

NELL [I5]: The number of the element on the left hand side of the fault.

NODL [I5]: The number of the dual node on the left hand side of the fault.

NELR [I5]: The number of the element on the right hand side of the fault.

NODR [I5]: The number of the dual node on the right hand side of the fault.

Cards 14 to 16: Isostatic compensation information

Field 1-5 6-15

NSEG	
NODIC	RHO
NODI	

These cards define the isostatic compensation which is to be applied at a given set of nodes. The parameter definitions are as follows:

NSEG [I5]: The number of segments over which isostatic compensation is to be applied.

NODIC [I5]: The number of nodes on a segment. There should be one of these cards for every NSEG.

RHO [F10.3]: The compensation density in kg m. There should be one of these cards for every NSEG.

NODI [I5]: The node numbers at which isostatic compensation is to be applied. There should be NODIC of these cards for every NSEG.

A.4.2 Input specification: Device 3

The data defining the thermal anomaly is input on device 3. The following cards are required:

```
 -----
|NNT  |
 ----------------
|NODT |DELT      |
 ----------------
```

The parameter definitions are as follows:

NNT [I5]: The number of nodes with temperature anomalies. The maximum number which can be defined is 350.

NODT [I5]: The node number. There should be NNT of these cards.

DELT [F10.3]: The temperature anomaly.

A.4.3 Input specification: Device 5

General information on the model is input on device 5. The following cards are required.

TITLE	
XMIN	XMAX
YMIN	YMAX
XPLTLEN	YPLTLEN

These cards define the title of the job and the plot scales. The parameters have the following definitions:

TITLE [8A4]: The title of the job.

XMIN [F10.3]: The minimum x co-ordinate to plot.

XMAX [F10.3]: The maximum x co-ordinate to plot.

YMIN [F10.3]: The mimimum y co-ordinate to plot.

YMAX [F10.3]: The maximum y co-ordinate to plot.

XPLTLEN [F10.3]: The x length of the plot in inches.

YPLTLEN [F10.3]: The y length of the plot in inches.

A.4.4 Running the programs

The procedure for running the programs on NUMAC is described in this section.

Before running any models it is essential to compile ISOLIB. It has been found useful to store this in a permanent file, OBJISOLIB. This is because a considerable CPU time is required to compile these subroutines. This program can then be used for any number of finite element jobs unless the user wishes to modify the internal coding in the subroutines of ISOLIB.

Once ISOLIB has been compiled there are two steps in running the programs:

1. Compile ISOFELP. This should be performed whenever the calling sequence has been modified. It is performed by issuing the command

```
$RUN *FTNX SCARDS=ISOFELP SPUNCH=OBJISOFELP
```

2. Link and run the programs. At this stage the subroutines in ISOLIB must be linked with the external routines from the *HARWELL and *GHOST libraries. The command to run these programs is;

```
$RUN OBJISOFELP+OBJISOLIB+*HARWELL+*GHOST 3=TEMPS 4=MODEL 5=GINPUT
        6=*SINK* 7=RESULTS 8=VISCOUT 9=PLOT 10=FAULTOUT
```

Where:

TEMPS is an input file described in section A.4.2.

MODEL is an input file described in section A.4.1.

GINPUT is an input file described in section A.4.3.

RESULTS contains the displacements and stress vectors.

VISCOUT contains information on the convergence of the visco-elastic routines.

PLOT is the plot file.

FAULTOUT contains information on the convergence of the fault model.

A.5 Program Listings

```
C
C***** ISOFELP : A CALLING PROGRAM FOR USE WITH ISOLIB *****
C*****                                                 *****
C*****                    WRITTEN AT DURHAM UNIVERSITY *****
C*****                          BY G.D.WAGHORN         *****
C
C
      IMPLICIT REAL*8 (A-H,O-W)
      REAL*8 KN,KS,MU
      COMMON /CONS/ NTRI,NQUAD,NINCS,NNOD,KSIZE,KSBW,NNOD2,NMAT,INITEM,
     +              IDATE(3),TIMINC,TITLE(4),PI,ZUF(4)
      COMMON /NODS/ XCOM0(700),DUMP(1400),XCOM1(2400)
      COMMON /FALE/ STR0(4,350),CFAIL(4,300),FANGL(4,300),IFAIL(4,300)
      COMMON /ELEM/ NODEL(8,300),ICOM2(1500),COM4(61500)
      COMMON /FIXT/ DFIX(2,100),ICOM3(300),NFIX
      COMMON /MATS/ CMAT(73),ITYP(300)
      COMMON /STNR/ PREVST(3,300),XCENT(300),YCENT(300),INC,ICALL
      COMMON /VARS/ COMB(129),ICOM1(5)
      COMMON /VISC/ VCOM(33800)
      COMMON /GAPT/ S,T,SHAPE(8),COM7(1633)
      COMMON /STIF/ ELK(18,18),GLOBK(700,185)
      COMMON /NEWS/ BSTRES(64,300),SCREP(16,300),OSCREP(16,300),
     +              STRST(16,300)
      COMMON /FALT/ KN,KS,MU,FAC,DEFAULT(12,2,50),
     +  DEPTH(50,2),THETA(50),FLTCRP(24,50),DFLTCR(24,50),
     +              STFBGN(24,50),NONOD(50,2),NELF(50,2),NITS,NFS
C
      CALL TIME(0,1)
      NINCS=0
      TIMINC=0.0D+00
      CALL READ
C     CALL ECHO
      CALL FORMK
      INITEM=0
C     CALL TANOM
C     CALL BODY4S
      CALL ISOS
      CALL BOUNDS
      CALL ELVIS
C     CALL FSHEAR
      CALL DISOUT
      CALL STRESS
      CALL FAIL
      CALL STOUT
C     CALL VSTOUT
      CALL PAMS
C     CALL GRID
C     CALL FRAME
      CALL DISVEC
      CALL FRAME
      CALL VECPLT
C     CALL OUTLIN
C     CALL FRAME
C     CALL DEVST
C     CALL VECPLT
      CALL FRAME
      CALL SURF
      CALL GREND
C
      STOP

      END
```

```
C
C
C***** ISOLIB : AN ISOPARAMETRIC FINITE ELEMENT SUBROUTINE
C*****          LIBRARY FOR FINDING LITHOSPHERIC STRESS
C*****          DISTRIBUTIONS.
C*****
C*****          WRITTEN AT DURHAM UNIVERSITY BY G.WAGHORN
C*****
C
      SUBROUTINE READ
C     ===============
C
C***** READ IN ALL INFORMATION REQUIRED TO SET UP MODEL
C
      IMPLICIT REAL*8 (A-H,O-W)
      REAL*8 KN,KS,MU
      COMMON /CONS/ NTRI,NQUAD,NINCS,NNOD,KSIZE,KSBW,NNOD2,NMAT,NST,
     +              IDATE(3),TIMINC,TITLE(4),PI,ZUF(4)
      COMMON /NODS/ X(350),Y(350),DISP(700),FORCE(700),XCOM1(2400)
      COMMON /ELEM/ NODEL(6,300),NGAUSS(300),NOTEL(300),NOQEL(300),
     +              NOD4S(100),NOIS4S(100),NLOAD(100),NCOM1(300),FNOD(200),
     +              FNORM(100),FTAN(100),FNTOT(100),FTTOT(100),
     +              COMO(60900)
      COMMON /FALT/ KN,KS,MU,FAC,DFAULT(12,2,50),
     +  DEPTH(50,2),THETA(50),FLTCRP(24,50),DFLTCR(24,50),
     +              STFBGN(24,50),NONOD(50,2),NELF(50,2),NITS,NFS
      COMMON /FIXT/ DFIX(2,100),NCFIX(100),IFLAG(2,100),NFIX
      COMMON /MATS/ EM(9),PM(9),TM(9),RHOM(9),ETAM(9),C(9,3),ITYP(300)
      COMMON /VARS/ COMB(129),NOSECT,NOIS,NOIR,ICOMX(2)
C
C***** READ TITLE OF JOB
C
      WRITE(6,10)
   10 FORMAT(1H0,'PLEASE GIVE TITLE (4A8)'/
     +       ' ----------------------------------')
      READ(5,20)TITLE
   20 FORMAT(4A8)
C
C***** READ IN MODEL INFORMATION
C
      READ(4,30)NNOD,NTRI,NQUAD,NMAT,NFIX,NOIR,NSEG,NSI,NST,NFS
   30 FORMAT(11I5)
      NNOD2=NNOD*2
C
C***** READ IN NODAL INFORMATION
C
      DO 50 INOD=1,NNOD
      READ(4,40)JNOD,X(JNOD),Y(JNOD)
   40 FORMAT(I5,2F10.3)
C
C***** EXPRESS CO-ORDINATES IN S.I. UNITS (METRES)
C
      IF (NSI.NE.0) GO TO 50
      X(JNOD)=X(JNOD)*1.0E3
      Y(JNOD)=Y(JNOD)*1.0E3
   50 CONTINUE
C
C***** READ IN PROPERTIES OF MATERIAL TYPES
C
      DO 70 IMAT=1,NMAT

      READ(4,60)EM(IMAT),PM(IMAT),RHOM(IMAT),TM(IMAT),ETAM(IMAT)
   60 FORMAT(D10.3,2F10.3,2D10.3)
   70 CONTINUE
C
C***** READ ELEMENT TOPOLOGIES MATERIAL NO'S AND NO GAUSS POINTS
C
      IF (NTRI.EQ.0)GO TO 100
      DO 90 IEL=1,NTRI
      READ(4,80) JEL,(NODEL(KEL,JEL),KEL=1,6),ITYP(JEL),NGAUSS(JEL)
   80 FORMAT(9I5)
      NOTEL(IEL)=JEL
   90 CONTINUE
C
  100 IF (NQUAD.EQ.0) GO TO 125
C
```

```
      DO 120 IEL=1,NQUAD
      READ(4,110) JEL,(NODEL(KEL,JEL),KEL=1,8),ITYP(JEL),NGAUSS(JEL)
  110 FORMAT(11I5)
      NOQEL(IEL)=JEL
  120 CONTINUE
C
C**** INITIALIZE FORCE VECTOR
C
  125 DO 130 IFO=1,NNOD2
      FORCE(IFO)=0.0
  130 CONTINUE
C
C
C**** READ IN DIRECT NODAL FORCE COMPONENTS
C
      NDIS=0
      IF (NDIR.EQ.0) GO TO  141
      DO 140 I=1,NDIR
      READ(4,150)NOD4S(I),FNOD(2*I-1),FNOD(2*I)
  150 FORMAT(I5,2(4X,D11.4))
      FORCE(2*NOD4S(I)-1)=FNOD(2*I-1)
  140 FORCE( 2*NOD4S(I) )=FNOD( 2*I )
C
C**** READ IN DISTRIBUTED SURFACE TRACTIONS
C
  141 IF (NSEG.EQ.0) GO TO 144
C
      DO 142 I=1,NSEG
      READ(4,150)NODSEG
      DO 143 J=1,NODSEG
      READ(4,150)NDIS4S(J),FNORM(J),FTAN(J)
      NLOAD(NDIS+J)=NDIS4S(J)
      FNTOT(NDIS+J)=FNORM(J)
      FTTOT(NDIS+J)=FTAN(J)
  143 CONTINUE
      NOSECT=(NODSEG-1)/2
      CALL GLOBF
      NDIS=NDIS+NODSEG
  142 CONTINUE
C
C**** READ PRESCRIBED DISPLACEMENTS
C
  144 IF (NFIX.EQ.0)GO TO 180
      DO 170 I=1,NFIX
      READ(4,160)NOFIX(I),(IFLAG(J,I),DFIX(J,I),J=1,2)

  160 FORMAT(I5,2(I5,D10.3),F10.3)
  170 CONTINUE
  185 IF (NFS.EQ.0) GO TO 180
C
C**** READ IN DATA ON THE FAULT
C
      READ(4,30 )NITS
      READ(4,250)KN,KS
      READ(4,250)MU,FAC
  250 FORMAT(2E10.3)
      DO 210 I=1,NFS
  210 READ(4,30)NELF(I,1),NONOD(I,1),NELF(I,2),NONOD(I,2)
C
  180 WRITE(6,190)
  190 FORMAT('0READING OF DATA COMPLETED')
      CALL TIME(1,1)
C
      RETURN
      END
C
C
C*********************************************************************************************
C
```

```
C
      SUBROUTINE GLOBF
C     ================
C
C**** CALCULATE THE CONTRIBUTION TO THE GLOBAL FORCE VECTOR
C**** OF NORMAL AND TANGENTIAL NODAL PRESSURES.
C
      IMPLICIT REAL*8 (A-H,O-W)
      COMMON /NODS/ X(350),Y(350),DISP(700),FORCE(700),XCOM1(2400)
      COMMON /GAPT/ S,T,SHAPE(8),DNXDS(8),DNXDT(8),PCOM(1611),
     +              PLACEL(3),WEILIN(3)
      COMMON /ELEM/ NODEL(8,300),NGAUSS(300),NOTEL(300),NOQEL(300),
     +              NOD4S(100),NDIS4S(100),NLOAD(100),NCOM1(300),FNOD(200),
     +              FNORM(100),FTAN(100),FNTOT(100),FTTOT(100),
     +              COMO(60900)
      COMMON /VARS/ COMB(129),NOSECT,
     +              NDIS,NDIR,ICOMX(2)
C
C**** CALCULATE GLOBAL FORCE COMPONENT FOR EACH ELEMENT EDGE
C
      DO 80 IS=1,NOSECT
      LNOD2=2*IS
      LNOD1=LNOD2-1
      LNOD3=LNOD2+1
      NOD1=NDIS4S(LNOD1)
      NOD2=NDIS4S(LNOD2)
      NOD3=NDIS4S(LNOD3)
C
C**** EVALUATE THE CONTRIBUTION TO THE FORCE VECTOR AT EACH GAUSS POINT
C
      DO 60 IG=1,3
      S=PLACEL(IG)
      DS=WEILIN(IG)
      SS=S*S
      SHAPE(1)=(SS-S)/2.0
      SHAPE(2)=1.0-SS
      SHAPE(3)=(SS+S)/2.0

      DNXDS(1)=S-0.5
      DNXDS(2)=-2.0*S
      DNXDS(3)=S+0.5
      DXXDS=DNXDS(1)*X(NOD1)+DNXDS(2)*X(NOD2)+DNXDS(3)*X(NOD3)
      DYXDS=DNXDS(1)*Y(NOD1)+DNXDS(2)*Y(NOD2)+DNXDS(3)*Y(NOD3)
      PN=FNORM(LNOD1)*SHAPE(1)+FNORM(LNOD2)*SHAPE(2)+
     +   FNORM(LNOD3)*SHAPE(3)
      PT=  FTAN(LNOD1)*SHAPE(1)+ FTAN(LNOD2)*SHAPE(2)+
     +    FTAN(LNOD3)*SHAPE(3)
      DSX=(PT*DXXDS-PN*DYXDS)*DS
      DSY=(PN*DXXDS+PT*DYXDS)*DS
      FORCE(2*NOD1-1)=SHAPE(1)*DSX+FORCE(2*NOD1-1)
      FORCE( 2*NOD1 )=SHAPE(1)*DSY+FORCE( 2*NOD1 )
      FORCE(2*NOD2-1)=SHAPE(2)*DSX+FORCE(2*NOD2-1)
      FORCE( 2*NOD2 )=SHAPE(2)*DSY+FORCE( 2*NOD2 )
      FORCE(2*NOD3-1)=SHAPE(3)*DSX+FORCE(2*NOD3-1)
      FORCE( 2*NOD3 )=SHAPE(3)*DSY+FORCE( 2*NOD3 )
   60 CONTINUE
   80 CONTINUE
  100 CONTINUE
C
      RETURN
      END
C
C
C*****************************************************************************
C
C
      SUBROUTINE ECHO
C     ===============
C
C**** ECHO'S DATA INPUT TO DEVICE 7
C
      IMPLICIT REAL*8 (A-H,O-W)
      REAL*8 KN,KS,MU
      COMMON /CONS/ NTRI,NQUAD,NINCS,NNOD,KSIZE,KSRW,NNOD2,NMAT,NST,
     +              IDATE(3),TIMINC,TITLE(4),PI,ZUF(4)
```

```
      COMMON /NODS/ X(350),Y(350),DISP(700),FORCE(700),XCOM1(2400)
      COMMON /ELEM/ NODEL(8,300),NGAUSS(300),NOTEL(300),NOQEL(300),
     +              NOD4S(100),NDIS4S(100),NLOAD(100),NCOM1(300),FNOD(200),
     +                 FNORM(100),FTAN(100),FNTOT(100),FTTOT(100),
     +                 COMD(60900)
      COMMON /FALT/ KN,KS,MU,FAC,BFAULT(12,2,50),
     +  DEPTH(50,2),THETA(50),FLTCRP(24,50),OFLTCR(24,50),
     +                 STFBGN(24,50),NONOD(50,2),NELF(50,2),NITS,NFS
      COMMON /FIXT/ OFIX(2,100),NOFIX(100),IFLAG(2,100),NFIX
      COMMON /MATS/ EM(9),PM(9),TM(9),RHOM(9),ETAM(9),C(9,3),ITYP(300)
      COMMON /VARS/ COMB(129),NOSECT,NDIS,NDIR,ICOMX(2)
C
      CALL TIME(5,0,IDATE)
C
C**** WRITE HEADINGS
C
      WRITE(7,10)IDATE,TITLE
   10 FORMAT(1H0,12X,3A4,34X,'** INPUT TO ISOFELP **'/
     +                 1H+,58X,'   ----------------'/1H0,55X,4A8)
C
C**** WRITE NODAL INFORMATION
C
      WRITE(7,20)NNOD
C
   20 FORMAT(1H0,10X,'NUMBER OF NODES =',I4)
C
      WRITE(7,30)
   30 FORMAT(1H0,10X,'NODAL COORDINATES'/
     +       1H+,10X,'               '/
     +       1H0,30X,'NODE',I4X,'X(I): M',15X,'Y(I): M'/1H0)
      DO 40 I=1,NNOD
   40 WRITE(7,50)I,X(I),Y(I)
   50 FORMAT(31X,I4,2(12X,1PE10.3))
C
C**** WRITE INFORMATION ON TRIANGULAR ELEMENTS
C
      WRITE(7,60)NTRI
   60 FORMAT(1H0,10X,'NUMBER OF TRIANGULAR ELEMENTS =',I4)
      IF (NTRI.EQ.0) GO TO 100
      WRITE(7,70)
   70 FORMAT(1H0,10X,'TRIANGULAR ELEMENTS'/
     +       1H+,10X,'                  '/
     +       1H0,10X,'ELEMENT',3X,'NODE1',3X,'NODE2',3X,'NODE3',3X,
     +               'NODE4',3X,'NODE5',3X,'NODE6',3X,'MAT',3X,
     +               'GAUSS PT'/1H0)
      DO 80 I=1,NTRI
      NUMEL=NOTEL(I)
   80 WRITE(7,90)NUMEL,(NODEL(J,NUMEL),J=1,6),ITYP(NUMEL),NGAUSS(NUMEL)
   90 FORMAT(11X,I4,5X,6(I4,4X),I3,5X,I4)
C
C**** WRITE INFORMATION ON TRIANGUALR ELEMENTS
C
  100 WRITE(7,110)NQUAD
  110 FORMAT(1H0,10X,'NUMBER OF QUADRILATERAL ELEMENTS =',I4)
      IF (NQUAD.EQ.0) GO TO 150
      WRITE(7,120)
  120 FORMAT(1H0,10X,'QUADRILATERAL ELEMENTS'/
     +       1H+,10X,'                  '/
     +       1H0,10X,'ELEMENT',3X,'NODE1',3X,'NODE2',3X,'NODE3',3X,
     +           'NODE4',3X,'NODE5',3X,'NODE6',3X,'NODE7',3X,'NODE8',
     +           3X,'MAT',3X,'GAUSS PT'/1H0)
      DO 130 I=1,NQUAD
      NUMEL=NOQEL(I)
  130 WRITE(7,140)NUMEL,(NODEL(J,NUMEL),J=1,8),ITYP(NUMEL),NGAUSS(NUMEL)
  140 FORMAT(11X,I4,5X,8(I4,4X),I3,5X,I4)
C
C**** WRITE MATERIAL PROPERTIES
C
  150 WRITE(7,160)
  160 FORMAT(1H0,10X,'MATERIAL PROPERTIES'/
     +       1H+,10X,'                  '/
     +       1H0,8X,'MATERIAL NUMBER',3X,15HYOUNG'S MODULUS,
     +       7X,15HPOISSON'S RATIO,7X,'DENSITY',12X,'VISCOSITY',
     +          10X,'TENSILE STRENGTH'/
     +       17X,'I',11X,'E(I): N/SQ.M',12X,'NU(I)',
     +       9X,'RHO(I): KG/CU.M',5X,'ETA(I): NS/SQ.M'/1H0)
```

```
      DO 180 I=1,NMAT
  180 WRITE(7,190)I,EM(I),PM(I),RHOM(I),ETAM(I),TM(I)
  190 FORMAT(14X,I4,12X,E10.3,12X,F6.3,12X,F7.1,2(12X,E10.3))
C
C**** WRITE INFORMATION ON DIRECT FORCES\
C
      IF (NDIR.GT.0)GO TO 210
      WRITE(7,200)

  200 FORMAT(1H0,10X,'NO DIRECT FORCES')
      GO TO 250
  210 WRITE(7,220)NDIR
  220 FORMAT(1H0,10X,'DIRECT FORCES'/
     +       1H+,10X,'          ',3X,I4,' IN TOTAL'/
     +       1H0,14X,'NODE',19X,'APPLIED FORCES'/
     +       14X,'NUMBER',12X,'FX: N',17X,'FY: N'/1H0)
      DO 230 I=1,NDIR
  230 WRITE(7,240)NOD4S(I),FNOD(2*I-1),FNOD(2*I)
  240 FORMAT(14X,I4,2(11X,1PE11.4))
C
C**** WRITE INFORMATION ON DISTRIBUTED FORCES
C
  250 IF (NDIS.GT.0) GO TO 270
      WRITE(7,260)
  260 FORMAT(1H0,10X,'NO DISTRIBUTED FORCES')
      GO TO 300
  270 WRITE(7,280)NDIS
  280 FORMAT(1H0,10X,'DISTRIBUTED FORCES'/
     +       1H+,10X,'          ',3X,I4,' IN TOTAL'/
     +       1H0,14X,'NODE',19X,'APPLIED FORCES'/
     +       14X,'NUMBER',10X,'FNORM: N',14X,'FTAN: N'/1H0)
      DO 290 I=1,NDIS
  290 WRITE(7,240)NLOAD(I),FNTOT(I),FTTOT(I)
      WRITE(7,7030)
 7030 FORMAT(1H0,10X,'GLOBAL FORCE COMPONENTS CALCULATED',
     +               'FROM DISTRIBUTED FORCES'/
     +       1H0,14X,'NODE',19X,'APPLIED FORCES'/
     +           14X,'NUMBER',12X,'FX: N',17X,'FY: N'/1H0)
C
      DO 7010 I=1,NDIS
      L=2*NLOAD(I)
      K=L-1
 7010 WRITE(7,240)NLOAD(I),FORCE(K),FORCE(L)
C
C**** WRITE INFORMATION ON FIXED DISPLACEMENTS
C
  300 IF (NFIX.GT.0) GO TO 320
      WRITE(7,310)
  310 FORMAT(1H0,10X,'NO FIXED DISPLACEMENTS')
      GO TO 360
  320 WRITE(7,330)NFIX
  330 FORMAT(1H0,10X,'FIXED DISPLACEMENTS'/
     +       1H+,10X,'          ',3X,I4,' IN TOTAL'/
     +       1H0,13X,'NODE',I2X,'XFLAG',6X,'X DISPLACEMENT',
     +       6X,'Y FLAG',6X,'Y DISPLACEMENT'/1H0)
      DO 340 I=1,NFIX
  340 WRITE(7,350)NOFIX(I),(IFLAG(J,I),DFIX(J,I),J=1,2)
  350 FORMAT(14X,2(I4,12X),1PE10.3,6X,I4,12X,1PE10.3)
  360 CONTINUE
C
C
C**** WRITE INFORMATION  ON FAULT
C
      IF (NFS.EQ.0) GO TO 450
C
      WRITE(7,400)NFS,KN,KS,MU,FAC
  400 FORMAT(1H0,10X,'FAULT DATA'/
     +       1H+,10X,'          ',3X,I4,' FAULT SECTIONS'/
     +       1H0,10X,'NORMAL STIFFNESS ',1PE10.3,13X,
     +               'SHEAR STIFFNESS ',1PE10.3/
     +       1H0,10X,'COEFFICIENT OF FRICTION ',F10.3,
     +           7X,'CONVERGENCE FACTOR ',1PE10.3/
     +       1H0,10X,'DUAL NODES'/
     +       1H+,10X,'          '/
     +       1H0,2(12X,'NODE',7X,'X:M',12X,'Y:M')/1H0)
```

```
C
      DO 420 IF=1,NFS
      NEL1=NELF(IF,1)
      NEL2=NELF(IF,2)
      DO 410 IN=1,3
      NOD1=NODEL(IN,NEL1)
      NOD2=NODEL(IN,NEL2)
      X1=X(NOD1)
      X2=X(NOD2)
      Y1=Y(NOD1)
      Y2=Y(NOD2)
      WRITE(7,430)NOD1,X1,Y1,NOD2,X2,Y2
  430 FORMAT(2(11X,I4,4X,1PE10.3,4X,1PE10.3))
  410 CONTINUE
  420 CONTINUE
  450 CONTINUE
      WRITE(6,370)
  370 FORMAT('0ECHO-CHO-CHOMPLETED')
      CALL TIME(1,1)
      RETURN
      END
C
C
C*************************************************************************************
C
C
      SUBROUTINE FORMK
C     ================
C
C
C**** CALCUALTE THE GLOBAL STIFFNESS FROM EACH ELEMENT STIFFNESS
C
      IMPLICIT REAL*8 (A-H,O-W)
      REAL*8 KN,KS,MU
      COMMON /CONS/ NTRI,NQUAD,NINCS,NNOD,KSIZE,KSBW,NNOD2,NMAT,NST,
     +              IDATE(3),TIMINC,TITLE(4),PI,ZUF(4)
      COMMON /ELEM/ NODEL(8,300),NGAUSS(300),NOTEL(300),NOQEL(300),
     +            NOTCOL(300),NOQCOL(300),DIFFOP(9,300),BLIB(144,300),
     +              COM1(15600)
      COMMON /MATS/ EM(9),PM(9),TM(9),RHOM(9),ETAM(9),C(9,3),ITYP(300)
      COMMON /STIF/ ELK(18,18),GLOBK(700,185)
      COMMON /FALT/ KN,KS,MU,FAC,BFAULT(12,2,50),
     +  DEPTH(50,2),THETA(50),FLTCRP(24,50),DFLTCR(24,50),
     +              STFBGN(24,50),NONOD(50,2),NELF(50,2),NITS,NFS
      COMMON /NEWS/ BSTRES(64,300),SCREP(16,300),DSCREP(16,300),
     +            STRST(16,300)
      COMMON /GAPT/ S,T,SHAPE(8),DNXDS(8),DNXDT(8),TSHAPE(6,36),
     +              TDNXDS(6,36),TDNXDT(6,36),TW1W2(6,6),QSHAPE(3,72),
     +              QDNXDS(3,72),QDNXDT(3,72),QW1W2(3,9),COM2(258)
      COMMON /VARS/ W1W2,DETJ,C1,C2,C3,DNXDX(8),DNXDY(8),B(3,18),
     +              COM3(54),NO,NO1,NO2,NUMEL,IG
C
      CALL PREK
C
C**** EVALUATE THE STIFFNESS OF EACH TRIANGULAR ELEMENT
C
      IF (NTRI.EQ.0)GO TO 40
      NO=6
      NO2=NO*2
      NO1=NO2-1
C
      DO 30 IEL=1,NTRI
C
C**** INITIALIZE TH EUPPER TRIANGLE OF THE ELEMENT STIFFNESS
C
      DO 700 I=1,NO2
      DO 800 J=I,NO2
  800 ELK(I,J)=0.000
  700 CONTINUE
C
      NUMEL=NOTEL(IEL)
      MAT=ITYP(NUMEL)
      C1=C(MAT,1)
```

```
      C2=C(MAT,2)
      C3=C(MAT,3)
      NGAUS=NGAUSS(NUMEL)
      NROW=NOTCOL(IEL)
C
C**** IF NGAUS IS NOT EQUAL TO THE DESIRED STRESS LOCATIONS
C**** COMPUTE THE STRAIN MATRIX OF THE STRESS LOCATIONS
C
      IF (NGAUS.EQ.6) GO TO 999
C
      DO 314 IG=4,6
      IPOS=(IG-1)*6
      KPOS=(IG-4)*12
      DO 300 IV=1,6
      JPOS=IPOS+IV
      DNXDS(IV)=TDNXDS(1,JPOS)
  300 DNXDT(IV)=TDNXDT(1,JPOS)
C
      CALL BFORM
C
      DO 312 I=1,6
      L=2*I
      K=L-1
      BSTRES(KPOS+K,NUMEL)=DNXDX(I)
  312 BSTRES(KPOS+L,NUMEL)=DNXDY(I)
  314 CONTINUE
C
C**** ENTER NUMERICAL INTEGRATION LOOP TO OBTAIN THE STIFFNESS
C****                    OF EACH ELEMENT
C
  999 DO 20 IG=1,NGAUS
      IPOS=(IG-1)*NO
      JPOS=IPOS*2
      DO 10 IV=1,NO
      DNXDS(IV)=TDNXDS(NROW,IPOS+IV)
   10 DNXDT(IV)=TDNXDT(NROW,IPOS+IV)
      W1W2=TW1W2(NROW,IG)
C
      CALL BFORM
C
C**** STORE B FOR VISCO-ELASTIC PROBLEMS AND WHEN
C**** GAUSS POINTS ARE AT DESIRED STRESS LOCATIONS
C
      IF (NINCS.EQ.0.AND.NGAUS.NE.6) GO TO 11
      DO 12 I=1,NO
       L=2*I
      K=L-1
      BLIB(JPOS+K,NUMEL)=DNXDX(I)
   12 BLIB(JPOS+L,NUMEL)=DNXDY(I)
   11 CONTINUE
      CALL ELSTIF
   20 CONTINUE
C
C**** LOAD THE ELEMENT STIFFNESS INTO THE GLOBAL STIFFNESS MATRIX
C
      CALL LOADK
C
   30 CONTINUE
C
C**** EVALUATE  THE  STIFFNESS  OF  EACH   QUADRILATERAL  ELEMENT
C
   40 IF (NQUAD.EQ.0)GO TO 80
      NO=8
      NO2=NO*2
      NO1=NO2-1
C
      DO 70 IEL=1,NQUAD
C
C**** INITIALIZE TH EUPPER TRIANGLE OF THE ELEMENT STIFFNESS
C
      DO 5 I=1,NO2
      DO 6 J=I,NO2
    6 ELK(I,J)=0.0
    5 CONTINUE
      NUMEL=NOQEL(IEL)
      MAT=ITYP(NUMEL)
      C1=C(MAT,1)
```

```
      C2=C(MAT,2)
      C3=C(MAT,3)
      NGAUS=NGAUSS(NUMEL)
      NROW=NOQCOL(IEL)
C
C**** IF NGAUS IS NOT EQUAL TO THE DESIRED STRESS LOCATIONS
C**** COMPUTE THE STRAIN MATRIX OF THE STRESS LOCATIONS
C
      IF (NGAUS.EQ.4) GO TO 888
C
      DO 414 IG=1,4
      IPOS=(IG-1)*8
      KPOS=IPOS*2
      DO 400 IV=1,8
      JPOS=IPOS+IV
      DNXDS(IV)=QDNXDS(1,JPOS)
  400 DNXDT(IV)=QDNXDT(1,JPOS)
C
      CALL BFORM
C
      DO 412 I=1,8
      L=2*I
      K=L-1
      BSTRES(KPOS+K,NUMEL)=DNXDX(I)
  412 BSTRES(KPOS+L,NUMEL)=DNXDY(I)

  414 CONTINUE
C
C**** ENTER THE NUMERICAL INTEGRATION LOOP TO OBTAIN THE
C**** STIFFNESS OF THIS ELEMENT
C
  888 DO 60 IG=1,NGAUS
      IPOS=(IG-1)*NO
      JPOS=IPOS*2
      DO 50 IV=1,NO
      DNXDS(IV)=QDNXDS(NROW,IPOS+IV)
      DNXDT(IV)=QDNXDT(NROW,IPOS+IV)
   50 CONTINUE
      W1W2=QW1W2(NROW,IG)
C
      CALL BFORM
C
C**** STORE B FOR VISCO-ELASTIC PROBLEMS OR WHEN GAUSS
C**** POINTS ARE AT DESIRED STRESS LOCATIONS
C
      IF (NINCS.EQ.0.AND.NGAUS.NE.4) GO TO 95
      DO 90 I=1,NO
      L=2*I
      K=L-1
      BLIB(JPOS+K,NUMEL)=DNXDX(I)
   90 BLIB(JPOS+L,NUMEL)=DNXDY(I)
   95 CONTINUE
      CALL ELSTIF
C
   60 CONTINUE
C
C**** LOAD THE ELEMENT STIFFNESS INTO THE GLOBAL STIFFNESS MATRIX
C
      CALL LOADK
C
   70 CONTINUE
C
C**** CALCUALTE THE FAULT STIFFNESS
C
   80 IF (NFS.EQ.0) GO TO 120
      CALL PREFLT
      CALL KFAULT
  120 CONTINUE
C
      WRITE(6,100)
  100 FORMAT('0STIFFNESS MATRIX FORMED')
      CALL TIME(1,1)
      RETURN
      END
C
C
C*********************************************************************************************
C
```

```
C
C
      SUBROUTINE PREK
C     ===============
C
C**** EVALUATE THE BANDWIDTH, ELASTICITY MATRIX, GAUSS QUADRATURE POINTS
C**** THE SHAPE FUNCTIONS AND THEIR DERIVATIVES
C
      IMPLICIT REAL*8 (A-H,O-W)
      REAL*8 KN,KS,MU
      COMMON /CONS/ NTRI,NQUAD,NINCS,NNOD,KSIZE,KSBW,NNOD2,NMAT,NST,
     +              IDATE(3),TIMINC,TITLE(4),PI,ZUF(4)
      COMMON /ELEM/ NODEL(8,300),NGAUSS(300),NOTEL(300),NOQEL(300),
     +          NOTCOL(300),NOQCOL(300),COM4(61500)
      COMMON /MATS/ EM(9),PM(9),TH(9),RHOM(9),ETAM(9),C(9,3),ITYP(300)
      COMMON /STIF/ ELK(18,18),GLOBK(700,185)
      COMMON /FALT/ KN,KS,MU,FAC,BFAULT(12,2,50),
     +  DEPTH(50,2),THETA(50),FLTCRP(24,50),DFLTCR(24,50),
     +              STFBGN(24,50),NONOD(50,2),NELF(50,2),NITS,NFS
      COMMON /GAPT/ S,T,SHAPE(8),DNXDS(8),DNXDT(8),TSHAPE(6,36),
     +              TDNXDS(6,36),TDNXDT(6,36),TW1W2(6,6),QSHAPE(3,72),
     +              QDNXDS(3,72),QDNXDT(3,72),QW1W2(3,9),WEITRI(12,6),
     +    WEIQAD(18,3),PLACET(12,6),PLACEQ(18,3),PLACEL(3),WEILIN(3)
      COMMON /VARS/ COM5(21),B(3,18),COMA(54),ICOM1(5)
      DIMENSION NOGT(6),NOGQ(3),NOD(6)
C
C**** CALCULATE THE SEMIBANDWIDTH FROM THE MAXIMUM
C**** NODAL DIFFERENCE OF EACH ELEMENT
C
      MAX=0
      IF(NTRI.EQ.0)GO TO 40
C
      DO 30 IEL=1,NTRI
      NUMEL=NOTEL(IEL)
      DO 20 J=1,5
      IST=J+1
      NOD1=NODEL(J,NUMEL)
      DO 10 K=IST,6
      IDIF=IABS(NOD1-NODEL(K,NUMEL))
   10 MAX=MAX0(IDIF,MAX)
   20 CONTINUE
   30 CONTINUE
C
   40 IF(NQUAD.EQ.0)GO TO 80
C
      DO 70 IEL=1,NQUAD
      NUMEL=NOQEL(IEL)
      DO 60 J=1,7
      IST=J+1
      NOD1=NODEL(J,NUMEL)
      DO 50 K=IST,8
      IDIF=IABS(NOD1-NODEL(K,NUMEL))
   50 MAX=MAX0(IDIF,MAX)
   60 CONTINUE
   70 CONTINUE
   80 IF (NFS.EQ.0) GO TO 73
      DO 71 IF=1,NFS
      NUMEL=NELF(IF,1)
      NOD(1)=NODEL(1,NUMEL)
      NOD(2)=NODEL(2,NUMEL)
      NOD(3)=NODEL(3,NUMEL)
      NUMEL=NELF(IF,2)
      NOD(4)=NODEL(1,NUMEL)
      NOD(5)=NODEL(2,NUMEL)
      NOD(6)=NODEL(3,NUMEL)
      DO 72 I=1,5
      IST=1+I
      DO 72 J=IST,6

      IDIF=IABS(NOD(I)-NOD(J))
   72 MAX=MAX0(IDIF,MAX)
   71 CONTINUE
   73 CONTINUE
C
      KSBW=2*(MAX+1)
      KSIZE=2*KSBW-1
      IF (MAX.EQ.0) CALL CRASH
```

```
      IF (KSIZE.GT.185) CALL BADLUK
C
C**** INITIALIZE ARRAYS B AND GLOBK
C
      DO 90 I=1,KSIZE
      DO 90 J=1,NNOD2
      GLOBK(J,I)=0.0D0
   90 CONTINUE
C
      DO 100 I=1,3
      DO 100 J=1,16
  100 B(I,J) = 0.0D0
C
C**** CALCULATE THE ELASTICITY MATRIX FOR EACH MATERIAL TYPE
C
      DO 120 MAT=1,NMAT
      E=EM(MAT)
      P=PM(MAT)
C
      IF(NST.EQ.1) GO TO 110
C
C**** CALCULATE THE ELASTICITY MATRIX FOR PLANE STRAIN
C
      C(MAT,1)=E*(1.0D0-P)/((1.0D0+P)*(1.0D0-2.0D0*P))
      C(MAT,2)=C(MAT,1)*P/(1.0D0-P)
      C(MAT,3)=E/(2.0D0*(1.0D0+P))
C
      GO TO 120
C
C**** CALCULATE THE ELASTICITY MATRIX FOR PLANE STRESS
C
  110 C(MAT,1)=E/(1.0D0-(P*P))
      C(MAT,2)=P*C(MAT,1)
      C(MAT,3)=((1.0D0-P)/2.0D0)*C(MAT,1)
C
  120 CONTINUE
C
C**** SET UP THE GAUSS QUADRATURE POINTS
C
      CALL GAUSSQ
C
C**** EVALUATE SHAPE FUNCTIONS AND THEIR DERIVATIVES AT THE
C**** TRIANGULAR GAUSS POINTS USED IN THIS JOB (STARTING WITH
C**** THE DESIRED STRESS GAUSS POINTS).
C
      IF (NTRI.EQ.0) GO TO 160
       NOGT(1)=6
      NOTGP=1
C
      DO 150 IEL=1,NTRI
      NUMEL=NOTEL(IEL)
      NGAUS=NGAUSS(NUMEL)

      DO 130 IMP=1,NOTGP
      IF (NOGT(IMP).EQ.NGAUS) GO TO 140
  130 CONTINUE
      NOTGP=NOTGP+1
      NOGT(NOTGP)=NGAUS
      NOTCOL(IEL)=NOTGP
      GO TO 150
  140 NOTCOL(IEL)=IMP
  150 CONTINUE
C
      DO 230 NOP=1,NOTGP
      NGAUS=NOGT(NOP)
      DO 220 IG=1,NGAUS
      SPOS=2*IG
      TPOS=SPOS-1
      S=PLACET(SPOS,NGAUS)
      T=PLACET(TPOS,NGAUS)
      W1=WEITRI(SPOS,NGAUS)
      W2=WEITRI(TPOS,NGAUS)
C
      CALL TSHAPN
      CALL DTSHAP
```

```
      IPOS=(IG-1)*6
      DO 210 IV=1,6
      JPOS=IPOS+IV
      TSHAPE(NOP,JPOS)=SHAPE(IV)
      TDNXDS(NOP,JPOS)=DNXDS(IV)
  210 TDNXDT(NOP,JPOS)=DNXDT(IV)
      TW1W2(NOP,IG)=W1
C     WRITE(7,320)TW1W2(NOP,IG)
C 320 FORMAT('0W1*W2=',1PE10.3)
  220 CONTINUE
  230 CONTINUE
C
C**** EVALUATE SHAPE FUNCTIONS AND THEIR DERIVATIVES AT THE
C**** QUADRILATERAL GAUSS POINTS USED IN THIS JOB (STARTING WITH
C**** THE DESIRED STRESS GAUSS POINTS).
C
  160 IF (NQUAD.EQ.0) GO TO 270
C
      NOGQ(1)=4
      NOQGP=1
      DO 190 IEL=1,NQUAD
      NUMEL=NOQEL(IEL)
      NGAUS=NGAUSS(NUMEL)
      DO 170 IMP=1,NOQGP
      IF (NOGQ(IMP).EQ.NGAUS) GO TO 180
  170 CONTINUE
      NOQGP=NOQGP+1
      NOGQ(NOQGP)=NGAUS
      NOQCOL(IEL)=NOQGP
      GO TO 190
  180 NOQCOL(IEL)=IMP
  190 CONTINUE
  200 CONTINUE
C
      DO 260 NOP=1,NOQGP
      NGAUS=NOGQ(NOP)
      LCOL=1
C
      IF (NGAUS.EQ.9) LCOL=2
      DO 250 IG=1,NGAUS
      SPOS=2*IG
      TPOS=SPOS-1
      S=PLACEQ(SPOS,LCOL)
      T=PLACEQ(TPOS,LCOL)
      W1=WEIQAD(SPOS,LCOL)
      W2=WEIQAD(TPOS,LCOL)
C
      CALL QSHAFN
      CALL DQSHAP
C
      IPOS=(IG-1)*8
      DO 240 IV=1,8
      JPOS=IPOS+IV
      QSHAPE(NOP,JPOS)=SHAPE(IV)
      QDNXDS(NOP,JPOS)=DNXDS(IV)
  240 QDNXDT(NOP,JPOS)=DNXDT(IV)
      QW1W2(NOP,IG)=W1*W2
  250 CONTINUE
  260 CONTINUE
C
  270 RETURN
      END
C
C
C
C*********************************************************************
C
C
      SUBROUTINE GAUSSQ
C     =================
C
C**** SET UP THE GAUSSIAN INTEGRATION POINTS
```

```
C
      IMPLICIT REAL*8 (A-H,O-W)
      COMMON /GAPT/ COM6(1385),WEITRI(12,6),WEIQAD(18,3),PLACET(12,6),
     +              PLACEQ(18,3),PLACEL(3),WEILIN(3)
C
C**** SET UP THE POSITIONS OF THE TRAINGULAR GAUSS POINTS
C
      PLACET(1,1)=0.33333333333333D0
      PLACET(2,1)=PLACET(1,1)
C
      G1=0.666666666666667D0
      G2=0.166666666666667D0
C
      PLACET(1,3)=G1
      PLACET(2,3)=G2
      PLACET(3,3)=G2
      PLACET(4,3)=G1
      PLACET(5,3)=G2
      PLACET(6,3)=G2
C
      G1=0.6D0
      G2=0.2D0
C
      PLACET(1,4)=PLACET(1,1)
      PLACET(2,4)=PLACET(1,1)
      PLACET(3,4)=G1

      PLACET(4,4)=G2
      PLACET(5,4)=G2
      PLACET(6,4)=G1
      PLACET(7,4)=G2
      PLACET(8,4)=G2
C
      G1=0.816847572980459D0
      G2=0.091576213509771D0
      G3=0.108103018168070D0
      G4=0.445948490915965D0
C
      PLACET(1,6)=G1
      PLACET(2,6)=G2
      PLACET(3,6)=G2
      PLACET(4,6)=G1
      PLACET(5,6)=G2
      PLACET(6,6)=G2
      PLACET(7,6)=G3
      PLACET(8,6)=G4
      PLACET(9,6)=G4
      PLACET(10,6)=G3
      PLACET(11,6)=G4
      PLACET(12,6)=G4
C
C
C**** SET UP QUADRILATERAL GAUSS POINTS
C
C
      G1=-0.57735026918962D0
      G2=-G1
C
      PLACEQ(1,1)=G1
      PLACEQ(2,1)=G1
      PLACEQ(3,1)=G1
      PLACEQ(4,1)=G2
      PLACEQ(5,1)=G2
      PLACEQ(6,1)=G1
      PLACEQ(7,1)=G2
      PLACEQ(8,1)=G2
C
      G1=-0.774596669241483D0
      G2=0.0D0
      G3=-G1
C
      PLACEQ(1,2)=G1
      PLACEQ(2,2)=G1
      PLACEQ(3,2)=G1
      PLACEQ(4,2)=G2
      PLACEQ(5,2)=G1
```

```
      PLACEQ(6,2)=G3
      PLACEQ(7,2)=G2
      PLACEQ(8,2)=G1
      PLACEQ(9,2)=G2
      PLACEQ(10,2)=G2
      PLACEQ(11,2)=G2
      PLACEQ(12,2)=G3
      PLACEQ(13,2)=G3
      PLACEQ(14,2)=G1
      PLACEQ(15,2)=G3
      PLACEQ(16,2)=G2

      PLACEQ(17,2)=G3
      PLACEQ(18,2)=G3
C
C**** SET UP ARRAY CONTAINING TRAIANGULAR WEIGHTS
C
      WEITRI(1,1)=0.5D0
      WEITRI(2,1)=0.5D0
C
      DO 10 I=1,6
   10 WEITRI(I,3)=.16666666666666 67D0
C
      WEITRI(1,4)=-0.28125D0
      WEITRI(2,4)=WEITRI(1,4)
      DO 20 I=3,8
   20 WEITRI(I,4)=.260416666666666 7D0
C
      DO 30 I=1,6
   30 WEITRI(I,6)=.5497587182766 09D-1
      DO 40 I=7,12
   40 WEITRI(I,6)=0.1116907948390055D0
C
C**** SET UP THE QUADRILATERAL WEIGHTS
C
C
      DO 50 I=1,8
   50 WEIQAD(I,1)=1.0D0
C
      G1=0.5555555555555 6D0
      G2=0.8888888888888 9D0
      G3=G1
C
      WEIQAD(1,2)=G1
      WEIQAD(2,2)=G1
      WEIQAD(3,2)=G1
      WEIQAD(4,2)=G2
      WEIQAD(5,2)=G1
      WEIQAD(6,2)=G3
      WEIQAD(7,2)=G2
      WEIQAD(8,2)=G1
      WEIQAD(9,2)=G2
      WEIQAD(10,2)=G2
      WEIQAD(11,2)=G2
      WEIQAD(12,2)=G3
      WEIQAD(13,2)=G3
      WEIQAD(14,2)=G1
      WEIQAD(15,2)=G3
      WEIQAD(16,2)=G2
      WEIQAD(17,2)=G3
      WEIQAD(18,2)=G3
C
      RETURN
      END
C
C*****************************************************************************
C
C
      SUBROUTINE TSHAFN
      =================
C
C
C**** CALCULATE THE SHAPE FUNCTIONS OF A TRIANGULAR ELEMENT
```

```
C
      IMPLICIT REAL*8 (A-H,O-W)
      REAL *8 L3
      COMMON /GAPT/ S,T,SHAPE(8),COM7(1633)
C
      L3=1.0D0-S-T
      SHAPE(1)=2.0D0*S*S-S
      SHAPE(3)=2.0D0*T*T-T
      SHAPE(5)=2.0D0*L3*L3-L3
      SHAPE(2)=4.0D0*S*T
      SHAPE(4)=4.0D0*T*L3
      SHAPE(6)=4.0D0*S*L3
C
      RETURN
      END
C
C
C*****************************************************************************
C
C
      SUBROUTINE QSHAFN
C     =================
C
C
C**** CALCULATE THE QUADRILATERAL SHAPE  FUNCTIONS
C
      IMPLICIT REAL*8 (A-H,O-W)
      COMMON /GAPT/ S,T,SHAPE(8),COM7(1633)
C
      S2=S*2.0D0
      T2=T*2.0D0
      SS=S*S
      TT=T*T
      SST=SS*T
      STT=S*TT
      ST=S*T
C
      SHAPE(1)=(-1.0D0+ST+SS+TT-SST-STT)/4.0D0
      SHAPE(2)=(1.0D0-T-SS+SST)/2.0D0
      SHAPE(3)=(-1.0D0-ST+SS+TT-SST+STT)/4.0D0
      SHAPE(4)=(1.0D0+S-TT-STT)/2.0D0
      SHAPE(5)=(-1.0D0+ST+SS+TT+SST+STT)/4.0D0
      SHAPE(6)=(1.0D0+T-SS-SST)/2.0D0
      SHAPE(7)=(-1.0D0-ST+SS+TT+SST-STT)/4.0D0
      SHAPE(8)=(1.0D0-S-TT+STT)/2.0D0
C
      RETURN
      END
C
C
C*****************************************************************************
C
C
      SUBROUTINE DTSHAP
C     =================
C
C
C**** EVALUATE THE DERIVATIVES OF THE TRIANGULAR SHAPE FUNCTIONS
C
      IMPLICIT REAL*8 (A-H,O-W)
      COMMON /GAPT/ S,T,SHAPE(8),DNXDS(8),DNXDT(8),COM8(1617)
C
C
      T4=4.0D0*T
      S4=4.0D0*S
C
C**** CALCUALTE THE DERIVATIVES OF THE SHAPE FUNCTIONS WITH
C**** RESPECT  TO  THE  S  CO-ORDINATE OF THIS  GAUSS POINT
C
      DNXDS(1)=S4-1.0D0
```

```
      DNXDS(3)=0.0D0
      DNXDS(5)=S4+T4-3.0D0
      DNXDS(2)=T4
      DNXDS(4)=-T4
      DNXDS(6)=4.0D0-T4-2.0D0*S4
C
C**** CALCULATE THE DERIVATIVES OF THE SHAPE FUNCTIONS WITH
C**** RESPECT  TO  THE  T  CO-ORDINATE OF THIS  GAUSS POINT
C
      DNXDT(1)=0.0D0
      DNXDT(3)=T4-1.0D0
      DNXDT(5)=S4+T4-3.0D0
      DNXDT(2)=S4
      DNXDT(4)=4.0D0-S4-2.0D0*T4
      DNXDT(6)=-S4
C
      RETURN
      END
C
C*************************************************************************
C
      SUBROUTINE DQSHAP
      =================
C
C**** CALCULATE THE DERIVATIVES OF THE QUAORATIC SHAPE FUNCTIONS
C
      IMPLICIT REAL*8 (A-H,O-W)
      COMMON /GAPT/ S,T,SHAPE(8),DNXDS(8),DNXDT(8),COM8(1617)
C
      TT=T*T
      SS=S*S
      ST=S*T
      T2=2.0D0*T
      S2=2.0D0*S
      ST2=2.0D0*ST
C
C**** CALCULATE THE DERIVATIVES OF THE SHAPE FUNCTIONS WITH
C**** RESPECT  TO  THE  S  CO-ORDINATE  OF THIS GAUSS POINT
C
      DNXDS(1)=(S2+T-ST2-TT)/4.0D0
      DNXDS(2)=ST-S
      DNXDS(3)=(TT-ST2-T+S2)/4.0D0
      DNXDS(4)=(1.0D0-TT)/2.0D0
      DNXDS(5)=(ST2+TT+S2+T)/4.0D0
      DNXDS(6)=-ST-S
      DNXDS(7)=(S2-T+ST2-TT)/4.0D0
      DNXDS(8)=-DNXDS(4)
C
C**** CALCULATE THE DERIVATIVES OF THE SHAPE FUNCTIONS WITH
C**** RESPECT  TO  THE  T CO-ORDINATE OF  THIS  GAUSS POINT
C

      DNXDT(1)=(S+T2-SS-ST2)/4.0D0
      DNXDT(2)=(SS-1.0D0)/2.0D0
      DNXDT(3)=(T2-S+ST2-SS)/4.0D0
      DNXDT(4)=-ST-T
      DNXDT(5)=(SS+ST2+S+T2)/4.0D0
      DNXDT(6)=-DNXDT(2)
      DNXDT(7)=(T2-S+SS-ST2)/4.0D0
      DNXDT(8)=ST-T
C
      RETURN
      END
C
C*************************************************************************
C
```

```
C
      SUBROUTINE BFORM
C     ================
C
C**** CALCULATE THE COMPONENTS (DNXDX,DNXDY) OF THE STRAIN MATRIX
C
      IMPLICIT REAL*8 (A-H,O-W)
      REAL*8 JAC,JACINV
      COMMON /NODS/ X(350),Y(350),COM9(1400),XCOM1(2400)
      COMMON /ELEM/ NODEL(8,300),ICOM2(1500),COM4(61500)
      COMMON /VARS/ W1W2,DETJ,C1,C2,C3,DNXDX(8),
     +              DNXDY(8),B(3,18),JAC(2,2),JACINV(2,2),
     +              COM10(46),NO,NO1,NO2,NUMEL,IG
      COMMON /GAPT/ S,T,SHAPE(8),DNXDS(8),DNXDT(8),COM8(1617)
C
C**** CALCULATE THE JACOBIAN TRANSFORMATION OF THIS GAUSS POINT
C
      JAC(1,1)=0.0D0
      JAC(1,2)=0.0D0
      JAC(2,1)=0.0D0
      JAC(2,2)=0.0D0
      DO 10 INOD=1,NO
      XNOD=X(NODEL(INOD,NUMEL))
      YNOD=Y(NODEL(INOD,NUMEL))
      JAC(1,1)=JAC(1,1)+DNXDS(INOD)*XNOD
      JAC(1,2)=JAC(1,2)+DNXDS(INOD)*YNOD
      JAC(2,1)=JAC(2,1)+DNXDT(INOD)*XNOD
      JAC(2,2)=JAC(2,2)+DNXDT(INOD)*YNOD
   10 CONTINUE
C
C**** EVALUATE THE DETERMINANT AND THE INVERSE OF THE JACOBIAN
C
      DETJ=JAC(1,1)*JAC(2,2)-JAC(1,2)*JAC(2,1)
      JACINV(1,1)= JAC(2,2)/DETJ
      JACINV(1,2)=-JAC(1,2)/DETJ
      JACINV(2,1)=-JAC(2,1)/DETJ
      JACINV(2,2)= JAC(1,1)/DETJ
C
C
C**** EVALUATE THE STRAIN MATRIX, B
C
      DO 20 I=1,NO
      DNXDX(I)=JACINV(1,1)*DNXDS(I)+JACINV(1,2)*DNXDT(I)
      DNXDY(I)=JACINV(2,1)*DNXDS(I)+JACINV(2,2)*DNXDT(I)
   20 CONTINUE

C
      RETURN
      END
C
C
C*********************************************************************************
C
C
      SUBROUTINE ELSTIF
C     =================
C
C**** CALCUALTE THE ELEMENT STIFFNESS
C
      IMPLICIT REAL*8 (A-H,O-W)
      COMMON /ELEM/ NODEL(8,300),ICOM2(1500),DIFFOP(9,300),
     +              BLIB(144,300),COM1(15600)
      COMMON /STIF/ ELK(18,18),GLOBK(700,185)
      COMMON /VARS/ W1W2,DETJ,C1,C2,C3,DNXDX(8),DNXDY(8),B(3,18),
     +              BTC(18,3),NO,NO1,NO2,NUMEL,IG
C
C**** CALCULATE NON ZERO COMPONENTS OF  (B)T(C)
C
      DO 10 I=1,NO
      L=2*I
      K=L-1
      B(1,K)=DNXDX(I)
      B(2,L)=DNXDY(I)
      B(3,K)=DNXDY(I)
      B(3,L)=DNXDX(I)
      BTC(K,1)=B(1,K)*C1
      BTC(K,2)=B(1,K)*C2
      BTC(K,3)=B(3,K)*C3
      BTC(L,1)=B(2,L)*C2
      BTC(L,2)=B(2,L)*C1
```

```
      BTC(L,3)=B(3,L)*C3
   10 CONTINUE
C
C**** CALCULATE THE NUMERICAL INTEGRATION OPERATOR, DV
C
      DV=W1W2*DABS(DETJ)
      DIFFOP(IG,NUMEL)=DV
C
C**** EVALUATE THE UPPER TRIANGLE OF THE ELEMENT STIFFNESS
C**** MATRIX BY GAUSSIAN NUMERICAL INTEGRATION
C
      DO 40 NROW=1,NO2
      DO 30 NCOL=NROW,NO2
      DUM=0.0
      DO 20 J=1,3
      DUM=DUM+BTC(NROW,J)*B(J,NCOL)
   20 CONTINUE
      ELK(NROW,NCOL)=ELK(NROW,NCOL)+DUM*DV
   30 CONTINUE
   40 CONTINUE
C
      RETURN
      END
C
C
C*****************************************************************************
C
C
      SUBROUTINE LOADK
      ================
C
C**** TO LOAD THE ELEMENT STIFFNESS INTO THE GLOBAL STFFNESS MATRIX
C
      IMPLICIT REAL*8 (A-H,O-W)
      COMMON /CONS/ NTRI,NQUAD,NINCS,NNOD,KSIZE,KSBW,NNOD2,NMAT,NST,
     +              IDATE(3),TIMINC,TITLE(4),PI,ZUF(4)
      COMMON /ELEM/ NODEL(8,300),ICOM2(1500),COM4(61500)
      COMMON /STIF/ ELK(18,18),GLOBK(700,185)
      COMMON /VARS/ COMB(129),NO,NO1,NO2,NUMEL,IG
C
C**** FILL IN THE LOWER TRIANGLE OF THE ELEMENT STIFFNESS
C
      DO 10 KFIL=1,NO1
      DO 10 LFIL=KFIL,NO2
      ELK(LFIL,KFIL)=ELK(KFIL,LFIL)
   10 CONTINUE
C
C****  LOAD THE ELEMENT STIFFNESS INTO THE GLOBAL STFFNESS MATRIX
C
      DO 50 I=1,NO
      I1=2*NODEL(I,NUMEL)-2+KSBW
      NK1=2*I-2
      DO 40 J=1,2
      J1=I1+J
      NK=NK1+J
      DO 30 K=1,NO
      K1=2*NODEL(K,NUMEL)-2
      MK1=2*K-2
      DO 20 L=1,2
      KROW=K1+L
      KCOL=J1-KROW
      MK=MK1+L
      GLOBK(KROW,KCOL)=GLOBK(KROW,KCOL)+ELK(MK,NK)
   20 CONTINUE
   30 CONTINUE
   40 CONTINUE
   50 CONTINUE
C
      RETURN
      END
C
C
C
C*****************************************************************************
```

```
C
C
      SUBROUTINE BOUNDS
C     =================
C
C**** APPLY BOUNDARY CONDITIONS
C
      IMPLICIT REAL*8 (A-H,O-W)
      COMMON /CONS/ NTRI,NQUAD,NINCS,NNOD,KSIZE,KSBW,NNOD2,NMAT,INITEM,
     +         IDATE(3),TIMINC,TITLE(4),PI,ZUF(4)
      COMMON /STIF/ ELK(18,18),GLOBK(700,185)

      COMMON /NODS/ X(350),Y(350),DISP(700),FORCE(700),XCOM1(2400)
      COMMON /FIXT/ OFIX(2,100),NOFIX(100),IFLAG(2,100),NFIX
C
      IF (NFIX.EQ.0) GO TO 40
C
      DO 30 I=1,NFIX
      DO 30 J=1,2
      IF (IFLAG(J,I).LE.0) GO TO 20
C
C**** ZERO APPROPRIATE ROW OF STIFFNESS MATRIX
C
      K=2*NOFIX(I)+J-2
      DO 10 L=1,KSIZE
   10 GLOBK(K,L)=0.0D0
C
C**** SET THE DIAGONAL VALUE OF GLOBK TO A LARGE VALUE
C**** AND REPLACE FORCE(J) BY DISP(J) * ( THAT VALUE )
C
      GLOBK(K,KSBW)=1.0D12
      IF (IFLAG(J,I).EQ.1) FORCE(K)=OFIX(J,I)*1.0D12
      IF (IFLAG(J,I).EQ.2) FORCE(K)=0.0D0
   20 CONTINUE
   30 CONTINUE
C
   40 WRITE(6,50)
   50 FORMAT('0BOUNDARY CONDITIONS APPLIED')
      CALL TIME(1,1)
C
      RETURN
      END
C
C
C*********************************************************************************************
C
C
      SUBROUTINE BODY4S
C     =================
C
C**** CALCUALTE THE CONTRIBUTIONS TO THE GLOBAL FORCE VECTOR
C**** FOR BODY FORCES ACTING IN THE POSITIVE Y DIRECTION
C
      IMPLICIT REAL*8 (A-H,O-W)
      COMMON /CONS/ NTRI,NQUAD,NINCS,NNOD,KSIZE,KSBW,NNOD2,NMAT,INITEM,
     +         IDATE(3),TIMINC,TITLE(4),PI,ZUF(4)
      COMMON /NODS/ X(350),Y(350),DISP(700),FORCE(700),XCOM1(2400)
      COMMON /ELEM/ NODEL(8,300),NGAUSS(300),NOTEL(300),NOQEL(300),
     +          NOTCOL(300),NOQCOL(300),DIFFOP(9,300),BLIB(144,300),
     +        PRINC(16,300),CREEP(36,300)
      COMMON /MATS/ EM(9),PM(9),TM(9),RHOM(9),ETAM(9),C(9,3),ITYP(300)
      COMMON /GAPT/ S,T,SHAPE(8),DNXDS(8),DNXDT(8),TSHAPE(6,36),
     +          TDNXDS(6,36),TDNXDT(6,36),TW1W2(6,6),QSHAPE(3,72),
     +          QDNXDS(3,72),QDNXDT(3,72),QW1W2(3,9),WEITRI(12,6),
     +     WEIQAD(18,3),PLACET(12,6),PLACEQ(18,3),PLACEL(3),WEILIN(3)
C
      IF (NTRI.EQ.0) GO TO 40
C
      DO 30 IEL=1,NTRI
      NUMEL=NOTEL(IEL)
      MAT=ITYP(NUMEL)
      NGAUS=NGAUSS(NUMEL)

      NROW=NOTCOL(IEL)
      FLOAD=-RHOM(MAT)*9.81
      DO 20 IG=1,NGAUS
```

```
      IPOS=(IG-1)*6
      DV=DIFFOP(IG,NUMEL)
      DO 10 INT=1,6
      SHAPE(INT)=TSHAPE(NROW,IPOS+INT)
      NOD=NODEL(INT,NUMEL)
      FORCE(2*NOD)=SHAPE(INT)*FLOAD*DV+FORCE(2*NOD)
   10 CONTINUE
   20 CONTINUE
   30 CONTINUE
C
   40 IF (NQUAD.EQ.0) GO TO 80
C
      DO 70 IEL=1,NQUAD
      NUMEL=NOQEL(IEL)
      MAT=ITYP(NUMEL)
      NGAUS=NGAUSS(NUMEL)
      NROW=NOQCOL(IEL)
      FLOAD=-RHOM(MAT)*9.81
      DO 60 IG=1,NGAUS
      DV=DIFFOP(IG,NUMEL)
      IPOS=(IG-1)*8
      DO 50 INT=1,8
      SHAPE(INT)=QSHAPE(NROW,IPOS+INT)
      NOD=NODEL(INT,NUMEL)
      FORCE(2*NOD)=SHAPE(INT)*FLOAD*DV+FORCE(2*NOD)
   50 CONTINUE
   60 CONTINUE
   70 CONTINUE
C
   80 WRITE(6,90)
   90 FORMAT('0BODY FORCES APPLIED')
      CALL TIME(1,1)
C
      RETURN
      END
C
C
C*********************************************************************************
C
C
      SUBROUTINE ISOS
C     ===============
C
C**** APPLY ISOSATIC COMPENSATION AT SPECIFIED NODES
C
      IMPLICIT REAL*8 (A-H,O-W)
      COMMON /CONS/ NTRI,NQUAD,NINCS,NNOD,KSIZE,KSBW,NNOD2,NMAT,INITEM,
     +        IDATE(3),TIMINC,TITLE(4),PI,ZUF(4)
      COMMON /STIF/ ELK(18,18),GLOBK(700,185)
      COMMON /NODS/ X(350),Y(350),DISP(700),FORCE(700),XCOM1(2400)
      COMMON /GAPT/ S,T,SHAPE(8),DNXDS(8),DNXDT(8),TSHAPE(6,36),
     +              TDNXDS(6,36),TDNXDT(6,36),TW1W2(6,6),QSHAPE(3,72),
     +              QDNXDS(3,72),QDNXDT(3,72),QW1W2(3,9),WEITRI(12,6),
     +     WEIQAD(18,3),PLACET(12,6),PLACEQ(18,3),PLACEL(3),WEILIN(3)
      DIMENSION NODE(3),FISOS(6,6),NOD(100),NN(6)
C
C
C**** READ NUMBER OF SEGMENTS
C
      READ(4,10)NSEG
   10 FORMAT(I5,F10.3)
C
      DO 170 IT=1,NSEG
C
C**** READ THE NUMBER OF NODES ON THIS SEGMENT AND
C**** THE DENSITY OF COMPENSATION
C
      READ(4,10)NODCOM,RHO
      DO 30 I=1,NODCOM
   30 READ(4,10)NOD(I)
      FLOAD=RHO*9.81
      NOSECT=(NODCOM-1)/2
C
      DO 160 IS=1,NOSECT
C
```

```
C**** INITIALISE THE ISOSTATIC MATRIX
C
      DO 50 I=1,6
      DO 40 J=1,6
      FISOS(J,I)=0.0D0
   40 CONTINUE
   50 CONTINUE
C
      L2=2*IS
      L1=L2-1
      L3=L2+1
      NODE(1)=NOD(L1)
      NODE(2)=NOD(L2)
      NODE(3)=NOD(L3)
      X1=X(NODE(1))
      X2=X(NODE(2))
      X3=X(NODE(3))
      Y1=Y(NODE(1))
      Y2=Y(NODE(2))
      Y3=Y(NODE(3))
C
C**** EVALUATE THE CONTRIBUTION TO THE ISOSTATIC MATRIX
C**** AT EACH GAUSS POINT
C
      DO 110 IG=1,3
      S=PLACEL(IG)
      DS=WEILIN(IG)
      SS=S*S
      SHAPE(1)=(SS-S)/2.0D0
      SHAPE(2)=1.0D0-SS
      SHAPE(3)=(SS+S)/2.0D0
      DNXDS(1)=S-0.5
      DNXDS(2)=-2.0D0*S
      DNXDS(3)=S+0.5
      DXXDS=DNXDS(1)*X1+DNXDS(2)*X2+DNXDS(3)*X3
      DYXDS=DNXDS(1)*Y1+DNXDS(2)*Y2+DNXDS(3)*Y3
      DSX=DYXDS*DS
      DSY=DXXDS*DS
C
C**** CALCULATE THE ISOSTATIC MATRIX
C
   80 DO 100 I=1,3

      DO 90 J=1,3
      SHAPEF=SHAPE(J)*SHAPE(I)
      FISOS(I*2-1,J*2)=FISOS(I*2-1,J*2)-SHAPEF*DSX
      FISOS( I*2 ,J*2)=FISOS( I*2 ,J*2)+SHAPEF*DSY
   90 CONTINUE
  100 CONTINUE
  110 CONTINUE
C
C**** MULTIPLY THE ISOSTATIC MATRIX BY THE LOAD
C
      DO 130 I=1,6
      DO 120 J=1,6
      FISOS(J,I)=FISOS(J,I)*FLOAD
  120 CONTINUE
  130 CONTINUE
C
C**** SUBTRACT THE ISOSTATIC MATRIX FROM THE STIFFNESS MATRIX
C
      DO 150 I=1,3
      I1=2*NODE(I)-2+KSBW
      NK1=2*I-2
      DO 151 J=1,2
      J1=I1+J
      NK=NK1+J
      DO 152 K=1,3
      K1=2*NODE(K)-2
      MK1=2*K-2
      DO 153 L=1,2
      KROW=K1+L
      KCOL=J1-KROW
      MK=MK1+L
  153 GLOBK(KROW,KCOL)=GLOBK(KROW,KCOL)+FISOS(MK,NK)
  152 CONTINUE
```

```
  151 CONTINUE
  150 CONTINUE
  160 CONTINUE
  170 CONTINUE
C
      WRITE(6,180)
  180 FORMAT('0ISOSTATIC COMPENSATION APPLIED')
      CALL TIME(1,1)
C
      RETURN
      END
C
C
C*********************************************************************************
C
C
      SUBROUTINE ELVIS
C     ================
C
C**** TO SOLVE FOR VISCO-ELASTIC STRESSES AND STRAINS
C
      IMPLICIT REAL*8 (A-H,O-W)
      REAL *8 KN,KS,MU
      COMMON /CONS/ NTRI,NQUAD,NINCS,NNOD,KSIZE,KSBW,NNOD2,NMAT,INITEM,
     +              IDATE(3),TIMINC,TITLE(4),PI,ZUF(4)
      COMMON /NODS/ X(350),Y(350),DISP(700),FORCE(700),XCOM1(2400)
      COMMON /ELEM/ NODEL(8,300),NGAUSS(300),NOTEL(300),NOQEL(300),
     +              NOTCOL(300),NOQCOL(300),DIFFOP(9,300),BLIB(144,300),
     +              PRINC(16,300),CREEP(36,300)
      COMMON /FALT/ KN,KS,MU,FAC,BFAULT(12,2,50),
     +  DEPTH(50,2),THETA(50),FLTCRP(24,50),DFLTCR(24,50),
     +              STFBGN(24,50),NONOD(50,2),NELF(50,2),NITS,NFS
      COMMON /MATS/ EM(9),PM(9),TM(9),RHOM(9),ETAM(9),C(9,3),ITYP(300)
      COMMON /STIF/ ELK(18,18),GLOBK(700,185)
      COMMON /NEWS/ BSTRES(64,300),SCREP(16,300),DSCREP(16,300),
     +              STRST(16,300)
      COMMON /VISC/ DCREEP(36,300),PRESTR(36,300),STRBGN(36,300),
     +              FINIT(700),FCREEP(700)
      COMMON /FIXT/ DFIX(2,100),NOFIX(100),IFLAG(2,100),NFIX
      COMMON /VARS/ CONV,C1,C2,C3,COMC(125),NO,NUMEL,NGAUS,ITER,NSGAUS
      COMMON /STNR/ PREVST(3,300),XCENT(300),YCENT(300),INC,ICALL
C
C**** IF NINCS.LE.0 AN ELASTIC SOLUTION IS GIVEN
C
      IF (NINCS.NE.0)GO TO 20
   10 CALL SOLVE
      RETURN
C
C**** ASSIGN PARAMETER VALUES
C
   20 PT=1.0
      NUM=700
      NITER=30
      VERGE=1.0D4
      WRITE (7,30) NINCS,TIMINC,VERGE
   30 FORMAT(1H0/1H0,I4,' TIME INCREMENTS, EACH OF ',D7.1,' YRS.'/
     1       1H0,5X,'CONVERGENCE LIMIT =',D7.1,' N PER SQ.M'/1H0)
      TIMINC=TIMINC*3.16D7
C     WRITE (8,40) IDATE,TITLE
   40 FORMAT (1H0,12X,3A4,40X,8A4/1H0)
C
C**** INITIALIZE ARRAYS  & STORE INITIAL FORCES IN FINIT
C
      NEL=NTRI+NQUAD
      DO 55 J=1,NEL
      NOG=NGAUSS(J)*4
      DO 50 I=1,NOG
   50 CREEP(I,J)=0.0
      DO 56 I=1,16
   56 SCREP(I,J)=0.0
   55 CONTINUE
      IF (NFS.EQ.0) GO TO 59
      DO 57 IF=1,NFS
      DO 58 I=1,24
   58 FLTCRP(I,IF)=0.0
```

```
   57 CONTINUE
   59 CONTINUE
      DO 60 I=1,NNOD2
   60 FINIT(I)=FORCE(I)
C
C**** START LOOP OVER NINCS TIME INCREMENTS
C
      TOTIME=0.000
      ICALL=2
      ISKIP=0
      DO 260 INC=1,NINCS
      TOTIME=TOTIME+TIMINC

      MTIM=INC-100*(INC/100)
      LTIM=MTIM-10*(MTIM/10)
      IF (MTIM.LT.14) LTIM=MTIM
      IF (LTIM.GT.4.OR.LTIM.EQ.0) LTIM=4
      WRITE(8,1919) INC,ZUF(LTIM),TOTIME
 1919 FORMAT(1H0/1H0,I4,A4,'TIME INCREMENT, ENDING AT ',D9.3,' S.'/1H )
C
      DO 75 J=1,NEL
      NOG=NGAUSS(J)*4
      DO 70 I=1,NOG
      DCREEP(I,J)=0.0
   70 PRESTR(I,J)=0.0
      DO 71 I=1,16
   71 DSCREP(I,J)=0.0
   75 CONTINUE
      IF (NFS.EQ.0) GO TO 78
      DO 76 IF=1,NFS
      DO 77 I=1,24
   77 DFLTCR(I,IF)=0.0
   76 CONTINUE
   78 CONTINUE
C
C**** START SOLUTION ITERATIONS
C
      DO 190 ITER=1,NITER
      CONV=0.0
C
C**** INITIALISE FCREEP , COPY FORCE INTO DISP
C**** AND SOLVE THE STIFFNESS EQUATION
C
      DO 80 IF=1,NNOD2
      FCREEP(IF)=0.0
      DISP(IF)=FORCE(IF)
   80 CONTINUE
      CALL MA07BD(GLOBK,DISP,NUM,NNOD2,KSIZE,PT)
      PT=0.0
C
C**** OBTAIN THE CREEP FORCE, FCREEP, BY INTEGRATION OF
C**** THE CREEP STRAINS AT EACH GAUSS POINT OF EACH ELEMENT
C
      IF (NTRI.EQ.0) GO TO 100
      DO 90 IEL=1,NTRI
      NO=6
      NUMEL=NOTEL(IEL)
      NGAUS=NGAUSS(NUMEL)
      CALL CREEPS
      IF (NGAUS.EQ.6) GO TO 90
      NSGAUS=3
      CALL SCREEP
   90 CONTINUE
C
  100 IF (NQUAD.EQ.0) GO TO 120
C
      DO 110 IEL=1,NQUAD
      NO=8
      NUMEL=NOQEL(IEL)
      NGAUS=NGAUSS(NUMEL)
      CALL CREEPS
      IF (NGAUS.EQ.4) GO TO 110
      NSGAUS=4

      CALL SCREEP
  110 CONTINUE
```

```
  120 IF(NFS.EQ.0) GO TO 125
C
C
C**** ENSURE THAT 'FIXED' DISPLACEMENTS REMAIN FIXED
C
  125 IF (NFIX.EQ.0) GO TO 160
      DO 150 I=1,NFIX
      DO 140 J=1,2
      IF (IFLAG(J,I)-1) 140,130,140
  130 K=2*NOFIX(I)+J-2
      FCREEP(K)=0.0
  140 CONTINUE
  150 CONTINUE
C
C**** TEST FOR CONVERGENCE OF CREEP STRESSES OVER THIS TIME INCREMENT
C
  160 IF (ITER.EQ.1) GO TO 170
      CONV=CONV/VERGE
      LTER=ITER-10*(ITER/10)
      IF (ITER.LT.14) LTER=ITER
      IF (LTER.GT.4.OR.LTER.EQ.0) LTER=4
C
C**** WRITE INFORMATION ON CONVERGENCE ON DEVICE 8
C
      IF (CONV.GE.999.999) GO TO 1025
      WRITE(8,1929) ITER,ZUF(LTER),CONV
 1929 FORMAT(1H ,I4,A4,'ITERATION; NORMALISED STRESS DIFFERENCE=',F7.3)
      GO TO 1206
 1025 WRITE(8,1928) ITER,ZUF(LTER),CONV
 1928 FORMAT(1H ,I4,A4,'ITERATION; NORMALISED STRESS DIFFERENCE=',D11.3)
 1206 IF (CONV.LT.1.0) GO TO 220
C
C**** INCORPORATE TOTAL CREEP STRAIN INTO FORCE VECTOR
C
  170 DO 180 LBOUN=1,NNOD2
      FORCE(LBOUN)=FINIT(LBOUN)+FCREEP(LBOUN)
  180 CONTINUE
  190 CONTINUE
C
C
C**** CONVERGENCE HAS FAILED
C
      WRITE(6,200)INC,ZUF(LTIM),CONV
  200 FORMAT(1HO,I4,A4,'TIME INCREMENT HAS NOT CONVERGED'/
     1       9X,'RESIDUAL= ',D10.3/)
      WRITE(7,210)
  210 FORMAT(1HO,10X,'** RUN ABORTED **')
      CALL TIME(1,1)
      STOP
C
  220 CONTINUE
C
C
C**** INCORPORATE INCREMENTAL CREEP INTO TOTAL CREEP VECTOR
C
      IF (NTRI.EQ.0) GO TO 763
C
      DO 762 IEL=1,NTRI

      NUMEL=NOTEL(IEL)
      NGAUS=NGAUSS(NUMEL)
      NOG=NGAUS*4
      DO 760 I=1,NOG
  760 CREEP(I,NUMEL)=CREEP(I,NUMEL)+DCREEP(I,NUMEL)
      IF (NGAUS.EQ.6) GO TO 762
      DO 761 I=1,12
  761 SCREP(I,NUMEL)=SCREP(I,NUMEL)+DSCREP(I,NUMEL)
  762 CONTINUE
C
  763 IF (NQUAD.EQ.0) GO TO 767
      DO 766 IEL=1,NQUAD
      NUMEL=NOQEL(IEL)
      NGAUS=NGAUSS(NUMEL)
      NOG=NGAUS*4
      DO 764 I=1,NOG
  764 CREEP(I,NUMEL)=CREEP(I,NUMEL)+DCREEP(I,NUMEL)
```

```
      IF (NGAUS.EQ.4) GO TO 766
      DO 765 I=1,16
  765 SCREP(I,NUMEL)=SCREP(I,NUMEL)+DSCREP(I,NUMEL)
  766 CONTINUE
C
  767 IF (NFS.EQ.0) GO TO 770
      DO 769 IF=1,NFS
      DO 768 I=1,24
  768 FLTCRP(I,IF)=FLTCRP(I,IF)+DFLTCR(I,IF)
  769 CONTINUE
  770 CONTINUE
C
C**** SET UP FORCE VECTORS FOR NEXT TIME INCREMENT
C
      DO 240 NEXTF=1,NNOD2
      FINIT(NEXTF)=FINIT(NEXTF)+FCREEP(NEXTF)
      FORCE(NEXTF)=FINIT(NEXTF)
  240 CONTINUE
      WRITE(6,250) INC,ZUF(LTIM)
  250 FORMAT(1H0,I4,A4,'TIME INCREMENT COMPLETE')
      CALL TIME(1,1)
C
  260 CONTINUE
      TIMINC=TIMINC/3.1607
C
      RETURN
      END
C
C
C*************************************************************************************:
C
C
      SUBROUTINE SOLVE
C     ================
C
C
C**** SOLVE THE STIFFNESS EQUATION
C
      IMPLICIT REAL*8 (A-H,O-W)
      REAL*8 KN,KS,MU
      COMMON /CONS/ NTRI,NQUAD,NINCS,NNOD,KSIZE,KSBW,NNOD2,NMAT,INITEM,
     +              IDATE(3),TIMINC,TITLE(4),PI,ZUF(4)
      COMMON /NODS/ X(350),Y(350),DISP(700),FORCE(700),XCOM1(2400)
      COMMON /FALT/ KN,KS,MU,FAC,BFAULT(12,2,50),
     +  DEPTH(50,2),THETA(50),FLTCRP(24,50),DFLTCR(24,50),
     +              STFRGN(24,50),NONOD(50,2),NELF(50,2),NITS,NFS
      COMMON /STIF/ ELK(18,18),GLOBK(700,185)
      COMMON /ELEM/ NODEL(8,300),NGAUSS(300),NOTEL(300),NOQEL(300),
     +          NOTCOL(300),NOQCOL(300),DIFFOP(9,300),BLIB(144,300),
     +         PRINC(16,300),CREEP(36,300)
C
C
C**** COPY FORCE INTO DISP AND SOLVE THE STIFFNESS EQUATION
C
      DO 10 I=1,NNOD2
   10 DISP(I)=FORCE(I)
C
      NUM=700
      PT=1.0
      CALL MA07BD(GLOBK,DISP,NUM,NNOD2,KSIZE,PT)
C
   15 WRITE(7,20)
   20 FORMAT(1H0,10X,'ELASTIC ANALYSIS')
C
      WRITE(6,30)
   30 FORMAT('0EQUATION SOLVED')
      CALL TIME(1,1)
C
      RETURN
      END
C
C*************************************************************************************:
C
C
      SUBROUTINE STRESS
C     =================
```

```
C
C**** CALCULATE THE STRESS AT EACH GAUSS POINT
C
C
      IMPLICIT REAL*8 (A-H,O-W)
      COMMON /CONS/ NTRI,NQUAD,NINCS,NNOD,KSIZE,KSBW,NNOD2,NMAT,INITEM,
     +              IDATE(3),STMAX,TITLE(4),PI,ZUF(4)
      COMMON /NODS/ X(350),Y(350),DISP(700),FORCE(700),XSTPOS(4,300),
     +              YSTPOS(4,300)
      COMMON /ELEM/ NODEL(8,300),NGAUSS(300),NOTEL(300),NOQEL(300),
     +          NOTCOL(300),NOQCOL(300),DIFFOP(9,300),BLIB(144,300),
     +        PRINC(16,300),CREEP(36,300)
      COMMON /MATS/ EM(9),PM(9),TM(9),RHOM(9),ETAM(9),C(9,3),ITYP(300)
      COMMON /NEWS/ BSTRES(64,300),SCREP(16,300),DSCREP(16,300),
     +            STRST(16,300)
      COMMON /GAPT/ S,T,SHAPE(8),DUM1(16),TSHAPE(6,36),
     +              TDNXDS(6,36),TDNXDT(6,36),TW1W2(6,6),QSHAPE(3,72),
     +              QDNXDS(3,72),QDNXDT(3,72),QW1W2(3,9),WEITRI(12,6),
     +    WEIQAD(18,3),PLACET(12,6),PLACEQ(18,3),PLACEL(3),WEILIN(3)
      COMMON /VARS/ CO(2),C1,C2,C3,DNXDX(8),DNXDY(8),Q(18),COM12(36),
     +              DNXDS(8),DNXDT(8),CO14(38),NO,NUMEL,NGAUS,MAT,IG
C
      IF(NTRI.EQ.0)GO TO 70
      NO=6
C
C**** START TO EVALUATE THE STRESS IN TRIANGULAR ELEMENTS
C
      DO 60 IEL=1,NTRI

      NUMEL=NOTEL(IEL)
      MAT=ITYP(NUMEL)
      NGAUS=NGAUSS(NUMEL)
      C1=C(MAT,1)
      C2=C(MAT,2)
      C3=C(MAT,3)
      IF (NGAUS.NE.6) GO TO 5
      IF (NINCS.EQ.0) GO TO 1001
      DO 6 IS=1,12
    6 SCREP(IS,NUMEL)=CREEP(12+IS,NUMEL)
 1001 DO 7 IS=1,36
    7 BSTRES(IS,NUMEL)=BLIB(36+IS,NUMEL)
C
C**** UNLOAD THE DISPLACEMENTS FOR THIS ELEMENT
C
    5 DO 10 J=1,6
      Q(2*J-1)=DISP(2*NODEL(J,NUMEL)-1)
      Q( 2*J )=DISP( 2*NODEL(J,NUMEL) )
   10 CONTINUE
C
C**** CALCULATE THE POSITION AND RECALL THE STRAIN MATRIX
C**** FOR EACH GAUSS POINT AT WHICH STRESS IS TO BE COMPUTED
C
      DO 50 IG=1,3
      IPOS=(IG+2)*6
      KPOS=(IG-1)*12
      XPOS=0.0
      YPOS=0.0
      DO 30 IV=1,NO
      SHAPE(IV)=TSHAPE(1,IPOS+IV)
      NOD=NODEL(IV,NUMEL)
      XPOS=XPOS+SHAPE(IV)*X(NOD)
      YPOS=YPOS+SHAPE(IV)*Y(NOD)
      L=2*IV
      K=L-1
      DNXDX(IV)=BSTRES(KPOS+K,NUMEL)
      DNXDY(IV)=BSTRES(KPOS+L,NUMEL)
   30 CONTINUE
C
      XSTPOS(IG,NUMEL)=XPOS
      YSTPOS(IG,NUMEL)=YPOS
C
C****  EVALUATE THE PRINCIPAL STRESSES
C
      CALL PRINCS
C
   50 CONTINUE
```

```
   60 CONTINUE
C
C**** START TO EVALUATE STRESSES IN QUADRILATERAL ELEMENTS
C
   70 IF(NQUAD.EQ.0)GO TO 140
      NO=8
      DO 130 IEL=1,NQUAD
      NUMEL=NOQEL(IEL)
      NGAUS=NGAUSS(NUMEL)
      MAT=ITYP(NUMEL)
      C1=C(MAT,1)
      C2=C(MAT,2)
      C3=C(MAT,3)

      IF (NGAUS.NE.4) GO TO 79
      IF (NINCS.EQ.0) GO TO 1000
      DO 71 IS=1,16
   71 SCREEP(IS,NUMEL)=CREEP(IS,NUMEL)
 1000 DO 72 IS=1,64
   72 BSTRES(IS,NUMEL)=BLIB(IS,NUMEL)
C
C**** UNLOAD THE DISPLACEMENTS FOR THIS ELEMENT
C
   79 DO 80 J=1,NO
      Q(2*J-1)=DISP(2*NODEL(J,NUMEL)-1)
      Q( 2*J )=DISP( 2*NODEL(J,NUMEL) )
   80 CONTINUE
C
C**** CALCULATE THE POSITION AND RECALL THE STRAIN MATRIX
C**** FOR EACH GAUSS POINT AT WHICH STRESS IS TO BE COMPUTED
C
C

      DO 120 IG=1,4
      IPOS=(IG-1)*NO
      KPOS=IPOS*2
      XPOS=0.0
      YPOS=0.0
      DO 100 IV=1,NO
      JPOS=IPOS+IV
      SHAPE(IV)=QSHAPE(1,JPOS)
      NOD=NODEL(IV,NUMEL)
      XPOS=XPOS+SHAPE(IV)*X(NOD)
      YPOS=YPOS+SHAPE(IV)*Y(NOD)
      L=2*IV
      K=L-1
      DNXDX(IV)=BSTRES(KPOS+K,NUMEL)
      DNXDY(IV)=BSTRES(KPOS+L,NUMEL)
  100 CONTINUE
      XSTPOS(IG,NUMEL)=XPOS
      YSTPOS(IG,NUMEL)=YPOS
C
C****  EVALUATE THE PRINCIPAL STRESSES
C
      CALL PRINCS
  120 CONTINUE
  130 CONTINUE
C
140   WRITE(6,150)
  150 FORMAT('0PRINCIPAL STRESSES COMPUTED')
      CALL TIME(1,1)
      RETURN
      END
C
C
C*********************************************************************************
C
C
      SUBROUTINE PRINCS
C     =================
C
C**** CALCULATE THE PRINCIPAL STRESSES
C
      IMPLICIT REAL*8 (A-H,O-W)
      REAL *8 PLACET,PLACEQ

      COMMON /CONS/ NTRI,NQUAD,NINCS,NNOD,KSIZE,KSBW,NNOD2,NMAT,INITEM,
```

```
     +                IDATE(3),STMAX,TITLE(4),PI,ZUF(4)
      COMMON /ELEM/ NODEL(8,300),NGAUSS(300),NOTEL(300),NOQEL(300),
     +             NOTCOL(300),NOQCOL(300),DIFFOP(9,300),BLIB(144,300),
     +           PRINC(16,300),CREEP(36,300)
      COMMON /MATS/ EM(9),PM(9),TM(9),RHOM(9),ETAM(9),C(9,3),ITYP(300)
      COMMON /NEWS/ BSTRES(64,300),SCREP(16,300),DSCREP(16,300),
     +           STRST(16,300)
      COMMON /VARS/ CO(2),C1,C2,C3,DNXDX(8),DNXDY(8),Q(18),STRN(4),
     +              STRES(4),COM11(82),NO,NUMEL,NGAUS,MAT,IG
      COMMON /GAPT/ S,T,SHAPE(8),DNXDS(8),DNXDT(8),TSHAPE(6,36),
     +              TDNXDS(6,36),TDNXDT(6,36),TW1W2(6,6),QSHAPE(3,72),
     +              QDNXDS(3,72),QDNXDT(3,72),QW1W2(3,9),COM2(258)
      COMMON /FALE/ STR0(4,350),CFAIL(4,300),FANGL(4,300),IFAIL(4,300)
C
      E=EM(MAT)
      P=PM(MAT)
      STRN(1)=0.0
      STRN(2)=0.0
      STRN(3)=0.0
      STRN(4)=0.0
C
C**** EVALUATE THE NON-ZERO COMPONENTS OF STRAIN, STRN=(B)(Q)
C
      INDEX=(IG-1)*4
      DO 10 I=1,NO
      L=2*I
      K=L-1
      STRN(1)=STRN(1)+DNXDX(I)*Q(K)
      STRN(2)=STRN(2)+DNXDY(I)*Q(L)
      STRN(3)=STRN(3)+DNXDX(I)*Q(L)+DNXDY(I)*Q(K)
   10 CONTINUE
C
      IF (INITEM.EQ.0)GO TO 150
C
C**** CALCULATE INITIAL STRAINS IF A TEMPERATURE ANOMALY IS PRESENT
C
      STOX=0.0D0
      STOY=0.0D0
      STOXY=0.0D0
      STOZ=0.0D0
C
      IF (NO.EQ.8) GO TO 100
C
      IPOS=(IG+2)*NO
      DO 90 I=1,NO
      NOD=NODEL(I,NUMEL)
      SHAP=TSHAPE(1,IPOS+I)
      STOX=STOX+SHAP*STR0(1,NOD)
      STOY=STOY+SHAP*STR0(2,NOD)
   90 STOXY=STOXY+SHAP*STR0(3,NOD)
      GO TO 110
C
  100 IPOS=(IG-1)*NO
      DO 120 I=1,NO
      NOD=NODEL(I,NUMEL)
      SHAP=QSHAPE(1,IPOS+I)
      STOX=STOX+SHAP*STR0(1,NOD)
      STOY=STOY+SHAP*STR0(2,NOD)
  120 STOXY=STOXY+SHAP*STR0(3,NOD)

C
  110 STRN(1)=STRN(1)-STOX
      STRN(2)=STRN(2)-STOY
      STRN(3)=STRN(3)-STOXY
      STRN(4)=-STOX/1.25
  150 CONTINUE
C
      IF (NINCS.EQ.0)GO TO 30
      DO 20 I=1,4
   20 STRN(I)=STRN(I)-SCREP(I+INDEX,NUMEL)
30    STRN(1)=STRN(1)+P*STRN(4)
      STRN(2)=STRN(2)+P*STRN(4)
C
C**** FORM STRESSES FROM STRAINS
C
      STRES(1)=C1*STRN(1)+C2*STRN(2)
```

```
      STRES(2)=C2*STRN(1)+C1*STRN(2)
      STRES(3)=C3*STRN(3)
      STRES(4)=P*(STRES(1)+STRES(2))+E*STRN(4)
C
C**** FORM THE PRINCIPAL STRESSES
C
      JPOS=(IG-1)*4
      IF(STRES(1).NE.STRES(2))GO TO  40
      THETA=PI/4.0
      GO TO  50
   40 THETA=0.5*(DATAN(2.0*STRES(3)/(STRES(1)-STRES(2))))
      IF(THETA.LE.0.0)THETA=THETA+PI/2.0
   50 PRINC(1+JPOS,NUMEL)=STRES(1)*(DCOS(THETA)*DCOS(THETA))+
     1                    STRES(2)*(DSIN(THETA)*DSIN(THETA))+
     2                    STRES(3)*DSIN(2.0*THETA)
      PRINC(2+JPOS,NUMEL)=STRES(1)+STRES(2)-PRINC(1+JPOS,NUMEL)
      PRINC(3+JPOS,NUMEL)=STRES(4)
      PRINC(4+JPOS,NUMEL)=THETA*180.0/PI
C
C**** FIND THE MAXIMUM STRESS IN THE BODY
C
      STMAX=DMAX1(DABS(PRINC(1+JPOS,NUMEL)),DABS(PRINC(2+JPOS,NUMEL)),
     1      DABS(PRINC(3+JPOS,NUMEL)),STMAX)
C
      RETURN
      END
C
C
C*********************************************************************************
C
C
      SUBROUTINE DISOUT
C     =================
C
C**** OUTPUT OF DISPLACEMENTS
C
      IMPLICIT REAL*8 (A-H,O-W)
      REAL *8 PLACET,PLACEQ
      COMMON /CONS/ NTRI,NQUAD,NINCS,NNOD,KSIZE,KSBW,NNOD2,NMAT,INITEM,
     +              IDATE(3),TIMINC,TITLE(4),PI,ZUF(4)
      COMMON /NODS/ X(350),Y(350),DISP(700),FORCE(700),XSTPOS(4,300),
     +              YSTPOS(4,300)
C
      WRITE(7,10)TITLE
C
   10 FORMAT(1H0/1H ,50X,4A8/1H0,10X,'NODAL DISPLACEMENTS'/
     +       1H+,10X,                                    /
     +       1H0,30X,'NODE',12X,'DISP(X): M',12X,'DISP(Y): M'/1H0)
C
      DO 20 IDIS=1,NNOD
      WRITE(7,30) IDIS,DISP(2*IDIS-1),DISP(2*IDIS)
   30 FORMAT(31X,I4,2(9X,1PE13.6))
   20 CONTINUE
C
      WRITE(6,40)
   40 FORMAT('0DISPLACEMENTS WRITTEN')
      CALL TIME(1,1)
C
      RETURN
      END
C
C
C
C*********************************************************************************
C
C
      BLOCK DATA
C     ==========
C
C**** INITIALIZE PI, SUFFIX ARRAY, AND LINE GAUSS POINTS
C
      IMPLICIT REAL*8 (A-H,O-W)
      COMMON /CONS/ NDUM1(12),TDUM1(5),PI,ZUF(4)
      COMMON /GAPT/ S,T,SHAPE(8),DNXDS(8),DNXDT(8),PCOM(1611),
     +              PLACEL(3),WEILIN(3)
C
```

```
      DATA PI /3.14159265358979300/
      DATA ZUF /'ST. ','ND. ','RD. ','TH. '/
      DATA PLACEL/.77459666924148300,0.0D0,
     +           -.77459666924148300/,
     +     WEILIN/.55555555555555600,
     +            .88889888888888900,
     +            .55555555555555600/
C
      END
C
C
C*****************************************************************************
C
C
C
      SUBROUTINE CRASH
C     ================
C
      WRITE(7,10)
   10 FORMAT(1H0,'** RUN ABORTED **'/'BANDWIDTH EQUALS ZERO')
      CALL TIME(1,1)
C
      STOP
      END
C
C
C*****************************************************************************
C
C
C
      SUBROUTINE BADLUK
C     =================
C
      IMPLICIT REAL*8 (A-H,O-W)
      COMMON /CONS/ NTRI,NQUAD,NINCS,NNOD,KSIZE,KSBW,NNOD2,NMAT,NST,
     +              IDATE(3),TIMINC,TITLE(4),PI,ZUF(4)
C
      WRITE(7,10)KSIZE
   10 FORMAT(1H0,'** RUN ABORTED **'/
     +       'BANDWIDTH =',I5,', AND EXCEEDS STORAGE SPACE')
      CALL TIME(1,1)
C
      STOP
      END
C
C
C*****************************************************************************
C
C
      FUNCTION RAMAX(X,N)
C     ===================
C**** TO FIND THE MAXIMUM VALUE OF AN ARRAY                          *****
C
      DIMENSION X(N)
      RAMAX=X(1)
      DO 700 IMAX=2,N
      RAMAX=AMAX1(RAMAX,X(IMAX))
700   CONTINUE
C
      RETURN
      END
C
C
C*****************************************************************************
C
C
      FUNCTION RAMIN(X,N)
C     ===================
C**** TO FIND THE MINIMUM VALUE OF AN ARRAY                          *****
C
      DIMENSION X(N)
      RAMIN=X(1)
      DO 701 IMIN=2,N
      RAMIN=AMIN1(RAMIN,X(IMIN))
701   CONTINUE
```

```
C
      RETURN
      END
C
CCCCC**********************************************************************
CCC
      SUBROUTINE GRID
      ===============
C
C**** PLOT ELEMENT MESH WITH CIRCLES DRAWN AT NODES
C
      IMPLICIT REAL*8 (A-H,O-W)
      COMMON /CONS/ NTRI,NQUAD,NINCS,NNOD,KSIZE,KBW,NNOD2,NMAT,INITEM,
     +              IDATE(3),TIMINC,TITLE(4),PI,ZUF(4)
      COMMON /NODS/ X(350),Y(350),COM9(1400),XCOM1(2400)
      COMMON /ELEM/ NODEL(8,300),NGAUSS(300),NOTEL(300),NOQEL(300),
     +              NOTCOL(300),NOQCOL(300),COM4(61500)
      COMMON /VARS/ XMAX,XMIN,YMAX,YMIN,XOMAX,XOMIN,YOMAX,YOMIN,
     +              XSP,YSP,PLT(124),KCOM(5)
      DIMENSION XPL(9),YPL(9)
C
      XSP1=XSP+0.2
      CALL CSPACE(0.2,XSP1,0.0,1.0)
      CALL PSPACE(0.2,XSP1,0.1,1.0)
      CALL MAP(XMIN,XMAX,YMIN,YOMAX)
C
C**** PLOT A CIRCLE AT EACH NODE
C
      CALL CTRSET(4)
      CALL CTRMAG(15)
      CALL PTPLOT(X,Y,1,NNOD,54)
      CALL CTRSET(1)
C
C**** DRAW ELEMENTS
C
      IF (NTRI.EQ.0) GO TO 30
C
      DO 20 IEL=1,NTRI
      NUMEL=NOTEL(IEL)
      DO 10 I=1,6
      NOD=NODEL(I,NUMEL)
      XPL(I)=X(NOD)
      YPL(I)=Y(NOD)
   10 CONTINUE
      XPL(7)=XPL(1)
      YPL(7)=YPL(1)
      CALL CURVEO(XPL,YPL,1,3)
      CALL CURVEO(XPL,YPL,3,5)
      CALL CURVEO(XPL,YPL,5,7)
   20 CONTINUE
C
   30 IF (NQUAD.EQ.0) GO TO 60
C
      DO 50 IEL=1,NQUAD
      NUMEL=NOQEL(IEL)
      DO 40 I=1,8
      NOD=NODEL(I,NUMEL)
      XPL(I)=X(NOD)
      YPL(I)=Y(NOD)
   40 CONTINUE
      XPL(9)=XPL(1)
      YPL(9)=YPL(1)
      CALL CURVEO(XPL,YPL,1,3)
      CALL CURVEO(XPL,YPL,3,5)
      CALL CURVEO(XPL,YPL,5,7)
      CALL CURVEO(XPL,YPL,7,9)
   50 CONTINUE
C
C**** ANNOTATE AXES
C
   60 XSP1=XSP+0.4
```

```
      CALL CSPACE(0.0,XSP1,0.0,1.0)
      CALL PSPACE(0.0,XSP1,0.0,1.0)
      CALL MAP(XOMIN,XOMAX,YOMIN,YOMAX)
      CALL LABEL
C
      WRITE(6,90)
   90 FORMAT('0ELEMENT MESH DRAWN')
C
      RETURN
      END
C
CCC*****************************************************************************
CCC
C
      SUBROUTINE PAMS
      ===============
C
CCC
CCC**** P.A.M.S. = PLOTTING AREA AND MAPPING SPACE ************************
CCC
C
      IMPLICIT REAL*8 (A-H,O-W)
      REAL*4 RAMAX,RAMIN
      COMMON /CONS/ NTRI,NQUAD,NINCS,NNOD,KSIZE,KSBW,NNOD2,NMAT,INITEM,
     +              IDATE(3),TIMINC,TITLE(4),PI,ZUF(4)
      COMMON /NODS/ X(350),Y(350),COM9(1400),XCOM1(2400)
      COMMON /VARS/ XMAX,XMIN,YMAX,YMIN,XOMAX,XOMIN,YOMAX,YOMIN,
     +              XSP,YSP,PLT(124),KCOM(5)
C
CCC
CCC**** START PLOTFILE ****************************************************
C
      CALL PAPER(1)
C
      WRITE(6,10)
   10 FORMAT('0PLEASE STATE X-COORDINATE OF START AND END OF PLOT'/
     +       '0??????.....')
      READ(5,60)XMIN,XMAX
      WRITE(6,20)
   20 FORMAT('0PLEASE GIVE Y-COORDINATE OF BOTTOM AND TOP OF PLOT'/
     +       '0??????.....')
      READ(5,60)YMIN,YMAX
   60 FORMAT(2F10.3)
C
CCC**** READ IN DESIRED PSPACE FOR MODEL ***********************************
C
      WRITE(6,19)
   19 FORMAT('0PLEASE GIVE X AND Y PSPACE'/
     1       '0?????.....')
      READ(5,18)XSP,YSP
   18 FORMAT(2F5.2)
C
CCC**** CALCULATE MAP AREA FOR PSPACE **************************************
C
      XMIN=XMIN*1000.0
      XMAX=XMAX*1000.0
      YMIN=YMIN*1000.0
      YMAX=YMAX*1000.0
      XSC=(XMAX-XMIN)/(XSP*10.0)
      YSC=(YMIN-YMAX)/(YSP*10.0)
C
      XOMIN=XMIN-XSC*2.0
      XOMAX=XMIN+(XSC*(XSP+0.2)*10.0)
      YOMIN=YMIN+YSC
      YOMAX=YMAX-(YSC*(0.9-YSP)*10.0)
      WRITE(6,101)
  101 FORMAT('0PAMS COMPLETED')
C
      RETURN
      END
C
CCC
CCC*****************************************************************************
CCC
C
```

```
      SUBROUTINE LABEL
C     ================
C
C**** WRITE TITLE AND ANNOTATE AXES ***************************************
C
      IMPLICIT REAL*8 (A-H,O-W)
      COMMON /CONS/ NTRI,NQUAD,NINCS,NNOD,KSIZE,KSBW,NNOD2,NMAT,INITEM,
     +              IDATE(3),TIMINC,TITLE(4),PI,ZUF(4)
      COMMON /VARS/ XMAX,XMIN,YMAX,YMIN,XOMAX,XOMIN,YOMAX,YOMIN,
     +              XSP,YSP,PLT(124),KCOM(5)
C
C**** ANNOTATE PLOT *******************************************************
C
      XCEN=(XMAX+XMIN)*0.5
      XMAP1=(XMAX-XMIN)/XSP
      CALL CTRMAG(20)
      XST=XCEN-((16.0/58.0)*XMAP1)
      YST=(YMAX-YMIN)*0.45
      CALL PLOTCS(XST,YST,TITLE,32)
      CALL CTRMAG(15)
      IYKM=YMIN/1.0E3
      XST=XMIN-5.0E03
      CALL PLOTNI(XST,YMIN,IYKM)
      IYKM=YMAX/1.0E3
      CALL PLOTNI(XST,YMAX,IYKM)
      YST=(YMIN-YMAX)*1.09
      IXKM=XMIN/1.0E3
      CALL PLOTNI(XMIN,YST,IXKM)
      XST=XCEN-((7.0/77.0)*XMAP1)
      CALL PLOTCS(XST,YST,'DISTANCE ( KM )',15)
      IXKM=XMAX/1.0E3
      CALL PLOTNI(XMAX,YST,IXKM)
C
C**** DRAW A BORDER AROUND THE MODEL **************************************
C
      XSP2=XSP+0.2
      YSP1=YSP+0.1
      CALL PSPACE(0.2,XSP2,0.1,YSP1)
      CALL BORDER
      WRITE(6,12)
   12 FORMAT('0LABEL DRAWN')
      RETURN
      END
C
C
C*****************************************************************************
C
C
      SUBROUTINE VECPLT
C     =================
C
C**** PLOT STRESS VECTORS AT EACH STRESS GAUSS POINT
C
      IMPLICIT REAL*8 (A-H,O-W)
      REAL*8 KN,KS,MU
      COMMON /NODS/ X(350),Y(350),COM9(1400),XCOM1(2400)
      COMMON /FALT/ KN,KS,MU,FAC,BFAULT(12,2,50),
     +  DEPTH(50,2),THETA(50),FLTCRP(24,50),DFLTCR(24,50),
     +              STFBGN(24,50),NONOD(50,2),NELF(50,2),NITS,NFS
      COMMON /CONS/ NTRI,NQUAD,NINCS,NNOD,KSIZE,KSBW,NNOD2,NMAT,INITEM,
     +              IDATE(3),STMAX,TITLE(4),PI,ZUF(4)
      COMMON /VARS/ XMAX,XMIN,YMAX,YMIN,XOMAX,XOMIN,YOMAX,YOMIN,
     +         XSP,YSP,XVECS,YVECS,PLT0(123),NO,NUMEL,NGAUS,LCOM(2)
      COMMON /ELEM/ NODEL(8,300),NGAUSS(300),NOTEL(300),NOQEL(300),
     +            NOTCOL(300),NOQCOL(300),DIFFOP(9,300),BLIB(144,300),
     +          PRINC(16,300),CREEP(36,300)
      DIMENSION XPLT(3),YPLT(3)
C
      XSP1=XSP+0.2
      CALL CSPACE(0.0,XSP1,0.0,1.0)
      CALL PSPACE(0.2,XSP1,0.1,1.0)
      CALL MAP(XMIN,XMAX,YMIN,YOMAX)
C
C**** FIND SCALE FACTORS
C
```

```
      XVECS=(ABS(XMAX-XMIN)/(25.0*XSP))*1.5
      YVECS=(ABS(YMAX-YMIN)/(25.0*YSP))*1.5
C
      IF (NTRI.EQ.0) GO TO 30
      DO 20 IEL=1,NTRI
      NUMEL=NOTEL(IEL)
      NGAUS=3
      CALL STPLOT
   20 CONTINUE
   30 IF (NQUAD.EQ.0) GO TO 50
      DO 40 IEL=1,NQUAD
      NUMEL=NOQEL(IEL)
      NGAUS=4
      CALL STPLOT
   40 CONTINUE
   50 CONTINUE
C
C**** PLOT POSITION OF FAULT, IF ONE IS PRESENT
C
      IF (NFS.EQ.0) GO TO 60
C
      DO 70 IF=1,NFS
      NUMEL=NELF(IF,1)
      NOD1=NODEL(1,NUMEL)
      NOD2=NODEL(2,NUMEL)
      NOD3=NODEL(3,NUMEL)
      XPLT(1)=X(NOD1)
      YPLT(1)=Y(NOD1)
      XPLT(2)=X(NOD2)
      YPLT(2)=Y(NOD2)

      XPLT(3)=X(NOD3)
      YPLT(3)=Y(NOD3)
   70 CALL CURVED(XPLT,YPLT,1,3)
C
C**** ANNOTATE PLOT ************************************************************
C
   60 XSP1=XSP+0.4
      CALL PSPACE(0.0,XSP1,0.0,1.0)
      CALL MAP(XOMIN,XOMAX,YOMIN,YOMAX)
      XMAP1=(XMAX-XMIN)/XSP
      XCEN=(XMAX+XMIN)*0.5
      CALL CTRMAG(15)
      XST=XCEN-((13.0/77.0)*XMAP1)
      YST=(YMAX-YMIN)*0.25
      CALL ITALIC(1)
      CALL PLOTCS(XST,YST,'( DOTTED LINES TENSIONAL )',26)
      CALL ITALIC(0)
      XLABEL=XST
      YLABEL=(YMAX-YMIN)*0.15
      CALL POSITN(XLABEL,YLABEL)
      XLABEL=XLABEL+2.0E8/STMAX*XVECS
      CALL JOIN (XLABEL,YLABEL)
      CALL PLOTCS(XLABEL,YLABEL,'  100 MPA',9)
      XST=XCEN-((7.0/77.0)*XMAP1)
      YST=(YMAX-YMIN)*0.32
      CALL PLOTCS(XST,YST,'STRESS VECTORS',14)
C
C**** ADD TITLE AND LABEL AXES *************************************************
C
      CALL LABEL
C
      WRITE(6,11)
   11 FORMAT('0VECTOR PLOT PRODUCED')
      RETURN
      END
C
CCCCC**************************************************************************
CCCCC
C
      SUBROUTINE STOUT
C     ================
C
C**** OUTPUT STRESSES ON DEVICE 7
```

```
C
      IMPLICIT REAL*8 (A-H,O-W)
      COMMON /CONS/ NTRI,NQUAD,NINCS,NNOD,KSIZE,KSBW,NNOD2,NMAT,INITEM,
     +              IDATE(3),STMAX,TITLE(4),PI,ZUF(4)
      COMMON /NODS/ X(350),Y(350),DISP(700),FORCE(700),XSTPOS(4,300),
     +              YSTPOS(4,300)
      COMMON /ELEM/ NODEL(8,300),NGAUSS(300),NOTEL(300),NOQEL(300),
     +            NOTCOL(300),NOQCOL(300),DIFFOP(9,300),BLIB(144,300),
     +          PRINC(16,300),CREEP(36,300)
      COMMON /FALE/ STRO(4,350),CFAIL(4,300),FANGL(4,300),IFAIL(4,300)
C
      WRITE(7,10)STMAX
   10 FORMAT(1H0,10X,'STRESSES'/
     +       1H+,10X,'        '/
     +   1H0,10X,'MAXIMUM STRESS =',1PD10.3,'N/SQ.M (ABSOLUTE VALUE)'/
     +       1H0,10X,'EL',5X,'X: (M)',7X,'Y: (M)',8X,
     +               'PRINCIPAL STRESSES',9X,'ANGLE',5X,'ZSTRESS ,
     +        5X,'CFAIL',5X,'IFAIL',4X,'THETA'/1H0)
C
      NOEL=NTRI
      NO=3
      DO 50 IS=1,2
      IF (IS.EQ.1) GO TO 200
      NOEL=NQUAD
      NO=4
  200 IF (NOEL.EQ.0) GO TO 70
      DO 40 IEL=1,NOEL
      IF (IS.EQ.1)NUMEL=NOTEL(IEL)
      IF (IS.EQ.2)NUMEL=NOQEL(IEL)
      DO 30 IG=1,NO
      JPOS=(IG-1)*4
      WRITE(7,20)NUMEL,XSTPOS(IG,NUMEL),YSTPOS(IG,NUMEL),
     +           PRINC(1+JPOS,NUMEL),PRINC(2+JPOS,NUMEL),
     +           PRINC(4+JPOS,NUMEL),PRINC(3+JPOS,NUMEL),
     +      CFAIL(IG,NUMEL),IFAIL(IG,NUMEL),FANGL(IG,NUMEL)
   20 FORMAT(8X,I3,5X,E10.3,3X,E10.3,3X,E10.3,3X,E10.3,
     +       3X,F8.3,3X,E10.3,3X,E10.3,3X,I3,3X,E10.3)
   30 CONTINUE
   40 CONTINUE
   70 NOEL=NQUAD
      NO=4
   50 CONTINUE
C
      WRITE(6,90)
   90 FORMAT('0STRESSES WRITTEN')
      CALL TIME(1,1)
C
      RETURN
      END
C
C*********************************************************************
C
C
      SUBROUTINE CREEPS
C     =================
C
C**** CALCULATE THE CREEP FORCE OF THIS ELEMENT,
C**** USING A NEWTONIAN VISCO-ELASTIC RHEOLOGY.
C
      IMPLICIT REAL*8 (A-H,O-W)
      COMMON /CONS/ NTRI,NQUAD,NINCS,NNOD,KSIZE,KSBW,NNOD2,NMAT,INITEM,
     +              IDATE(3),TIMINC,TITLE(4),PI,ZUF(4)
      COMMON /NODS/ X(350),Y(350),DISP(700),FORCE(700),XCOM1(2400)
      COMMON /ELEM/ NODEL(8,300),NGAUSS(300),NOTEL(300),NOQEL(300),
     +            NOTCOL(300),NOQCOL(300),DIFFOP(9,300),BLIB(144,300),
     +          PRINC(16,300),CREEP(36,300)
      COMMON /MATS/ EM(9),PM(9),TM(9),RHOM(9),ETAM(9),C(9,3),ITYP(300)
      COMMON /VISC/ DCREEP(36,300),PRESTR(36,300),STRBGN(36,300),
     +              FINIT(700),FCREEP(700)
      COMMON /VARS/ CONV,C1,C2,C3,DNXDX(8),
     +              DNXDY(8),Q(18),STRN(4),STRES(4),DEVST(4),STINIT(4),
     +              STRDIF(4),COMD(71),NO,NUMEL,NGAUS,ITER,NSGAUS
      COMMON /GAPT/ S,T,SHAPE(8),DNXDS(8),DNXDT(8),TSHAPE(6,36),
     +              TDNXDS(6,36),TDNXDT(6,36),TW1W2(6,6),QSHAPE(3,72),
     +              QDNXDS(3,72),QDNXDT(3,72),QW1W2(3,9),COM2(258)
```

```
      COMMON /FALE/ STRO(4,350),CFAIL(4,300),FANGL(4,300),IFAIL(4,300)
      MAT=ITYP(NUMEL)
      E=EM(MAT)
      P=PM(MAT)
      ETA=ETAM(MAT)
      IF (ETA.NE.0.0D0)VISCO=TIMINC/(2.0D0*ETA)
      C1=C(MAT,1)
      C2=C(MAT,2)
      C3=C(MAT,3)
C
      DO 10 I=1,NO
      Q(2*I-1)=DISP(2*NODEL(I,NUMEL)-1)
      Q( 2*I  )=DISP( 2*NODEL(I,NUMEL) )
   10 CONTINUE
C
C**** OBTAIN THE CREEP FORCE, FCREEP, FOR THIS ELEMENT
C**** BY GAUSSIAN NUMERICAL INTEGRATION
C
      DO 110 IG=1,NGAUS
      DV=DIFFOP(IG,NUMEL)
      JPOS=(IG-1)*NO*2
      INDEX=(IG-1)*4
C
      STRN(1)=0.0
      STRN(2)=0.0
      STRN(3)=0.0
      STRN(4)=0.0
C
C**** CALCULATE THE INITIAL ELASTIC STRAINS
C
      DO 20 I=1,NO
      L=2*I
      K=L-1
      DNXDX(I)=BLIB(JPOS+K,NUMEL)
      DNXDY(I)=BLIB(JPOS+L,NUMEL)
      STRN(1)=STRN(1)+DNXDX(I)*Q(K)
      STRN(2)=STRN(2)+DNXDY(I)*Q(L)
      STRN(3)=STRN(3)+DNXDX(I)*Q(L)+DNXDY(I)*Q(K)
   20 CONTINUE
C
      IF (INITEM.EQ.0) GO TO 150
C
      STOX=0.0D0
      STOY=0.0D0
      STOXY=0.0D0
      STOZ=0.0D0
C
      IF (NO.EQ.8) GO TO 1000
      IPOS=(IG-1)*NO
      DO 190 I=1,NO
      NOD=NODEL(I,NUMEL)
      SHAP=TSHAPE(1,IPOS+I)
      STOX=STOX+SHAP*STRO(1,NOD)
  190 STOY=STOY+SHAP*STRO(2,NOD)
      GO TO 1110
 1000 IPOS=(IG-1)*NO
      DO 1120 I=1,NO
      NOD=NODEL(I,NUMEL)
      SHAP=QSHAPE(1,IPOS+I)
      STOX=STOX+SHAP*STRO(1,NOD)

 1120 STOY=STOY+SHAP*STRO(2,NOD)
 1110 STRN(1)=STRN(1)-STOX
      STRN(2)=STRN(2)-STOY
      STRN(3)=STRN(3)-STOXY
      STRN(4)=-STOX/1.25
  150 CONTINUE
      DO 30 I=1,4
      STRN(I)=STRN(I)-CREEP(INDEX+I,NUMEL)-DCREEP(INDEX+I,NUMEL)
   30 CONTINUE
C
      STRN(1)=STRN(1)+P*STRN(4)
      STRN(2)=STRN(2)+P*STRN(4)
C
C**** FORM STRESSES FROM STRAINS
C
```

```
      STRES(1)=C1*STRN(1)+C2*STRN(2)
      STRES(2)=C2*STRN(1)+C1*STRN(2)
      STRES(3)=C3*STRN(3)
      STRES(4)=P*(STRES(1)+STRES(2))+E*STRN(4)
C
C**** STORE STRESSES AT THE START OF THE TIME INCREMENT
C
      IF(ITER.GT.1)GO TO 50
      DO 40 I=1,4
      STRBGN(INDEX+I,NUMEL)=STRES(I)
   40 CONTINUE
C
C**** FORM THE CREEP STRAIN, STINIT, FOR THIS GAUSS POINT
C
   50 DO 60 I=1,4
      STRES(I)=(STRES(I)+STRBGN(INDEX+I,NUMEL))/2.0D0
   60 CONTINUE
C
      HYDST=(STRES(1)+STRES(2)+STRES(4))/3.0D0
      DEVST(1)=STRES(1)-HYDST
      DEVST(2)=STRES(2)-HYDST
      DEVST(3)=2.0D0*STRES(3)
      DEVST(4)=STRES(4)-HYDST
C
      IF (ETA.EQ.0.0D0) GO TO 90
C
      DO 70 I=1,4
      STINIT(I)=DEVST(I)*VISCO
      DCREEP(INDEX+I,NUMEL)=STINIT(I)
   70 CONTINUE
C
      STINIT(1)=STINIT(1)+P*STINIT(4)
      STINIT(2)=STINIT(2)+P*STINIT(4)
C
C**** FIND THE CREEP FORCE, FCREEP, BY NUMERICAL INTEGRATION
C
      DO 80 I=1,NO
      L=2*I
      K=L-1
      LOC2=2*NODEL(I,NUMEL)
      LOC1=LOC2-1
      FCREEP(LOC1)=(DNXDX(I)*C1*STINIT(1)+DNXDX(I)*C2*STINIT(2)+
     1             DNXDY(I)*C3*STINIT(3))*DV+FCREEP(LOC1)
      FCREEP(LOC2)=(DNXDY(I)*C2*STINIT(1)+DNXDY(I)*C1*STINIT(2)+
     1             DNXDX(I)*C3*STINIT(3))*DV+FCREEP(LOC2)

   80 CONTINUE
C
C**** CALCUALTE CONV, A MEASURE OF CONVERGENCE
C
   90 DO 100 I=1,4
      STRES(I)=DABS(STRES(I))
      STRDIF(I)=DABS(STRES(I)-PRESTR(INDEX+I,NUMEL))
      CONV=DMAX1(CONV,STRDIF(I))
      PRESTR(INDEX+I,NUMEL)=STRES(I)
  100 CONTINUE
  110 CONTINUE
C
      RETURN
      END
C
C*******************************************************************************
C
C
      SUBROUTINE SCREEP
C     =================
C
C**** CALCULATE THE INCREMENTAL CREEP STRAIN AT EACH STRESS GAUSS POINT
C
      IMPLICIT REAL*8 (A-H,O-W)
      COMMON /CONS/ NTRI,NQUAD,NINCS,NNOD,KSIZE,KSBW,NNOD2,NMAT,INITEM,
     +              IDATE(3),TIMINC,TITLE(4),PI,ZUF(4)
      COMMON /NODS/ X(350),Y(350),DISP(700),FORCE(700),XCOM1(2400)
      COMMON /ELEM/ NODEL(3,300),NGAUSS(300),NOTEL(300),NOQEL(300),
     +              NOTCOL(300),NOQCOL(300),DIFFOP(9,300),BLIB(144,300),
     +              PRINC(16,300),CREEP(36,300)
```

```
      COMMON /MATS/ EM(9),PM(9),TM(9),RHOM(9),ETAM(9),C(9,3),ITYP(300)
      COMMON /NEWS/ BSTRES(64,300),SCREP(16,300),DSCREP(16,300),
     +              STRST(16,300)
      COMMON /VISC/ DCREEP(36,300),PRESTR(36,300),STRBGN(36,300),
     +              FINIT(700),FCREEP(700)
      COMMON /VARS/ CONV,C1,C2,C3,DNXDX(8),
     +              DNXDY(8),Q(18),STRN(4),STRES(4),DEVST(4),STINIT(4),
     +              STRDIF(4),COMD(71),NO,NUMEL,NGAUS,ITER,NSGAUS
      COMMON /GAPT/ S,T,SHAPE(8),DNXDS(8),DNXDT(8),TSHAPE(6,36),
     +              TDNXDS(6,36),TDNXDT(6,36),TW1W2(6,6),QSHAPE(3,72),
     +              QDNXDS(3,72),QDNXDT(3,72),QW1W2(3,9),COM2(258)
      COMMON /FALE/ STRO(4,350),CFAIL(4,300),FANGL(4,300),IFAIL(4,300)
      MAT=ITYP(NUMEL)
      E=EM(MAT)
      P=PM(MAT)
      ETA=ETAM(MAT)
      IF (ETA.NE.0.0D0)VISCO=TIMINC/(2.0D0*ETA)
      C1=C(MAT,1)
      C2=C(MAT,2)
      C3=C(MAT,3)
C
      DO 10 I=1,NO
      Q(2*I-1)=DISP(2*NODEL(I,NUMEL)-1)
      Q( 2*I )=DISP( 2*NODEL(I,NUMEL) )
   10 CONTINUE
C
C**** OBTAIN THE CREEP FORCE, FCREEP, FOR THIS ELEMENT
C**** BY GAUSSIAN NUMERICAL INTEGRATION.
C
      DO 90 IG=1,NSGAUS

      JPOS=(IG-1)*NO*2
      INDEX=(IG-1)*4
C
      STRN(1)=0.0
      STRN(2)=0.0
      STRN(3)=0.0
      STRN(4)=0.0
C
C**** CALCULATE THE INITIAL ELASTIC STRAINS
C
      DO 20 I=1,NO
      L=2*I
      K=L-1
      DNXDX(I)=BSTRES(JPOS+K,NUMEL)
      DNXDY(I)=BSTRES(JPOS+L,NUMEL)
      STRN(1)=STRN(1)+DNXDX(I)*Q(K)
      STRN(2)=STRN(2)+DNXDY(I)*Q(L)
      STRN(3)=STRN(3)+DNXDX(I)*Q(L)+DNXDY(I)*Q(K)
   20 CONTINUE
C
      IF (INITEM.EQ.0) GO TO 150
C
      STOX=0.0D0
      STOY=0.0D0
      STOXY=0.0D0
      STOZ=0.0D0
C
      IF (NO.EQ.8) GO TO 1000
      IPOS=(IG-1)*NO
      DO 190 I=1,NO
      NOD=NODEL(I,NUMEL)
      SHAP=TSHAPE(1,IPOS+I)
      STOX=STOX+SHAP*STRO(1,NOD)
  190 STOY=STOY+SHAP*STRO(2,NOD)
      GO TO 1110
 1000 IPOS=(IG-1)*NO
      DO 1120 I=1,NO
      NOD=NODEL(I,NUMEL)
      SHAP=QSHAPE(1,IPOS+I)
      STOX=STOX+SHAP*STRO(1,NOD)
 1120 STOY=STOY+SHAP*STRO(2,NOD)
 1110 STRN(1)=STRN(1)-STOX
      STRN(2)=STRN(2)-STOY
      STRN(3)=STRN(3)-STOXY
      STRN(4)=-STOX/1.25
```

```
  150 CONTINUE
C
      DO 30 I=1,4
      STRN(I)=STRN(I)-SCREP(INDEX+I,NUMEL)-OSCREP(INDEX+I,NUMEL)
   30 CONTINUE
C
      STRN(1)=STRN(1)+P*STRN(4)
      STRN(2)=STRN(2)+P*STRN(4)
C
C**** FORM STRESSES FROM STRAINS
C
      STRES(1)=C1*STRN(1)+C2*STRN(2)
      STRES(2)=C2*STRN(1)+C1*STRN(2)
      STRES(3)=C3*STRN(3)
      STRES(4)=P*(STRES(1)+STRES(2))+E*STRN(4)
C
C**** STORE STRESSES AT THE START OF THE TIME INCREMENT
C
      IF(ITER.GT.1)GO TO 50
      DO 40 I=1,4
      STRST(INDEX+I,NUMEL)=STRES(I)
   40 CONTINUE
C
C**** FORM THE CREEP STRAIN, STINIT, FOR THIS GAUSS POINT
C
   50 DO 60 I=1,4
      STRES(I)=(STRES(I)+STRST(INDEX+I,NUMEL))/2.0D0
   60 CONTINUE
C
      HYDST=(STRES(1)+STRES(2)+STRES(4))/3.0D0
      DEVST(1)=STRES(1)-HYDST
      DEVST(2)=STRES(2)-HYDST
      DEVST(3)=2.0D0*STRES(3)
      DEVST(4)=STRES(4)-HYDST
C
      IF (ETA.EQ.0.0D0) GO TO 90
C
      DO 70 I=1,4
      DSCREP(INDEX+I,NUMEL)=DEVST(I)*VISCO
   70 CONTINUE
   90 CONTINUE
C
      RETURN
      END
C
C*********************************************************************************
C
C
      SUBROUTINE STPLOT
      =================
C
C
C**** PLOT STRESS VECTORS AT EACH STRESS GAUSS POINT
C
      IMPLICIT REAL*8 (A-H,O-W)
      COMMON /CONS/ NTRI,NQUAD,NINCS,NNOD,KSIZE,KSBW,NNOD2,NMAT,INITEM,
     +              IDATE(3),STMAX,TITLE(4),PI,ZUF(4)
      COMMON /VARS/ XMAX,XMIN,YMAX,YMIN,XOMAX,XOMIN,YOMAX,YOMIN,
     +          XSP,YSP,XVECS,YVECS,PLTO(123),NO,NUMEL,NGAUS,LCOM(2)
      COMMON /NODS/ X(350),Y(350),DISP(700),FORCE(700),XSTPOS(4,300),
     +              YSTPOS(4,300)
      COMMON /ELEM/ NODEL(8,300),NGAUSS(300),NOTEL(300),NOQEL(300),
     +          NOTCOL(300),NOQCOL(300),DIFFOP(9,300),BLIB(144,300),
     +          PRINC(16,300),CREEP(36,300)
C
      DO 711  IG=1,NGAUS
      KPLT=1
      IPOS=(IG-1)*4
      XPOS=XSTPOS(IG,NUMEL)
      YPOS=YSTPOS(IG,NUMEL)
      CALL GPOINT(XPOS,YPOS)
C
C**** ADJUST ANGLES FOR PLOTTING
C
      IF (DABS(PRINC(4+IPOS,NUMEL)-90.0).LT.1.0E-7)GO TO 713
      TTHETA=PRINC(4+IPOS,NUMEL)*PI/180.0
```

```
      CTHETA=DCOS(TTHETA)
      STHETA=DSIN(TTHETA)
      GO TO 714
  713 CTHETA=0.0
      STHETA=1.0
  714 CONTINUE
C
      XPLT=XPOS+(PRINC(1+IPOS,NUMEL)*CTHETA/STMAX*XVECS)
      YPLT=YPOS+(PRINC(1+IPOS,NUMEL)*STHETA/STMAX*YVECS)
  715 CALL POSITN(XPLT,YPLT)
C
C**** IF STRESS IS TENSIONAL PLOT A BROKEN LINE
C****                 OTHERWISE PLOT A FULL LINE
C
      IF (PRINC(KPLT+IPOS,NUMEL).LT.0.0) GO TO 700
C
      XPLT1=0.4*XPOS+0.6*XPLT
      YPLT1=0.4*YPOS+0.6*YPLT
      CALL JOIN(XPLT1,YPLT1)
      XPLT1=1.6*XPOS-0.6*XPLT
      YPLT1=1.6*YPOS-0.6*YPLT
      CALL POSITN(XPLT1,YPLT1)
  700 XPLT1=2.0*XPOS-XPLT
      YPLT1=2.0*YPOS-YPLT
      CALL JOIN (XPLT1,YPLT1)
      IF (KPLT.EQ.2)GO TO 711
      IF (CTHETA.EQ.0.0)GO TO 720
      COP=CTHETA
      CTHETA=STHETA
      STHETA=COP
      GO TO 718
  720 STHETA=0.0
      CTHETA=1.0
  718 XPLT=XPOS-(PRINC(2+IPOS,NUMEL)*CTHETA/STMAX*XVECS)
      YPLT=YPOS+(PRINC(2+IPOS,NUMEL)*STHETA/STMAX*YVECS)
      KPLT=KPLT+1
      GO TO 715
  711 CONTINUE
      RETURN
      END
C
CCC
C*********************************************************************************
CCC
C
       SUBROUTINE KFAULT
       =================
C
CCC
C**** CALCULTE THE FAULT STIFFNESS
C
      IMPLICIT REAL*8 (A-H,O-W)
      REAL*8 KS,KN,LENGTH,MU
      COMMON /ELEM/ NODEL(8,300),ICOM2(1500),COM4(61500)
      COMMON /NODS/ X(350),Y(350),DISP(700),FORCE(700),XCOM1(2400)
      COMMON /GAPT/ S,T,SHAPE(8),DNXDS(8),DNXDT(8),PCOM(1611),
     +              PLACEL(3),WEILIN(3)
      COMMON /STIF/ ELK(18,18),GLOBK(700,185)
      COMMON /CONS/ NTRI,NQUAD,NINCS,NNOD,KSIZE,KSBW,NNOD2,NMAT,NST,
     +              IDATE(3),TIMINC,TITLE(4),PI,ZUF(4)
      COMMON /FALT/ KN,KS,MU,FAC,BFAULT(12,2,50),

     +  DEPTH(50,2),THETA(50),FLTCRP(24,50),OFLTCR(24,50),
     +              STFBGN(24,50),NONOD(50,2),NELF(50,2),NITS,NFS
      DIMENSION FK(3,12,12),RK(12,12),FGLOBK(12,12),NOD(6)
C
CCC
C**** INITIALISE THE UPPER TRIANGLE OF THE UPPER LEFT HAND PARTITION
C**** OF THE LOCAL FAULT SIFFNESS MATRIX FOR THE TWO GAUSS POINTS,
C**** FK(1,...) AND FK(2,...)
C
      DO 10 I=1,5
      DO 10 J=I,6
      FK(1,I,J)=0.0D0
      FK(2,I,J)=0.0D0
   10 FK(3,I,J)=0.0D0
C
```

```
C**** CALCULATE THE SHAPE FUNCTIONS, AND THE LOCAL FAULT STIFFNESSES
C**** FOR THE TWO GAUSS POINTS, USING THEIR PARTITIONED SYMMETRY
C
      DO 50 IG=1,3
      S=PLACEL(IG)
      SS=S*S
      SHAPE(1)=(SS-S)/2.0D0
      SHAPE(2)=1.0D0-SS
      SHAPE(3)=(SS+S)/2.0D0
C
      DO 20 I=1,3
      L=I*2
      K=L-1
      DO 20 J=1,3
      M=J*2
      N=M-1
      FK(IG,K,N)=SHAPE(I)*SHAPE(J)*KN
   20 FK(IG,L,M)=SHAPE(I)*SHAPE(J)*KS
C
      DO 30 I=1,5
      DO 30 J=I,6
   30 FK(IG,J,I)=FK(IG,I,J)
C
      DO 40 I=1,6
      DO 40 J=1,6
      FK(IG,I+6,J+6)=FK(IG,I,J)
      FK(IG,I,J+6)=-FK(IG,I,J)
   40 FK(IG,I+6,J)=-FK(IG,I,J)
C
   50 CONTINUE
C
C**** INITIALISE THE GLOBAL FAULT STIFFNESS, FGLOBK
C
      DO 150 IF=1,NFS
      DO 55 I=1,12
      DO 55 J=1,12
   55 FGLOBK(I,J)=0.0D0
C
C**** CALCUALTE THE GLOBAL FAULT STIFFNESS BY NUMERICAL INTEGRATION
C
      NUMEL=NELF(IF,1)
      NOD1=NODEL(1,NUMEL)
      NOD2=NODEL(2,NUMEL)
      NOD3=NODEL(3,NUMEL)
C

      DO 80 IG=1,3
      S=PLACEL(IG)
      DS=WEILIN(IG)
      DNXDS(1)=S-0.5D0
      DNXDS(2)=-2.0D0*S
      DNXDS(3)=S+0.5D0
      DXXDS=DNXDS(1)*X(NOD1)+DNXDS(2)*X(NOD2)+DNXDS(3)*X(NOD3)
      DYXDS=DNXDS(1)*Y(NOD1)+DNXDS(2)*Y(NOD2)+DNXDS(3)*Y(NOD3)
      LENGTH=1.0/(2.0*(DXXDS**2+DYXDS**2))
      DSXL=DS*LENGTH
C
C**** OBTAIN THE GLOBAL FAULT STIFFNESS BY MULTIPLYING THE LOCAL FAULT
C**** STIFFNESSES BY THE ROTATION MATRICES (ONLY DOING THOSE MULTIPLICATIONS
C**** WHICH YIELD A NON ZERO ANSWER), AND INTEGRATING
C
      DO 60 I=1,6
      L=I*2
      K=L-1
      DO 60 J=1,6
      M=J*2
      N=M-1
      RK(K,N)=-DYXDS*FK(IG,K,N)
      RK(K,M)=-DXXDS*FK(IG,L,M)
      RK(L,N)=DXXDS*FK(IG,K,N)
   60 RK(L,M)=-DYXDS*FK(IG,L,M)
C
      DO 70 I=1,6
      L=I*2
      K=L-1
      DO 70 J=1,6
```

```
      M=J*2
      N=M-1
      FGLOBK(K,N)=(-DYXDS*RK(K,N)-DXXDS*RK(K,M))*DSXL+FGLOBK(K,N)
      FGLOBK(K,M)=(DXXDS*RK(K,N)-DYXDS*RK(K,M))*DSXL+FGLOBK(K,M)
      FGLOBK(L,N)=(-DYXDS*RK(L,N)-DXXDS*RK(L,M))*DSXL+FGLOBK(L,N)
   70 FGLOBK(L,M)=(DXXDS*RK(L,N)-DYXDS*RK(L,M))*DSXL+FGLOBK(L,M)
C
   80 CONTINUE
C
C
C**** LOAD THE FAULT STIFFNESS INTO THE GLOBAL STIFFNESS MATRIX
C
      NEL1=NELF(IF,1)
      NEL2=NELF(IF,2)
      NOD(1)=NODEL(1,NEL1)
      NOD(2)=NODEL(2,NEL1)
      NOD(3)=NODEL(3,NEL1)
      NOD(4)=NODEL(1,NEL2)
      NOD(5)=NODEL(2,NEL2)
      NOD(6)=NODEL(3,NEL2)
C
      DO 130 I=1,6
      I1=2*NOD(I)-2+KSBW
      NK1=2*I-2
      DO 131 J=1,2
      J1=I1+J
      NK=NK1+J
      DO 132 K=1,6
      K1=2*NOD(K)-2
      MK1=2*K-2
      DO 133 L=1,2

      KROW=K1+L
      KCOL=J1-KROW
      MK=MK1+L
  133 GLOBK(KROW,KCOL)=GLOBK(KROW,KCOL)+FGLOBK(MK,NK)
  132 CONTINUE
  131 CONTINUE
  130 CONTINUE
C
  150 CONTINUE
C
      WRITE(6,160)
  160 FORMAT('0FAULT STIFFNESS CALCULATED')
C     CALL TIME(1,1)
C
      RETURN
      END
C
C
C*********************************************************************************************
C
C
      SUBROUTINE PREFLT
C     =================
C
C**** CALCULATE THE STRAIN MATRIX FOR NODES ON THE FAULT, AND
C**** CALCULATE THE TANGENT TO EACH DUAL NODE ON THE FAULT
C
      IMPLICIT REAL*8 (A-H,O-W)
      REAL*8 KS,KN,MU
      COMMON /ELEM/ NODEL(8,300),NGAUSS(300),NOTEL(300),NOQEL(300),
     +              NOTCOL(300),NOQCOL(300),DIFFOP(9,300),BLIB(144,300),
     +              COM1(15600)
      COMMON /NODS/ X(350),Y(350),DISP(700),FORCE(700),XCOM1(2400)
      COMMON /GAPT/ S,T,SHAPE(8),DNXDS(8),DNXDT(8),PCOM(1611),
     +       PLACEL(3),WEILIN(3)
      COMMON /FALT/ KN,KS,MU,FAC,BFAULT(12,2,50),
     +  DEPTH(50,2),THETA(50),FLTCRP(24,50),DFLTCR(24,50),
     +              STFBGN(24,50),NONOD(50,2),NELF(50,2),NITS,NFS
      COMMON /VARS/ CONV,D,C1,C2,C3,DNXDX(8),DNXDY(8),COMFLT(108),
     +              NO,IDOT,NGAUS,NUMEL,IX
      DATA TS/0.33333333333333D0/,TT/0.33333333333333D0/
C
      DO 70 IF=1,NFS
C
C**** COMPUTE THE STRAIN MATRIX, BFAULT, AT THE CENTROID OF
```

```
C**** EACH FAULT ELEMENT
C
      DO 50 IS=1,2
      NO=6
      NUMEL=NELF(IF,IS)
      S=TS
      T=TT
      CALL TSHAFN
      CALL DTSHAP
      CALL BFORM
      YPOS=0.0
      DO 30 J=1,NO
      L=2*J
      K=L-1
      YPOS=YPOS+SHAPE(J)*Y(NODEL(J,NUMEL))

      BFAULT(K,IS,IF)=DNXDX(J)
   30 BFAULT(L,IS,IF)=DNXDY(J)
      DEPTH(IF,IS)=YPOS
   50 CONTINUE
C
C**** COMPUTE ROTATION ANGLE FOR THIS FAULT SECTION
C
      NUMEL=NELF(IF,1)
      NOD1=NODEL(1,NUMEL)
      NOD2=NODEL(2,NUMEL)
      NOD3=NODEL(3,NUMEL)
C
      S=0.000
      DNXDS(1)=S-0.5
      DNXDS(2)=-2.0*S
      DNXDS(3)=S+0.5
      DXXDS=DNXDS(1)*X(NOD1)+DNXDS(2)*X(NOD2)+DNXDS(3)*X(NOD3)
      DYXDS=DNXDS(1)*Y(NOD1)+DNXDS(2)*Y(NOD2)+DNXDS(3)*Y(NOD3)
      DXXDY=DXXDS/DYXDS
      THETA(IF)=DATAN(-DXXDY)
   70 CONTINUE
C
      RETURN
      END
C
C
C*********************************************************************************
C
C
      SUBROUTINE FSHEAR
C     =================
C
C**** ITERATE TO REMOVE EXCESS SHEAR FROM THE FAULT
C
      IMPLICIT REAL*8 (A-H,O-W)
      REAL*8 KS,KN,MU
      COMMON /FALT/ KN,KS,MU,FAC,BFAULT(12,2,50),
     +  DEPTH(50,2),THETA(50),FLTCRP(24,50),DFLTCR(24,50),
     +              STFBGN(24,50),NONOD(50,2),NELF(50,2),NITS,NFS
      COMMON /CONS/ NTRI,NQUAD,NINCS,NNOD,KSIZE,KSBW,NNOD2,NMAT,INITEM,
     +              IDATE(3),TIMINC,TITLE(4),PI,ZUF(4)
      COMMON /NODS/ X(350),Y(350),DISP(700),FORCE(700),XCOM1(2400)
      COMMON /ELEM/ NODEL(8,300),ICOM2(1500),COM4(61500)
      COMMON /MATS/ EM(9),PM(9),TM(9),RHOM(9),ETAM(9),C(9,3),ITYP(300)
      COMMON /STIF/ ELK(18,18),GLOBK(700,185)
      COMMON /GAPT/ S,T,SHAPE(9),DNXDS(8),DNXDT(8),PCOM(1611),
     +              PLACEL(3),WEILIN(3)
      DIMENSION SHEAR(2),SNORM(2),STEXS(50),Q(12),IIT(50)
C
      PT=0.0
      NUM=700
      DO 912 INOD=1,NFS
  912 IIT(INOD)=0
C
      DO 120 ITER=1,NITS
      DO 90 IF=1,NFS
      ANG=THETA(IF)
      COS2=DCOS(ANG)*DCOS(ANG)
      SIN2=DSIN(ANG)*DSIN(ANG)
      SINCOS=DSIN(ANG)*DCOS(ANG)
```

```
C
      DO 50 IS=1,2
      NUMEL=NELF(IF,IS)
      MAT=ITYP(NUMEL)
      C1=C(MAT,1)
      C2=C(MAT,2)
      C3=C(MAT,3)
      P=PM(MAT)
      RHO=RHOM(MAT)
      NO=6
C
      DO 10 J=1,NO
      Q(2*J-1)=DISP(2*NODEL(J,NUMEL)-1)
   10 Q( 2*J )=DISP( 2*NODEL(J,NUMEL) )
C
C**** CALCULATE THE STRESS AT EACH DUAL NODE
C
      STRN1=0.0D0
      STRN2=0.0D0
      STRN3=0.0D0
C
      DO 20 IV=1,NO
      L=IV*2
      K=L-1
      DNXDX=BFAULT(K,IS,IF)
      DNXDY=BFAULT(L,IS,IF)
      STRN1=STRN1+DNXDX*Q(K)
      STRN2=STRN2+DNXDY*Q(L)
   20 STRN3=STRN3+DNXDX*Q(L)+DNXDY*Q(K)
C
      STRS1=C1*STRN1+C2*STRN2
      STRS2=C2*STRN1+C1*STRN2
      STRS3=C3*STRN3
C
C**** OBTAIN AVERAGE STRESS, ROTATE STRESS, AND FIND EXCESS STRESS
C
C
C**** ADD IN LITHOSTATIC PRESSURE
C
C     SLITH=RHO*9.81*DEPTH(IF,IS)
      SLITH=2911.0*9.81*DEPTH(IF,IS)
      SNORM(IS)=(STRS1*COS2+STRS2*SIN2+2.0*STRS3*SINCOS)+SLITH
      SHEAR(IS)=(STRS2-STRS1)*SINCOS+STRS3*(COS2-SIN2)
   50 CONTINUE
C
      YP=(Y(NODEL(3,NUMEL))+Y(NODEL(1,NUMEL)))/2.0
      POREP=YP*1000.0D0*9.81D0
      SNAV=((SNORM(1)+SNORM(2))/2.0D0)-POREP
      SHAV=(SHEAR(1)+SHEAR(2))/2.0D0
      IF (SNAV.GT.0.0D0) SNAV=0.0D0
      FRS=MU*DABS(SNAV)
      IF (FRS.GE.DABS(SHAV)) GO TO 101
  103 IF (SHAV.LT.0.0D0) GO TO 102
      STEXS(IF)=SHAV-FRS
      GO TO 65
  102 STEXS(IF)=SHAV+FRS
      GO TO 65
  101 IF (ITER.EQ.1) IIT(IF)=1
      IF (IIT(IF).EQ.0) GO TO 103
      STEXS(IF)=0.0D0

   65 WRITE(10,200) SNAV,SHAV,STEXS(IF)
  200 FORMAT(' SNORM',1PE10.3,' SHEAR',1PE10.3,' EXCESS',1PE10.3)
   70 CONTINUE
   90 CONTINUE
C
C**** TEST FOR CONVERGENCE
C
      DO 75 IF=1,NFS
      IF (DABS(STEXS(IF)).GT.1.0D5) GO TO 100
   75 CONTINUE
C
      WRITE(6,78)
   78 FORMAT('0SUBROUTINE FSHEAR COMPLETED')
      CALL TIME(1,1)
      RETURN
```

```
C
C
C**** CALCUALTE THE GLOBAL FORCE COMPONENTS, BY NUMERICAL INTEGRATION
C
  100 DO 110 IF=1,NFS
      NEL1=NELF(IF,1)
      NEL2=NELF(IF,2)
      NOD1=NODEL(1,NEL1)
      NOD2=NODEL(2,NEL1)
      NOD3=NODEL(3,NEL1)
      NOD4=NODEL(1,NEL2)
      NOD5=NODEL(2,NEL2)
      NOD6=NODEL(3,NEL2)
C
      DO 80 IG=1,3
      S=PLACEL(IG)
      SS=S*S
      OSCOEFT(IG)
      SHAPE(1)=(SS-S)/2.0
      SHAPE(2)=1.0-SS
      SHAPE(3)=(SS+S)/2.0
      DNXDS(1)=S-0.5
      DNXDS(2)=-2.0*S
      DNXDS(3)=S+0.5
C
      DXXDS=DNXDS(1)*X(NOD1)+DNXDS(2)*X(NOD2)+DNXDS(3)*X(NOD3)
      DYXDS=DNXDS(1)*Y(NOD1)+DNXDS(2)*Y(NOD2)+DNXDS(3)*Y(NOD3)
      TAU=(SHAPE(1)*STEXS(IF)+SHAPE(2)*STEXS(IF)+
     +     SHAPE(3)*STEXS(IF))*FAC
      S1DST=SHAPE(1)*DS*TAU
      S2DST=SHAPE(2)*DS*TAU
      S3DST=SHAPE(3)*DS*TAU
C
      FORCE(2*NOD1-1)=FORCE(2*NOD1-1)+(S1DST*DXXDS)
      FORCE( 2*NOD1 )=FORCE( 2*NOD1 )+(S1DST*DYXDS)
      FORCE(2*NOD2-1)=FORCE(2*NOD2-1)+(S2DST*DXXDS)
      FORCE( 2*NOD2 )=FORCE( 2*NOD2 )+(S2DST*DYXDS)
      FORCE(2*NOD3-1)=FORCE(2*NOD3-1)+(S3DST*DXXDS)
      FORCE( 2*NOD3 )=FORCE( 2*NOD3 )+(S3DST*DYXDS)
      FORCE(2*NOD4-1)=FORCE(2*NOD4-1)-(S1DST*DXXDS)
      FORCE( 2*NOD4 )=FORCE( 2*NOD4 )-(S1DST*DYXDS)
      FORCE(2*NOD5-1)=FORCE(2*NOD5-1)-(S2DST*DXXDS)
      FORCE( 2*NOD5 )=FORCE( 2*NOD5 )-(S2DST*DYXDS)
      FORCE(2*NOD6-1)=FORCE(2*NOD6-1)-(S3DST*DXXDS)
   80 FORCE( 2*NOD6 )=FORCE( 2*NOD6 )-(S3DST*DYXDS)

  110 CONTINUE
C
C**** RESOLVE STIFFNESS EQUATION
C
      DO 115 ICOP=1,NNOD2
  115 DISP(ICOP)=FORCE(ICOP)
      CALL MA07BD(GLOBK,DISP,NUM,NNOD2,KSIZE,PT)
      WRITE(6,620)ITER
  620 FORMAT(' END OF ITERATION',I4)
  120 CONTINUE
C
      WRITE(6,140)
  140 FORMAT('0**** EXECUTION STOPPED IN FSHEAR : ',
     +       'EXCESS SHEAR STRESS HAS NOT CONVERGED')
      CALL TIME(1,1)
      STOP
      END
C
C
C*********************************************************************************
C
C
      SUBROUTINE SURF
C     ===============
C
C**** PLOT THE DISPLACEMENT PROFILE OF SPECIFIED NODES
C
      IMPLICIT REAL*8 (A-H,O-W)
      COMMON /NODS/ X(350),Y(350),DISP(700),FORCE(700),XCOM1(2400)
      DIMENSION NN(2),XP(2,50),YDISP(2,50),XPLT(50),YPLT(50)
```

```
C
      XSTART=1.0E50
      XEND=0.0
      YBOT=0.0
      YTOP=0.0
      READ(4,10)NOSECT
   10 FORMAT(I5)
      DO 20 IS=1,NOSECT
      READ(4,10)NN(IS)
      NO=NN(IS)
      DO 20 IN=1,NO
      READ(4,10)NOD
      XP(IS,IN)=X(NOD)
      YDISP(IS,IN)=DISP(2*NOD)
      YD=YDISP(IS,IN)
      XD=XP(IS,IN)
      XSTART=AMIN1(XSTART,XD)
      XEND=AMAX1(XEND,XD)
      YBOT=AMAX1(YBOT,YD)
   20 YTOP=AMIN1(YTOP,YD)
C
      XSTART=XSTART/1000.0
      XEND=XEND/1000.0
      CALL CSPACE(0.0,1.2,0.0,1.0)
      CALL PSPACE(0.1,1.1,0.25,0.5)
      CALL MAP(XSTART,XEND,YTOP,YBOT)
      CALL AXES
C
      DO 30 IS=1,NOSECT
      NO=NN(IS)

      DO 40 IN=1,NO
      XPLT(IN)=XP(IS,IN)/1.0E3
   40 YPLT(IN)=YDISP(IS,IN)
   30 CALL CURVEO(XPLT,YPLT,1,NO)
C
      RETURN
      END
C
C
C*********************************************************************************
C
C
      SUBROUTINE FAIL
      ===============
C
C
C**** CALCULATES WHETHER FAILURE HAS OCCURED AT EACH STRESS
C**** GAUSS POINT IN EACH ELEMENT
C
      IMPLICIT REAL*8 (A-H,O-W)
      COMMON /CONS/ NTRI,NQUAD,NINCS,NNOD,KSIZE,KSBW,NNOD2,NMAT,INITEM,
     +              IDATE(3),STMAX,TITLE(4),PI,ZUF(4)
      COMMON /NODS/ X(350),Y(350),DISP(700),FORCE(700),XSTPOS(4,300),
     +              YSTPOS(4,300)
      COMMON /ELEM/ NODEL(8,300),NGAUSS(300),NOTEL(300),NOQEL(300),
     +          NOTCOL(300),NOQCOL(300),DIFFOP(9,300),BLIB(144,300),
     +      PRINC(16,300),CREEP(36,300)
      COMMON /FALE/ STRO(4,350),CFAIL(4,300),FANGL(4,300),IFAIL(4,300)
      COMMON /MATS/ EM(9),PM(9),TM(9),RHOM(9),ETAM(9),C(9,3),ITYP(300)
C
      FMU=1.0
      PHI=DATAN(1.0/FMU)*90.0/PI
      NOEL=NTRI
      NO=3
C
C**** START LOOP OVER TRIANGULAR AND QUADRILATERAL ELEMENTS
C
      DO 700 IT=1,2
      IF (IT.EQ.1) GO TO 20
      NOEL=NQUAD
      NO=4
   20 IF (NOEL.EQ.0) GO TO 700
C
      DO 550 IEL=1,NOEL
      IF (IT.EQ.1)NUMEL=NOTEL(IEL)
      IF (IT.EQ.2)NUMEL=NOQEL(IEL)
```

```
      MAT=ITYP(NUMEL)
      T=TM(MAT)
      SC=-4.19*T
      DO 555 IG=1,NO
      JPOS=(IG-1)*4
C
C**** ADD LITHOSTATIC PRESSURE TO EACH OF THE PRINCIPAL STRESSES
C
      DEPTH=YSTPOS(IG,NUMEL)
      HYD=RHOM(ITYP(NUMEL))*9.81*DEPTH
C
      P1=PRINC(1+JPOS,NUMEL)+HYD
      P2=PRINC(2+JPOS,NUMEL)+HYD
C
      S1=DMAX1(P1,P2)

      S3=DMIN1(P1,P2)
      SM=(S1+S3)/2.0
      TB=(S1-S3)/2.0
C
C**** TENSIONAL REGION
C
      IF (SM.LT.T) GO TO 551
      IFAIL(IG,NUMEL)=-1
      CFAIL(IG,NUMEL)=(T-SM)/T
      FANGL(IG,NUMEL)=0.0
      GO TO 555
  551 IF (SM.LT.-T)GO TO 552
      IFAIL(IG,NUMEL)=1
      CFAIL(IG,NUMEL)=(T-S1)/(T-SM)
      FANGL(IG,NUMEL)=0.0
      GO TO 555
C
C**** OPEN CRACK COMPRESSIONAL REGION
C
  552 SA=SC-2.0*T
      IF(SM.LT.SA) GO TO 553
      IFAIL(IG,NUMEL)=2
      TF=DSQRT(-4.0*T*SM)
      CFAIL(IG,NUMEL)=1.0-TB/TF
      FANGL(IG,NUMEL)=DARCOS(-TF/SM/2.0)*90.0/PI
      GO TO 555
C
C**** INTERMEDIATE REGION
C
  553 BETA=2.0/FMU*DSQRT(1.0-SC/T)+SC/T
      SB=SC*(1.0+FMU*FMU)+BETA*FMU*FMU*T
      TC=BETA*FMU*T-FMU*SC
      IF (SM.LT.SB) GO TO 554
      IFAIL(IG,NUMEL)=3
      CFAIL(IG,NUMEL)=1.0-TB/DSQRT((SM-SC)*(SM-SC)+TC*TC)
      FANGL(IG,NUMEL)=DATAN(TC/(SC-SM))*90.0/PI
      GO TO 555
C
C**** CLOSED CRACK COMPRESSIONAL REGION
C
  554 ALPHA=DSQRT(1.0+FMU*FMU)/FMU
      IFAIL(IG,NUMEL)=4
      CFAIL(IG,NUMEL)=1.0-ALPHA*TB/(BETA*T-SM)
      FANGL(IG,NUMEL)=PHI
  555 CONTINUE
  550 CONTINUE
  700 CONTINUE
C
      WRITE(6,10)
   10 FORMAT('0FAILURE CRITERIA CALCULATED')
      CALL TIME(1,1)
C
  600 RETURN
      END
C
C
C*********************************************************************************
C
C
C
```

```
      SUBROUTINE DISVEC
C     =================
C
C**** PLOTS THE DISPLACEMENT VECTOR AT EACH NODE
C
      IMPLICIT REAL*8 (A-H,O-W)
      REAL*8 KN,KS,MU
      COMMON /NODS/ X(350),Y(350),DISP(700),FORCE(700),XCOM1(2400)
      COMMON /FALT/ KN,KS,MU,FAC,BFAULT(12,2,50),
     +  DEPTH(50,2),THETA(50),FLTCRP(24,50),OFLTCR(24,50),
     +              STFBGN(24,50),NONOD(50,2),NELF(50,2),NITS,NFS
      COMMON /CONS/ NTRI,NQUAD,NINCS,NNOD,KSIZE,KSBW,NNOD2,NMAT,INITEM,
     +              IDATE(3),STMAX,TITLE(4),PI,ZUF(4)
      COMMON /VARS/ XMAX,XMIN,YMAX,YMIN,XOMAX,XOMIN,YOMAX,YOMIN,
     +          XSP,YSP,XVECS,YVECS,PLTO(123),NC,NUMEL,NGAUS,LCOM(2)
      COMMON /ELEM/ NODEL(8,300),NGAUSS(300),NOTEL(300),NOQEL(300),
     +          NOTCOL(300),NOQCOL(300),DIFFOP(9,300),BLIB(144,300),
     +          PRINC(16,300),CREEP(36,300)
      DIMENSION XPLT(3),YPLT(3)
C
C**** FIND THE LARGEST DISPLACEMENT, DIMAX
C
      DIMAX=0.0D0
      DO 10 I=1,NNOD
      DVEC=DSQRT(DISP(I*2-1)**2+DISP(I*2)**2)
   10 DIMAX=DMAX1(DVEC,DIMAX)
C
C**** SET UP PLOT COORDINATES
C
      XSP1=XSP+0.2
      CALL CSPACE(0.2,XSP1,0.0,1.0)
      CALL PSPACE(0.2,XSP1,0.0,1.0)
      CALL MAP(XMIN,XMAX,YOMIN,YOMAX)
C
C**** PLOT A CIRCLE AT EACH NODE
C
      CALL CTRSET(4)
      CALL CTRMAG(7)
      CALL PTPLOT(X,Y,1,NNOD,54)
      CALL CTRMAG(15)
      CALL CTRSET(1)
C
C**** PLOT DISPLACEMENT VECTOR
C
      XVECS=ABS(XMAX-XMIN)/(25.0*XSP)
      YVECS=ABS(YMAX-YMIN)/(25.0*YSP)
      SCALEX=XVECS/DIMAX
      SCALEY=YVECS/DIMAX
      DO 20 I=1,NNOD
      CALL POSITN(X(I),Y(I))
      XPL=X(I)+(DISP(I*2-1)*SCALEX)
      YPL=Y(I)+(DISP(I*2)*SCALEY)
   20 CALL JOIN(XPL,YPL)
C
C**** PLOT POSITION OF FAULT, IF ONE IS PRESENT
C
      IF (NFS.EQ.0) GO TO 60
C
      DO 70 IF=1,NFS
      NUMEL=NELF(IF,1)

      NOD1=NODEL(1,NUMEL)
      NOD2=NODEL(2,NUMEL)
      NOD3=NODEL(3,NUMEL)
      XPLT(1)=X(NOD1)
      YPLT(1)=Y(NOD1)
      XPLT(2)=X(NOD2)
      YPLT(2)=Y(NOD2)
      XPLT(3)=X(NOD3)
      YPLT(3)=Y(NOD3)
   70 CALL CURVED(XPLT,YPLT,1,3)
C
C**** ANNOTATE THE PLOT
C
   60 XSP1=XSP+0.4
      CALL PSPACE(0.0,XSP1,0.0,1.0)
```

```
      CALL CSPACE(0.0,XSP1,0.0,1.0)
      CALL MAP(XOMIN,XOMAX,YOMIN,YOMAX)
      XMAP1=(XMAX-XMIN)/XSP
      XCEN=(XMAX+XMIN)*0.5
      XLABEL=XCEN-((13.0/77.0)*XMAP1)
      YLABEL=(YMAX-YMIN)*0.15
      CALL POSITN(XLABEL,YLABEL)
      XLABEL=XLABEL+100.0*SCALEX
      CALL JOIN(XLABEL,YLABEL)
      CALL PLOTCS(XLABEL,YLABEL,'  100 METRES',12)
      XST=XCEN-((7.0/77.0)*XMAP1)
      YST=(YMAX-YMIN)*0.32
      CALL PLOTCS(XST,YST,'DISPLACEMENT VECTORS',20)
C
C**** ADD TITLE AND LABEL AXES
C
      CALL LABEL
C
      WRITE(6,11)
   11 FORMAT('0DISPLACEMENTS PLOTTED')
      RETURN
      END
C
C
C*********************************************************************************
C
C
      SUBROUTINE TANOM
      ================
C
C
C**** INCORPORATE INITIAL STRAINS DUE TO TEMPERATURE
C**** ANNOMALIES INTO THE FORCE VECTOR
C
      IMPLICIT REAL*8 (A-H,O-W)
      REAL*8 KN,KS,MU
      COMMON /CONS/ NTRI,NQUAD,NINCS,NNOD,KSIZE,KSBW,NNOD2,NMAT,INITEM,
     +              IDATE(3),TIMINC,TITLE(4),PI,ZUF(4)
      COMMON /ELEM/ NODEL(8,300),NGAUSS(300),NOTEL(300),NOQEL(300),
     +            NOTCOL(300),NOQCOL(300),DIFFOP(9,300),BLIB(144,300),
     +             COM1(15600)
      COMMON /MATS/ EM(9),PM(9),TM(9),RHOM(9),ETAM(9),C(9,3),ITYP(300)
      COMMON /GAPT/ S,T,SHAPE(8),DNXDS(8),DNXDT(8),TSHAPE(6,36),
     +              TDNXDS(6,36),TDNXDT(6,36),TW1W2(6,6),QSHAPE(3,72),
     +              QDNXDS(3,72),QDNXDT(3,72),QW1W2(3,9),COM2(258)
      COMMON /NODS/ X(350),Y(350),DISP(700),FORCE(700),XCOM1(2400)

      COMMON /FALE/ STR0(4,350),CFAIL(4,300),FANGL(4,300),IFAIL(4,300)
      DIMENSION NOD(8)
C
C**** INITIALISE, THEN READ IN NO. NODES WITH TEMP ANOM
C
      INITEM=1
      DO 10 I=1,4
      DO 10 J=1,NNOD
   10 STR0(I,J)=0.0D0
      READ(3,20)NNODT
   20 FORMAT(I5,F10.3)
C
C**** READ IN THE TEMP ANOMALY OF EACH NODE, AND CALCULATE THE
C**** INITIAL STRAIN COMPONENTS
C
      DO 30 I=1,NNODT
      READ(3,20)NODT,DELT
      ALPH=1.0E-5
      STR0(1,NODT)=-1.25*ALPH*DELT
      STR0(2,NODT)=STR0(1,NODT)
   30 CONTINUE
C
C**** CALCUALTE THE FORCE VECTOR FOR EACH  ELEMENT
C
      NOEL=NTRI
      NO=6
      DO 90 IT=1,2
      IF (IT.EQ.1) GO TO 200
      NOEL=NQUAD
      NO=8
```

```
  200 IF (NOEL.EQ.0) GO TO 90
C
      DO 80 IEL=1,NOEL
      IF (IT.EQ.2) GO TO 800
      NUMEL=NOTEL(IEL)
      NROW=NOTCOL(IEL)
      GO TO 900
  800 NUMEL=NOQEL(IEL)
      NROW=NOQCOL(IEL)
  900 CONTINUE
      IUSE=0
      DO 40 I=1,NO
      NOD(I)=NODEL(I,NUMEL)
      IF (IUSE.EQ.0.AND.STRO(1,NOD(I)).NE.0.0) IUSE=1
   40 CONTINUE
C
      IF (IUSE.EQ.0) GO TO 80
C
      NGAUS=NGAUSS(NUMEL)
      MAT=ITYP(NUMEL)
      C1=C(MAT,1)
      C2=C(MAT,2)
      C3=C(MAT,3)
      DO 70 IG=1,NGAUS
      DV=DIFFOP(IG,NUMEL)
      IPOS=(IG-1)*NO
      JPOS=IPOS*2
      STOX=0.0D0
      STOY=0.0D0
      STOXY=0.0D0

C
C**** CALCUALTE INITIAL STRAIN AT THIS GAUSS POINT
C
      IF(IT.EQ.2) GO TO 100
      DO 50 IV=1,NO
      SHAP=TSHAPE(NROW,IPOS+IV)
      STOX=STOX+SHAP*STRO(1,NOD(IV))
      STOY=STOY+SHAP*STRO(2,NOD(IV))
   50 STOXY=STOXY+SHAP*STRO(3,NOD(IV))
      GO TO 110
  100 DO 120 IV=1,NO
      SHAP=QSHAPE(NROW,IPOS+IV)
      STOX=STOX+SHAP*STRO(1,NOD(IV))
      STOY=STOY+SHAP*STRO(2,NOD(IV))
  120 STOXY=STOXY+SHAP*STRO(3,NOD(IV))
  110 CONTINUE
C
C**** OBTAIN THE INITIAL STRAIN FORCE VECTOR BY NUMERICAL INTEGRATION
C
      P=PM(MAT)
      STOZ=STOX/(1.0+P)
      STOX=STOX+P*STOZ
      STOY=STOY+P*STOZ
      DO 60 I=1,NO
      L=2*I
      K=L-1
      DNDX=BLIB(JPOS+K,NUMEL)
      DNDY=BLIB(JPOS+L,NUMEL)
      FORCE(2*NOD(I)-1)=FORCE(2*NOD(I)-1)+((DNDX*C1*STOX
     +                  +DNDX*C2*STOY+DNDY*C3*STOXY)*DV)
      FORCE(2*NOD(I))=FORCE(2*NOD(I))+((DNDY*C2*STOX
     +                +DNDY*C1*STOY+DNDX*C3*STOXY)*DV)
   60 CONTINUE
   70 CONTINUE
   80 CONTINUE
   90 CONTINUE
C
      WRITE(6,160)
  160 FORMAT('0STRAINS DUE TO TEMPERATURE ANOMALY CALCULATED')
      CALL TIME(1,1)
C
      RETURN
      END
C
C
C*******************************************************************************
```

```
C
C
      SUBROUTINE DEVST
      ================
C
C
C**** CALCULATES THE DEVIATORIC STRESS VECTORS
C**** AND STORES THEM IN PRINC
C
      IMPLICIT REAL*8 (A-H,O-W)
      COMMON /CONS/ NTRI,NQUAD,NINCS,NNOD,KSIZE,KSBW,NNOD2,NMAT,INITEM,
     +              IDATE(3),STMAX,TITLE(4),PI,ZUF(4)
      COMMON /ELEM/ NODEL(8,300),NGAUSS(300),NOTEL(300),NOQEL(300),
     +          NOTCOL(300),NOQCOL(300),DIFFOP(9,300),BLIB(144,300),
     +         PRINC(16,300),CREEP(36,300)

      STMAX=0.0
      NSGAUS=3
      NEL=NTRI
      DO 50 IS=1,2
      IF (IS.EQ.1) GO TO 10
      NSGAUS=4
      NEL=NQUAD
   10 CONTINUE
      DO 40 IEL=1,NEL
      IF (IS.EQ.1) NUMEL=NOTEL(IEL)
      IF (IS.EQ.2) NUMEL=NOQEL(IEL)
      DO 30 IG=1,NSGAUS
      JPOS=(IG-1)*4
      HYD=(PRINC(JPOS+1,NUMEL)+PRINC(JPOS+2,NUMEL)+
     +     PRINC(JPOS+3,NUMEL))/3.0
      DO 20 I=1,3
   20 PRINC(JPOS+I,NUMEL)=PRINC(JPOS+I,NUMEL)-HYD
      STMAX=DMAX1(DABS(PRINC(1+JPOS,NUMEL)),DABS(PRINC(2+JPOS,NUMEL)),
     1     DABS(PRINC(3+JPOS,NUMEL)),STMAX)
   30 CONTINUE
   40 CONTINUE
   50 CONTINUE
C
      RETURN
      END
```

REFERENCES

Andrews, D.J. and Sleep, N.H., 1974. Numerical modelling of tectonic flow behind island arcs. Geophys. J. R. astr. Soc., 38, 237-251.

Artyushkov, E.V., 1973. Stresses in the lithosphere caused by crustal thickness inhomogeneities. J. Geophys. Res., 78, 7675-7708.

Ashby, M.F. and Verrall, R.A., 1978. Micromechanisms of flow and fracture and their relevance to the rheology of the upper mantle. Phil. Trans. R. Soc., 200A, 59-95.

Barazangi, M. and Isacks, B., 1971. Lateral variations of seismic wave attenuation in the upper mantle above the inclined earthquake zone of the Tonga island arc system: deep anomaly in the upper mantle. J. Geophys. Res., 76, 8493-8516.

Barazangi, M., Pennington, W. and Isacks, B., 1975. Global study of seismic wave attenuation in the upper mantle behind island arcs using pP waves. J. Geophys. Res., 80, 1079-1092.

Barker, P.F. and Hill, I.A., 1981. Back arc extension in the Scotia Sea. Phil. Trans. R. Soc. Lond. A, 300, 249-262.

Barlow, J., 1976. Optimal stress locations in finite elements. Int. J. Numer. Meth. Eng., 10, 241-251.

Barrel, J., 1914. The strength of the earths crust. J. Geol., 22, 729.

Benioff, H., 1954. Orogenesis and deep crustal structure: additional evidence from seismology. Geol. Soc. Amer. Bull., 65, 385-400.

Bibee, L.D., Shor, G.C., and Lu, R., 1980. Inter-arc spreading in the Mariana trough. Marine Geol., 35, 183-197.

Bodine, J.H. and Watts, A.B., 1979. Lithospheric flexure seaward of the Bonin and Mariana trenches. Earth Planet. Sci. Lett., 43, 132-148.

Bott, M.H.P., 1971. The interior of the earth, Arnold.

Bott, M.H.P., 1982a. The interior of the earth (2nd Edition). Arnold.

Bott, M.H.P., 1982b. The mechanism of continental splitting. Tectonophysics, 81, 301-309.

Bott, M.H.P. and Dean, D.S., 1972. Stress systems at young continental margins. Nature (Phys. Sci.), 235, 23-25.

Bott, M.H.P. and Kusznir, N.J., 1979. Stress distributions associated with compensated plateau uplift structures with application the continental splitting mechanism. Geophys. J. R. astr. Soc., 56, 451-459.

Brace, W.F., 1964. Brittle fracture of rocks. In: W.R. Judd (editor). State of stress in the earth's crust. Elsevier, New York, N.Y., 111-174.

Caldwell, J.G, Haxby, W.F., Karig, D.E. and Turcotte, D.L., 1976. On the applicability of a universal elastic trench profile. Earth Planet. Sci. Lett., 31, 239-246.

Carter, N.L., 1976. Steady state flow of rcoks. Rev. Geophys. Space Phys., 14, 301-360.

Chapman, M.E. and Talwani, M., 1982. Geoid anomalies over deep sea trenches. Geophys. J. R. Astr. Soc., 68, 349-369.

Chapple, W.M. and Tullis, T.E., 1977. Evaluation of the forces that drive the plates. J. Geophys. Res., 82, 1967-1984.

Chapple, W.M. and Forsyth, D.W.., 1979. Earthquakes and bending of the plate at trenches. J. Geophys. Res., 84, 6729-6749.

Christensen, D.H. and Ruff, L.J., 1983. Outer rise earthquakes and seismic coupling. Geophys. Res. Lett., 10, 697-700.

Chase, C., 1978. Extension behind island arcs and motions relative to hotspots. J. Geophys. Res., 83, 5385-5387.

Chen, A.T., Frohlich, C. and Latham, G.V., 1982. Seismicity of the

forearc marginal wedge (accretionary prism). J. Geophys. Res., 87, 3679-3690.

Cook, R.D., 1981. Concepts and applications of finite element analysis (2nd Edition). Wiley.

Davies, G.F., 1980. Mechanics of subducted lithosphere. J. Geophys. Res, 85, 6304-6318.

Davies, G.F., 1981. Regional compensation of subducted lithosphere: effects on geoid, gravity and topography from a preliminary model. Earth Planet. Sci. Lett., 54, 431-441.

Davies, G.F., 1983. Subduction zone stresses: constraints from mechanisms and from topographic and geoid anomalies. Tectonophysics, 99, 85-98.

Dean, D.S., 1973. Stress analysis of the lithosphere. Unpublished Ph.D. thesis. University of Durham.

Desai, C.S. and Abel, J.F., 1972. Introduction to the finite element method. Van Nostrand Reinhold.

Dickenson, W.R. and Seely, D.R., 1979. Structure and stratigraphy of fore-arc regions. Bull. Am. Petrol. Geol., 63, 2-31.

Eguchi, T., Uyeda, S. and Maki, T., 1979. Seismotectonics and tectonic history in the Andaman sea. Tectonophysics, 57, 35-51.

Eisenberg, M.A. and Malvern, L.E., 1973. On finite element integration in natural co-ordinates. Int. J. Numer. Meth. Eng., 7, 574-575.

Elsasser, W.M., 1969. Convection and stress propagation in the upper mantle. In: S.K. Runcorn (Editor), The application of modern physics to the earth and planetry interiors. Wiley. New York. 223-246.

Elsasser, W.M., 1971. Sea floor spreading as thermal convection. J. Geophys. Res., 76, 1101-1112.

Engdahl, E.R. and Scholz, C.H., 1977. A double Benioff zone beneath the

Aleutians: an unbending of the lithosphere. Geophys. REs. Lett., 4, 473-476.

England, P. and Wortel, R., 1980. Some consequences of the subduction of young slabs. Earth Planet. Sci. Lett., 47, 403-415.

Felippa, C.A., 1966. Refined finite element analysis of linear and nonlinear two dimensional structures. Unpublished Ph.D. thesis. University of California, Berkley.

Forsyth, D.W., 1977. The evolution of the upper mantle beneath mid ocean ridges. Tectonophysics, 38, 89-118.

Forsyth, D.W. and Uyeda, S., 1975. On the relative importance of the driving forces of plate motion. Geophys J. R. astr. Soc., 43, 163-200.

Fujita, K. and Kanamori, H., 1981. Double seismic zones and stresses of intermediate depth earthquakes. Geophys. J. R. Astr. Soc., 66, 131-156.

Goldsmith, W., Sackman, J.L and Ewert, F., 1976. Static and dynamic strength of Barre granite. Int. J. rock Mech. Ming. Sci., 13, 303-309.

Goodman, R.E., Taylor, R.E., and Brekke, T.L., 1968. A model for the mechanics of jointed rock. J. Soil Mech. and Found. Proc. ASCE., 94, 637-658.

Grellet, C. and Dubois, J., 1982. The depth of trenches as function of the subduction rate and age of the lithosphere. Tectonophysics, 82, 45-56.

Griggs, D.T., 1972. The sinking lithosphere and the focal mechanism of deep earthquakes. In: E.C. Robertson (Editor), Nature of the solid earth. McGraw-Hill, New York, N.Y., 361-384.

Hanks, T.C., 1971. The Kuril trench-Hokkaido rise system: large shallow

earthquakes and simple models of deformation. Geophys. J. R. astr. Soc., 23, 173-189.

Harper, J.F., 1975. On the driving forces of plate tectonics. Geophys. J. R. astr. Soc., 40, 465-474.

Hasebe, K., Fujii, N. and Uyeda, S., 1970. Thermal processes under island arcs. Tectonophysics, 10, 335-355.

Haxby, W.F. and Turcotte, D.L., 1976. Stresses induced by the addition or removal of overburden and associated thermal effects. Geology, 4, 181-184.

Hayes, D.E. and Ewing, M., 1970. Pacific boundary structure. In: A.E. Maxwell (editor), The Sea. Ideas and observations on progress in the study of the seas. 4, 29-72. Wiley-Interscience, New York. N.Y.

Hsui, A.T. and Toksoz, M.N., 1981. Back arc spreading: trench migration, continental pull or induced convection ?. Tectonophysics, 74, 89-98.

Isacks, B., Oliver, J. and Sykes, L.R., 1968. Seismology and the new global tectonics. J. Geophys. Res., 73, 5855-5899.

Isacks, B. and Molnar, P., 1969. Mantle earthquake mechanisms and the sinking of the lithosphere. Nature, 223, 1121-1124.

Isacks, B. and Molnar, P., 1971. Distribution of stresses in the descending lithosphere from a global survey of focal mechanism solutions of mantle earthquakes. Rev. Geophys. Space Phys., 9, 103-174

Isacks, B. and Barazangi, M., 1977. Geometry of Benioff zones: lateral segmentation and downwards bending of the subducted lithosphere. In: M. Talwani and W.C. Pittman III (Editors), Island arcs, deep sea trenches and back arc basins. Maurice Ewing Ser., Am. Geophys. Union, 1, 163-174.

Jaeger, J.C. and Cook, N.G.W., 1976. Fundamentals of rock mechanics.

Second edition, Chapman and Hall science paperbacks.

Jurdy, D.M., 1979. Global plate reorganisations and spreading in back arc basins. J. Geophys. Res, 84, 6796-6802.

Kanamori, H., 1977. Seismic and aseismic slip along subduction zones and their tectonic implications. In: M. Talwani and W.C. Pittman III (Editors), Island arcs, deep sea trenches and back arc basins. Maurice Ewing Ser., Am. Geophys. Union, 1, 163-174.

Karig, D.E., 1970. Ridges and basins of the Tonga-Kermadec island arc system. J. Geophys. Res., 75, 239-254.

Karig, D.E., 1971a. Origin and development of marginal basins in the Western Pacific. J. Geophys. Res., 76, 2542-2561.

Karig, D.E., 1971b. Structural history of the Mariana island arc system. Geol. Soc. Am. Bull., 82, 323-344.

Karig, D.E., 1974. Evolution of arc systems in the Western Pacific. Ann. Rev. Earth Planet. Sci., 2, 51-68.

Karig, D.E. and Mammerickx, J., 1972. Tectonic framework of the New Hebrides island arc. Marine Geol., 12, 187-205.

Karig, D.E., Anderson, R.N. and Bibee, L.D., 1978. Characteristics of back arc spreading in the Mariana trough. J. Geophys. Res., 83, 1213-1226.

Karner, G.D., Steckler, M.S. and Thorne, J.A., 1983. Long term thermo-mechanical properties of the continental lithosphere. Nature, 304, 250-253.

Kirby, S.H., 1983. Rheology of the lithosphere. Rev. Geophys. Space Phys., 21, 1458-1487.

Kulm, L.D., Schweller, W.J. and Masais, A., 1977. A preliminary analysis of the subduction processes along the Andean continental margin, 6 to 45 S. In: M. Talwani and W.C. Pittman III (Editors), Island arcs,

deep sea trenches and back arc basins. Maurice Ewing Ser., Am. Geophys. Union, 1, 163-174.

Kusznir, N.J., 1976. Theoretical studies of the geodynamics of accretion boundaries in plate tectonics. Unpublished Ph.D. thesis. University of Durham.

Kusznir, N.J. and Bott, M.H.P., 1977. Stress concentration in the upper lithosphere caused by underlying visco-elastic creep. Tectonophysics, 43, 247-256.

Lathram, E.H. and 14 others, 1974. Circum-Pacific and Caribbean orogens: Alaska. In: A.M. Spencer (Editor), Mesozoic-Cenozoic orogenic belts. Scottish academic press. Edinburgh.

Leeds, A.R., Knopoff, L. and Kanssel, E.G., 1974. Variations of an upper mantle structure under the Pacific ocean. Science, 186, 141-143.

Le Pichon, X., 1968. Sea floor spreading and continental drift. J. Geophys. Res., 73, 3661-3697.

Le Pichon, X., Francheteau, J. and Bonnin, J., 1973. Plate tectonics. Elsevier.

Le Pichon, X. and Angelier, J., 1981. The Aegean sea. Phil. Trans. R. Soc. Lond. A., 300, 357-372.

Linton, M.D., 1982. Elastic wave propagation in embankment dams. Unpublished Ph.D. thesis. University of Durham.

Ludwig, W., Den, N. and Murachi, S., 1973. Seismic reflection measurements of Southwest Japan margin. J. Geophys. Res., 78, 2508-2516.

McAdoo, D.C., Caldwell, J.G and Turcotte, D.L., 1978. On the elastic-perfectly plastic bending of the lithosphere under generalised loading with application to the Kurile trench. Geophys. J.R. astr. Soc., 54, 11-26.

McKenzie, D.P., 1969. Speculations on the causes and consequences of plate motions. Geophys. J. R. Astr. Soc., 18, 1-32.

McKenzie, D.P. and Parker, D.L., 1967. The North Pacific: an example of tectonics on a sphere. Nature, 216, 1276-1280.

Megard, F. and Phillip, H., 1976. Plio-Quaternary tectono-magmatic zonation and plate tectonics in the central Andes. Earth Planet. Sci. Lett., 33, 231-245.

Melosh, H.J. and Raefsky, A., 1981. A simple and effective method for introducing faults into finite element computations. Bull. Seism. Soc. Am., 71, 1391-1400.

Melosh, H.J. and Fleitout, L., 1982. The earthquake cycle in subduction zones. Geophys. Res. Lett., 9, 21-24.

Minear, J.W. and Toksoz, M.N., 1970a. Thermal regime of a downgoing slab and new global tectonics. J. Geophys. Res., 75, 1397-1419.

Minear, J.W. and Toksoz, M.N., 1970b. Thermal regime of a downgoing slab. Tectonophysics, 10, 367-390.

Minster, J.B., Jordan, T.H., Molnar, P. and Haines, E., 1974. Numerical modelling of instantaneous plate tectonics. Geophys. J. R. astr. Soc., 36, 541-576.

Minster, J.B. and Jordan, T.H., 1978. Present-day plate motions. J. Geophys. Res., 83, 5331-5354.

Mithen, D.P., 1980. Numerical investigations into the mechanism of graben formation. Unpublished Ph.D. thesis. University of Durham.

Molnar, P. and Sykes, L.R., 1969. Tectonics of the Caribbean and middle America regions from focal mechanism and seismicity. Geol. Soc. Am. Bull., 80, 1639-1684.

Molnar, P. and Atwater, T., 1978. Interarc spreading and Cordilleran tectonics as alternatives to the age of the subducted lithosphere.

Earth Planet. Sci. Lett., 41, 330-340.

Molnar, P., Freedman, D. and Shih, J.S.F., 1979. Lengths of intermediate and deep seismic zones and temperatures in downgoing slabs of lithosphere. Geophys. J. R. Astr. Soc., 56, 41-54.

Morgan, W.J., 1968. Rises, trenches, great faults and crustal blocks. J. Geophys. Res., 73, 1959-1982.

Nakamura, K. and Uyeda, S., 1980. Stress gradient in back arc regions and plate subduction. J. Geophys. Res., 85, 6419-6428.

Ngo, D. and Scordelis, A.C., 1967. Finite element analysis of reinforced concrete beams. J. Amer. Concrete. Inst., 64, 152-163.

Nicholas, A. and Poirier, J.P., 1976. Crystalline plasticity and solid state flow in metamorphic rocks. John Wiley and sons, London, New York, Sydney and Toronto.

Oliver, J. and Isacks, B., 1967. Deep earthquake zones, anomalous structures in the upper mantle and lithosphere. J. Geophys. Res, 72, 4259-4275.

Park, M.J.M., 1981. Numerical analysis of deformation of the upper part of subduction zones. Unpublished Ph.D. thesis. University of Durham.

Parsons, B. and Molnar, P., 1976. The origin of the outer topographic rise associated with trenches. Geophys. J.R. astr. Soc., 45, 707-712.

Parsons, B. and Sclater, J.G., 1977. An analysis of the variation of the ocean floor bathymetry and heat flow with age. J. Geophys. Res., 82, 803-827.

Pitman, W.C., III, and Hayes, D.E., 1968. Sea-floor spreading in the gulf of Alaska. J. Geophys. Res., 73, 6571-6580.

Plafker, G., 1965. Tectonic deformation associated with the 1964 Alaskan earthquake. Science, 148, 1675-1687.

Plafker, G., 1976. Tectonic aspects of the Guatemala earthquake of 4 Feb. 1976. Science, 193, 1201-1208.

Press, F., 1970. Regionalised earth models. J. Geophys. Res., 75, 6575-6581.

Richardson, R.M., Soloman, S.C. and Sleep, N.H., 1979. Tectonic stress in the plates. Rev. Geophys. Space Phys., 17, 981-1019.

Richter, F.M., 1973. Dynamical models for sea floor spreading. Rev. Geophys. Space Phys., 11, 223-287.

Ringwood, A.E., 1977. Petrogenesis and island arc systems. In: M. Talwani and W.C. Pittman III (Editors), Island arcs, deep sea trenches and back arc basins. Maurice Ewing Ser., Am. Geophys. Union.

Ruff, L. and Kanamori, H., 1980. Seismicity and the subduction process. Phys. Earth Planet. Inter., 23, 240-252.

Ruff, L. and Kanamori, H., 1983a. The rupture process and asperity distribution of three great earthquakes from long period P-waves. Phys. Earth Planet. Inter., 31, 202-230.

Ruff, L. and Kanamori, H., 1983b. Seismic coupling and uncoupling at subduction zones. Tectonophysics, 99, 99-117.

Schubert, G., Yuen, D.A. and Turcotte, D.L., 1975. Role of phase transitions in a dynamic mantle. Geophys. J. R. astr. Soc., 42, 705-735.

Seely, D.R., Vail, P.R. and Walton, G.G., 1974. Trench slope model. In: C.A. Burke and C.L. Drake (editors), The geology of continental margins. Springer-Verlag. New York. 249-260.

Service, K.G. and Douglas, A., 1973. Boundaries and fractures in finite element models of geological structures. Geophys. J. R. astr. Soc., 32, 1-14.

Sleep, N.H., 1979. The double seismic zone in downgoing slabs and the viscosity of the mesosphere. J. Geophys. Res., 84, 4565-4571.

Sleep, N.H. and Toksoz, M.N., 1971. Evolution of marginal basins. Nature, 233, 548-550.

Smith, A.T. and Toksoz, M.N., 1972. Stress distribution beneath island arcs. Geophys. J. R. astr. Soc., 29, 289-318.

Stauder, W., 1968. Tensional character of earthquake foci beneath the Aleutian trench with relation to sea floor spreading. J. Geophys. Res., 73, 7693-7701.

Stauder, W., 1975. Subduction of the Nazca plate under Peru as evidenced by focal mechanisms and seismicity. J. Geophys. Res., 80, 1053-1064.

Sykes, L.R., 1966. The seismicity and deep structure of island arcs. J. Geophys. Res., 71, 2981-3006.

Stefani, J.P., Geller, R.J. and Kroger, G.C., 1982. A direct measurement of the distance between a hypocenter in a Benioff-Wadati zone and the slab-asthenosphere contact. J. Geophys. Res., 87, 323-328.

Thatcher, W., Matsuda, T., Kato, T., and Rundle, J.B., 1980. Lithospheric loading by the 1896 Riku-uu Earthquake, Northwest Japan: Implications for plate flexure and asthenospheric rheology. J. Geophys. Res., 85, 6429-6435.

Toksoz, M.N., Minear, J.W. and Julian, B.R., 1971. Temperature fiels and geophysical effects of a downgoing slab. J. Geophys. Res., 76, 1113-1138.

Toksoz, M.N., Sleep, N.H. and Smith, A.T., 1973. Evolution of the downgoing lithosphere and the mechanisms of deep focus eartquakes. Geophys. J. R. astr. Soc., 35, 285-310.

Toksoz, M.N. and Bird, P., 1977. Formation and evolution of marginal

basins and continental plateaus. In: M. Talwani and W.C. Pittman III (Editors), Island arcs, deep sea trenches and back arc basins. Maurice Ewing Ser., Am. Geophys. Union, 1, 379-393.

Toksoz, M.N. and Hsui, A.T., 1978. Numerical studies of back arc convection and the formation of marginal basins. Tectonophysics, 50, 177-196.

Tovish, A., Schubert, G. and Luyendyk, B.P., 1978. Flow pressure and the angle of subduction: non-Newtonian corner flows. J. Geophys. Res., 83, 5892-5898.

Turcotte, D.L, 1974. Membrane tectonics. Geophys. J. R. astr. Soc., 36, 33-42.

Turcotte, D.L. and Oxburgh, E.R., 1969. Convection in a mantle with variable physical properties. J. Geophys. Res, 74, 1458-1474.

Turcotte, D.L. and Schubert, G.C., 1971. Structure of the olivine-spinel phase boundary in the descending lithosphere. J. Geophys. Res., 76, 7980-7987.

Turcotte, D.L., Torrance, K.E. and Hsui, A.T., 1973. Convection in the earths mantle. In: B.A. Bolt (Editor), Methods of computational physics, 13. Academic press, New York, N.Y., 431-453.

Turcotte, D.L. and Oxburgh, E.R., 1976. Stress accumulation in the lithosphere. Tectonophysics, 35, 183-199.

Turcotte, D.L., McAdoo, D.C. and Caldwell, J.G., 1978. An elastic-perfectly plastic analysis of the bending of the lithosphere at a trench. Tectonophysics, 47, 193-205.

Utsu, T., 1971. Seismological evidence for anomalous structure of island arcs with special reference to the Japanese region. Rev. Geophys. Space Phys., 9, 839-890.

Uyeda, S., 1982. Subduction zones: an introduction to comparative

subductology. Tectonophysics, 81, 133-159.

Uyeda, S. and Kanamori, H., 1979. Back arc opening and the mode of subduction. J. Geophys. Res., 84, 1049-1061.

Veith, K.F., 1977. The nature of the dual zone of seismicity in the Kuriles arc. Trans. Am. Geophys. Union, 58, 1232.

Vetter, U.R. and Meissner, R.O., 1979. Rheologic properties of the lithosphere and applications to passive continental margins. Tectonophysics, 59, 367-380.

Vine, F.J. and Matthews, D.H., 1963. Magnetic anomalies over oceanic ridges. Nature, 199, 947-949.

Walcott, R.I., 1970. Flexural rigidity, thickness and viscosity of the lithosphere. J. Geophys. Res., 75, 3941-3954.

Walcott, R.I., 1976. Lithospheric flexure, analysis of gravity anomalies, and the propagation of seamount chains. In: G.H. Sutton, M.N. Manghnani and R. Moberly (Editors), The geophysics of the Pacific ocean basin and its margin. Geophys. Monogr. Ser. Am. Geophys. Union. Washington, D.C. 431-438.

Watts, A.B., 1978. An analysis of isostacy in the worlds oceans: 1 Hawaiian-Emperor seamount chain. J. Geophys. Res., 83, 5989-6004.

Watts, A.B. and Talwani, M., 1974. Gravity anomalies seaward of deep sea trenches and their tectonic implications. Geophys. J. R. astr. Soc., 36, 57-90.

Watts, A.B and Cochran, J.R., 1974. Gravity anomalies and flexure of the lithosphere along the Hawaiian-Emperor seamount chain. Geophys. J. R. astr. Soc., 38, 119-141.

Watts, A.B., Cochran, J.R. and Selzer, G., 1975. gravity anomalies and flexure of the lithosphere: a three dimensional study of the Great Meteor seamount, Northeast Atlantic. J. Geophys. Res., 80,

1391-1398.

Watts, A.B., Karner, G.D. and Steckler, M.S., 1980. Observations of flexure and the state of stress in the oceanic lithosphere. J. Geophys. Res., 85, 6369-6376.

Weissel, J.K., 1977. Evolution of the Lau basin by the growth of small plates. In: M. Talwani and W.C. Pitman III (editors). Island arcs, deep sea trenches and back arc basins. Maurice Ewing Ser., Am. Geophys. Union, 1, 429-436.

Weissel, J.K., 1981. Magnetic lineations in marginal basins of the Western Pacific. Phil. Trans. R. Soc. Lond. A., 300, 223-247.

Westbrook, G.K., 1975. Unpublished PhD. thesis. University of Durham.

Westbrook, G.K., 1982. The Barbados ridge complex: tectonics of a mature forearc system. In: J.K. Legett (editor), Trench-forearc geology. Blackwell. London. 275-294.

Woodward, D.J., 1976. Visco-elastic finite element analysis of subduction zones. Unpublished Ph.D. thesis. University of Durham.

Wortel, R., 1982. Seismicity and rheology of subducted slabs. Nature, 296, 553-556.

Zienkiewicz, O.C., 1977. The finite element method in engineering science. McGraw-Hill.

Zienkiewicz, O.C., Watson, M. and King, I.P., 1968. A numerical method of visco-elastic stress analysis. Int. J. Mech. Sci., 10, 807-827.